Title

Lung Structure and the Intrinsic Challenges of Gas Exchange.

Journal

Comprehensive Physiology, 6(2)

ISSN

2040-4603

Authors

Hsia, Connie CW
Hyde, Dallas M
Weibel, Ewald R

Publication Date

2016-03-01

DOI

10.1002/cphy.c150028

Peer reviewed

HHS Public Access

Author manuscript

Compr Physiol. Author manuscript; available in PMC 2016 September 16.

Published in final edited form as:

Compr Physiol. ; 6(2): 827–895. doi:10.1002/cphy.c150028.

Lung Structure and the Intrinsic Challenges of Gas Exchange

Connie C.W. Hsia[*,1], **Dallas M. Hyde**[2], and **Ewald R. Weibel**[*,3]

[1]Department of Internal Medicine, University of Texas Southwestern Medical Center, Dallas, Texas, USA [2]California National Primate Research Center, University of California at Davis, Davis, California, USA [3]Institute of Anatomy, University of Bern, Bern, Switzerland

Abstract

Structural and functional complexities of the mammalian lung evolved to meet a unique set of challenges, namely, the provision of efficient delivery of inspired air to all lung units within a confined thoracic space, to build a large gas exchange surface associated with minimal barrier thickness and a microvascular network to accommodate the entire right ventricular cardiac output while withstanding cyclic mechanical stresses that increase several folds from rest to exercise. Intricate regulatory mechanisms at every level ensure that the dynamic capacities of ventilation, perfusion, diffusion, and chemical binding to hemoglobin are commensurate with usual metabolic demands and periodic extreme needs for activity and survival. This article reviews the structural design of mammalian and human lung, its functional challenges, limitations, and potential for adaptation. We discuss (i) the evolutionary origin of alveolar lungs and its advantages and compromises, (ii) structural determinants of alveolar gas exchange, including architecture of conducting bronchovascular trees that converge in gas exchange units, (iii) the challenges of matching ventilation, perfusion, and diffusion and tissue-erythrocyte and thoracopulmonary interactions. The notion of erythrocytes as an integral component of the gas exchanger is emphasized. We further discuss the signals, sources, and limits of structural plasticity of the lung in alveolar hypoxia and following a loss of lung units, and the promise and caveats of interventions aimed at augmenting endogenous adaptive responses. Our objective is to understand how individual components are matched at multiple levels to optimize organ function in the face of physiological demands or pathological constraints.

Introduction

This review discusses the origin and complexities of lung structure and the challenges that must be surmounted to optimize pulmonary gas exchange in mammalian lungs, and their implications for induced adaptation in response to ambient hypoxia or loss of lung units. The fundamental challenges to any gas exchange system are to: (i) transfer inspired oxygen onto circulating hemoglobin without physically mixing air and blood, (ii) maximize transfer efficiency while maintaining the integrity of the air-tissue-blood interface, (iii) provide feedback mechanisms that match each step of the transfer process to one another and to whole body metabolic demands, (iv) incorporate sufficient structural and functional reserves

*Correspondence to connie.hsia@utsouthwestern.edu; ewald.weibel@ana.unibe.ch.

and the ability to rapidly recruit reserves as demand increases, and (v) provide versatile adaptive mechanisms to compensate for the unexpected loss of capacity, and preserve or restore gas-exchange function in the face of external insults or disease. These topics are organized in the following order:

1. The origin and development of vertebrate and human lung architecture are discussed in the perspective of organismic function and evolution.

2. Structure-function correlations in the pulmonary gas exchanger are quantitatively assessed by the structural determinants of pulmonary diffusing capacity (DL) on the basis of a morphometric model that is subjected to critical examination, considering the issue of oxygen capture by alveolar-capillary blood, and the comparison of morphometric versus physiological estimates of DL. This is followed by a description of the architecture of lung parenchyma and its influence on gas exchange function, discussing the principle of connectivity, which ensures that all parts work in concert, the dynamic modulation of the gas exchanger with the respiratory cycle, and the important role of capillary erythrocytes. The correlated complexities of the ventilation-perfusion system are presented, including how airways and pulmonary arteries and veins connect to the gas exchanger to effect ventilation-perfusion convergence in the acinus, the basic unit of gas exchange. To understand the functional implications of acinar structure, we consider a typical path model of the human acinus and its effects on diffusion screening of oxygen uptake on the basis of physical principles, discussing the limitations of the screening model. Finally, we consider the implications of acinar path length, or stratified inhomogeneity, on gas exchange.

3. Components of pulmonary gas transport must be matched so as to load incoming oxygen onto hemoglobin in the most efficient manner possible, all of the transfer steps must be well matched to one another and to whole body metabolic demands. This section briefly reviews the fundamental concepts of ventilation-perfusion and perfusion-diffusion matching, the tissue-erythrocyte interactions, and the interdependence in structure-function between the lung and the thorax. The consequences of physiological mismatch are discussed. The influence of body size on gas exchange structure and function, and the role of the spleen as an extrapulmonary source of gas exchange reserve, are described.

4. Induced structural adaptation and its functional consequences. This section considers the sources of adaptive mechanisms invoked following the loss of lung units, for example, caused by pneumonectomy as a model of restrictive lung disease, or during exposure to alveolar hypoxia, for example, high-altitude residence. The consequences of dysanaptic, or mismatched, lung growth and adaptation are presented.

Origin and Architecture of the Mammalian Lung

Evolutionary origins

All vertebrates require a continuous supply of oxygen (O_2) to maintain metabolism and life. August Krogh termed this essential need “the call for oxygen” (215), while Max Kleiber called it “the fire of life” (208). The intracellular fire or combustion occurs within the mitochondrion (Fig. 1A) where enzymes of the Krebs tricarboxylic acid cycle break down stepwise small molecules derived from nutrients (such as pyruvate from sugars or fatty acids from lipids), the end product being CO_2. Along the cycle hydrogen ions (H^+) are released that are transferred to the respiratory chain by means of pyridine nucleotides (NADH) to finally react with O_2 to produce H_2O (Fig. 1B). The energy thus released is eventually transferred to F1-ATPase to generate high-energy phosphate bonds of adenosine-triphosphate (ATP) that can move into the cytoplasm to transfer energy to drive the vital functions of the cell. While the process of mitochondrial ATP generation by oxidative phosphorylation depends on the supply of both fuels and O_2, there is an important difference: whereas fuels, carbohydrates and fat, taken up in the gut can be stored both in liver and fat tissue as well as within the cytoplasm (Fig. 1A), O_2 cannot be stored. It is, therefore, essential that O_2 is supplied to the mitochondria continuously in proportion to the instantaneous needs of the cell. In higher organisms delivery is ensured by taking in O_2 from environmental air, binding it to circulating hemoglobin in erythrocytes in the lungs, and transporting it via the cardiovascular system to the cells. Conversely, the waste gas CO_2 that derives from the Krebs cycle is eliminated via the lung.

Gas transport in air or fluid is accomplished by convection (mass transport) and molecular diffusion. Diffusion is driven by O_2 and CO_2 pressure gradients, influenced by the conductance of the carrier (i.e., blood or air) and its carrying capacity for O_2 and CO_2. Of note, the O_2 carrying capacity of blood via binding to hemoglobin is the same as the O_2 capacity of air, that is, 20 mL O_2 per 100 mL of air or blood. This is of particular interest in comparative physiology as it reveals remarkable convergence in respiration between air-filled tracheae in insects that penetrate deep into the muscle cells to reach the mitochondria, and the muscle capillaries in mammals, in both cases with similar O_2 content.

In mammals, the O_2 cascade from air to cells requires convection into the external gas exchanger (lungs) by ventilation through the airways, diffusion of O_2 into the blood, convective flow of blood into the tissues, and diffusion into cells to the mitochondria. The driving force is the partial pressure of oxygen (PO_2) that declines stepwise (Fig. 2).

All vertebrate gas exchangers exhibit extensive exchange surfaces where air and blood come into intimate contact. This exchange surface is ventilated through a system of airways and perfused with blood from the branched pulmonary artery into the pulmonary veins. There are two basic lung designs: (i) *Alveolar lungs*, found in mammals, amphibians and reptiles, are ventilated by to-and-fro movement of air into a large and varying volume of parenchyma that serves as bellows driven by the chest and diaphragm. At the periphery, the airways form alveoli as cul-de-sac structures where air is exposed to blood along a complicated surface; as a result of to-and-fro ventilation the PO_2 of alveolar air and arterial blood are lower than that of inspired air (Fig. 3). (ii) *Bird lungs* are compact, stiff organs that are ventilated from large

air sacs in a continuous unidirectional flow through a set of parabronchi with air capillaries in close contact with blood capillaries; gas exchange occurs in a cross-current pattern of blood and air flow and thus enables ~25% more efficient extraction of O_2 as compared to alveolar type lungs (81) (Fig. 3). There is speculation based on computational and fossil evidence that this more efficient bird-style lung may have evolved in Sauropod Dinosaurs. The computational argument is offered by a mathematical model for ventilation with an 11-m-long trachea where the work of breathing becomes limiting in a bellows type of lung (66,279). The fossil evidence is the presence of pneumatic foramina in Sauropod skeleton that would be necessary for airflow to air sacs (368). Other evidence of the greater efficiency of the bird lung compared to mammalian lung is provided by the limit in the size of the largest flying mammal, a bat (*Pteropus edulis*, 1.38 kg), as compared to the largest bird capable of steady flapping flight (the trumpeter swan, *Olor buccinator*, 12.5 kg) (45,234). One may speculate that the less favorable scaling of pulmonary gas exchange parameters relative to body mass in the bat than bird might be an important reason why bats have not evolved to the larger body size of the largest flying bird.

Why has mammalian evolution not adopted the avian blueprint of a more efficient pulmonary gas exchanger? (399). Perhaps the most important reason is that the small, dense, and extremely delicate avian lung is a rigid system. The structures that mechanically support the air capillaries are extremely reduced, essentially comprised of the densely arranged blood capillaries with a minimal complement of lining cells and connective tissue (165). Mechanical support is achieved by apposing the lung to the stiff thoracic spine with fused thoracic vertebrae that keep the trunk of the body, the origin of wing muscles, stiff during flight (81). This arrangement would not be compatible with the high degree of flexibility that the spine of mammals, including humans, must allow in locomotion, particularly in quadrupeds where running and galloping involve the entire trunk musculature in conjunction with the legs (2). In the mammalian skeleton designed for supporting locomotion, there would be no suitable stiff support for a dense and delicate avian-type lung. Thus, mammals compromised with a seemingly less efficient alveolar lung; however, most of the efficiency deficits can be overcome by adaptation in other parts of the system.

Functional performance of the mammalian lung design

Performance of the lung must be considered in the framework of the pathway for O_2 that begins with inspiration of fresh air and ends at the mitochondrial respiratory chain where O_2 is consumed in the process of oxidative phosphorylation (Fig. 2), and where mitochondrial PO_2 is close to zero. Under steady-state conditions, O_2 flow rate $\left(\dot{V}\,O_2\right)$ is the same through each step of the respiratory cascade: it must equal the total O_2 consumption in all mitochondria of the body, and it must correspond to the rate of O_2 uptake from environmental air in the lung. At each step *i*, the $\dot{V}\,O_2$ can be expressed as the product of the prevailing pressure difference with the conductance for O_2 transfer G(*i*) (Fig. 2). In the circulation, the conductance of blood G(B) is the product of blood flow and O_2 capacitance of blood, in the lung the conductance from air to blood G(A-B) is the lung diffusing capacity (DL), which depends crucially on structural parameters such as alveolocapillary surface area, thickness of the tissue diffusion barrier, and capillary blood volume. Similar relations

hold for the conductance of O_2 transfer from capillary blood to cells G(B-C), and for the transfer of O_2 through oxidative phosphorylation in the mitochondria (376,395).

One may postulate that this complex system is well designed if the conductances are matched to overall functional requirements, which are determined by the energetic needs of the cells. The hypothesis of "*symmorphosis*" (395) is defined as regulated morphogenesis resulting in structural design commensurate with functional needs. In this concept, formation of structural elements is regulated to satisfy but not exceed functional requirements of the system, a principle of economy. Functional requirements are defined as the highest rate of O_2 consumption achieved in maximal exercise when all muscles, the body's largest organ system, are active (344). By comparative physiology, one can show that the mammalian respiratory system evolved approximately in agreement with the hypothesis of symmorphosis (396), that is, across species the lung is built reasonably to meet the needs of gas exchange and the nonrespiratory functions of the pulmonary vasculature. The maximal lung volume is confined by the thoracic cavity and the components of the lung must be efficiently packaged. This is accomplished by a set of interdigitating trees for air, venous, and arterial blood that converge in the small gas-exchange units at the end of their branches. The proximal conducting bronchi, arteries, and veins comprise the *conducting zone*, while the distal gas exchange units comprise the *respiratory zone*. Connective tissue enwraps the conducting airways and vessels and extends into the respiratory zone to provide three-dimensional support from the hilum to the pleural surface thereby ensuring mechanical stability and connectivity of all parts in this large organ.

In all mammals, the gas exchanger is built on the same architectural blueprint and uses the same building blocks of tissue and cells; it differs essentially by quantitative characteristics in that the alveolar gas-exchange surface increases with body size nearly in proportion to body mass (Fig. 4) (396). The alveoli become smaller as body mass decreases so that the surface per unit volume (surface density) in the smallest mammal, the Etruscan shrew weighing a mere 2 g, is 6.5 times greater than that in human lung (Fig. 5) (112). This size difference also allows economizing on the tissue support of the alveolocapillary complex. Figure 6A shows an alveolar capillary of a monkey lung with an endothelial cell lining the blood space and a type-1 alveolar epithelial cell lining the alveolus, separated by a thin interstitial space with basement membranes and some connective tissue fibers for support. Both cells are characterized by forming rather attenuated cytoplasmic leaflets that form the major part of the gas-exchange barrier and measuring a mere 0.3 μm in the thinnest areas; in the human lung the cytoplasmic leaflet of an average type-1 cell covers an area of 5000 μm^2 (58, 372); the cell bodies are tucked away in niches between capillaries to minimize the effective harmonic mean barrier thickness (0.6 μm).

We can discern the limitations in the adaptation of the alveolar-capillary membrane by examining the thinnest membrane that occurs in the Etruscan shrew (Fig. 6B): the linings of endothelium and epithelium are reduced to minimal cytoplasmic leaflets consisting of two plasma membranes combined with a minimal interstitium that measures only 0.02 μm in the thinnest parts, resulting in a harmonic mean thickness of 0.23 μm (112). Figure 6B shows another mechanism for minimizing cell structures while still maintaining their vitality. Type-1 alveolar epithelial cells achieve their large covering area (5000 μm^2) via branching

cytoplasmic leaflets without losing their connections to the nucleus (372). This complex cell structure occurs in all mammalian lungs, but is pushed to the extreme in the Etruscan shrew (Fig. 6B) where perinuclear cytoplasm gives rise to four very thin cytoplasmic leaflets two of which split again at a certain distance—a most remarkable feature to minimize tissue mass as well as barrier thickness. Other structural modifications observed in shrews include larger heart and lung volume to body weight ratios. These same structural modifications are also observed in the lungs of flying mammals (bats) and highlight the potentials of structural modifications in the mammalian lung (234). These modifications: a larger lung volume, a high density of gas-exchanging surface and a very thin air-blood barrier, coupled with functional adaptations, such as high heart and respiration rates, are observed in species requiring very high O_2 consumption and pulmonary diffusion.

In conclusion, despite its apparent gas exchange inefficiency as compared to avian lungs, the mammalian alveolar lung has been evolutionarily successful. It allows for evolution of organisms adapted to an enormous range of habitats and life styles. For example, the range of body size that can be supplied with energy extends from the minuscule Etruscan shrew (2 g) and a similarly sized bat—the same size as the smallest hummingbird—to cows and horses (half a ton) and to elephants (4 tons), thus over 6 orders of magnitude without any changes to the lung's blueprint. This design also allows instantaneous augmentation of energetic needs by a factor of 10 or more when an animal changes from a state of rest or quiet roaming to running, either for food or for escaping a predator; the lung can easily accommodate the rapidly increasing blood flow that the heart generates, for example, by allowing the capillary volume to increase. The alveolar lung also allows adaptation to athletic life styles such as in dogs, horses, and in the pronghorn antelopes of the Rocky Mountains, the mammalian elite athlete whose maximal O_2 consumption is more than twice that of the dog and that even sustains low ambient O_2 tensions at high altitude without loss in performance. Adaptability is possible because the alveolar lung allows for a multitude of modulations and fine-tuning, such as varying the density of gas exchange surface or the thickness of diffusion barrier without compromising mechanical robustness of the microstructure or the overall organ. The basis for this adaptability will be discussed in detail in the following sections.

Developing an integrated complex of airways and blood vessels for gas exchange

To function as a gas exchanger, the mammalian lung must establish an extensive surface over which blood comes into close contact with inspired air. Developmentally, this raises the question how a coupled "sprinkler system" for air and blood can be built to ensure efficient and matched ventilation and perfusion to each of the 400 million gas-exchange units from the central sources, the trachea, pulmonary artery, and veins, respectively. Another linked problem is how to fold this large surface into the confined chest cavity and ensure ventilation and perfusion access to each point in space. Both problems are solved during development by adhering to two architectural principles: (i) the principle of *complexity*, based in the growth processes related to fractal geometry (235) is most prominent in the gradual construction of an airway system with a branched tree of airways that become "decorated" by a complex alveolar surface in the last generations; (ii) the principle of *correlativity* between airways and blood vessels, which must be designed to match the air space geometry

to allow gas exchange, arteries and veins diverging from the hilar region in concert with the airways, and then converging with the alveoli in the gas-exchange region (376,384).

Lung development begins with a pair of primary lung buds that form at the distal end of the tracheal tube and separate from the foregut. The lung buds grow laterally into a loose mass of mesenchyme bounded by the splanchnopleura. At this stage the left and right pulmonary arteries form from the sixth aortic arches and grow along the tracheal tube into the mesenchymal bed where they link up with the loose vascular network that enwraps the gut and lung. This network is reached from the caudal side by the primitive pulmonary vein stem derived from the left side of the heart's atrium. By this early process, the pulmonary artery becomes closely related to the airway bud and its subsequent branches whereas the pulmonary vein is located in a more peripheral region of the mesenchymal bed. This spatial correlation between the airways and the two blood vessels remains throughout development and determines the correlated architecture of the mature lung.

Morphogenesis of lung architecture is governed by complex but systematic branching of the airways and blood vessels with the mesenchyme following suit. The primitive lung buds grow laterally in length and then begin to branch. The branch grows to a certain length then its terminal bulb splits into two daughter branches; these grow and split, and so on to systematically build an airway tree (Fig. 7). This dichotomous or bifurcating, branching process does not need to be symmetric. In some cases, one of the two daughters remains as large as the parent branch and continues to grow in its direction, while the other is much smaller and branches sideways. The result of this type of branching, also called *domain branching* (254), is the formation of a more or less straight airway stem with many lateral branches. Domain branching establishes a strong asymmetry of branching and is more prevalent in some animal lungs (e.g., mouse or dog) where some lobes are rather long slim structures between the heart and the chest wall. It is less prominent in the human lung with its more compact shape. As branching proceeds toward the periphery, the pattern of dichotomy prevails, but there still is some degree of asymmetry between the two daughter branches imposed by the prevailing space constraints, such as when a branch approaches a larger airway or blood vessel, an interlobular septum or the pleura. While branching occurs only at the tips all airways grow in length and diameter, about in proportion to overall lung growth. The result is a space-filling tree with a quite even distribution of the terminal tips in the lung volume. This growth process has all the characteristics of a fractal tree (Fig. 8) (235, 378): the branching process is self-similar, that is, the proportions between parent and daughter branch dimensions is about the same from one generation to the next, and the tips are space-filling. The functional consequences of this architectural principle will be further discussed later.

While the airway tree develops by growth and branching, the mesenchyme and the vasculature undergo related changes (Fig. 7). Those airways that do not further branch become ensheathed by a layer of dense mesenchyme from which smooth muscle cells and cartilage derive. The arteries and veins also receive a dense mesenchymal sheath with a varying amount of smooth muscle cells. The peripheral tufts of branched airway tubes that will eventually develop into gas exchange structures are embedded in looser mesenchyme containing a network of capillaries. The terminal airway buds, where further branching can

occur, are in close contact with a cell-rich mesenchyme, a decisive factor because the formation of a new pair of branches is induced by interaction of epithelial cells with the mesenchyme through a complex system of growth factors and receptors, (1,4,47,328).

In this early stage of morphogenesis, growth and branching occurs in a system of epithelial tubes lined by columnar epithelium resembling that of a gland (Fig. 7). This "*pseudoglandular stage*" of lung development lasts, in humans, until ~20 weeks of gestation when histogenesis of the gas-exchange structures begins by thinning the epithelium of the most peripheral generations combined with gradual widening of the ducts, the "*canalicular stage*" followed by the "*saccular stage*" shortly before birth (40, 41). This process leads to significant transformations in which mesenchyme becomes much reduced to form slim septa between the saccules (Fig. 9A). The capillaries, originally loosely spread in the vast mesenchyme, now approach the saccular surfaces forming a denser network closely apposed to the epithelial basement membrane. The saccular epithelium differentiates into the secretory alveolar type-2 cells that begin to produce surfactant, and the thin and vast squamous type-1 cells that form the potential air-blood barrier together with the apposed capillary endothelial cells (382).

This transformation occurs, in the human lung, over the six to eight most peripheral generations of the airway tree that together form the anlage of the acini. In the proximal airway tubes, a columnar epithelium forms the lining of conducting airways with ciliated and secretory cells developing gradually while the mesenchymal sheath forms a smooth muscle sleeve and, in the major airways, cartilage plates.

In the saccular stage, which lasts until the last weeks of gestation, each saccule is provided with its own capillary network so that the intersaccular septa characteristically contain a double capillary network (39) (Fig. 9A). This becomes radically changed in the last stage of morphogenesis, the "*alveolar stage*," when a network of strong connective tissue fiber strands, that had formed in the saccular walls, begin to lift off the saccular surface toward the center thus forming alveoli as side chambers of alveolar ducts and sacs (Fig. 9B). These fiber tracts form a network that is continuous with the fibrous sheath of the terminal bronchioles connecting the saccules and alveolar ducts to the conducting airway tree. This transformation rapidly increases alveolar surface area by increasing surface complexity (Fig. 10). In rats, the alveolar surface increases twice as fast as lung volume in the first three postnatal weeks, the phase of most intense alveolar formation (39). After this period, the surface continues to increase but at a slower rate, mostly due to hypertrophy, but there still seems to be some formation of new alveoli. In the human lung the pattern is similar, also beginning around birth, but continuing for a longer period, from fetal week 36 to 1 to 2 years of age (41). In this process, the capillary architecture is transformed to a simple network in the interalveolar septa (40).

The mature architecture of the gas exchanger is now reached: in human lung, the conducting airway tree ends in ~30,000 tufts of gas exchanging air ducts that form the acini, the complex of six to eight generations of branched alveolar ducts decorated with alveoli and a dense capillary network (Fig. 11) (394). As the lung enlarges with body growth, these structures enlarge, accompanied by a gradual increase in the number of alveoli, but it is

unclear how long the increase can continue. In mice and rats, new alveoli can form even late in life (88,349); whether this is also true in humans is debated.

As the airway tree grows, the pulmonary arteries and veins follow suit to form an integrated system of three interdigitating trees with their stems in the hilar region and their terminal branches converging in the gas-exchanging distal region (Fig. 12). The pulmonary arteries remain closely related to the airways and branch in parallel with these. In the last phase, when acinar structures begin to evolve as gas exchange units the arteries branch more frequently forming “supernumerary” branches to reach the much smaller and more numerous capillary gas exchange units that are about the size of alveoli (394). The pulmonary veins remain in a peripheral or interacinar position connecting to the outlet of capillary units with a greater number of branches than the alveolar ducts.

In summary, this morphogenetic process combined with growth of the organ generates complexity in the architecture of the airway tree and vasculature leading to the gas exchanger that solves the combined problem of gradually folding up a very large surface in direct relation to the structures serving an efficient and well-distributed ventilation and perfusion of this surface, and all this before gas exchange even begins, that is, before birth. The design of the airways results from a combination of branching at the tips, thus multiplying the number of gas-exchange units, with growth of the stems and branches such that, at each branch point, the length and diameter of the daughter branches is reduced by a similar factor corresponding to the principle of self-similarity that is a central characteristic of fractal geometry (235). In the final step, the formation of wide saccules in the terminal airway generations followed by adding alveoli to enlarge their surface, also mimics the fractal process of adding folds upon folds to increase the surface density without increasing the containing volume (40,384).

Structure-Function Correlations

Physiological design principles of the pulmonary gas exchanger

The pulmonary gas exchanger is characterized by a close relationship between the air spaces and the blood capillaries over a large surface area and across a minimal tissue barrier. Alveoli are formed around terminal branches of the airway tree; and in the walls of these alveoli, a dense capillary network is connected to the terminal branches of pulmonary artery and pulmonary vein. The airways and blood vessels converge on a very large interface of close contact. The conducting airways and pulmonary arteries are designed to minimize both dead space and flow resistance and are provided with substantial wall structures, such as smooth muscle layers, controlling the distribution of air and blood flow; by contrast, in the gas exchanger part the air and blood volumes are maximized and spread over an extensive surface while the tissue barrier that separates air and blood is minimized.

The formation of alveoli as side pockets of peripheral airways (Fig. 13) not only augments parenchymal air volume but also substantially increases the surface-to-volume ratio of distal airways. The slim alveolar walls contain a close-meshed capillary network that spans between the terminal branches of the pulmonary artery and pulmonary vein (Fig. 14). The tissue supporting these alveolar wall structures is very thin so that the capillary blood

occupies about half the volume of the alveolar septa (Fig. 15). This dense arrangement of capillaries in the alveolar walls that are in direct air contact on both sides causes a high density of capillary blood volume and surface area in the peripheral air spaces with a minimal tissue barrier thus creating favorable conditions for efficient gas exchange.

The very thin alveolar tissue barrier that separates blood and air is comprised of two continuous cell layers, epithelium and capillary endothelium, and an interstitial space of variable composition and thickness (Fig. 16) (383). It is functionally essential that both the alveolar and capillary surfaces are lined by a complete and tight cell layer to control the transfer between the extracellular fluid spaces: plasma and interstitial and alveolar surface lining fluid (Fig. 17). The existence of a complete alveolar epithelium constituted of two cell types was first demonstrated by Frank Low under electron microscopy (232). Figure 16 shows that both the endothelial cells and the type-1 alveolar epithelial cells form thin continuous cytoplasmic leaflets that extend from the slim cell body with the nucleus to cover the alveolocapillary surface. This constitutes the very thin cellular lining of the air-blood barrier, a minimization that reduces the resistance to gas diffusion. The alveolar epithelium is a mosaic of two cell types (Fig. 18): type-1 cells form very thin cytoplasmic leaflets that cover 95% of the alveolar surface; interspersed within epithelium we find a seemingly larger type-2 cell that secretes both the phospholipid and protein components of surfactant (Fig. 19). There are remarkable size differences between these two cell types (58): what is often called the “large” type-2 cell has a mean volume of ~900 μm^3 and covers 180 μm^3 of alveolar surface, whereas the type-1 cell has a volume of 1800 μm^3 and covers 5000 μm^2 of surface. Even though there are twice as many type-2 cells 95% of the alveolar surface is covered by type-1 cells. It is noteworthy that type-1 cells are extraordinarily complex (discussed in Section above, Origin and architecture of the mammalian lung). Whereas a typical epithelial cell has one apical face bounded by a cell junction complex, the type-1 epithelial cell branches to form multiple apical faces at varying distances from the nucleus (Fig. 6); these had been seen by early histologists who called them “non-nuclear plates” but they are not disjoined from the nucleated cell body but connected by cytoplasmic stems (372). This peculiarity is a further example for the special efforts in minimizing the barrier to gas diffusion from air to blood.

The interstitium of the alveolar septum is the space between the epithelial and endothelial basement membranes (Fig. 16); it is associated with connective tissue fibers that form a fine network interwoven with the capillary network (Fig. 20). Owing to this arrangement, an actual interstitial space occurs only on one side of each capillary, whereas on the other side there is no interstitial space because the basement membranes of the thin endothelial and epithelial leaflets are fused (Fig. 16). This is a further feature for minimizing barrier thickness as on about half the barrier surface the fusion of epithelial and endothelial basement membranes does not allow interstitial fluid to accumulate. The alveolar interstitial space is complex (Fig. 21). Besides the septal fiber system (collagen and elastic fibers), we find fibroblasts that form very long extensions and serve multiple functions. For one they are responsible for the formation and maintenance of the fiber system. They also form elements of myofibroblasts, mostly in the form of focal actomyosin bundles that span across the septum from the basement membrane of one epithelial cell to that on the other side thus serving as braces of the interstitial space (382). The support function of these interstitial

structures becomes accentuated at the free edge of the septum where a strong alveolar entrance ring made of connective tissue fibers and some smooth muscle cells forms (Fig. 21B); the architectural importance of these structures will be discussed below. A special interstitial cell type is the pericyte, a derivative of fibroblasts with myofibroblast characteristics, that is closely associated with capillaries (Fig. 21B) (374).

Model of pulmonary gas-exchange capacity

Gas exchange between alveolar air and capillary blood depends on ventilation that maintains alveolar P_{O_2} at an adequate level and on perfusion of the capillary network with mixed venous blood from the pulmonary arteries (Fig. 22); as blood flows along the surface of the air-blood barrier, it receives O_2 that diffuses across the barrier and eventually leaves the gas exchanger as oxygenated blood into pulmonary veins. The rate of O_2 uptake by diffusion is described by the equation of Christian Bohr (26):

$$\dot{V}_{O_2} = (PA_{O_2} - P\bar{c}_{O_2}) \cdot DL_{O_2} \quad (1)$$

where PA_{O_2} is the O_2 partial pressure in alveolar air (in mmHg), $P\bar{c}_{O_2}$ the mean P_{O_2} in pulmonary capillary blood, and DL_{O2} the lung's O_2 conductance or the pulmonary diffusing capacity (in mL [min mmHg]$^{-1}$). Bohr introduced this theoretical proposition (26) because he found that the P_{O_2} of capillary blood at the end of transit through the capillary bed, that is, the arterial P_{O_2}, was often larger than alveolar P_{O_2}. Consequently, he rejected the theory that O_2 was exchanged purely by diffusion and postulated that active secretion must in part be invoked as a mechanism for O_2 transfer from air to blood, and he found support for this view from J. S. Haldane (128). However, this postulate was soon disproved by Marie and August Krogh (216) on the basis of greatly improved measurements, thus establishing the basic validity of Eq. (1). But this equation is too much simplified with regards to the nature of the term DL_{O2}, which is related not only to physical diffusion alone but also depends on the chemical reaction of O_2 with hemoglobin within erythrocytes, as worked out by Roughton and Forster (305).

The mean capillary P_{O_2} depends on blood flow and gas exchange and is obtained by integration of the progression of O_2 loading onto hemoglobin in erythrocytes (Fig. 22): erythrocytes enter the capillary network at low O_2 saturation corresponding to the P_{O_2} of mixed venous blood, $P\bar{v}_{O2}$, and leave the capillaries nearly saturated at arterial Pa_{O2}. Alveolar P_{O_2} is generally taken to be a homogeneous parameter, but varies considerably within the peripheral air spaces, in part because of the serial arrangement of alveoli and the gas exchange units along the ventilation pathway. All parameters to the right of Eq. (1) are significantly affected by anatomical features. DL_{O2} is largely determined by the surface area and the air-blood barrier thickness. The P_{O_2} difference is established by ventilation and perfusion of the gas-exchange units, which may be affected by the design of the airway and vascular trees within the acinus.

Structural determinants of pulmonary diffusing capacity—In Eq. (1), DL_{O2} is the total conductance for O_2 diffusion from alveolar air into capillary erythrocytes until it is bound to hemoglobin. The conductance of the system may be theoretically estimated from the physical dimensions and material properties of the gas exchanger, considering the geometry of the alveoli, tissue barrier, and capillary blood. As proposed by Roughton and Forster (305), this conductance consists of two serial steps (Fig. 23): (i) diffusive O_2 flow across the barrier, the so-called membrane conductance DM_{O2}, and (ii) O_2 binding to hemoglobin in the red blood cells or the conductance of capillary blood De_{O2} (both in $mL \cdot min^{-1} \cdot torr^{-1}$). Their overall effect on O_2 flow is obtained by adding their resistances or the reciprocal of the conductance:

$$1/DL_{O_2} = 1/DM_{O_2} + 1/De_{O_2} \quad (2)$$

DM_{O2} is the conductance of a barrier that offers "passive" resistance to diffusion and depends essentially on the material properties of the barrier, estimated by a diffusion coefficient K, and on the dimensions of the barrier: the larger the surface area S and the thinner the barrier thickness t the greater the DM_{O2}, according to the formula $DM_{O2} = K\,S/t$. In contrast, De_{O2} is related to the composite process of diffusion into erythrocytes and the nonlinear binding of O_2 to hemoglobin (184,305).

Membrane conductance (DM_{O2})—The membrane barrier (Fig. 23) comprises a tissue barrier and a layer of blood plasma. In addition, a lining fluid layer of varying thickness spreads over the epithelial surface (Fig. 17). Even though these layers have distinct characteristics, they act as a single diffusion barrier (388). The two bounding surfaces of the tissue barrier are lined by independent cell layers, epithelium and endothelium, related to two separate functional spaces, alveoli and capillaries. The two surfaces are not perfectly matched and the thickness of the barrier varies considerably (Figs. 16, 21, and 23). Over about half the surface, the tissue barrier shows minimal thickness compatible with an intact structure: the thin cytoplasmic leaflets of type-1 epithelial cells are joined to the thin extensions of endothelial cells by the fused basement membranes leaving no interstitial space. In this region, the surface lining layer is very thin. Over the other half, the barrier is thicker because of the presence of connective tissue fibers (see Fig. 21) and cell bodies of epithelial and endothelial cells as well as fibroblasts.

The plasma layer shows even greater variation in thickness and distribution (Fig. 23). Since erythrocytes are corpuscular and of similar dimension as the capillaries the plasma layer can be vanishingly thin where the erythrocyte nearly touches the wall. But elsewhere there are "plugs" of thick plasma of varying size (87, 163, 388). The distortable erythrocytes contribute to the variable thicknesses of the plasma layer between erythrocyte and capillary surface. Furthermore, occasional leukocytes can impede O_2 diffusion into erythrocytes. The diffusion distance from capillary wall to erythrocyte membrane can vary from a few nm to several micrometers.

Strictly speaking the two layers of the barrier, tissue and plasma, offer different O_2 diffusion resistances (371). However, this distinction is unimportant under normal conditions (388).

Indeed, flow velocity of the plasma layer is much lower than the diffusion of O_2 so that plasma is quasistatic with respect to diffusion. Furthermore, under normal conditions the surface areas of alveoli, capillaries, and erythrocytes do not differ much, and the diffusion coefficients of tissue and plasma are also quite similar. We could therefore estimate the membrane diffusing capacity by considering O_2 diffusion from the alveolar surface to the interior of erythrocyte as:

$$\mathrm{DM}_{\mathrm{O2}}=K_{\mathrm{b}}\cdot \mathrm{S}\left(\mathrm{b}\right)/\tau_{\mathrm{hb}}=K_{\mathrm{b}}\cdot\left[S\left(A\right)+S\left(c\right)\right]/2\cdot\tau_{\mathrm{hb}} \quad (3)$$

where K_{b} is Krogh's permeation coefficient which is the product of two material properties of the barrier: the diffusion coefficient for O_2 in the tissue, D_{O2}, and the O_2 solubility β_{O2}, and is estimated at $3.3\times\cdot10^{-8}$ $cm^2\cdot min^{-1}\cdot mmHg^{-1}$. $S(b)$ is the surface area of the barrier, estimated as the mean of the alveolar and capillary surface areas, $S(A)$ and $S(c)$, respectively, the two most robust measures of the area of air-blood contact. The harmonic mean barrier thickness τ_{hb} is the mean of the reciprocals of the distance from the alveolar surface to the nearest erythrocyte membrane (Figs. 23 and 24). The harmonic mean is chosen as parameter for the diffusion resistance because the local rate of O_2 diffusion is inversely proportional to the diffusion distance; thus, summing or averaging the local conductances that support O_2 diffusion in parallel implies averaging the reciprocal thicknesses or obtaining their harmonic mean (388,392). The τ_{hb} can be estimated on sections of properly sampled lung tissue using stereological methods (159,264,375,388,391). One approach is to superimpose on electron micrographs a set of test lines made of a sampling segment (solid line) followed by a guard extension (broken line) (Fig. 24): when the solid sampling line segment hits the alveolar surface the distance to the nearest erythrocyte membrane is measured as the barrier intercept length l_{b}, preferably using a logarithmic scale, resulting in a nearly log-normal distribution of intercept lengths. From the data the harmonic mean total barrier thickness is obtained as:

$$\tau_{\mathrm{hb}}=(2/3)\cdot l_{\mathrm{hb}}=\frac{2}{3}\frac{n}{\sum_{i=1}^{n} l_i^{-1}} \quad (4)$$

where l_{hb} is the harmonic mean of the intercept lengths l_{b} (388,392).

The presence of a surface lining layer in the living lung may modify the barrier geometry as visualized on electron micrographs (9) with the consequence that both the barrier thickness and the alveolar surface are reduced to a similar degree because some thicker parts of the barrier become shifted beneath the surfactant pools (Fig. 17). The net effect on the estimate of DL_{O2} is therefore not very large (398) (discussed later).

Erythrocyte conductance—Erythrocyte conductance for O_2 (De_{O2}) involves three coupled events: (i) O_2 diffusion across erythrocyte membrane, (ii) diffusion to hemoglobin molecules within the erythrocyte interior, and (iii) nonlinear chemical reaction of O_2 with hemoglobin. To empirically account for this complexity Roughton and Forster (305)

expressed De_{O2} as the product of the pulmonary capillary blood volume (Vc) and a coefficient θ_{O2} (in mL O_2 $\cdot min^{-1} \cdot torr^{-1} \cdot mL(blood)^{-1}$) for the rate of O_2 binding to hemoglobin per unit of pressure gradient and whole blood volume:

$$De_{O_2} = \theta_{O_2} \cdot Vc \quad (5)$$

The specific conductance θ_{O2} is estimated *in vitro* on whole blood by stop-flow procedures, where a deoxygenated blood sample is rapidly mixed with a bolus of oxygenated plasma and the oxygenation rate of hemoglobin is measured spectroscopically (141,142,184,256,330,410). Because this is a difficult procedure, the reported estimates of θ_{O2} vary from 0.9 to 2.7 mL O_2 mL^{-1} min^{-1} $mmHg^{-1}$. In addition, θ_{O2} depends on the hematocrit or hemoglobin concentration, and is reduced in anemia (214). Furthermore, θ_{O2} is affected by blood properties, as expressed by Holland et al. (1977):

$$\theta_{O_2} = k'c \cdot (0.0587 \cdot \alpha_{O_2}) \cdot (1 - S_{O_2}) \cdot 0.01333 \cdot [\mathrm{Hb}] \quad (6)$$

where $k'c$ is the initial reaction velocity ($mmol^{-1}$ s^{-1}) of erythrocytes exposed to O_2 in solution; α_{O2} is the Bunsen solubility coefficient of O_2; S_{O2} is the (fractional) O_2 saturation of hemoglobin at the start of the stop-flow experiment; and [Hb] is hemoglobin content (g/100 mL). Considerable uncertainty remains about the value of $k'c$, which is estimated by the stopped flow method using rapid reaction devices. The main problem is the occurrence of an unstirred layer of plasma that surrounds the erythrocytes in the measuring chamber, which slows the reaction because it adds a diffusion barrier of unknown thickness. Holland et al. (141) estimated this slowing factor to be about 2. Correcting for this effect, Yamaguchi et al. (410) estimated θ_{O2} at 3.9 mL O_2 mL^{-1} min^{-1} $mmHg^{-1}$ for human blood. Heidelberger and Reeves (132) have avoided this problem by studying naked thin films of whole blood directly exposed to air. Erythrocyte size also affects θ_{O2}—reaction rate is faster in small erythrocytes, for example, in goats. A key problem is that $k'c$ is measured on desaturated blood, whereas pulmonary capillary blood saturation ranges from 30% in mixed venous blood to 98% in the end-capillary blood, and that $k'c$ falls rapidly above 75% saturation; therefore, θ_{O2} falls from about 4 to 1 mL O_2 mL^{-1} min^{-1} $mmHg^{-1}$ (132) as blood transits through the lung so that an “effective mean” value of θ_{O2} must be estimated by Bohr integration (Fig. 22) (199,376).

For normal human lungs and a blood [Hb] of 15 g/100 mL, an estimated θ_{O2} = 1.8 mL O_2 mL^{-1} min^{-1} $mmHg^{-1}$ is reasonable (410), but if the actual [Hb] varies an adjusted value can be approximated by multiplying this standard value by a proportionality factor: Adjusted θ_{O2} = unadjusted θ_{O2} ([Hb]/15.0).

Morphometry of the human lung in relation to diffusing capacity

Estimating theoretical diffusing capacity of human lung—With the aforementioned model in hand, we can attempt to estimate the diffusing capacity of the human lung on the basis of morphometric data in Table 1. These data, obtained by electron microscopy on seven young adults (average body mass 70 kg) (109, 388), reveal an alveolar

surface area of ~130 m^2 and a capillary surface ~10% smaller. These values are higher than the older data most commonly quoted in textbooks that had been derived from light microscopic studies, which did not adequately resolve the alveolar surface texture. The harmonic mean thickness of the tissue barrier is ~0.6 μm, whereas the harmonic mean total barrier thickness, measured from alveolar epithelium to erythrocyte surface (Fig. 24), is ~1.11 μm. The capillary volume is ~200 mL. With these data we calculate D_{LO_2} for the adult human lung to be ~150 to 200 mL $O_2 \cdot min^{-1} \cdot mmHg^{-1}$, the variation essentially depending on the choice of θ_{O2}. These data answer the question how the resistance to O_2 diffusion is distributed. Table 1 shows that the diffusion conductance of the "membrane" and that of the erythrocytes are similar, that is, resistance to O_2 uptake is nearly equally divided between membrane and erythrocyte.

The validity of morphometric estimates of diffusing capacity, based on reasonable model assumptions, must be established by comparison to physiological estimates. A typical physiological value of DL_{O2} measured in a healthy adult at rest is ~30 mL $O_2 \cdot min^{-1} \cdot torr^{-1}$, considerably less than that based on morphometric estimates. This large difference arises because (i) under resting conditions, O_2 flow required to support metabolism is only one-tenth of what the lungs are capable of transporting under heavy exercise, and (ii) physiological diffusing capacity increases in a linear relationship with respect to pulmonary blood flow from rest to peak exercise (152). Thus, lung structure provides large O_2 transport reserves that are not needed at rest but may be rapidly recruited upon exercise. Any comparison of the pulmonary *capacity* for diffusive O_2 uptake must be gauged to the highest achievable metabolic rate because the structural features determining DL_{O2} cannot be increased at short notice when demand fluctuates. The estimates of DL_{O2} in exercising humans are ~100 mL $O_2 \cdot min^{-1} \cdot mmHg^{-1}$ (129), that is, ~50% lower than the morphometric estimate. The remaining difference likely reflects the deconditioned state of modern humans where the "*true*" structural diffusing capacity is not completely exploited even at heavy exercise except perhaps in elite endurance athletes. Any inhomogeneity in the distribution of ventilation-to-perfusion or perfusion-to-diffusion would also limit the degree to which "true" diffusing capacity can be exploited (discussed later when considering the effect of acinus design on gas exchange).

Is the theoretical value of DL_{O2} calculated from accurate morphometric data and the best available physical coefficients trustworthy? As this question cannot easily be answered on the human lung, we resort to experimental studies where physiological and morphometric measurements can be done on the same lungs and under exercise conditions. In practice, lung diffusing capacity is estimated physiologically using CO as a tracer gas that binds avidly to hemoglobin, and the theoretical values of DL_{CO} are calculated with the same morphometric approach as described earlier, except that physical coefficients for CO rather than O_2 are used (124, 157). One such set of studies using normal dogs and dogs following the surgical removal of lung units by pneumonectomy (156, 160, 338) show a close correspondence between DL_{CO} estimated by physiological methods at heavy exercise and that estimated by morphometry at postmortem. Because the dog is a highly athletic species that can reach a maximal O_2 uptake (per kilogram of body weight) nearly twice that of an elite human athlete, these findings suggest that (i) athletic animals recruit nearly all of their

structural reserves for gas exchange under peak metabolic demand and (ii) we can accept the theoretical estimate of DL_{O2} (and DL_{CO}) in general and for the human lung in particular as reflecting the limit to O_2 uptake imposed by the structural parameters of the gas exchanger.

Critical review of the morphometric model of pulmonary diffusing capacity: Ideal versus real diffusing capacity—The term "*capacity*" signifies a *maximum* amount that can be contained in a vessel, or the *maximal* output of an operation, thus referring to the *upper limit of a process*, in this case, the diffusing capacity for O_2 uptake is the upper limit of O_2 transfer from the air to blood. To use the term for estimates of O_2 transfer rate (flux) measured under resting or basal conditions is, in fact, incorrect ["transfer factor" is more appropriate (184)]. The approach followed here is to find an estimate of the ideal pulmonary diffusing capacity on the basis of model calculations considering the physical processes that occur within a structural apparatus whose relevant dimensions can be estimated. This morphometric model must result in an estimate that is higher than what can be measured functionally even under optimal conditions—just as the capacity of a wine glass must be larger than the quantity of wine we can sip without spilling some on our shirt.

Considering the meaning and uncertainties of the morphometric estimation of DL_{O2}, we note that it is based on a static global analysis of the physical properties of the alveolar-capillary complex, under the condition of maximal expansion of the alveolar surface and complete filling of the capillary network with blood whose hematocrit is close to that in venous blood (371). The "ideal" value of DL_{O2} thus obtained estimates the maximal possible conductance for O_2 diffusion and binding. It is therefore not surprising that physiological estimates of DL_{O2} in humans at heavy exercise are around 100 $mL \cdot min^{-1} \cdot mmHg^{-1}$ (129) compared to 158 $mL \cdot min^{-1} \cdot mmHg^{-1}$ as obtained by the morphometric model (381). Thus, it appears that the pulmonary gas exchanger in humans and sedentary animals possess "excess" DL_{O2} of which only about 2/3 is utilized at maximal O_2 uptake $\left(\dot{V}_{O_2}max\right)$, In contrast, athletic mammals, such as dogs or horses, utilize their entire DL_{O2} at $\dot{V}_{O_2}max$ (55,199). The lack of excess DL in dogs explains why maximal DL_{CO} measured physiologically in dogs before and after pneumonectomy is well predicted by morphometric DL_{CO} estimated on the same animals (157). The structure-function correspondence of DL_{CO} in athletic but not sedentary species suggests that the apparent "excess" diffusing capacity in sedentary species is related to a lower capacity in the nonpulmonary steps of the O_2 transport cascade, that is, cardiovascular and skeletal muscle systems, that restrict $\dot{V}_{O_2}max$ before the reserves in pulmonary O_2 uptake are exhausted (152).

The morphometric estimate of DL_{O2} is obtained on fully inflated, fluid-filled lungs where the entire epithelial surface appears exposed to air. In air-filled lung, only part of this surface is exposed because the alveolar tissue is molded under the effect of surface tension and modulated by surfactant (7,114), resulting in a ~30% to 40% reduction of the free alveolar surface exposed to alveolar air (7–9,114); the resulting reduction in DL_{O2} is, however, less since the folding of the tissue barrier results in a thinner harmonic mean thickness because thicker parts are shifted into the depth of the septum retaining the thinnest parts on the

surface (398). The preparatory method may also cause uncertainties regarding the amount of capillary erythrocytes (36,357).

A critique of the fundamental concept of the structural basis of gas exchange discussed above was recently advanced (198). Instead of considering the entire lung and dissecting gas transfer according to the series resistance model of Rougthon and Forster (305) into a functional-structural hierarchy, this simulation (198) considers a “machine acinus” as the structural unit for gas exchange. In this unit O_2 flux is globally driven by the partial pressure difference between the inspired air entering the acinus and the mixed venous blood entering the capillary network (98). Oxygen flux is determined by an “integrative permeability” term (Ω) that accounts for the entire complexity of O_2 diffusion across the membrane-plasma-erythrocyte barrier and equilibration with hemoglobin, and is variable with time and place within the acinus. In essence, W is a black box that comprises, without differentiation, the functional and structural factors here considered in a coherent fashion. The only input structural parameters are the alveolar surface area and the number of acini. Even though some of the calculations appear reasonable, this approach does not appear very helpful for understanding the structural support of gas exchange. It is unclear whether the general conclusion of this study, that O_2 capture by erythrocytes is the only process that matters and the Roughton-Forster approach is incorrect, could be substantiated.

The problem of O_2 capture by the blood—The transfer of oxygen from the air phase to the hemoglobin molecules is a complex process that is only poorly considered in the basic model of pulmonary diffusing capacity. This has been assessed in some detailed simulation studies on simplified capillary geometry to predict the distribution of gas tension and flux into erythrocytes in a hypothetical alveolar capillary segment containing an arbitrary number of erythrocytes with known anatomical dimensions of the capillary and assumed diffusion and solubility coefficients. Results show that erythrocyte spacing is an important determinant of O_2 (87) and CO (173, 174, 178) flux (Fig. 25). By integrating the individual erythrocyte fluxes, total CO uptake (DL) and effective membrane conductance (DM) of the capillary for CO may be calculated. DL_{CO} thus estimated at two O_2 tensions are then introduced into the Roughton-Forster model [Eq. (2) and (4)] (305) to determine if the anatomically defined DM and capillary blood volume (Vc) could be recovered. The same hypothetical capillary segment was subjected to morphometric analysis to obtain estimates of DM and Vc. Comparison of Roughton-Forster, morphometric, and simulation approaches has uncovered fundamental errors in the lumped parameter Roughton-Forster model (305) when applied to a distributed process—the model assumes that DM and Vc are independent entities when in fact they are interrelated. Physiological maneuvers that promote close interactions between alveolar septal endothelium and capillary hemoglobin, for example, recruiting erythrocytes via increased perfusion (177), improving the uniformity of perfusion (288) or increasing capillary hematocrit (407), are associated with a higher DM while limiting alveolar-capillary erythrocyte recruitment impairs DM (161).

The comparison also clarifies the discrepancy where morphometric estimates of DM (structural capacity) consistently exceeds physiological estimates (dynamic flux or load) (173). Morphometric estimates of DM are sensitive to erythrocyte volume, surface area, and distribution following postmortem lung fixation under conditions that differ from that *in vivo*

(388). In addition, deformation of erythrocyte under high blood flow shield parts of the erythrocyte membrane from the endothelium, which impairs DM (174, 365) even as the deformed shapes improve hydrodynamics. Nonuniform erythrocyte distribution (unequal spacing) within and among capillary segments cause uneven matching of tissue-erythrocyte membrane interface, which also reduces the efficiency of gas diffusion (178) (Fig. 25). At any given hematocrit, uniform erythrocyte distribution yields the highest CO flux whereas erythrocyte clustering yields the lowest value. Random nonuniform erythrocyte distribution within a single capillary or among separate capillary segments reduces CO flux by 30% to 50%. Thus, alveolar microvascular recruitment to improve gas transfer depends not only on the number or volume of patent capillaries or the hematocrit but also on the optimal distribution of erythrocyte mass and flow. Future improvements in these models will be needed to really understand what is happening in the dense alveolar capillary network, where erythrocyte flow is not “single file” along a long straight tube but may be tumbling from one capillary mesh to the next—characterized by what has been called sheet flow through a flat sheet with posts (107).

Applying a similar analysis to alveolar O_2 diffusion (99), one finds that at a given hematocrit the erythrocyte resistance to O_2 transfer increases as capillary O_2 saturation (SO_2) rises in transit: from 7% of total resistance at the capillary inlet (SO_2 = 75%) to 30% at the outlet (SO_2 = 95%). Total diffusing capacities for O_2 or CO increase as hematocrit increases, approaching a plateau near a hematocrit of ~40% while the corresponding diffusing capacities per erythrocyte decline due to competition between the membrane surfaces of adjacent erythrocyte for O_2 influx.

Recent advances in functional magnetic resonance imaging and spectroscopy allow evaluation of the diffusion characteristics of inspired hyperpolarized ^{129}Xe across alveolar tissue-plasma barrier and into erythrocytes in normal and diseased lungs (200, 201). By quantitatively mapping regional diffusion gradients *in vivo*, these techniques provide both structural and functional data and may yield new insight into the mechanisms of diffusion-perfusion mismatch.

Comparing morphometric and physiological estimates of lung diffusing capacity—*A critical comparison between the morphometric and the physiological approach to estimate pulmonary diffusing capacity is important to appreciate the validity of these estimates and to understand the reasons for discrepancies in the results. The basic approach is to attempt tightly correlated estimates of diffusing capacity by morphometric and physiological methods*. Oxygen conductance across alveolar tissue-plasma-erythrocyte barrier and its binding to hemoglobin may be noninvasively estimated *in vivo* from the uptake of an inspired tracer gas such as CO (DL_{CO}) or NO (DL_{NO}). According to the Roughton-Forster model (305) the measured DL may be partitioned into the membrane (DM) and blood (θ.Vc) components:

$$1/\mathrm{DL}=1/\mathrm{DM}+1/(\theta \cdot \mathrm{Vc}) \quad (7)$$

This serial resistance model is also the basis of the morphometric approach (Eqs. 2 and 5). In the classical physiological approach, the partition is done by measuring DL_{CO} at two alveolar O_2 tensions taking advantage of the competitive binding of O_2 and CO to hemoglobin (305). Another method of partition takes advantage of the extremely high hemoglobin binding affinity of NO by assuming that DL_{NO} is proportional to DM_{CO} ($DL_{NO} \approx k.DM_{CO}$) (28, 340). This latter approach implies that peri- and intraerythrocyte resistance to NO uptake is negligible and the resistance to NO uptake across the lung resides mainly in the tissue membrane. Although DL_{NO} has been used to empirically assess "membrane" diffusing capacity in normal and abnormal lungs (282, 340), it has become apparent that the erythrocyte in fact offers significant resistance to NO diffusion (27,29). Therefore, a mechanistic interpretation of DL_{NO} measurement and its relationship to DL_{CO} remains to be fully understood.

Correlated physiological and morphometric studies of DL_{CO} were undertaken by Crapo and co-workers (59,60). The physiological estimates were obtained in anesthetized dogs by a rebreathing technique at different inspired O_2 concentrations and partly on isolated perfused lungs. For morphometric studies, the lungs were fixed either by airway instillation or vascular perfusion. The results showed that physiological DL_{CO} was about half that obtained by morphometry with considerable differences between the estimates of DM_{CO} and Vc. Similar results were obtained in a combined physiological and morphometric study of four species of canids (397). Some of the differences may have been due to the use of the original morphometric model where the thickness of tissue and plasma barriers were considered as two barriers in series (371) which results in higher estimates of DM as compared to a later method where the tissue and plasma layers are considered as an integral barrier (388). The major reason for the observed discrepancy lies in the fact that the physiological estimates were obtained in resting or anesthetized animals where the true diffusing "capacity" is not exploited. Indeed, when the study is done on exercising foxhounds the physiological DL_{CO} varies in proportion to blood flow and increase with exercise intensity (48) reaching a value in close agreement with the morphometric estimate near maximal O_2 uptake $\dot{V}_{O_2}max$ (Fig. 26). This is true for intact lungs as well as for lungs after left pneumonectomy (156) and after compensatory growth of the left lung following right pneumonectomy in immature dogs (338) (Fig. 26).

It thus appears that in well-trained dog's morphometric DL closely characterizes the functional capacity for CO or O_2 uptake by the lung and that the full exploitation of this capacity depends on pulmonary blood flow, which determines capillary transit time, the period available for gas exchange. This was found to be about 0.3 s in dogs running at their $\dot{V}_{O_2}max$; calculation of the profile of capillary PO_2 along the capillary transit by Bohr integration showed that at least 75% of the capillary path was needed to reach arterial PO_2 in these athletic animals, whereas less athletic goats achieved saturation after 40% of transit time (199), suggesting that athletic species nearly fully exploit their morphometric diffusing capacity whereas more sedentary species would have some reserve capacity. This conclusion was supported by the observation that goats can maintain their $\dot{V}_{O_2}max$ if inspired O_2 concentration was reduced to 16% whereas dogs could not tolerate any reduction in inspired

O_2 concentration (199). As discussed earlier, nonathletic humans also have a reserve diffusing capacity of about 30%.

Architecture of lung parenchyma and its effect on gas-exchange function

Connectivity as architectural principle ensuring that all parts work in concert

—To maintain a complex alveolar surface area of 130 m^2 expanded in an air space of a few liters with only about 300 g of tissue requires a structural support system that gives all gas-exchange units an equal chance to be exposed to air flow through the airways. The air volume must be variable according to ventilatory demands so that the support structures must be made of soft flexible tissue. The architectural solution is to build an integral connective tissue fiber continuum that spans the entire lung from the main stem bronchus at the hilum along the airways to the pleura and traversing all alveolar septa and capillaries (383,384,386,402) (Fig. 27A). This fiber system is built of a hierarchy in three categories: (a) Axial fibers form a sleeve of the airways, first the connective tissue sheet of the bronchi and bronchioles which continues into the alveolar ducts of the acinus; (b) peripheral fibers that form the shell of the pleural bag from which it penetrates into the lung parenchyma as interlobular septa; (c) septal fibers that weave through the interalveolar septa with their capillaries with which they are interlaced (Fig. 20), connecting to both the peripheral and the axial fibers (375). As a result, the fiber support structures concentrate mainly on one side of the capillary so as to minimize the alveolocapillary barrier on the opposite side of the capillary where the epithelial and endothelial basement membranes are fused, and thicker on the side where fibers and fibroblasts, including myofibroblasts, are intercalated between the two basement membranes (Fig. 21). This system adheres to the principle of *connectivity* in which there are no loose ends. This allows inspiratory movements of the chest wall to be transmitted from the peripheral fiber system to the septal fibers that become extended as they pull on the axial fibers as cantilever, thus spreading the capillary network on the alveolar surface. In architectural terms the lung is a “tensegrity structure” (106, 189) with the complex fiber system spanning from the thoracic cage to the hilum as the stiff elements. The structure is stable as long as all fibers are connected at both ends to the system and tensed, but can partially collapse if some fibers are snapped, such as in emphysema.

It is noteworthy that the axial fiber system extends into the acinus as the network of fibers that form alveolar entrance rings and thus appear as a “virtual” wall of the alveolar duct; by this the alveolar spaces are widely connected with the air ducts (Fig. 27B). This fiber network is primarily responsible for alveolar formation during development (40).

The axial fiber network also plays an important role in keeping alveoli open against surface forces (402). Under static conditions, the surface force is determined by surface tension and the local surface curvature (Fig. 28): in the hollow of the alveoli the surface tension is negative tending to shrink the alveolus, on the free edge of alveolar septa the surface tension is positive tending to push the alveolar wall outward. Since on the edge the radius of curvature is very small the surface force is particularly high, but it is supported by strong fibers and some smooth muscle cells (Gig. 21B). For the alveolar septum attached to this free edge to be stable the surface tension must be low (6). Therefore, the actual configuration

of the lung's fibrous backbone depends on the molding effect of surface forces modulated by surface tension.

Dynamic modulation of gas exchanger with respiratory cycle—In air-filled lungs the alveolar surface forces are modulated by surfactant (6,7) resulting in functionally relevant modification of the configuration of the alveolar septum and capillaries (Fig. 29): the capillaries do not protrude on the alveolar surface as much and the exposed tissue surface is smoother and more homogeneous in thickness with bulky components such as cell bodies or fibers shifted into deeper parts of the septum (Fig. 29B) (398). In addition, this configuration is subject to changes with lung inflation (Fig. 30). The free alveolar surface increases strongly when inflation gradually increases from a collapsed state up to total lung capacity (TLC) by opening up collapsed alveoli; upon deflation surface area falls on a flatter slope when the lung is deflated to 40% TLC (114); when reinflated back to 80% TLC the surface expands to the same value as upon deflation from TLC (7). Consequently, in the range of physiological respiration, that is, between 40% and 80% TLC, variation of air volume by a factor of 2 due to the ventilatory cycle causes a change in alveolar surface area by only ~1.2-fold, that is, the major increase in volume occurs in the alveolar ducts while alveolar walls are only slightly stretched (Fig. 31). This is the result of a high surface tension that acts on the free edge of the alveolar septum, the network-like "wall" of the alveolar ducts, because of the high curvature of the saddle-shaped edge (Fig. 28) (386, 402). The distinct enlargement of alveolar ducts versus sacs is physiologically important. It is sometimes claimed that alveoli pop open upon lung inflation, and collapse upon deflation (127). That claim is correct when starting with a deflated lung, but that is not how we breathe. The normal breathing cycle operates on the deflation slope of the pressure-volume curve (Fig. 30) with small hysteresis, a state that is maintained by periodically taking a deep sigh. In this condition, surface tension is kept low because the surfactant lining is spread out and alveoli do not collapse.

Surface tension also affects alveolar capillary configuration, depending on the balance between capillary distending pressure and the counterpressure exerted by surface tension at the alveolar surface (Fig. 32). At low inflation, surface tension is nearly zero and capillaries bulge toward the alveolar surface (Fig. 17). As surface tension increases with inflation, the surface pressure can flatten the surface and reduce their cross-section on the flat parts of the septum, whereas capillaries can remain larger in the "corners" where three septa meet (Fig. 33A) (9, 398). This means that blood flow pattern depends crucially on capillary configuration as a three-dimensional network of dense meshes (Fig. 14B): these capillary "sheets" (107) extend from one alveolar wall into the next where three septa meet at triple lines forming a honeycomb-like structure (Fig. 28); here "corner" capillaries are subjected to three surface tension vectors as compared to two in the flat part of the septum. Corner capillaries can be wide even when surface tension is high because each of the three surface tension vectors acts against an opposed septum to "pull" the corner capillary open (Fig. 28). Capillary configuration and volume are also affected by perfusion. In Figure 33, rabbit lungs fixed by vascular perfusion at 60% TLC under (A) zone II and (B) zone III conditions (400) show partial capillary flattening in the mid-region of the septum with wider corner

capillaries in zone II compared to rounded profiles of well-filled capillaries in the entire septum in zone III (9).

Dynamic modulations of septal configuration have consequences on the estimate of DL_{O2} from morphometric data. In Table 2 the dynamic variation of morphometric parameters with respiratory cycle, obtained on perfusion-fixed rabbit lungs (6, 7, 398), have been applied to the human lung data of Gehr et al. (109). The free alveolar surface varies between 68 and 88 m^2, which means that a significant part of the anatomical alveolar surface area (130 m^2) is hidden beneath the surface lining layer (Fig. 29B). Capillary surface is also reduced but to a lesser extent, so that the effective surface, as defined earlier, varies between 80 and 91 m^2 as the lung is inflated from 40% to 80% TLC, and capillary volume is only mildly reduced. A significant difference is observed in the barrier thickness because the modulatory effect of surfactant preferentially retains thin parts of the tissue barrier on the surface whereas thicker parts (cell bodies or fibers) shift deeper (398) (Fig. 29B). Since erythrocytes are not preserved in perfusion-fixed lungs the total barrier thickness cannot be measured; in first approximation we have reduced, in Table 2, the total barrier thickness by the amount of tissue barrier reduction.

Introducing these modified morphometric data pertaining to an air-filled lung into the model for diffusing capacity we find that DL_{O2} in air-filled lungs is reduced by no more than 10% to 15% with respect to the theoretical value obtained above, and in the range of dynamic respiration it varies by only about 5% (Table 2).

Disposition of erythrocytes in alveolar capillaries—Human erythrocytes are of a similar size as the diameter of alveolar capillaries so they pass, in principle, single file through the capillary network; they take tortuous paths through the narrow-meshed capillary network of interalveolar walls but travel in packets along preferred tracks (267). Figure 34 shows such an alveolar wall in a rabbit lung where blood plasma was labeled with colloidal gold 2 min before interrupting blood flow to the lung (212): the black stain shows gold-labeled plasma in which erythrocytes stand out as greyish rings or bars depending on their orientation. Red stains are nuclei of the various cell types, including leukocytes. The erythrocytes are irregularly spaced and missing in some capillary segments; in Figure 35 the center-to-center distance between erythrocytes is measured along the capillary path showing that many erythrocytes are closely packed but ~10% to 15% of capillary segments are devoid of erythrocytes. This irregular distribution can also be observed in human lung (Fig. 15B). The dense erythrocyte arrangement is not surprising since they normally occupy nearly half the capillary space (capillary hematocrit is ~0.43) (388). The arrangement of erythrocytes has functional significance in that local O_2 flux is highest over the center of an erythrocyte and falls off in adjacent plasma regions. Theoretically, this effect is small if hematocrit is in the physiological range due to the dense stacking of erythrocytes, but becomes significant at low hematocrit values.

Architecture of ventilation and perfusion system: Correlated complexities

The major functional challenge to the ventilation and perfusion structures is how to efficiently distribute the gases and blood to the millions of gas-exchange units so that all

units function under similar conditions. On inspiration, a relatively small bolus of fresh air flows through a branched system of tubes toward the gas-exchange units, thus imperfectly replenishing the residual air. There will be some inhomogeneity of gas composition (concentration) between and along the airways. Of particular functional significance is what is called *stratified inhomogeneity* in the most peripheral airways; this topic is dealt with by Verbanck and Paiva (356) emphasizing mainly the physical processes involved; here we will discuss those aspects that are caused or related to the design feature of airways and vasculature, as well as their interaction in the gas exchange units. A further challenge results from the fact that the matched bronchovascular trees are constrained by the irregular thoracic cavity into which they develop to generate a scaffold with gas exchange units evenly occupying all parts of the available space. The pathways from the entrance— trachea and pulmonary artery—to the pleura vary in space and may also cause inherent inhomogeneities in ventilation and perfusion. The intrinsic challenge to structural design is to minimize the ill effects of such irregularities on the efficiency of gas exchange.

Architecture of the airway tree

Design and morphometry of the human airway tree: Human airway branching goes on for on average 23 generations, and because of the doubling of branches with each generation, there are on average 2^{23} or ~8 million end-branches, called alveolar sacs (369, 389). In reality, the number of branching generations needed to reach the alveolar sacs is quite variable, ranging from ~18 to 30; variability results from the fact that the endings of an airway tree (Fig. 12) must be homogeneously distributed in space and reach every corner and gap in the chest cavity where the lung develops. Some spaces are filled rapidly and the airways cannot continue to divide, whereas elsewhere more branches are needed to fill the space.

This branching process is accompanied by growth in total length and cross-sectional diameter of the airway segments between the branching nodes. The length of each segment is adjusted to cover the distances needed to fill the space homogeneously with endings, whereas the diameter is grossly proportional to the volume of peripheral lung that is supplied with air by a given branch. As airways bifurcate from central to peripheral branches, the lengths and diameters of each generation become gradually reduced. Bifurcation is asymmetric in that the two daughter branches differ in length and diameter; asymmetry is more pronounced in animal lungs than human lungs. Figure 36 shows a human airway tree cast used to measure the diameters and lengths of the first 10 generations of branches (369,389); Figure 37 shows a portion of an airway cast that extends to peripheral generations such as that in Figure 12.

Despite asymmetric branching some general rules govern the progression of dimensions along the tree. The diameter of daughter branches is smaller than that of the parent in that the diameter reflects the volume of peripheral lung it supplies with air (369); so when one daughter branch serves a smaller lung region than the other its diameter will be smaller. It has long been suggested that the progression of airway diameters follows a law formulated by Hess (136) and Murray (259) that predicts optimization of convective flow, providing the

lowest resistance for the lowest dead space. This law predicts, that, in a dichotomous tree, the diameters of the daughter branches, d_1 and d_2, are related to the parent branch d_0 as:

$$d_0^3 = d_1^3 + d_2^3. \quad (8)$$

For a simple symmetric tree in which $d_1 = d_2$ this becomes:

$$d_1 = d_0 \cdot 2^{-1/3} \quad (9)$$

which means that the airway diameter becomes reduced with each generation by an average factor of cube root of 1/2 (~0.79). This law should apply to all successive airway generations so that we predict the average diameter in generation *z* to be:

$$d_z = d_0 \cdot 2^{-z/3} \quad (10)$$

Do human airways follow this theoretical prediction? This was examined on a plastic cast of a human airway tree (Fig. 36), by measuring the length and diameter of airway segments from the trachea all the way out to generation 10 keeping track of the location of each segment in a pedigree chart of a dichotomous tree (369). Figure 38 shows the distributions of diameters and lengths for the first seven generations. While the diameters show a symmetric distribution the segment lengths is highly skewed ranging from 1 to 30 mm even in generation 7. The irregularity in branching is most visible in the variation of segment lengths as a consequence of distributing the gas-exchange units in an irregularly shaped organ (Fig. 36). This cast study was complemented by estimating the number and dimension of alveolar ducts and sacs on fixed specimens using morphometric methods leading to the conclusion that the total number of generations to reach the alveolar sacs is ~23 of which the first 15 generations are conducting airways (369,389). To test the theoretical prediction of optimized design according to the Hess-Murray law, we first simplify the system to a symmetric tree taking the mean diameter per generation as the characteristic. The mean diameters of the first 10 generations are plotted as circles semilogarithmically against generations (Fig. 39); the regression line $d_z = d_0 \cdot 2^{-z/3}$ represents the sequence of these diameters quite well (389) so that conducting airways appear sized to optimize ventilation. Acinar airways do not fit this regression line. In a later study, the dimensions of acinar airways were measured accurately and in relation to the branching tree on silicon rubber casts that extended all the way out to the alveolar sacs also filling alveoli (126). This study showed that the transitional bronchiole marking the transition between conduction and gas-exchange regions falls close to the theoretical regression line, while the acinar airways indeed follow another much shallower course (Fig. 40), leading to the conclusion that, in the human lung, the dimensions of conducting airways abide by the Hess-Murray law of optimization. The same conclusion was reached by Wilson (401) regarding the dimensions that would allow adequate ventilation with minimal entropy production.

However, a closer look at these data shows that the aforementioned conclusion is only approximately correct (248). It appears that the airway design follows the Hess-Murray law with a certain *safety factor*: the diameter of conducting airways is reduced by a factor of 0.83 rather than the physically optimal 0.79, which means that the smaller bronchioles are a bit larger than predicted. This is functionally important as it allows regulation of airway cross-section by contraction of the bronchiolar muscle sleeve without unduly increasing the flow resistance in small airways (Fig. 41) (278). Structural optimization is adjusted or slightly relaxed to ensure physiological robustness, another aspect of good design.

These considerations were based on meticulous study of a single lung preparation, with measurements verified by *in vivo* bronchograms (369, 389). In the meantime, better casts were prepared and analyzed in great detail with more parameters and more generations assessed (281); the results in general confirmed the original data but allowed a more detailed description of the branching pattern. Recently, it has also become possible to derive the basic architecture of the major airways from *in vivo* computed tomography (341,342), and sophisticated 3D computer models of the entire human airway tree have been generated (Fig. 42) (341). All the models were based on the principle of dichotomous branching through generations from the trachea as a stem, and allowing for irregularities or asymmetric branching.

An alternative approach is to regard the airway system as tubes converging from the periphery, the acinus, toward the center, the trachea (Fig. 43C) (149). By using an ascending ordering system that is employed in analyzing rivers (Strahler system), branches are grouped into orders according to the sequence of convergence, beginning with the smallest most peripheral branches, designated as order 1. This ordering pattern is particularly well adapted to formally describe an irregular dichotomy system because the size of branches in any one order varies less than with the generations-down model. This approach does not really account for the asymmetry of branching; rather it represents an attempt at extracting average data with less variability in each order. The degree of asymmetric branching is reflected in the branching ratio determined as the ratio of the number of branches in order μ to that in order $\mu + 1$ which is estimated at ~2.8 (149), as compared to ~2 in the generations-down model. Remarkably, the progression of diameters through the various orders is again roughly proportional to the cube root of the branching ratio. Hence, both models yield functionally comparable results.

The general conclusion drawn from this analysis is that the diameters of the conducting airways ensure optimal airflow, but physical optimality conditions are relaxed in the interest of physiological robustness. For the larger airways, optimization for flow and its distribution to peripheral units are essential features of good design. The total volume of the conducting airways down to generation 14 (the anatomic dead space) is about 150 mL; it is rapidly flushed by simple gas flow in the course of inhaling 500 mL of fresh air during quiet inspiration.

This airway design ends upon reaching the complex of alveoli arranged around peripheral airways (Fig. 44). The airway tree is thus subdivided into two major functional zones (Fig. 45): the first ~14 to 16 generations, on average, are designed to conduct air flow by

convection; these are followed by about eight generations of acinar airways where an axial channel (alveolar duct) is enwrapped by a sleeve of alveoli with gas exchange tissue on their surface (Fig. 44) (126). In human lung this transition is gradual. At some point the smooth bronchiolar wall becomes interrupted by one or two alveoli. This “transitional bronchiole” marks the entrance into an acinus. It is followed by some three generations of respiratory bronchioles where an increasing fraction of the wall surface is occupied by alveoli, until the alveolar ducts are reached where the central air duct is completely surrounded by alveoli (Fig. 45). These acinar airways continue to branch by dichotomy. Their length and diameter decrease with each generation, but the diameters of respiratory bronchioles and alveolar ducts change very little with each generation (Fig. 40). This arrangement does not imply less than an optimal design. On the contrary, the cube-root-of-1/2 law relates to optimizing mass flow of a liquid or air. In the most peripheral airways, mass airflow is only part of the means of transporting O_2 toward the air-blood barrier: Since the airways are blind-ending tubes and a sizable amount of residual air remains in the lung periphery after exhalation, O_2 molecules move into the residual air by diffusion (Fig. 46). Diffusion of O_2 in the gas phase is best served by establishing as large an interface as possible between residual air and the fresh air that flows in from the trachea. In fact, since the airway diameter remains nearly unchanged, the total airway cross section nearly doubles with each generation beyond generation 14.

The dimensions of the airway tree influence ventilatory airflow in several ways. Airflow velocity falls along the tree because the total cross-sectional area of the airways increases with every generation (Fig. 47); whereas the cross-sectional area of the trachea is ~2.5 cm^2, that of the 1024 airways in the tenth generation taken together is 13 cm^2, and as we approach the acinar airways, the total cross section reaches 300 cm^2. And since the same air volume flows through all generations, flow velocity falls by more than 100-fold from the trachea to the acinar airways: at rest, the mean flow velocity on inspiration is about 1 m s^{-1} in the trachea and less than 1 cm s^{-1} in the first-order respiratory bronchioles. In exercise, flow velocities are up to ten times greater, in proportion to the increased ventilation. This is discussed below when considering the relative importance of convection and diffusion in bringing O_2 to the alveolar surface.

The size of airways also determines the resistance to airflow, given by the reciprocal of the ratio of ventilatory airflow to the pressure difference between the mouth and alveoli, which is normally no greater than ~1 cmH_2O (mbar) or less than 1 mmHg. It is large enough, however, to potentially affect the distribution of ventilation to the many gas-exchange units attached to the end of the conducting airways because, in laminar flow, the resistance is inversely proportional to d^4 the distribution of air flow depends on a delicate balance of the size of parallel airway tracts. Even a slight narrowing of one of the two daughter branches at a branch-point will cause disproportionate airflow to the other branch and thus result in ventilation inhomogeneity.

Even though airway diameter decreases with branching (Fig. 39), their resistance does not increase toward the periphery as the major pressure drop along the airways occurs in medium-sized bronchi. Because airway diameter decreases by a factor larger than the optimal 0.79, resistance becomes very low in the small bronchioles (Fig. 41) (278). Flow resistance is further minimized by the widening of thin-walled bronchioles as the lung

expands on inspiration because they are tethered open by tissue tensions in the coarse fiber system. Therefore, airway resistance falls as lung volume increases. When tissue tension is disturbed, as in emphysema, small bronchioles may collapse, causing uneven ventilation of the peripheral lung units.

This biophysical examination of airway dimensions has recently been complemented by the alternative notion that bronchovascular trees are determined by the laws of fractal geometry (235). Fractal trees are formed by repetitive branching from one generation to the next (Fig. 8): If the proportion between parent and daughter branches remains the same it is called self-similarity. In a dichotomous tree, the diameter is ideally reduced by a factor of $2^{-1/Df}$ where D_f is the fractal dimension. Since the airway tree is nearly space-filling $D_f \sim 3$, which means that the Hess-Murray law [Eqs. (8) and (9)] also follows from fractal geometry as a rule of optimal design, but because the reduction factor is somewhat larger than $2^{-1/3}$, it follows that the actual fractal dimension of the airway tree is a bit larger than 3; this is possible because the tree is "cut off" at the entrance to the acini and the "space" becomes filled with alveoli.

Typical path models of the human airway tree: To make observations useful for biophysical considerations on ventilation or particle deposition, morphometric data of the airway tree can be abstracted into two types of models that extend from the trachea to the terminal alveolar sacs (370, 379): *model A* stresses the basic properties of airway branching by assuming regular dichotomy and thus defining a symmetric typical path model of the human lung; *model B* defines the irregularities of tree architecture as a consequence of asymmetric branching and defines the properties of a variable path model.

Model A: In the symmetric model, the airway branches in one generation z are assumed to all have the same diameter and length, corresponding to the mean dimensions estimated empirically from the original data set (Fig. 48). The model is bounded by the average total number of generations over which the airways must branch to reach the alveolar sacs; we estimate this number to be 23 so that the airways terminate in about 8 million alveolar sacs. Table 3 presents the number and characteristic dimensions of airway segments of the "typical path" human airway tree (369,379). Yeh and Schum (413) derived an identical model based on detailed analysis of silicon rubber casts (281). In their model, the lengths of airway segments are similar to Table 3 but the diameters are 20% to 30% larger. This is primarily due to standardization of Yeh's model to TLC, whereas the cast on which the data in Table 3 are based was prepared at ~75% TLC (369). Even though the differences are small it is uncertain which of the two data sets comes closer to the *in vivo* situation. The model of Table 3 is given as per generation number and the mean diameters are plotted against generations in Figure 40. But it may be more informative to represent the data along a geometric parameter such as the typical path length $L_p(z)$ that is the distance from the entrance (carina or larynx) to the end of generation z obtained by sequential addition of the segment lengths from generation 0 to z (Table 3). This is an important aspect because the segment lengths decrease drastically from a few centimeters in the major airways to <1 mm in the acinus. Accordingly, the total path length from the carina to the terminal alveolar sacs is ~15 cm, but only 0.93 cm of which are of acinar airways. In Figure 47 the total cross-sectional area, $A(z)$, of all airways in each generation is plotted against path length $L_p(z)$. It

is apparent that the total cross-sectional area increases dramatically toward the periphery mainly in the last few millimeters; for this feature, this airway model has been called "*trumpet model*." The total airway cross-section determines airflow velocity, which is the ratio of ventilation divided by $A(z)$; this velocity falls rapidly in the peripheral generations to very low values in the acinus.

The trumpet model shows the limitations of a symmetric tree, which suggests that all gas-exchange units are found at equal distance to the entrance airway. This is evidently a gross simplification because a brief look at Figures 12 and 37 reveals that some terminations of conducting airways end after a shorter distance than others. So the typical path model A must be complemented by a variable path model that considers asymmetric branching.

Model B: In developing a varying path model of the human airway tree, the solution is not to revert to the inverse description of orders in a confluent tree from the acinus to the carina (149) because this approach masks asymmetry rather than showing it. A further problem is that the inverse order model lacks connectivity so that pathways are difficult to construct. Fredberg and Moore (101) modified the approach to define a "*self-consistent tree*" which has an ascending "*principal path*" with groups of lower orders attached to it. The gas-exchange units are located at distances between 7 and 25 cm with a maximum ~15 cm, a value that coincides with the total typical path length of model A. This model is not trumpet- but pear-shaped (100).

A similar result is obtained with an asymmetric dichotomous tree model derived from the same data set as used for model A. The raw data on the first seven generations (Fig. 38) reveal considerable asymmetry by the distribution of the diameters and lengths, as discussed earlier (369). This is even more evident in the scatter plot of the diameter versus length of segments in generations 5 to 10 (Fig. 48). The starting point for defining the asymmetric model B is the finding that airways of a certain diameter d^* occur in several generations and at different distances from the origin (Fig. 49). Thus airways of 2 mm diameter are found in generations 4 to 14, with a maximum in generation 8. Alternatively we can estimate the distance from the origin of the trachea to 2 mm bronchi by adding the lengths of the segments intervening from the origin, and this shows that these bronchi are located at 18 to 31 cm from the origin of the trachea with a maximum at 24 cm. Note that in the symmetric model A, 2 mm bronchi were located in generation 8 and at 23.6 cm, in agreement with the maxima of the variable path-length model. Their real locations are shown on the trimmed cast in Figure 50. With this type of information one can calculate, for example, the distribution of airway cross-sections for all size classes. This is possible because in the dichotomous tree model the connectivity between branches and generations is well defined and because the original data were recorded in a pedigree chart that represents the correct order and connectivity of all branches.

The incomplete data on small airways do not allow estimation of the variation of bronchial path length all the way out to the acinar airways with a diameter of ~0.5 mm for the transitional bronchiole (126). An approximation can be attempted by extrapolating from the sufficiently complete data set (Fig. 51) of bronchial path length from 4 to 2 mm bronchi by halving the diameter to yield a normal distribution with a coefficient of variation of 20%

(369). A similar distribution was found for the path length within acinus, from the transitional bronchiole to alveolar sacs (126). On this basis, we calculated a putative path length distribution to the transitional bronchioles by convolution of the distribution shown in Figure 51 (for 2 mm bronchi) and reducing airway diameter ($d\mu$) from 2 to 0.5 mm (369). The resulting frequency distribution (Fig. 52) shows that transitional bronchioles are located between 20 and 35 cm from the tracheal origin, with a maximum at 27 cm and a standard deviation of 2.67 cm. If we accept this to represent the path length distribution to the entrance of acini, this function can be used to distribute the 30,000 acini on the total airway tree. Each acinus has a volume of 187 mm^3 and contains ~4500 mm^2 of alveolar surface (126). We can add the intra-acinar path length to the end of alveolar sacs (0.82 ± 0.14 cm) to the airway path length to complete the picture (open circles in Fig. 52). Note that this model is similar to that of Fredberg (100, 101) for a self-consistent confluent model in which the respiratory bronchioles were located between 6 and 25 cm from the carina (or 18–37 cm from the tracheal origin) with a maximal frequency around 15 and 27 cm, respectively. Thus, it does not really matter whether one arranges airways by "orders up" or "generations down" when constructing an asymmetric path model because in either case the longest path measures the extent of the distribution functions. In the confluent model this longest path, called the "*principal path*" (100), is indeed much larger than the "*typical path*" that characterizes the location of highest density of gas exchange structures. In fact, the difference between "*principal*" and "*typical*" path length is a measure of the irregularity of branching, just as is the distribution of path lengths.

Florens and co-workers (93) developed a geometrical model of the human airway tree that reproduces the irregular dichotomy of airway branching observed in various studies (150, 281, 369) and is particularly adapted to analytical studies of air flow and particle distributions, and has allowed the development of a model for surfactant replacement therapy (92).

Architecture of pulmonary arteries and veins—Pulmonary vascular architecture resembles that of the airways in their course and the pattern of dimensional changes. This is particularly true for pulmonary arteries that closely follow the airways to the smallest branches (Figs. 12 and 53) as a result of bronchovascular pairing during development. Together, the bronchoarterial bundle forms the axis of parenchymal units of varying order: acinus, lobule, segment, and lobe. Figure 54 shows that arteries continue branching right into the acinus. The pulmonary veins are differently disposed, lying in the boundary between two or three adjacent units (Figs. 53 and 55). Thus blood flows into the acinus along a central route, fans out through the capillary networks to be collected in the veins at the periphery of the acini, whereby the veins collect blood from several acini.

The diameter of each pulmonary artery branch approximates closely that of the accompanying bronchus, becoming slightly thinner in association with peripheral bronchioles (Fig. 54). Therefore, the diameter law presented for airways (Fig. 39) must also hold at least for the first ten generations of pulmonary arteries. However, pulmonary arteries divide more frequently than airways in the peripheral regions where small supernumerary branches leave the artery at right angles to supply parenchymal units adjacent to the bronchus (Fig. 53). These supernumerary arteries occur from about generation 9 on, that is,

when the main tract vessel diameter is less than 1.5 mm, and explain why the main tract arteries are smaller in diameter than the accompanying bronchus or bronchiole. This also explains why the arteries and veins branch over more generations than the airways. The number of terminal precapillaries that lead into the capillary network is about $300 \cdot \times 10^6$ so that the pulmonary arteries divide, on the average, over some 28 generations, as compared with 23 for the airways (369, 389). The diameter of terminal vessels is about 20 to 50 μm; if this range is plotted onto an extension of the graph of Figure 39 to generation 28, it falls on the curve extrapolated from the major branches so that $d_a(z) = d_0 \cdot 2^{-z/3}$. Thus, the pulmonary arteries abide to the cube-root-of-1/2 law from beginning to end, that is, blood is transported to the capillary bed by mass flow only. By adhering to this fundamental law of optimal design, the arteries allow blood flow with minimum entropy production.

In a recent thorough fractal analysis of the pulmonary vascular trees of animals and humans, the fractal dimension of both arteries and veins is estimated at 2.71, somewhat less than 3 (183); interestingly, Mandelbrot had predicted the fractal dimension of arteries to be 2.7 (235). The diameter reduction factor is therefore slightly smaller than cube-root-of-1/2 [Eqs. (2)–(8)], and the diameters follow the regression:

$$d_a(z) = d_{a0} \cdot 2^{-z/2.71} \quad (11)$$

In contrast to the airways, blood flow resistance increases along the pulmonary arteries and is highest in the most peripheral branches or arterioles, a pattern similar to that in the systemic circulation. This allows fine-tuned regulation of capillary perfusion at a local level.

Architecture of the acinus: Converging ventilation and perfusion for gas exchange—The model for structure-function correlation of the pulmonary gas exchanger so far discussed considered the whole lung: a gas-exchanging surface the size of a tennis court in humans with a capillary network containing ~200 mL of blood. The concept of diffusing capacity is based on the assumption that O_2 flow is driven by the partial pressure difference in alveolar air and capillary blood, both pressures assumed to be either equal in all parts of the lung or averages of some sort. Considering that the human lung is made of ~400 million gas exchange units—alveoli and their associated capillary networks—these assumptions must be critically assessed. It is of central importance to know how these gas-exchange units are connected to the airway tree and to the terminal branches of the pulmonary artery and vein. Because the architectural solutions are very different on the airway and the vascular side the effect of these structural arrangements on functional performance warrants a detailed discussion (394).

How airways lead air to the gas exchanger: In the human airway model (Fig. 45), there are two main functional zones: (i) the *conductive airways* constitute the first 15 generations and mediate convective air flow with minimal energy loss and dead space volume, thus distributing ventilation into all lung units as evenly as possible (149, 369, 376, 379, 389) and (ii) the *acinar airways* constitute generations 15 to 23 and continue their branching while adding alveoli that form a sleeve of air chambers around the duct (Fig. 44).

The pulmonary acinus is the “gas-exchange unit” (334, 408), defined as the branched complex of alveolated airways connected to the same first-order respiratory or transitional bronchiole, the point where the first alveolus appears on the airway wall to permit gas exchange (Fig. 45). This definition identifies the transitional bronchiole as the stem (126, 301). The use of the traditional “terminal bronchiole” as the stem of the acinus should be abandoned because some transitional bronchioles branch off *before* the conducting bronchiole ends (Fig. 44), particularly in animal lungs that, in general, show a higher degree of asymmetry than human lung (301,394). From the measured mean acinar volume, we estimate that there must be ~30,000 acini in an adult human lung (126) which, on a dichotomous tree, would locate their stem at generation 14 to 15 on average for a typical path model airway system of symmetric dichotomous branching, In the real tree with some degree of asymmetry, the acinar stem would be located in the range of generations 12 to 19 with a peak around generation 14 (394).

The geometry of pulmonary acini can be quantified on silicone rubber casts that reach the peripheral air space (315). After polymerization the tissue is removed by digestion and the preparation is dissected all the way out to the acini that appear as little “berries” (Fig. 56) where the transitional bronchiole is identified by the appearance of the first alveolar pocket. The human pulmonary acinus is on the order of a few millimeters in diameter. Microscopic dissection allows the different internal tracts to be separated (Fig. 57) and the airway system measured (126,301,315).

In a systematic study of three human lungs prepared by this method (126), the mean volume of acini was 187 ± 79 mm^3 (SD) (Fig. 58). In small mammals, the mean volume of acini range from 3.46 mm^3 (rabbit) and 1.9 mm^3 (rat) (301) to 0.15 mm^3 (mouse) (353). The human acinus is, however, not strictly comparable to that of rat and rabbit because at least three generations of acinar airways, the respiratory bronchioles, have very few alveoli in their wall and contribute little to gas exchange (Figs. 45 and 57). The “true acinus” where the air ducts are enwrapped by a complete alveolar sleeve occurs after the three generations of respiratory bronchioles in what is called a 1/8-subacinus (310, 394) whose averaged volume is about 23 mm^3 (see later).

The airway branching pattern for an average human acinus is shown in Figure 59. The segment lengths have been drawn to scale and the terminal clusters of alveoli of the alveolar sacs are marked by a dot. This acinus has been subdivided into its 8 subacini whose entrance airways are located in the third generation of acinar airways (126). The acinus shown in Figure 57 is comparable in size and structure. The transitional bronchiole and the two subsequent generations of respiratory bronchioles are clearly visible. By dissecting off part of the acinar cast a 1/8-subacinus is exposed.

The diameter of an average human transitional bronchiole measures 0.49 mm. For the very much smaller acini of rat and rabbit lungs, this diameter is ~0.24 mm, and in the mouse 0.15 mm; one finds that it is proportional to the size of the acinus it serves.

Figure 59 shows that the intra-acinar airways branch by irregular dichotomy; the number of segments doubles out to six acinar generations and then begins to drop off as the terminal

sacs are reached. The terminal sacs are located in acinar generations 6 to 11 so that the intra-acinar airways branch over an average of eight to nine generations.

The human intra-acinar airways shows a number of characteristic traits (126) (Fig. 60). The length of alveolar ducts gradually decreases from 1330 μm (generation 1) to 640 μm (generation 10). The length of alveolar sacs is greater than that of ducts located in the same generation; this is because the duct length comprises the depth of the terminal cluster of alveoli, which amounts to ~250 μm. Two values are estimated for the diameter of intra-acinar airways: The inner diameter, which characterizes the cross-section of the duct tube, and the outer diameter, which comprises the entire sleeve of alveoli enwrapping the duct. The inner diameter of human acinar airways decreases from ~500 μm (transitional bronchiole) to 270 μm (in generation 10), but the diameter of alveolar sacs (250 μm) is constant irrespective of the generation in which they occur. The outer diameter is nearly constant (~700 μm) for all intra-acinar airways. The difference between outer and inner diameters reflects the mean depth of the alveolar sleeve, which increases somewhat toward the periphery.

The total longitudinal path length for O_2 diffusion from the transitional bronchiole entrance to the terminal cluster of alveolar sacs (Fig. 61) averages 8.3 ± 1.4 mm (SD). Of this total path length 3.4 mm are for the first three generations of respiratory bronchioles whereas the path length of alveolar ducts and sacs comprised in the 1/8 subacinus (Fig. 59) averages 4.7 ± 0.88 mm (126). In the smaller acini of rat and rabbit, the respective mean longitudinal path lengths are 1.95 ± 0.36 mm and 1.46 ± 0.32 mm (301).

With these data in hand, we can put acinar airway dimensions into the perspective of the human airway tree, and define an idealized model acinus. We first estimate that the human lung contains 26,000 to 32,000 acini (126,394). With dichotomous branching this would locate the transitional bronchiole at generations 14 to 15. The average number of eight to nine intra-acinar branching generations would bring the terminal alveolar sacs into generations 23 to 24, the number of total generations originally estimated for the human lung (389). The average inner diameters of these airways can be plotted relating the average airway diameter to generation number (Fig. 40). The average diameter of transitional bronchiole falls onto the theoretical regression line predicted for conducting airways by the Hess-Murray law (126,136,259,369) and plotted through the estimated mean diameters of the bronchial tree. The inner diameter of acinar airways does not decrease with the same slope as that for conducting airways; the diameter reduction from the transitional bronchiole to the terminal sac over nine generations is only by a factor of 1/2. This confirms the original observation that the intra-acinar airway diameter falls less steeply than that of conducting airways and is thus larger than that predicted from the cube root of 1/2 rule (389).

How the pulmonary arteries and veins connect to the gas exchanger: Figures 53 to 55 show the relation between pulmonary vascular and airways trees. Pulmonary arteries closely follow the airway tree and branch according to the same pattern forming the bronchoarterial bundles at all levels from the segments to the lobules; the pulmonary veins take an intermediary course between these bronchoarterial bundles and are associated with interlobular septa (Fig. 55). This pattern changes toward the periphery as seen in Figure 54,

a higher magnification showing the central parts of an acinus where airways are decorated with alveoli. It is remarkable how the artery continues to branch into the acinus, still following the main tracts of alveolar ducts but also sending off supernumerary branches into the parenchyma, as seen in Figure 14 where the terminal branches of an artery and vein connect to the dense capillary network in alveolar walls. This arrangement ensures that the gas-exchange unit is an area of the capillary network that spans from a terminal pulmonary arteriole to a terminal pulmonary venule (Fig. 62). The diameter of such a roughly disk-shaped or polygonal unit is on the order of 500 μm with a surface area that corresponds to that of an alveolus even though alveoli and capillary unit are not congruent: the latter spans over several alveoli, and each alveolus is in contact with more than one capillary unit. Such "capillary units" are not well delineated and not even flat areas; they are simply a small domain in the 3D capillary network continuum that extends even beyond the bounds of an acinus. Their size is defined by the number of arterioles and venules that connect to the network.

How airway units and capillary units are joined in the acinus: Total surface of the gas exchanger is subdivided differently for the airways and for the blood vessels: whereas the conducting airway tree supplies some 30,000 acini as ventilatory units (Fig. 44), the blood vessels serve some 400,000,000 microvascular perfusion units, which are the actual gas-exchange sites individually supplied with blood (Fig. 14). Each acinus therefore accommodates some 12,000 microvascular gas-exchange units distributed along several peripheral airway generations that form the pulmonary acinus from the transitional to the last generation as a space-filling system (Fig. 63B). Note that the common representation of the alveolar-capillary unit as a terminal "bubble" of the airway tree (Fig. 63A) does not represent reality even if several bubbles are aligned in parallel each with an individual capillary. The correct model is represented in Figure 63B: the microvascular units are *serially* arranged along the branched airways, so they are *ventilated serially but perfused in parallel* (310,395).

This spatial arrangement has functional consequences because alveolar ventilation occurs in two steps: (i) bulk flow of inspiratory air carrying O_2 into acinus; 2) in peripheral airways flow velocity falls because the alveolar duct cross-section $A_d(z)$ increases as the number of branches doubles with each generation z, and O_2 moves toward the periphery by gas phase diffusion driven by the PO_2 gradient that becomes established as O_2 is absorbed at the alveolar surface (Fig. 64). Thus, in the most peripheral airways O_2 diffuses *longitudinally* along the alveolar ducts and *radially* into the alveoli to cross the tissue-blood barrier. Whereas all capillary units are individually perfused with venous blood the alveoli are not independently ventilated as their O_2 supply depends on their location along the airway tree (Fig. 63B). Both longitudinal and radial O_2 diffusion are driven by O_2 absorption at the alveolar surface at all levels out to the alveolar sacs (Fig. 64). The possibility that O_2 uptake in central alveoli could result in an O_2 concentration gradient along these peripheral airways depends on the competition between lateral and longitudinal diffusion, discussed later (120,310).

Typical path model of human acinus: To assess the effect of structural features on function, we attempt to develop a "typical path model" for an average human acinus (394). This model acinus has a volume of 0.187 cm^3 and an airway pattern as in Figure 59; its airways branch over 7 to 11 generations to reach terminal alveolar sacs. For simplicity, we assume the model acinar airways branch by regular symmetric dichotomy over eight generations (Fig. 45) so that, with each generation, the number of branches doubles to end with some 256 terminal alveolar sacs. Locating the transitional bronchiole ($z' = 0$) in generation 15 (Fig. 45), the terminal air sacs are in generation 23. From the estimates of the lengths and inner diameters of the airway segments, we derive overall parameters of functional significance (Table 4), such as the total airway cross-section per generation, $A_d(z')$, a determinant of air flow velocity. Finally, we estimate the distribution of alveolar surface area to the different generations, $S_{alv}(z')$, and of the associated capillary volume $V_{cap}(z')$. For an estimated alveolar surface of 130 m^2 in human lung (Table 1), there would be ~54 cm^2 of gas exchange surface and 7 μL of capillary blood per average acinus. Figure 65 shows the distribution of alveolar surface area and capillary volume to sequential generations; half of the gas exchange surface and half of the capillary blood volume are in the last generation— and ¾ are in the last two generations. A final check of this model is that the path length from the entrance transitional bronchiole to the end of the alveolar sacs is 8.4 mm, which agrees well with the mean path length estimated in the human acini (126,394).

Implications of acinar design for gas exchange: diffusion screening: In the acinar geometry described earlier O_2 is transported toward the alveolar surface by both convection and molecular diffusion; when absorbed at the alveolar surface it diffuses through the tissue membrane into blood to be bound by hemoglobin that serves as O_2 sink. Several physical parameters govern this process, such as airflow velocity, diffusion coefficient of O_2 in air, alveolar membrane permeability, blood hemoglobin content and its reaction rate with O_2. Conversely, CO_2 diffuses across the membrane from blood into alveolar gas and outward in the alveolar gas phase to the conducting zone to be expelled from the lung.

Since it is not possible to measure the distribution of O_2 or CO_2 concentration in different parts of the acini, several mathematical models have been developed. In an early model, incomplete intrapulmonary gas mixing, called stratification, was assigned to the finite diffusivity of O_2, preventing it from spreading evenly in the acinus during inspiration (314). Later, the respective roles of convection and diffusion in gas mixing were examined through numerical simulation (83,271,272,343) showing that concentration gradients may exist as a consequence of efficient capture of O_2 by hemoglobin; in these studies permeability of the alveolar membrane was considered as infinite but located at the end of the pathway.

Recent models consider the effect of the complex acinar hierarchy where alveolocapillary gas-exchange units are arranged laterally along the acinar air ducts from the first to the last generation (Fig. 63B). O_2 molecules entering the acinus from the conductive airways will diffuse both *along* the axis of acinar air ducts and *radially* into the alveoli and toward the membrane. They first encounter the surface of the alveolar membrane in the first generation: if membrane permeability is high, O_2 molecules are avidly absorbed in this early part of the acinar pathway so that distal generations may receive less O_2 for gas exchange, that is, they

are *screened* (89,310). In contrast, if membrane permeability is low, less O_2 is absorbed allowing enough O_2 to reach the deeper regions. The possibility of screening causing O_2 concentration gradients in the acinus, due to the serial arrangement of alveoli along the pathways, has been repeatedly discussed particularly with respect to comparative physiology (309,376,395). More complete studies (89–91,120,310) have shown that screening is determined by both physical parameters of molecular diffusion and morphological parameters of acinar geometry and size.

Determining the "diffusion cell" in human acinus at rest and in exercise: The effect of screening—that is, sequential absorption of O_2 from inspired air—begins, in principle, with the first gas exchange unit on the surface of transitional bronchiole, but it becomes quantitatively significant when convective air flow is slowed sufficiently for O_2 diffusion along the duct to become the major means of O_2 transport, a feature determined by the progressive increase of acinar airway cross-section (Table 3). In this concept, we define a "diffusion cell" as that part of the acinus where convection can be reasonably neglected so that O_2 moves by diffusion in the gas phase. The transition between convection and diffusion is quantified by the "*acinus Peclet number*" P_a which compares the air drift velocity U with the mean diffusion velocity to reach the deeper regions of the acinus. At any branching generation Z, the distance to cross to the end of the sacs is of order $(Z_{max} - Z)\,\lambda$, where λ is the mean length of an acinar duct (Table 4). Following (310) we define P_a as:

$$P_a = U(Z) \cdot (Z_{max} - Z) \cdot \lambda / D_{O2,air} \quad (12)$$

where flow velocity $U(Z)$ at stage Z is found from the progressive increase of total airway cross-section (Table 4). The velocity $U(Z)$ depends on the breathing regime. For exercising humans, air velocity increases by a factor of 10 above rest at all levels of the airway tree due to increased tidal volume and respiratory frequency. The resulting P_a values are shown in Figure 66. The logarithmic scale of the ordinate indicates that the P_a, and thus the convection velocity, falls rapidly from one generation to the next because of the rapid increase in cross-sectional area (Table 4 and Fig. 47). Consequently, the size of the part of the acinus considered as working in a purely diffusive manner remains approximately constant during inspiration or expiration. The convection-diffusion transition ($P_a = 1$) occurs for ($Z_{max} - Z$) of order 5 at rest and 2 at exercise. Thus, the diffusion cell is approximately a 1/8 subacinus at rest and a (much smaller) 1/64 subacinus at exercise (Fig. 66).

Predicting the effect of screening in human acinus on the basis of physical principles: In relating acinar structure to function, the process of O_2 transfer from the entrance into the acinar diffusion cell to the capillary erythrocytes is a balance between two conductances: a diffusion conductance Y_{cross} for O_2 to *cross* tissue-blood barrier, and a diffusion conductance Y_{reach} for O_2 to cross the air spaces and *reach* the tissue surface. Both conductances are determined by the product of (i) a physical parameter (the permeability coefficient W_{O2} for O_2 in tissue, and the diffusion coefficient D_{O2} for O_2 in air, respectively) and (ii) a morphometric parameter (gas-exchange surface S_{ac}, and a measure of the size of the diffusion cell: the diameter L of the smallest sphere enwrapping the acinus) (310):

$$Y_{\text{cross}}=\text{W}_{\text{O2}}\cdot S_{\text{ac}}, Y_{\text{reach}}=\text{D}_{\text{O2}}\cdot L \quad (13)$$

Here D_{O2} is the diffusion coefficient in air and W_{O2} is the diffusion capacity per unit surface area $W_{O2} = DL_{O2}/S_A$ depending on the thickness of tissue barrier and the capillary blood volume per alveolar surface, factors that vary little between species (373). On the other hand, acinus size and surface area vary considerably between large and small mammals and thus determine the efficiency of acinar gas exchange that appears best if Y_{cross} and Y_{reach} are about equal. If Y_{cross} were much smaller than Y_{reach} the low permeability of the gas exchanger would need to be compensated by a larger gas exchange surface, and this would inevitably entail a larger volume of the acinus to accommodate the surface and by that a longer diffusion distance. When the acinar size of different species is compared It appears that the condition $Y_{\text{cross}} \sim Y_{\text{reach}}$ is satisfied (310). The acinar size appears adjusted to ensure that the last generation of acinar airways is adequately supplied with O_2. This is important because the last generation contains half the gas-exchange surface of the acinus as a result of dichotomous branching (Table 4).

Once the diffusion cell is defined as discussed earlier, one can predict the quantitative effect of diffusional screening on gas exchange by modeling the alveolar PO_2 in each generation. Based on *real* acinar topology Felici et al. (90,91) computed the gas flux in the eight real 1/8 subacini shown in Figure 59, under the hypothesis that blood is an O_2 sink at constant partial pressure along the capillary path assumed to be mixed venous PO_2 all along the capillary. This was a problematic assumption that led to the conclusion that the acinus performs with an efficiency of ~33% at rest, which means that only about 1/3 of the alveolar surface was required for gas exchange; as will be discussed this resulted from the assumption of a much too large driving force for O_2 diffusion into the capillary. In exercise, the convection-diffusion transition occurs in the region ($Z_{\text{max}} - Z$) of order 2 (Fig. 66). The part of the exchanger where O_2 moves purely by diffusion has a volume of the order of $V_d/64 \approx 1.4 \times 10^{-3}$ cm^3 and the L_p of such a subregion of the acinus is of order 2.3 cm, now much smaller than the length $L_{O2} \sim 25$ cm for O_2 (Table 4). Thus, upon exercise the region beyond $Z = 21$ behaves as an optimized (i.e., unscreened) diffusion cell with an efficiency of about 90% (91).

Limitations of the screening model: The discussion so far relates only to inspiration when fresh O_2-rich air moves into the acinus. The reverse happens during expiration: CO_2 diffusing from the blood into the acinar air dilutes O_2 and the convection-diffusion front moves toward the bronchi. This was considered in a subsequent study by Sapoval's group (98). Figure 67 shows the variation of alveolar PO_2 along eight acinar generations for two ventilatory cycles during heavy exercise where PA_{O2} falls to ~110 mmHg at end-inspiration and ~80 mmHg at end-expiration. Note that this was still based on the assumption that capillary PO_2 equals mixed venous PO_2, and disregards the fact that capillary PO_2 increases along the capillary path due to O_2 binding to hemoglobin (Fig. 22) so that the driving force for O_2 diffusion decreases rapidly and on average is less than 1/3 that of assuming mixed venous PO_2.

More realistic conditions were considered by Swan and Tawhai (336) in a modeling study using the same geometric acinar model but allowing capillary PO_2 to increase along the capillary path length. While the *pattern* of alveolar PO_2 variation along the acinus was similar to that in the study of Foucqier et al. (98) the *reduction* of PA_{O2} was now much less reaching ~110 mmHg at end-expiration (Fig. 68). The effect of screening was thus much attenuated. Considering that half the gas-exchange surface is in the last acinar airway generation this means that most of the surface is exposed to an alveolar PO_2 that allows adequate oxygenation of the blood.

Implication of acinar path length—stratified inhomogeneity: The depth of the convective-diffusive interface moves peripherally as the inspiratory rate and tidal volume increase. The convection-diffusion transition can be detected from phase II of a single-breath nitrogen washout curve (50) as well as the axial nitric oxide "back-diffusion" from the airway tree into the alveolar region (325,326). The effects of diffusion limitation within alveolar airspace, termed gas-phase resistance or stratified inhomogeneity, on gas transfer have been simulated (139, 272, 313) and summarized recently (356). Because axial or gas phase conductance is at least 17.5 times higher than conductance across alveolar tissue-blood barrier, the relatively small magnitude of stratified inhomogeneity does not normally limit alveolar O_2 transfer (133, 270, 316). Stratified inhomogeneity becomes detectable when distal airways and acinar air spaces become elongated and dilated such as that in the expanded remaining lung following pneumonectomy (158, 167). Because the rate of gas diffusion within alveolar air spaces depends on molecular weight, stratified inhomogeneity may be detected by intravenously infusing dissolved inert gases of different molecular weights that equilibrate across the blood-gas barrier and are eliminated in the exhaled breath. A high molecular-weight inert gas (e.g., enflurane) is preferentially retained in the air space relative to a low molecular-weight inert gas (e.g., acetone); their differential retention and excretion profiles provide an indication of the presence of gas phase diffusion resistance (143,158). Density of the inspired gas mixture also affects alveolar gas diffusion; these effects are more pronounced for NO than CO uptake. Although NO and CO have comparable molecular weights, when breathing room air (containing 78% nitrogen), NO conductance across the lung (DL_{NO}) is approximately four to five times that of CO (DL_{CO}) due to much faster NO binding to capillary hemoglobin. When gas-phase resistance is increased by breathing a high-density gas mixture, for example, one containing sulfur hexafluoride, compared to that breathing a low density mixture, for example, helium, the reduction in DL_{NO} is significantly greater than that in DL_{CO} especially during exercise or in the presence of airspace enlargement (116, 167). However, the minimal gas phase resistance in normal lungs with an only modest elevation during heavy exercise and in the presence of gross airspace enlargement suggests that the normal size of the acinus is near-optimal.

The functional importance of acinar architecture

What is the virtue of a lung where the gas exchange surface is preferentially distributed along the last few generations of the branched airway tree? The first point is that the surface is partitioned into ~30,000 small acini in the human lung; this allows maximal packing of the alveolar surface into a limited space and to spread it along the air ducts thus optimizing the conditions for "*ventilation of the surface by O_2 diffusion*." With respect to the acinus the

rule is that “smaller is better—but not too small” (310); large acini are not efficient because the effects of stratified inhomogeneity and screening could become limiting, but too small acini would be wasteful with space. Second, to limit the size of the acini to only the few most peripheral of the 23 generations of the airway tree allows optimization of “*ventilation by air convection*” by designing a well-proportioned branched bronchial system whose tube diameters approach the conditions for minimal resistance and minimal dead space, whereas the acinar air ducts can follow a different rule. Third, the conducting airways can have a smooth surface lined by mucus or surfactant to efficiently capture the load of inspired nanoparticles and pollutants that should be prevented from reaching the vulnerable alveoli. Finally, to divide the gas exchanger into small *ventilator units*, the acini, allows the orderly convergence of the pulmonary arterial and venous systems on a sequence of even smaller gas exchange units, the alveolocapillary complexes, where the limitation of acinar size assumes additional importance because of the serial arrangement of the gas exchange units along the acinar ducts. The complex architecture of the lung is determined by the need to optimize various functional conditions that serve efficient gas exchange.

Matching the Components of Pulmonary Gas Transport and the Consequences of Mismatch

The heterogeneity of ventilation and blood flow result from combined factors including bronchovascular geometry and smooth muscle tone, hydrostatic and pleural pressure gradients, and regional differences in lung compliance. Efficient pulmonary gas exchange depends on the ability to dynamically adjust the magnitude as well as the distribution of disparate processes—alveolar ventilation, perfusion, diffusion, and capillary erythrocyte hemoglobin mass—relative to one another in all parts of the lung and in relation to systemic metabolic demand. Here, we briefly discuss the functional interactions of ventilation to perfusion $\left(\dot{V}_A/\dot{Q}\right)$, perfusion to diffusion $\left(\mathrm{DL}/\dot{\mathrm{Q}}\right)$ and tissue barrier to capillary erythrocyte or hemoglobin.

Ventilation-perfusion matching

In the normal lung, the closely correlated airway and vascular branching pattern creates well-matched $V_A/\dot{Q}$ distributions while active mechanisms of matching $\dot{V}_A/\dot{Q}$ are invoked mostly under perturbed conditions. The ideal gas-exchange unit receiving equal ventilation and perfusion has a $\dot{V}_A/\dot{Q}$ ratio of 1.0 (Fig. 69). Gas-exchange units that receive ventilation without perfusion $\left(\dot{V}_A/\dot{Q}=\text{infinity}\right)$, for example, caused by vascular occlusion or maldistribution, contribute to overall dead space or wasted ventilation. Release of vasoconstrictors and inflammatory mediators in these regions further impedes microvascular flow. In the hypoperfused regions, reflex hypocapnic bronchoconstriction (51, 115) normally develops to redistribute ventilation, minimize dead space, and maintain $\dot{V}_A/\dot{Q}$ matching. Conversely, gas exchange units that receive perfusion without ventilation $\left(\dot{V}_A/\dot{Q}=0\right)$ represent shunt, for example, caused by airway obstruction, atelectasis, inflammation, or

consolidation. In these hypoventilated regions reflex hypoxic vasoconstriction (239, 257, 286) normally develops to redistribute perfusion, minimize shunt and maintain $\dot{V}_A/\dot{Q}$ matching. Between shunt and dead space are gas exchange units of varying degrees of $\dot{V}_A/\dot{Q}$ mismatch. Units with high $\dot{V}_A/\dot{Q}$ (>1.0) reduce the efficiency of ventilation, leading to increased minute ventilation and elevated metabolic cost of breathing required to maintain a given level of alveolar ventilation. Units with low $V_A/\dot{Q}$ (<1.0) reduce the efficiency of oxygenation and increases the alveolar-arterial O_2 tension gradient (A-aPO_2), which can be seen even in normal subjects at rest (a modest 5–10 mmHg) and peak exercise (~25 mmHg) (312). The magnitude of $\dot{V}_A/\dot{Q}$ mismatch is directly related to the increase in pulmonary arterial pressure and minute ventilation during exercise at sea level, and inversely related to lung size (144,312,331).

Uneven $\dot{V}_A/\dot{Q}$ distribution among lung units is exaggerated in all types of airway, parenchyma, and vascular lung disease except pure alveolar hypoventilation, and constitutes the major cause of arterial hypoxemia (302). Anatomically, uneven ventilation can develop due to regional accumulation of airway secretion, peribronchiolar and interstitial fluid (53), and/or bronchoconstriction. In addition, changes in lung volume, regional compliance or airway wall stiffness differentially influence mechanical airway-parenchyma interdependence that opposes airway smooth muscle contraction, and can contribute to uneven bronchial tone, premature airway closure, and heterogeneous distribution of ventilation (16,75,125,207). Uneven regional perfusion can result from regional vascular obstruction, perivascular edema (311) and/or vasoconstriction. Bronchovascular tone is mediated via smooth muscle or myofibroblast-like cells that contain alpha-smooth muscle actin and are present in the pleura, airways, blood vessels, the entrance rings to alveolar sacs, alveolar ductal tissue as well as the septal interstitium (265,268). Even in normal lungs, $\dot{V}_A/\dot{Q}$ mismatch with increased spatial $\dot{V}\ A$ and $\dot{Q}$ heterogeneity may be accentuated by exposure to severe hypoxia and following prolonged high-intensity exercise (38,144,145), associated with a reduced DL_{CO} (113) and a long resolution time, suggesting the development of structural lesions such as interstitial edema similar to that seen during high altitude exposure and caused largely by inhomogeneous hypoxic pulmonary vasoconstriction (84) leading to uneven regional microvascular resistance, increased tissue permeability, perivascular edema, and possible disruption of alveolar capillaries. Figure 70 shows an example of anatomical lesions causing $\dot{V}_A/\dot{Q}$ mismatch. For detailed discussions on this topic, see separate reviews (117,287,333,360,418).

Perfusion-diffusion matching

Owing to the large air-tissue-blood interfaces, a dense capillary network and a thin tissue-blood barrier, alveolar diffusion does not normally limit O_2 uptake or contribute to an increasing A-aPO_2 from rest to exercise, except in elite athletes at maximal O_2 uptake or in the presence of reduced alveolar O_2 tension, for example, at high altitude. In diseased lungs, alveolar-capillary diffusion limitation may arise as a result of (i) a loss of alveolar-capillary surface areas, for example, due to alveolar consolidation or collapse, pneumonectomy, or pulmonary embolism, (ii) thickened tissue-plasma-erythrocyte diffusion barrier, for example,

interstitial edema or fibrosis, (iii) reduced capillary hemoglobin "sink" for O_2, for example, anemia or abnormal hemoglobins, and (iv) mismatch between diffusion and perfusion surfaces ($\mathrm{DL}/\dot{Q}$ mismatch due to either impaired alveolar-capillary recruitment or the uneven distribution of capillary hemoglobin in flowing blood.

Alveolar-capillary recruitment, an essential process that matches pulmonary O_2 uptake to metabolic O_2 demand, is evidenced by a linear increase in DL (~40% in average humans and up to 100% in dogs) with respect to lung expansion (303) and pulmonary perfusion $\left(\dot{Q}\right)$ from rest up to peak exercise (48, 152, 338) (Fig. 71). Increasing microvascular perfusion or pressure opens and distends capillaries, expands capillary volume, hemoglobin mass, and gas-exchange surface area, and improves the uniformity of capillary erythrocyte distribution with respect to tissue surfaces, that is, improving $\mathrm{DL}/\dot{Q}$ matching, reviewed in (152). In addition, lung inflation unfolds alveolar epithelial surfaces (7, 54), which accounts for about 20% of the overall increase in DL from rest to peak exercise (167, 177, 255). Alveolar-capillary recruitment prevents a fall in capillary $\mathrm{DL}/\dot{Q}$ ratio and erythrocyte transit time (Δt) during exercise, thereby maintaining adequate arterial blood oxygenation (Fig. 72). The flow and distribution of plasma and erythrocytes are separately regulated; recruitment of either increases the perfused surface area but only erythrocyte recruitment enhances DL (46, 196). Discordant patterns of alveolar membrane-plasma-erythrocyte recruitment can cause $\mathrm{DL}/\dot{Q}$ mismatch, impair diffusive equilibration across the blood-gas barrier, and increase *A-a*PO_2 in a manner analogous to that seen with $\dot{V}_A/\dot{Q}$ inequality.

The equilibration of hemoglobin O_2 saturation (Sc) from mixed venous $(S\overline{v})$ to alveolar end-capillary (Sc′) along a partial pressure gradient between alveolar air (P_A) and capillary blood (Pc) is described by the Bohr integral [Eq. (14)]:

$$\frac{\mathrm{DL}}{Q}=(\mathrm{O_2Cap})\int_{S\overline{v}}^{Sc'}\frac{\partial Sc}{(P_A-Pc)} \quad (14)$$

where O_2Cap = blood O_2 carrying capacity. The time course of oxygenation can be estimated if the relationship between Pc and erythrocyte O_2 saturation (Sc), that is, P_{50} (PO_2 at 50% saturation of heme-binding sites) of the oxyhemoglobin dissociation curve (ODC), is known. At a given P_A, $S\overline{v}$, and P_{50}, the $\mathrm{DL}/\dot{Q}$ ratio determines the Sc′O_2 due to diffusion equilibration. In hypoxia, the slope of the linear portion of the ODC between mixed venous and end-capillary blood is given by $\beta=\mathrm{O_2Cap}\frac{\partial \mathrm{S}}{\partial \mathrm{P}}$ in [mL O_2 (mL blood mmHg)$^{-1}$] (284):

$$\frac{\left(\mathrm{PA}-\mathrm{Pc}'\right)}{(\mathrm{PA}-\mathrm{P\overline{v}})}=\mathrm{e}^{-\mathrm{DL}/\beta Q} \quad (15)$$

The exponent $\mathrm{DL}/\beta\ \dot{Q}$ describes the effect of O_2 capacity or P_{50} on O_2 transfer (285). Equation (15) also applies to alveolar CO_2 exchange under conditions where the CO_2 dissociation curve is nearly linear (195). As $\dot{Q}$ increases from rest to exercise, $\mathrm{DL}/\ \dot{Q}$ ratio normally decreases. In average healthy subjects, $\mathrm{DL}/\ \dot{Q}$ declines without affecting $Sc'O_2$ even at maximal exercise. In elite athletes who achieve a higher maximal $\dot{Q}$, the $\mathrm{DL}/\ \dot{Q}$ ratio may decline sufficiently that $Sc'O_2$ falls upon exercise. Nonuniform distribution of DL with respect to $\dot{Q}$, either resulting from alveolar-capillary inflammation and fibrosis, or uneven capillary erythrocyte flow, further reduces $Sc'O_2$ at a given $\mathrm{DL}/\ \dot{Q}$ ratio leading to arterial hypoxemia (Fig. 72).

Tissue-erythrocyte interactions

Free capillary hemoglobin is more efficient than erythrocyte-encapsulated hemoglobin in O_2 transport (218) but induces avid vasoconstriction as a result of NO scavenging (71). Encapsulating hemoglobin within discrete erythrocytes prevents vasoconstriction but significantly increases the resistance to gas uptake, i.e., an example of evolutionary compromise (29, 352, 354, 355). The physical properties of erythrocytes, for example, size, shape, mass, concentration, distribution, and deformability, influence gas exchange in important ways. Their biconcave shape minimizes intraerythrocyte O_2 tension gradients, facilitates uniform O_2 binding to hemoglobin, and optimizes deformability and flow dynamics compared to spherical shape. Erythrocytes undergo dynamic deformation during capillary transit, which improves microvascular hydrodynamics but may reduce the effective erythrocyte-endothelial membrane interface for diffusion (174). Loss of erythrocyte deformability, for example, spherocytes, can cause nonuniform erythrocyte distribution, which impairs DL (21). Moderate isovolemic anemia or hemodilution reduces DL (57, 238) as well as ventilation-perfusion mismatch and pulmonary vascular resistance (72), resulting in improved convective transport (324) at the expense of lower diffusive transport, i.e., another example of evolutionary compromise. Polycythemia has the opposite effects (236).

Far from being a passive O_2 carrier, erythrocytes serve multiple regulatory functions: (i) erythrocytes retain hemoglobin within the circulation without causing vasoconstriction. Free hemoglobin has a half-life of several hours while human erythrocytes circulate on average for 120 days. (ii) Erythrocytes act as metabolic sensors (168) via the shifting binding affinity (P_{50}) of ODC (Fig. 73). At any given mean alveolar O_2 tension (PA_{O2}) the pressure gradient (ΔP) from alveoli to blood drives O_2 loading onto hemoglobin. The ΔP from blood to tissue mitochondria drives O_2 unloading from hemoglobin. Shifting the P_{50} alters the balance between O_2 loading and unloading in accordance with metabolic demands. For example, under stress of hypoxia or tissue acidosis the erythrocytes produce more 2,3-bisphosphoglycerate (225), an intermediate glycolytic product that binds to deoxyhemoglobin and stabilizes the “Tense” (deoxygenated) molecular conformation, thereby increasing P_{50} and improving O_2 unloading to tissue. Therefore, the transport function of erythrocytes is intrinsically coupled to its metabolism, making the erythrocyte an effective sensor of oxygenation. (iii) Erythrocytes enable O_2-CO_2 coupling via their allosteric interactions with hemoglobin as well as interactions with modulators such as

carbonic anhydrase (95) and membrane ion transporters, for example, anion exchanger-1 (AE-1) (253) and sodium-proton exchanger (NHE) (277), to optimize O_2-CO_2 exchange while preserving acid-base balance (Fig. 74). (iv) *Erythrocytes* enable O_2-NO coupling via separate oxygenation-dependent reactions with hemoglobin—NO scavenging by heme iron, and reacting with a sulfhydryl group of the cysteine residue (Cysβ93) to form S-nitrosothiol (SNO) and S-nitrosohemoglobin (SNO-Hb) (119,193). These allosteric interactions operating reciprocally in the lung and the periphery determine the local availability of NO to reach the endothelium and modulate regional vasomotor tone. (Fig. 75). In peripheral capillaries, preferential release of NO from SNO-Hb mediates hypoxic vasodilation. In alveolar capillaries, preferential NO scavenge by heme iron mediates hypoxic pulmonary vasoconstriction (78) and hence $\dot{V}_A/\dot{Q}$ and $\mathrm{DL}/\dot{Q}$ matching. (v) Erythrocytes synthesize NO under shear stress using L-arginine as substrate (209,351). In addition, glycolytic ATP produced and exported by erythrocytes stimulates endothelial production of NO and other vasodilators, thereby regulating peripheral perfusion to match O_2 demand (192).

The above evolutionarily conserved erythrocyte-based mechanisms permit extremely rapid coordination of local perfusion, gas exchange and metabolic waste elimination, with precise gradation of vasodilation or vasoconstriction linked to PO_2 (77,329). Decreased SNO-Hb concentration or erythrocyte-derived NO bioactivity is associated with pathological conditions characterized by pulmonary hypertension or tissue hypoxemia (78,252), while restoration of erythrocyte NO bioactivity benefit tissue oxygenation and recovery from injury (5,258,299). Thus, respiration is a three-gas exchange system (O_2, CO_2, and NO) where the lung, the cardiovascular circuit, and the peripheral tissue respond interdependently with the erythrocytes as mobile orchestrators (78).

Thoracopulmonary interactions

The relatively rigid thorax influences the fractal geometry of bronchovascular branching, resulting in parallel fractal behavior in physiological parameters such as ventilation, perfusion, and diffusion (3, 300, 363). The confined thoracic space can also be expected to influence the growth of lung parenchyma. Postnatal lung development is marked by (i) progressive increases in alveolar air, tissue, and microvascular volumes as well as alveolar-capillary surface areas, (ii) remodeling of gas exchange tissue leading to thinning of the air-blood barrier, and (iii) elongation and dilatation of conducting airways and blood vessels. The distending pressure generated by the outward recoil of a growing rib cage imposes mechanical stress on alveolar septa, resulting in tissue tension and deformation that opens ion channels, activate genes, and signals molecular regulatory pathways to initiate and sustain cellular growth (Fig. 76). Increasing pulmonary perfusion due to cardiovascular development also imposes mechanical strain and shear stress on alveolar microvascular endothelial cells and constitutes another stimulus for capillary growth. Additional stimuli (e.g., alveolar hypoxia and supplementing growth factors) imposed during this period could further augment lung growth (179). Lung growth relieves tissue tension and allows the rib cage to expand further in a feedback loop that continues until somatic maturity when bony epiphyseal union occurs (171). Thereafter, mechanical interactions between the lung and thorax diminish and both the lung and the thorax stop growing. Extending the age at which epiphyseal union occurs may explain the enhancement of lung growth observed during

chronic residence at high altitude by allowing a longer period of thoracic growth (317). Following epiphyseal union in adulthood, lung growth may be reinitiated if sufficiently intense intrathoracic mechanical stimuli are reimposed and space is available for expansion, for example, following pneumonectomy. Conversely, the inability to restore normal intrathoracic mechanical signals has hampered numerous attempts to reinitiate lung growth in emphysema.

Interference with mechanical thoracopulmonary interdependence during maturation could alter lung development. The best known example is congenital diaphragmatic hernia where the restricted intrathoracic space leads to lung hypoplasia (260). After surgical repair of the diaphragmatic defect, normal thoracopulmonary mechanical interactions are restored leading to “catch-up” lung growth that reverses pulmonary arterial hypertension (17) and nearly normalizes long-term lung function (188, 241). Severe childhood kyphoscoliosis is also associated with alveolar underdevelopment (20, 25, 67, 269) with fewer alveoli and larger distal airspaces. Conversely, inhibition of lung growth may deform the growing rib cage (233).

Thoracopulmonary interactions along with cyclic respiratory efforts and pulsatile pulmonary perfusion generate mechanical stresses that play a major role in lung development (179, 405). *In vitro* mechanical stretch of lung tissue stimulates epithelial proliferation (52, 230), apoptosis (308), signal transduction (52,229), ion transport (231,409), protein turnover of matrix (31, 409), and cytoskeleton (327), as well as gene and protein expression of cytokine growth factors (228,367) and surfactant-associated proteins (307). Increased airway pressure *in utero* accelerates fetal lung growth (273) associated with growth factor accumulation in the lung. Fetal chest expansion and respiratory movements are critical for lung development (130). Postnatal imposition of continuous positive airway pressure increases TLC, weight, protein and DNA content (425). Sustained segmental lung distension with perfluorocarbon accelerates lung growth in an age-dependent manner (262). Growth occurs preferentially at the lung periphery (97, 243) where bronchovascular support is lacking and septal mechanical stress is exaggerated compared to the central lung regions (417).

Much debate concerns whether postnatal lung growth occurs via alveolar hyperplasia (increased number) or hypertrophy (enlargement of existing alveoli). Human alveolar septal subdivisions are thought to increase only during early childhood even though lung volume, surface area and diffusing capacity continue to increase throughout somatic maturation (82,420,421). It should be noted that the structural parameters most relevant to gas exchange are alveolar-capillary surface area and the resistance of tissue-plasma-erythrocyte diffusion barrier (estimated from the harmonic mean barrier thickness) rather than the absolute number of alveoli. Surface complexity of the alveolar wall can be altered in various ways, for example, by tissue unfolding or the presence of a fluid lining layer—that influence gas exchange efficiency without altering the number of alveolar subdivisions. Experimental perturbation that increases the apparent number of alveoli does not necessarily increase gas exchange surface area or diffusing capacity (244,345). In addition, the 3D hierarchy of alveolar subdivision is complex and cannot always be accurately measured on random 2D sections. The definition of whether a tissue protrusion on a 2D image constitutes an alveolar septum could be arbitrary. In addition, earlier techniques for counting alveolar number are

prone to stereological bias; the disector, developed later, is the only unbiased technique currently available for estimating the number of alveoli through the Euler number of alveolar entrance rings, the network forming the wall of alveolar ducts (159).

Lung structure in relation to body size

Lungs from animals of different body sizes differ in various aspects of anatomy, development, and maturation. Rodents are born with the lung in the saccular stage; alveolization occurs from postnatal 4 to 14 days followed by alveolar wall thinning between 14 and 21 days (39). Because rodent epiphyses do not fully close (69), thoracic growth and alveolization can persist throughout life albeit at lower rates with age (346, 347). In comparison, guinea pigs are born with already formed alveoli (222, 304) containing more septal connective tissue (94) and less pulmonary vascular smooth muscle (350) than in mature lung. Their bony epiphyses begin to close at ~5 months of age (426) and the upper limit of thoracic and lung dimensions is reached by about 1 year of age. The alveoli of rabbits continue to form after birth up to 36 weeks but septal thinning occurs mostly before birth (213), resulting in a thinner alveolar blood-gas barrier and a higher capillary wall stress than in the dog or horse (23,246); septal thickness and capillary wall strength increase with postnatal maturation (105). Sheep are born with well-formed alveoli; postnatal growth only modestly increases alveolar number and complexity (68). Canine thoracopulmonary development and maturation is more similar to that in humans (247) except for a narrower elongated chest, which dictates the shape of the lobes and the partly monopodial airways. Pigs are born with well-developed lungs (404). Airspace expansion and septal thinning during the first postnatal week is associated with increased elastic recoil followed by vigorous septal subdivision and thickening (237,403). Quadruped primates (monkeys and baboons) possess a barrel-shaped thorax and an infracardiac lobe separating the heart from the diaphragm (337). This lobe is absent in bipedal animals. In monkeys, postnatal lung growth is associated with increasing alveolar size while the number of alveoli remains unchanged (138). However, later data using appropriate stereological techniques showed that alveoli increase in number, but not size during postnatal development in rhesus monkeys (187). As rhesus monkeys age, there is a significant loss of alveoli that is 30% greater in postmenopausal females than males (134). The great apes that assume an upright position exhibit anatomical relationships among lungs, thorax, heart, and diaphragm that closely resemble those in humans. Recent data in humans using appropriate stereological methods shows that alveoli are added in an exponential pattern during the first three years of postnatal growth with a rather shallow further increase until 15 years (135).

Compared to large animals, airway and vascular stratification is simpler in rodents. Respiratory bronchioles are few and short, or often absent, in rabbit, guinea pig, hamster, gerbil, rat and mice (11, 190, 197, 301). In human and large animal lungs, acinar airways bifurcate through several generations of respiratory bronchioles and alveolar ducts and eventually alveolar sacs. Airway stratification modulates not only ventilatory distribution but also the penetration and deposition of inhaled microparticles. Relative to rodent lungs, the highly stratified large lungs need more and stronger connective tissue fibers for support, which in turn mandates a more rigid rib cage to maintain stability without restricting truncal flexibility in locomotion. The longer mean acinar path length also requires more smooth

muscle and contractile elements along each generation to fine-tune $\dot{V}_A/\dot{Q}$ and $\mathrm{DL}/\dot{Q}$ matching. In contrast to the more symmetric dichotomous human airway tree, most quadrupeds including the mouse, rat, hamster, dog, pig, donkey, and horse, exhibit a monopodial branching pattern for the major airways of the slim and elongated lobes; the branches arising laterally from the central trunk then assume a fractal pattern as they reach the gas-exchange units (366). At a given diameter, the airway branches are shorter in animals than in humans (283).

In mammals, body size is an important determinant of O_2 needs and, in consequence, of pulmonary gas exchange and the sequential O_2 transfer functions from the lung to the mitochondria (see Fig. 2). The body's total O_2 needs vary with body mass in a nonlinear fashion: resting or basal $\dot{V}_{O2}$ increases with the ¾ power of body mass (208) because, for one, small animals need more energy to keep warm. When an animal engages in physical activity $\dot{V}_{O2}$ increases steadily until $\dot{V}_{O2}max$ is reached when the locomotor muscle mass is active at a level where aerobic metabolism can no longer satisfy the muscles' energy needs. In a human of 70 kg body mass $\dot{V}_{O2}$ is thus increased by over tenfold from rest to maximal exercise; this so-called aerobic scope is larger in larger mammals and less in small mammals; indeed, the smallest mammal, the Etruscan shrew of 2 g, is so active even at rest that exercise can increase $\dot{V}_{O2}$ by not much more than a factor 2. As a consequence, maximal $\dot{V}_{O2}$, measured in heavy exercise, increases more steeply than basal $\dot{V}_{O2}$, with body mass to the power 0.86 (Fig. 77) (396).

Considering the cascade of transfer steps from the lung through the circulation of blood to the mitochondria we must ask whether one or the other of these steps sets the limit reflected in this scaling. Figure 77 shows that $\dot{V}_{O2}max$ scales strictly in parallel with the mitochondrial volume in locomotor muscle; this suggests that the limit of aerobic work is set by the capacity of mitochondria for oxidative phosphorylation with the result that 1 ml of mitochondria consumes 5 mL O_2 per min at $\dot{V}_{O2}max$ in all species (147,387,390). Considering the supply of O_2 from the muscle capillaries to the mitochondria, it is found that the volume of capillary erythrocytes scales with the same exponent as the mitochondrial volume. And the transfer of O_2 by the circulation of blood follows the same scaling rule, though not in a simple fashion as the heart rate is a determinant functional parameter of blood flow (396). So in all these internal steps of the O_2 cascade, we note concordant scaling between the transfer steps and $\dot{V}_{O2}max$.

In a "perfectly designed" respiratory system (Fig. 2), one would expect the lung's capacity to transfer O_2 to the blood to be also proportional to $\dot{V}_{O2}max$, but this is not so: DL_{O2} is found to scale linearly with body mass (Fig. 77), a case of discordant scaling. It appears that in large mammals the diffusing capacity is significantly greater than what is needed to satisfy the body's O_2 needs in the lower parts of the cascade. What could be the reasons for this discordant scaling at the first step in the cascade? First, we have noted above that DL_{O2} has variable reserves that are only exploited in athletes and athletic animals; it can well be that this reserve is larger in large than small mammals. Second, one reason for designing the

lung with some reserve in DL_{O2} may be that the lung cannot enlarge by morphogenesis the structural elements of its functional capacity when the demands increase, for example, by training in athletes, in contrast to muscle mitochondria and capillaries as well as the heart, and this may be more important in large species. Third, we must consider that the diffusing capacity is not really the first step in the O_2 flow cascade: it is preceded by the ventilation of the peripheral gas exchange units through the system of airways that determine the reduction of PO_2 from inspired to alveolar values, particularly in the most peripheral acinar airways. It is well possible that the higher respiratory frequency of small animals improves acinar ventilation. But then there are significant size differences of the gas exchange units, the acini (Fig. 78A); this means that the longitudinal O_2 diffusion path length is much shorter in small lungs. For both these reasons, the reduction in alveolar PO_2 toward the most distant generation—which contains half the gas exchange surface of the acinus—(Fig. 68) could be less in small and greater in large animals (Fig. 78B) leading to a lower average PO_2 at the alveolar surface in the latter (310, 395, 396). A lower alveolar PO_2 means a lower driving force for O_2 diffusion so that larger lungs may need a larger alveolar surface to allow for the required transfer of O_2, whereas small animals could achieve the required transfer with a relatively smaller diffusing capacity. Whether this is a plausible explanation for the discordant scaling of pulmonary diffusing capacity needs further study.

Splenic reserves for gas exchange

There are reasonably tight allometric relationships in maximal O_2 uptake, alveolar surface area, capillary density, resting lung volume, and lung diffusing capacity across a wide range of species (377, 415). As structure-function capacities adapt in accordance with metabolic needs (380), species with a high aerobic capacity possess larger alveolar surface areas and higher membrane and blood conductance for O_2 per kg body weight than sedentary species of a similar size (393). Because lung size is constrained by the thorax, enhanced lung growth and remodeling alone is not sufficient to meet the O_2 transfer needs of highly athletic species (dogs, horses, and diving mammals); the hemoglobin pool must be correspondingly enlarged. Therefore, athletic species also possess larger circulating blood volume and total erythrocyte mass as well as a larger spleen compared to sedentary species (10, 43, 186). Contraction of their large spleen (~3% of body weight sequestering up to ~50% of total erythrocytes or ~13% of total blood volume at a hematocrit of 80%–90%) in response to exercise or sympathetic stimulation reversibly releases packed erythrocytes into the circulation to enhance both convective as well as diffusive O_2 transport in the lung (62, 161) and the peripheral tissue (361) by ~30%. Upon cessation of sympathetic stimulation, the erythrocytes are resequestered in the spleen. Demand-driven autologous blood-doping allows athletic animals to achieve an extremely high aerobic capacity without the adverse risks associated with chronic polycythemia. Splenectomy eliminates demand-driven polycythemia leading to significant reductions in maximal O_2 uptake, lung and membrane diffusing capacities, and alveolar microvascular recruitment (62, 161, 361). The same mechanisms are operative in human athletes, although the splenic reservoir is smaller (containing ~200 ml of blood) and the effect of splenic contraction is modest (3–5% increase in total circulating erythrocyte volume) (290,332). In small animals, for example, the guinea pig, the spleen comprises only ~0.3% of body weight (293) so its contribution to hematological O_2 carrying capacity and gas exchange is also limited.

The aforementioned structural variations contribute to interspecies differences in the *functional capacity* as well as *physiological reserves* for gas exchange, which in turn direct the utilization of adaptive mechanisms. In response to pathophysiological challenge, large athletic species compensate readily via recruitment of reserves, which mitigates the need for structural adaptation as the latter incurs higher metabolic costs. In contrast, small animals with limited physiological reserves rely heavily on structural sources of adaptation (see next section, Induced Structural Adaptation and its Functional Consequences).

Induced Structural Adaptation and its Functional Consequences

Normal pulmonary capacities for gas exchange are so vast they far exceed the capacities for other O_2 transport steps such as cardiovascular delivery and tissue extraction and utilization (Fig. 79). In the average healthy subject, a fraction of alveolar microvascular reserves for pulmonary gas exchange remain unexploited even at peak exercise. This is because in contrast to the muscular capacities that determine cardiovascular O_2 delivery and tissue O_2 extraction, the structural determinants of alveolar diffusion are not significantly altered by physical training or detraining; a training-induced increase in ventilatory capacity results mainly from adaptation of the respiratory muscles (151, 306). Only elite athletes, for example, human (74), thoroughbred horses (362) and foxhounds (158), that reach exceedingly high levels of alveolar ventilation and perfusion completely exhaust their pulmonary microvascular reserves at peak exercise where the efficiency of alveolar O_2 diffusion (indexed by the $\mathrm{DL}/\dot{Q}$ ratio) becomes limiting leading to the development of exercise-induced arterial hypoxemia. Experimental manipulation to increase O_2 flux across the normal lung by physical training (13, 146, 304), increasing metabolic O_2 demand (13, 108, 110, 146, 242), or cold exposure (110, 146) have not significantly altered the structural or functional capacities of the pulmonary gas exchanger, leading to the conclusion that manipulating alveolar-capillary O_2 flux along a concentration gradient is not an effective way of augmenting lung growth or function.

Alveolar-capillary gas exchange becomes the primary factor limiting O_2 transport under 2 specific conditions: (i) in alveolar hypoxia, for example, high-altitude residence or hypoventilation, where O_2 flux across the lung becomes the main bottleneck in O_2 transport, and (ii) in primary lung pathology, for example, parenchyma disease that causes inflammation, thickening and obliteration of alveolar-capillary units or bronchovascular disease that compromises convective O_2 transport. In each case, adaptation to the non-physiological conditions or to the loss of functioning lung units occurs via a combination of three general mechanisms to augment O_2 transfer: (i) recruitment of physiological reserves, (ii) remodeling of existing structure, for example, luminal dilatation, hypertrophy of airway or vascular wall, or thinning of alveolar septa, and (iii) regrowth of new gas exchange tissue capillaries.

While the general mechanisms of compensation are similar across species, their initiation thresholds differ with respect to body size and maturation. Owing to their limited microvascular and hematological reserves, rodents rely heavily on structural remodeling and new alveolar tissue-capillary growth to restore lost capacity caused by injury or resection. In contrast, large mammals such as dogs rely heavily on the recruitment of their extensive

physiological reserves; regeneration of new alveolar-capillary tissue, a metabolically costly option, is invoked only when existing reserves are exhausted. In both small and large species, compensatory lung growth is more easily invoked and more vigorous in young actively growing animals than in mature adults (274, 297, 338); the difference reflects the small microvascular reserves in immature lungs as well as the greater plasticity of the immature thorax as the enlarging ribcage creates space to permit lung growth without causing distortion. Another factor that influences the ease of growth reinitiation is the age at which epiphyseal union of the ribs occurs. In rodents, epiphyseal union is delayed and incomplete, with continuous epiphyseal remodeling (69, 85, 240, 323) that permit a prolonged duration of thoracic enlargement; the mechanical signals for lung growth diminish with age but do not cease. In contrast, in large mammals including humans the rib cage reaches its final dimensions upon complete epiphyseal closure at somatic maturation; thereafter lung growth is possible only when space is made available to accommodate the new structures without causing distortion. As a result of these fundamental differences, reinitiation of lung growth in response to injury and destruction is easily triggered in the rodent and young animals but much more difficult to trigger in adult large animals.

To date there are two well-characterized experimental models, pneumonectomy and alveolar hypoxia, that restrict pulmonary diffusive gas exchange and allow quantification of the adaptive response in otherwise “normal” lungs. These two models illustrate the signals, mechanisms, functional consequences, and limitations of structural plasticity in the lung, discussed in the following subsections: adaptation to pneumonectomy, adaptation to alveolar hypoxia at high altitude, comparison of response to pneumonectomy and alveolar hypoxia, and the limitations imposed by dysanaptic lung growth.

Adaptation to the loss of lung units—pneumonectomy

Pneumonectomy is a robust model that mimics the consequences of losing functioning lung units due to chronic restrictive disease regardless of specific etiology. Extensive literature has documented the physiologic, structural, cellular, and molecular events in this model. Unilateral pneumonectomy initiates rapid growth of the remaining lung in rodents, mice, rats, rabbits, ferrets and dogs (44, 169, 171, 292). Following pneumonectomy, various transcription factors are transiently upregulated, followed by increased synthesis of DNA and matrix protein, collagen and elastin as well as all major alveolar septal cell populations, leading to normalization of alveolar tissue volume and architecture, summarized in (171). In rodents, the rapid time course (1–2 weeks) and the accelerated proliferative activities promote tumorigenesis and tumor metastasis in the remaining lung (33–35).

Physical forces acting on the remaining lung are the major signals that trigger postpneumonectomy adaptation while alveolar hypoxia, cytokine growth factors, and hormones modulate the response. Following pneumonectomy, ventilation and perfusion shift to the remaining lung units, causing recruitment of alveolar surfaces, capillary volume, and erythrocytes. Alveolar endothelial permeability is acutely elevated (364) with influx of circulatory cells and proteins (249) including vital cytokines for growth and remodeling but it may also precipitate pulmonary edema if vascular reserves are inadequate. As long as the remaining lung units are normal, more than 60% of total lung mass must be resected before

pulmonary vascular resistance and capillary pressure increase at rest (348); neither vascular congestion nor extravasated protein and water contributes significantly to the gain in tissue weight or volume in the remaining lung (79,224).

In adult dogs following left pneumonectomy (42%–45% lung resection) the remaining lung volume quickly increases 80% to 90% due to air space enlargement. The remaining alveolar microvascular reserves are utilized resulting in an apparent increase in diffusing capacity of the remaining lung above that in a normal lung (152,172,181). Cellular response is selective and nonuniform. Alveolar type-2 epithelial cells, the resident epithelial progenitor cell, respond first by nearly doubling in volume before a significant response is seen in other resident alveolar cell types (160, 169). Alveolar tissue volume increases significantly only in the most caudal remaining lobe but not in other lobes (Fig. 80), so that overall alveolar tissue growth was slightly but not significantly higher than that in the control right lung (160,169,175).

After right pneumonectomy (55%–58% lung resection), microvascular reserves are exhausted and new alveolar tissue growth stimulated in all remaining lobes (176,182,412). Compensatory growth only partially normalizes lung diffusing capacity in adult canines (158,177) in contrast to the complete normalization in the growing lung of young canines (338), a fact that signifies the additive effects of developmental and postpneumonectomy stimuli and suggests the possibility of manipulating compensatory lung growth via amplification of the endogenous stimuli or via imposition of additional stimuli. In young canines early following right pneumonectomy, the volumes of interstitial cells and matrix increase disproportionately more than threefold while epithelial and endothelial cells increase less, associated with thickened remaining alveolar septa. Initial cellular proliferation is most prominent in the peripheral subpleural region (96). The early changes are followed by remodeling, which gradually restores the normal septal architecture and cell-matrix fractions, resulting in up to 2.5-fold increases in all tissue components relative to matched control lungs (Fig. 81). The volume and number of intra-acinar airways also increase (182). As the harmonic mean septal barrier thickness returns to normal lung diffusing capacity gradually improves. Alveolar endothelial cell volume and capillary blood volume increase proportionately with a significantly higher prevalence of double-capillary profiles reminiscent of the morphology of the immature lung (153, 412); this probably represent attempted neocapillary formation by the process of intussusception (76). These adaptive events progress over several months in dogs (176) in contrast to 2 to 3 weeks in rodents (358). Preventing postpneumonectomy mechanical lung stress using a space-occupying prosthesis impairs but does not completely eliminate compensatory growth or functional compensation (65, 164, 166, 296, 406, 422), suggesting a role for additional growth signals such as microvascular distention and shear or alveolar hypoxia.

In adult dogs following 65% to 70% lung resection, the remaining lobes expand up to three-fold (155, 416); alveolar growth per unit of remaining lung is even more vigorous than that following 58% resection (294); long-term lung diffusing capacity per unit of lung at a given pulmonary blood flow remains well preserved (155). Mechanical deformation of the parenchyma during passive inflation is nonuniform within and among the remaining lobes with indications that a limit of compensation may be approached (Fig. 80) (297). The

remaining acinar units outstrip their mechanical support, necessitating the deposition of new septal connective tissue in a patchy distribution that likely reflects the distribution of greater mechanical septal stress (416). In these patchy areas of thickened interstitium, alveolar capillaries and septal morphology are intact but resistance to O_2 transfer is likely increased. Acinar growth and compensation also outstrips that of conducting airways and blood vessels because the latter structures adapt exclusively by elongation and dilatation (63) to partially mitigate the increases in airflow and pulmonary vascular resistance (155,339). As a result of the discordant or dysanaptic adaptation between gas exchange tissue and conducting structures, postresection lung function is ultimately limited by pulmonary mechanical and hemodynamic impairment and not by diffusion impairment (Fig. 82).

The administration of supplemental growth factors augments selective features of compensatory lung growth (202–205, 412) but has not significantly improved function (64, 345). This is not surprising given that several hundred genes (220, 275) and multiple major homeostatic pathways (19,96,97,140,211,226,227,249,335,419,422,423) are activated following pneumonectomy. While broad gene activation is essential for achieving balanced growth of all gas-exchange components, it also means that the endogenous adaptive pattern is unlikely to be replicated by supplementation of any single factor. Nonetheless, targeted investigation of selected growth factors remains an important approach, not only for defining the contribution of individual factors to the overall response or the interactions among growth factors and with mechanical signals, but also because of the recognition that postpneumonectomy signaling is not simply a recapitulation of developmental events. Postpneumonectomy transcriptomic activation pattern differs from that during postnatal lung development (275), and at least one distinct nondevelopmental pathway involving anti-sense transcriptional upregulation of paracrine erythropoietin receptor signaling has been identified in the adult lung following pneumonectomy (424). Additional nondevelopmental pathways are likely recruited to modify a mature structural scaffold. This is a nascent area of active investigation.

Another emerging area is the role of stem cells in compensatory lung growth. Alveolar type-2 cells along with stem-like cells at the bronchoalveolar junction are thought to supply resident progenitor cells for the growth, maintenance, and repair of the alveolar epithelium (263, 385). Circulating bone marrow derived vascular progenitor cells have not been shown to contribute significantly to postpneumonectomy lung growth (359). Resident lung endothelial progenitor cells contribute to lung development (12) but the extent and mechanisms of their recruitment during compensatory lung growth remains unclear. It is also unclear whether compensatory lung growth involves the differentiation of stem or progenitor cells into a wide variety of structural cells of the alveolar wall or there is limited division of fully differentiated resident cells, or both.

Alveolar hypoxia or high-altitude exposure

Chronic alveolar hypoxia of high altitude is an established model of accelerated compensatory alveolar growth in actively growing animals (42, 171, 194, 221, 321). Native highlanders possess larger vital capacities and thoracic volumes than lowlanders (32, 73, 80, 102, 103, 131, 219). Native Tibetan infants born at high altitude show higher arterial O_2

saturation than infants whose mothers had migrated to high altitude two years previously (261). DL_{CO} is also higher in native highlanders and in adults born at sea level who subsequently acclimatize to high altitude (73, 298). Since altitude exposure induces reversible increases in respiratory compliance, microvascular pressures, blood volume, and hematocrit, an apparent increase in lung volume and DL_{CO} in highlanders may result from physiological or structural enhancement or both.

Hypoxia is associated with hypertrophy of gas exchange organs across animal phyla from the gills of fish and salamander (86), the skin folds of bullfrogs (37) to the placenta (70) and lung (276) in mammals; hypertrophy is independent of rhythmic stretch of the organ. This effect represents evolutionary adaptation to cope with oxygen-poor environments. Whereas severe hypoxia inhibits somatic growth (104, 317), postnatal exposure to a moderate altitude (<4000 m) has been shown to accelerate lung growth (*discussed below*). Space for the expanding lung is provided by passive rib cage expansion and caudal displacement of the diaphragm (194). As the altitude of exposure increases, inhibition of somatic (rib cage) growth becomes predominant so that although lung growth is initially stimulated, the effect diminishes with exposure duration as lung size becomes limited by the size of rib cage (221). Extreme hypoxia simulating an high altitude greater than 5000 m so retards rib cage growth as to prevent an absolute increase in lung volume, even though volume with respect to body weight is larger than in controls exposed to normoxia (291).

The mechanisms of adaptation to high-altitude residence differ among species. In rodents, chronic hypoxia accelerates alveolar growth (14, 15, 42, 61, 185, 320, 321, 347) in a maturity-dependent manner (24,245). Up to postnatal 14 days of age, hypoxia impairs alveolar septation. Between ages 14 and 40 days, hypoxia is associated with an increase in alveolar number consistent with stimulated septation. Older rats (23 d) raised in normoxia and then exposed to hypoxia show increased alveolar surface area and volume but unchanged alveolar number, consistent with airspace enlargement and surface unfolding (24). Hypoxia also enhances postpneumonectomy compensatory lung growth in rodents (318), indicating additive effects of separate stimuli. In addition, normoxic hypobaria can also accelerate cell proliferation and modify lung structure (319–322). Unlike humans, pulmonary gas exchange efficiency does not significantly limit O_2 transport in rats regardless of altitude (118). After rats exposed to chronic hypoxia return to normoxia, their lungs stop growing while the lungs of control animals residing in normoxia continue to grow; eventually lung size in the two groups become similar (291). The finding suggests reversibility of hypoxia-induced lung growth and highlights the plasticity of the rodent lung-thorax system where somatic as well as lung growth continues throughout life and the bony epiphyses do not fully close.

Compared to rodents, the bony epiphyses in guinea pigs begin to close at age ~20 wk (426). Weanling guinea pigs raised at simulated extreme high altitude (5100 m) initially show accelerated gain in lung volume and alveolar surface area (221) independent of hyperventilation (223), but the effect diminishes with age. When raised at a more tolerable altitude (3800 m), somatic growth is unaffected while alveolar structural dimensions and DL_{CO} are persistently enhanced throughout 6 to 11 months of exposure (180, 414). (Fig. 83) When weanling guinea pigs born at sea level are raised at 3800 m for 4 months followed by

return to an intermediate altitude (1200 m) for 7 to 8 months, some aspects of the high altitude-induced structural changes are no longer present whereas others persist (293). Results indicate at least partial reversibility structural adaptation following withdrawal of the high-altitude stimuli.

In large mammals, alveolar remodeling and hematological adaptation play a prominent role. Untrained young beagles born at sea level and raised to maturity at a moderate high altitude (3100 m) exhibit larger lung air and tissue volumes and higher DL_{CO} compared to matched controls raised at sea level, a finding consistent with hypoxia-enhanced lung growth (194). Following return to sea level, pulmonary vascular reactivity normalizes but right ventricular hypertrophy persists (123). Adult beagles raised at 3100 m for up to 3 years exhibit no evidence of structural or functional enhancement (194). The highly athletic foxhounds born at sea level and raised for 5 months during maturation at 3800 m altitude also exhibit enhancement of lung volume and diffusing capacity that persist following reacclimatization to sea level (162, 251). However, lung structure shows distal airspace enlargement and a lower harmonic mean thickness of the diffusion barrier without the addition of alveolar tissue or surface area (295). Instead, altitude-enhancement of alveolar-capillary conductance is due to a combination of thinning of alveolar septa, acinar airway enlargement, increased erythrocyte production, elevated circulating blood volumes, and splenic autotransfusion. A separate cohort of foxhounds that had been born at sea level and raised at 3800 m of altitude for 12 months until adulthood also fails to demonstrate enhanced lung growth compared to control animals simultaneously raised at sea level (*P Ravikumar, DM Dane and CC Hsia, unpublished observations*). The differences between sedentary and athletic canine breeds and between large and small species cannot be explained by the differences in altitude or duration of exposure. It appears that athletic animals preferentially utilize metabolically economical mechanisms—physiological recruitment, structural remodeling, and hematological augmentation—to compensate for the restricted O_2 transport at high altitude without resorting to the energetically costly process of generating new gas exchange tissue whereas rodents and guinea pigs readily reinitiate structural lung growth as the major mechanism of compensation.

Comparison of adaptation to pneumonectomy and hypoxia

These two models illustrate the range of stimulus-response relationships in the lung. Increasing mechanical stresses following incremental lung resection elicits progressively greater structural adaptation in the remaining lung up to a limit imposed by the extent of bronchovascular adaptation and by the need for additional mechanical support of the distal parenchyma. The *in vivo* adaptive limit is reached when postpneumonectomy lung expansion and hyperperfusion approach 2.5 to three-fold (155,416). In the high-altitude model, increasing hypoxia severity also increases the intensity of alveolar structural growth and remodeling up to a limit imposed by pulmonary arterial hypertension as well as by global suppression of somatic growth and metabolism; this limit is reached at about 5000 m of altitude (inspired O_2 tension ~80 Torr) (180,221). Alveolar hypoxia primarily amplifies preexisting active stimuli such as those in developing young animals or in the postpneumonectomy remaining lung. In the absence of active developmental growth signals, high-altitude exposure induces alveolar remodeling without new tissue growth. In contrast,

postpneumonectomy suprathreshold mechanical stresses induce alveolar-capillary growth *de novo* even in the adult lung. The magnitude of accelerated lung growth and remodeling during high altitude exposure is less than that seen postpneumonectomy, suggesting that mechanical stress elicits a stronger response than hypoxia. This may be because mechanical stress, in addition to altering cell and nuclear membrane permeability, cytoskeletal tension, and recruitment of chemoactive cells, also exaggerates PO_2 gradients within and among cells causing relative hypoxia in some cells. This notion is supported by the observation that pneumonectomy and hypoxia activate certain shared signaling pathways, for example, hypoxia-inducible factor-1α-erythropoietin-vascular endothelial growth factor (HIF-1α-EPO-VEGF) (96, 423); yet there are also important differences. For example, in hypoxia cellular HIF-1α protein level is typically elevated and its action enhanced via protein stabilization and nuclear translocation (30). Following pneumonectomy, HIF-1α mRNA and protein levels in the remaining lung are concordantly elevated indicating enhanced transcriptional activity (422, 423) typical of a mechanosensitive response (49). Hypoxia preferentially stimulates endocrine EPO signaling via its receptor (EPOR) on bone marrow erythroblasts leading to augmentation of circulating erythrocyte mass and blood volume (191) whereas pneumonectomy preferentially stimulates paracrine EPO signaling via EPOR localized to the remaining lung cells (96,423) with only minor transient increases in circulating erythrocyte and blood volumes.

Both pneumonectomy and alveolar hypoxia induce long-term acinar remodeling including (i) variable changes in the volume fractions of alveolar ducts and sacs, which at least partly reflect changes in airway smooth muscle tone, and (ii) reduction in the harmonic mean tissue-plasma-erythrocyte barrier which minimizes the resistance to O_2 transfer (175,180,295,411). Because the harmonic mean barrier thickness is proportional to the reciprocal of local absolute thicknesses, gas flux normally occurs predominantly through the "*thin side*" of the septum. At any given total septal tissue volume and absolute septal thickness, even minor redistribution of cells or matrix from the "thin" to the "thick" side of the septum significantly reduces the harmonic mean barrier thickness, and constitutes a metabolically efficient way of minimizing barrier resistance to diffusion. Pneumonectomy but not hypoxia induces a significant compensatory increase in the volume and branch points of respiratory bronchioles (182). Pulmonary vascular remodeling, medial hypertrophy, and resting pulmonary arterial hypertension are more prominent during chronic hypoxia exposure than following up to 58% lung resection. While hypoxic pulmonary vasoconstriction preserves ventilation-perfusion matching and protects distal microvasculature from flow-related mechanical stress and injury, it also prevents the prominent compensatory increase in capillary blood volume that augments gas exchange following pneumonectomy. It is unknown whether ambient hypoxia adds to the postpneumonectomy structural response in the lungs of adult large mammals.

Limitations imposed by mismatched (dysanaptic) lung growth

Developmental lung growth enlarges all compartments: alveolar cells, matrix, blood, and conducting structures as well as bony and muscular thorax; matched growth leads to proportional enhancement of gas exchange, mechanics, and hemodynamic function. In contrast, compensatory lung growth is less well matched as a result of the limited adaptive

potential of conducting bronchovasculature compared to that of the acini, resulting in dysanaptic (unequal) growth following pneumonectomy and hypoxia exposure. Dysanaptic lung growth originally refers to the variations in maximal expiratory flow rate relative to lung volume in normal subjects (121, 137, 148) and later to the smaller airway dimensions and lower maximal flow rates with respect to lung volume observed in native highlanders (32) and postpneumonectomy (122, 250). Airway-parenchyma mismatch could also occur as a long-term sequelae of bronchopulmonary dysplasia or chronic lung disease of prematurity where small airway obstruction persists despite normalization of lung volume and mechanics (22, 206). Dysanaptic growth leads to disproportionate impairment of pulmonary hemodynamics and airway mechanics relative to alveolar diffusion (Fig. 82).

Another type of dysanaptic growth results from the opposing effects of high-altitude exposure on the growth of lung and thorax where retardation of rib cage growth at extreme high altitude effectively limits the final dimension and functional capacity that could be achieved via stimulation of alveolar growth. A third type of dysanaptic growth results from the nonuniform stimulation of alveolar septal growth that leads to distortion of the blood-gas barrier. For example, selective pharmacological stimulation of alveolar cellular proliferation without corresponding stimulation of capillary blood supply could increase alveolar tissue volume without improving gas exchange. In fetal lambs with congenital diaphragmatic hernia, tracheal occlusion accelerates the generation of mesenchyme tissue but with fewer alveolar type-2 cells, leading to surfactant deficit (18) and distorted alveolar morphology that are incompatible with efficient gas exchange (289). Exogenous *all trans*-retinoic acid given to adult dogs following right pneumonectomy nonuniformly stimulates alveolar septal cell growth, which is accompanied by distortion of alveolar architecture and capillary morphology without significant enhancement of lung diffusing capacity or maximal O_2 uptake (64, 412). More double-capillary profiles typical of the immature lung are observed in retinoic acid-treated animals, consistent with an attempt at new capillary formation by intussusceptive growth of a tissue pillar into an existing capillary (76, 217). However, to be efficient in gas exchange, these newly stimulated double capillaries need to remodel into the single capillary morphology that are typical of the normal mature lung (Fig. 84). Exogenous *all trans*-retinoic acid given to emphysematous rats stimulates alveolar septation but the resulting smaller and more numerous alveoli are not accompanied by increases in surface area or lung diffusing capacity (244,345). The occurrence and consequences of structural distortion cannot be predicted from molecular or cellular studies alone but must be tested in the intact animal under appropriate physiological conditions.

Summary and Perspective—Intrinsic Challenges of Pulmonary Gas Exchange to Lung Structure

The mammalian lung has enabled aerobic life to thrive over a six-magnitude span in body size and survive a nearly 40% reduction in ambient O_2 tensions in diverse habitats from sea level to high altitude, in addition to accommodating a tenfold change in energetic needs as well as a fivefold change in blood flow from rest to maximal exercise. At its essence the lung is an assembly of conduits that evolved to meet a fundamental challenge—how to bring variable flows of air and blood, generated by two separately regulated pumps inside the

thoracic container, into close proximity with each other without actually mixing. Following pressure gradients and the fractal principle of self-similarity, branching morphogenesis meets this challenge by generating, during lung development, a hierarchical airway tree to which a vascular network is associated out of which two vascular trees, the pulmonary arteries and veins, form in close association with the airways. This allows a systematic approximation of the airways and the vessels in the gas-exchanging alveolar-capillary units in the acinus that comprises the last few generations of the branching trees. The result is a stratified scaffold ending in a blood-gas barrier composed of an extremely attenuated layer of cells and matrix establishing an extensive surface area across which gas transfer from air to blood occurs by simple diffusion and ending in a hemoglobin “sink” from where it is transported to the end-organ cells. All along these hierarchical lead structures a system of cells and connective tissue elements join to maintain the physical integrity of the scaffold—for example, binding airways and blood vessels together at all levels, optimally distributing the mechanical forces of ventilation to all parts, providing strength and elastic recoil, reducing surface tension, clearing foreign particles and mounting immune defenses against infection and inflammation.

The next major challenge, how to manage the dynamic interface of air, tissue and blood to maximize gas-exchange efficiency, requires local sensing and feedback mechanisms to coordinate the delivery of air and blood and to minimize wasted ventilation or perfusion. This is accomplished via contractile elements and smooth muscle cells that reflexively control airway and vascular tone in response to local changes in gas tensions, thereby matching the distributions of air and blood flows across the inflated perfused alveoli while diverting ventilation away from poorly perfused alveoli and blood flow away from poorly ventilated alveoli.

A third challenge is how to adjust pulmonary gas exchange in accordance with variable systemic metabolic demands so that the lung admits an O_2 flow sufficient to satisfy the highest energy needs, such as occur in heavy exercise, but not allow excessive amount of O_2, a potent cytotoxin, to enter the organism. This requires systemic feedback mechanisms that sense and report the needs of distant organs to the heart and lung. The functionally effective diffusion surface is a composite of epithelial-endothelial-erythrocyte interfaces; thus, the hemoglobin “sink” is an integral component of the gas exchanger. The physicochemical properties of erythrocytes— volume, size, shape, deformability, membrane area, flow, distribution, metabolism, hemoglobin content, and allosterism— critically determine gas exchange efficiency in the lung and the periphery. More than just a passive gas carrier, hemoglobin acts as a circulating metabolic sensor to regulate the on-and off-loading of O_2. Via allosteric coupling of O_2-CO_2, hemoglobin matches O_2 delivery to local metabolic CO_2 production. Via allosteric coupling of O_2-NO, hemoglobin controls NO scavenging and release to modulate local vasomotor tone and consequently O_2 uptake and delivery. In effect, erythrocytes function as mobile gas exchange regulators to meet the challenge of matching central O_2 supply to distant “consumer” demand.

A fourth challenge is to provide mechanisms for enhancing the animal’s survival as predator or prey. The complexity of extensive alveolar surface folding, the surfactant lining layer, and a low-pressure pulmonary microvasculature offer high capacitance for accommodating large

rapid increases in ventilation and perfusion from rest to peak exercise, allowing recruitment of lung diffusing capacity and preventing the development of arterial hypoxemia. In athletic species where alveolar-capillary recruitment alone may not be sufficient in meeting the high oxygen demand, a large splenic reservoir of sequestered erythrocytes is available for reversible autotransfusion and further augmentation of O_2 transport as needed.

A fifth challenge lies in providing versatile adaptive mechanisms to compensate for the loss of gas exchange capacity caused by environmental perturbation, organ injury or disease. In response to the destruction of lung units or to hypoxic environment, pulmonary physiological reserves are utilized as initial defense to maintain O_2 uptake, and erythropoiesis may be stimulated to enlarge the circulating O_2 reservoir. When these sources of compensation are nearly exhausted, the lung scaffold can undergo remodeling and redistribution of its constituents to optimize barrier conductance, but this offers limited potential for adaptation in adult lungs. In the presence of appropriate stimuli, growth of alveolar tissue-capillaries may be accelerated in developing lungs following loss of tissue, leading to long-term near-complete normalization of lung diffusing capacity. Limited alveolar-capillary growth may also be reinitiated in mature lungs leading to significant though incomplete functional compensation. For respiratory biologists, the ultimate challenges are to comprehend the mechanisms underlying plasticity of the lung, and find ways of fully exploiting the plasticity for the purpose of augmenting structural and functional capacities. These challenges remain to be met and understood.

Acknowledgments

The authors thank Kyrene H. Moe, Daniel Brönnimann, and Barbara Krieger for assistance with manuscript preparation, and acknowledge the important support by the National Heart, Lung, and Blood Institute, including the R01 grant HL40070 and the Lung Repair and Regeneration Consortium grant U01 HL111146 (CH) and National Institutes of Health Grants P01-ES-0628 and OD-011107 (DH). The content is solely the responsibility of the authors and does not necessarily represent the official views of the National Institutes of Health.

References

1. Alescio T, Cassini A. Induction in vitro of tracheal buds by pulmonary mesenchyme grafted on tracheal epithelium. J Exp Zool. 1962; 150:83–94. [PubMed: 14011906]
2. Alexander, RM. Principles of Animal Locomotion. Princeton, NJ: Princeton University Press; 2003. p. 371
3. Altemeier WA, McKinney S, Glenny RW. Fractal nature of regional ventilation distribution. J Appl Physiol. 2000; 88:1551–1557. [PubMed: 10797111]
4. Arora R, Metzger RJ, Papaioannou VE. Multiple roles and interactions of Tbx4 and Tbx5 in development of the respiratory system. PLoS Genet. 2012; 8:e1002866. [PubMed: 22876201]
5. Auten RL, Mason SN, Whorton MH, Lampe WR, Foster WM, Gold-berg RN, Li B, Stamler JS, Auten KM. Inhaled ethyl nitrite prevents hyperoxia-impaired postnatal alveolar development in newborn rats. Am J Respir Crit Care Med. 2007; 176:291–299. [PubMed: 17478622]
6. Bachofen H, Schurch S. Alveolar surface forces and lung architecture. Comp Biochem Physiol A Mol Integr Physiol. 2001; 129:183–193. [PubMed: 11369543]
7. Bachofen H, Schürch S, Urbinelli M, Weibel ER. Relations among alveolar surface tension, surface area, volume, and recoil pressure. J Appl Physiol. 1987; 62:1878–1887. [PubMed: 3597262]
8. Bachofen H, Wangensteen D, Weibel ER. Surfaces and volumes of alveolar tissue under zone II and zone III conditions. J Appl Physiol Respir Environ Exerc Physiol. 1982; 53:879–885. [PubMed: 7153122]

9. Bachofen H, Weber J, Wangensteen D, Weibel ER. Morphometric estimates of diffusing capacity in lungs fixed under zone II and zone III conditions. Respir Physiol. 1983; 52:41–52. [PubMed: 6346444]
10. Bakovic D, Valic Z, Eterovic D, Vukovic I, Obad A, Marinovic-Terzic I, Dujic Z. Spleen volume and blood flow response to repeated breath-hold apneas. J Appl Physiol. 2003; 95:1460–1466. [PubMed: 12819225]
11. Bal HS, Ghoshal NG. Morphology of the terminal bronchiolar region of common laboratory mammals. Lab Anim. 1988; 22:76–82. [PubMed: 3352222]
12. Balasubramaniam V, Mervis CF, Maxey AM, Markham NE, Abman SH. Hyperoxia reduces bone marrow, circulating, and lung endothelial progenitor cells in the developing lung: Implications for the pathogenesis of bronchopulmonary dysplasia. Am J Physiol Lung Cell Mol Physiol. 2007; 292:L1073–L1084. [PubMed: 17209139]
13. Bartlett D Jr. Postnatal growth of the mammalian lung: Influence of exercise and thyroid activity. Respir Physiol. 1970; 9:50–57. [PubMed: 5443579]
14. Bartlett D Jr. Postnatal growth of the mammalian lung: Influence of low and high oxygen tensions. Respir Physiol. 1970; 9:58–64. [PubMed: 5443580]
15. Bartlett D Jr, Remmers JE. Effects of high altitude on the lungs of young rats. Respir Physiol. 1971; 13:116–125. [PubMed: 5125910]
16. Bates JH, Lauzon AM. Parenchymal tethering, airway wall stiffness, and the dynamics of bronchoconstriction. J Appl Physiol (1985). 2007; 102:1912–1920. [PubMed: 17204575]
17. Beals DA, Schloo BL, Vacanti JP, Reid LM, Wilson JM. Pulmonary growth and remodeling in infants with high-risk congenital diaphragmatic hernia. J Pediatr Surg. 1992; 27:997–1001. discussion 1001–1002. [PubMed: 1403564]
18. Benachi A, Chailley-Heu B, Delezoide AL, Dommergues M, Brunelle F, Dumez Y, Bourbon JR. Lung growth and maturation after tracheal occlusion in diaphragmatic hernia. Am J Respir Crit Care Med. 1998; 157:921–927. [PubMed: 9517613]
19. Bennett RA, Colony PC, Addison JL, Rannels DE. Effects of prior adrenalectomy on postpneumonectomy lung growth in the rat. Am J Physiol. 1985; 248:E70–74. [PubMed: 3966552]
20. Berend N, Marlin GE. Arrest of alveolar multiplication in kyphoscoliosis. Pathology. 1979; 11:485–491. [PubMed: 523187]
21. Betticher DC, Reinhart WH, Geiser J. Effect of RBC shape and deformability on pulmonary diffusing capacity and resistance to flow in rabbit lungs. J Appl Physiol. 1995; 78:778–783. [PubMed: 7775318]
22. Bhandari A, Bhandari V. Pathogenesis, pathology and pathophysiology of pulmonary sequelae of bronchopulmonary dysplasia in premature infants. Front Biosci. 2003; 8:e370–380. [PubMed: 12700058]
23. Birks EK, Mathieu-Costello O, Fu Z, Tyler WS, West JB. Comparative aspects of the strength of pulmonary capillaries in rabbit, dog, and horse. Respir Physiol. 1994; 97:235–246. [PubMed: 7938920]
24. Blanco LN, Massaro D, Massaro GD. Alveolar size, number, and surface area: Developmentally dependent response to 13% O_2. Am J Physiol. 1991; 261:L370–377. [PubMed: 1767857]
25. Boffa P, Stovin P, Shneerson J. Lung developmental abnormalities in severe scoliosis. Thorax. 1984; 39:681–682. [PubMed: 6474402]
26. Bohr C. Über die spezifische Tätigkeit der Lungen bei der respiratorischen Gasaufnahme und ihr Verhalten zu der durch die Alveolarwand stattfindenden Gasdiffusion. Skandinavisches Archiv Für Physiologie. 1909; 22:221–280.
27. Borland C, Bottrill F, Jones A, Sparkes C, Vuylsteke A. The significant blood resistance to lung nitric oxide transfer lies within the red cell. J Appl Physiol (1985). 2014; 116:32–41. [PubMed: 24265283]
28. Borland CD, Higenbottam TW. A simultaneous single breath measurement of pulmonary diffusing capacity with nitric oxide and carbon monoxide. Eur Respir J. 1989; 2:56–63. [PubMed: 2707403]
29. Borland CDR, Dunningham H, Bottrill F, Vuylsteke A, Yilmaz C, Dane DM, Hsia CCW. Significant blood resistance to nitric oxide transfer in the lung. J Appl Physiol. 2010; 108:1052–1060. [PubMed: 20150569]

30. Brahimi-Horn MC, Pouyssegur J. HIF at a glance. J Cell Sci. 2009; 122:1055–1057. [PubMed: 19339544]
31. Breen EC. Mechanical strain increases type I collagen expression in pulmonary fibroblasts in vitro. J Appl Physiol. 2000; 88:203–209. [PubMed: 10642382]
32. Brody JS, Lahiri S, Simpser M, Motoyama EK, Velasquez T. Lung elasticity and airway dynamics in Peruvian natives to high altitude. J Appl Physiol. 1977; 42:245–251. [PubMed: 838649]
33. Brown LM, Malkinson AM, Rannels DE, Rannels SR. Compensatory lung growth after partial pneumonectomy enhances lung tumorigenesis induced by 3-methylcholanthrene. Cancer Res. 1999; 59:5089–5092. [PubMed: 10537279]
34. Brown LM, Welch DR, Rannels DE, Rannels SR. Partial pneumonectomy enhances melanoma metastasis to mouse lungs. Chest. 2002; 121:28S–29S. [PubMed: 11893665]
35. Brown LM, Welch DR, Rannels SR. B16F10 melanoma cell colonization of mouse lung is enhanced by partial pneumonectomy. Clin Exp Metastasis. 2002; 19:369–376. [PubMed: 12198764]
36. Bur S, Bachofen H, Gehr P, Weibel ER. Lung fixation by airway instillation: Effects on capillary hematocrit. Exp Lung Res. 1985; 9:57–66. [PubMed: 3933968]
37. Burggren W, Mwalukoma A. Respiration during chronic hypoxia and hyperoxia in larval and adult bullfrogs (Rana catesbeiana). I. Morphological responses of lungs, skin and gills. J Exp Biol. 1983; 105:191–203. [PubMed: 6604781]
38. Burnham KJ, Arai TJ, Dubowitz DJ, Henderson AC, Holverda S, Buxton RB, Prisk GK, Hopkins SR. Pulmonary perfusion heterogeneity is increased by sustained, heavy exercise in humans. J Appl Physiol (1985). 2009; 107:1559–1568. [PubMed: 19745192]
39. Burri PH. The postnatal growth of the rat lung. 3. Morphology. Anat Rec. 1974; 180:77–98. [PubMed: 4416419]
40. Burri PH. Fetal and postnatal development of the lung. Annu Rev Physiol. 1984; 46:617–628. [PubMed: 6370120]
41. Burri PH. Structural aspects of postnatal lung development – alveolar formation and growth. Biol Neonate. 2006; 89:313–322. [PubMed: 16770071]
42. Burri PH, Weibel ER. Morphometric estimation of pulmonary diffusion capacity. II. Effect of PO_2 on the growing lung, adaption of the growing rat lung to hypoxia and hyperoxia. Respiration physiology. 1971; 11:247–264. [PubMed: 5540208]
43. Cabanac A, Folkow LP, Blix AS. Volume capacity and contraction control of the seal spleen. J Appl Physiol (1985). 1997; 82:1989–1994. [PubMed: 9173968]
44. Cagle PT, Thurlbeck WM. Postpneumonectomy compensatory lung growth. American Review of Respiratory Disease. 1988; 138:1314–1326. [PubMed: 3059893]
45. Calder, A. Consequence of body size for avian energetics. In: Payrastre, B., editor. Avian Energetics. Cambridge, MA: Nuttal Ornithological Club; 2009. p. 86-151.
46. Capen RL, Latham LP, Wagner WW Jr. Diffusing capacity of the lung during hypoxia: Role of capillary recruitment. J Appl Physiol. 1981; 50:165–171. [PubMed: 7204185]
47. Cardoso WV, Lu J. Regulation of early lung morphogenesis: Questions, facts and controversies. Development. 2006; 133:1611–1624. [PubMed: 16613830]
48. Carlin JI, Hsia CC, Cassidy SS, Ramanathan M, Clifford PS, Johnson RL Jr. Recruitment of lung diffusing capacity with exercise before and after pneumonectomy in dogs. J Appl Physiol. 1991; 70:135–142. [PubMed: 2010368]
49. Chang H, Shyu KG, Wang BW, Kuan P. Regulation of hypoxia-inducible factor–1alpha by cyclical mechanical stretch in rat vascular smooth muscle cells. Clin Sci (Lond). 2003; 105:447–456. [PubMed: 12780343]
50. Chang HK. Convection, diffusion and their interaction in the bronchial tree. Adv Exp Med Biol. 1988; 227:39–52. [PubMed: 3289322]
51. Chang HK, Tremblay J, Boileau R, Martin RR. Regional hypoventilation and bronchoconstriction during pulmonary air embolism. Bull Eur Physiopathol Respir. 1982; 18:877–883. [PubMed: 6927540]

52. Chess PR, Toia L, Finkelstein JN. Mechanical strain-induced proliferation and signaling in pulmonary epithelial H441 cells. Am J Physiol Lung Cell Mol Physiol. 2000; 279:L43–51. [PubMed: 10893201]
53. Coates G, O'Brodovich H, Jefferies AL, Gray GW. Effects of exercise on lung lymph flow in sheep and goats during normoxia and hypoxia. J Clin Invest. 1984; 74:133–141. [PubMed: 6736245]
54. Colebatch HJH, Ng CKY. Estimating alveolar surface area during life. Respir Physiol. 1992; 88:163–170. [PubMed: 1626135]
55. Constantinopol M, Jones JH, Weibel ER, Taylor CR, Lindholm A, Karas RH. Oxygen transport during exercise in large mammals. II. Oxygen uptake by the pulmonary gas exchanger. J Appl Physiol. 1989; 67:871–878. [PubMed: 2793687]
56. Costa EL, Lima RG, Amato MB. Electrical impedance tomography. Curr Opin Crit Care. 2009; 15:18–24. [PubMed: 19186406]
57. Cotes JE, Dabbs JM, Elwood PC, Hall AM, McDonald A, Saunders MJ. Iron-deficiency anemia: Its effect on transfer factor for the lung (diffusing capacity) and ventilation and cardiac frequency during sub-maximal exercise. Clin Sci. 1972; 42:325–335. [PubMed: 5013875]
58. Crapo JD, Barry BE, Gehr P, Bachofen M, Weibel ER. Cell number and cell characteristics of the normal human lung. AmRevRespirDis. 1982; 126:332–337.
59. Crapo JD, Crapo RO. Comparison of total lung diffusion capacity and the membrane component of diffusion capacity as determined by physiologic and morphometric techniques. Respiration physiology. 1983; 51:183–194. [PubMed: 6844754]
60. Crapo JD, Crapo RO, Jensen RL, Mercer RR, Weibel ER. Evaluation of lung diffusing capacity by physiological and morphometric techniques. J Appl Physiol (1985). 1988; 64:2083–2091. [PubMed: 3391907]
61. Cunningham EL, Brody JS, Jain BP. Lung growth induced by hypoxia. J Appl Physiol. 1974; 37:362–366. [PubMed: 4414528]
62. Dane DM, Hsia CC, Wu EY, Hogg RT, Hogg DC, Estrera AS, Johnson RL Jr. Splenectomy impairs diffusive oxygen transport in the lung of dogs. J Appl Physiol. 2006; 101:289–297. [PubMed: 16601302]
63. Dane DM, Johnson RL Jr, Hsia CCW. Dysanaptic growth of conducting airways after pneumonectomy assessed by CT scan. J Appl Physiol. 2002; 93:1235–1242. [PubMed: 12235020]
64. Dane DM, Yan X, Tamhane RM, Johnson RL Jr, Estrera AS, Hogg DC, Hogg RT, Hsia CCW. Retinoic acid-induced alveolar cellular growth does not improve function after right pneumonectomy. J Appl Physiol. 2004; 96:1090–1096. [PubMed: 14506099]
65. Dane DM, Yilmaz C, Estrera AS, Hsia CC. Separating in vivo mechanical stimuli for postpneumonectomy compensation: Physiological assessment. J Appl Physiol. 2013; 114:99–106. [PubMed: 23104695]
66. Daniels CB, Pratt J. Breathing in long necked dinosaurs; did the sauropods have bird lungs. Comp Biochem Physiol [A]. 1992; 101(1):43–46.
67. Davies G, Reid L. Effect of scoliosis on growth of alveoli and pulmonary arteries and on right ventricle. Arch Dis Child. 1971; 46:623–632. [PubMed: 5118050]
68. Davies P, Reid L, Lister G, Pitt B. Postnatal growth of the sheep lung: A morphometric study. Anat Rec. 1988; 220:281–286. [PubMed: 3364753]
69. Dawson AB. Additional evidence of the failure of epiphyseal union in the skeleton of the rat. Studies on wild and captive Norway rats. Anat Rec. 1934; 60:501–511.
70. de Grauw TJ, Myers RE, Scott WJ. Fetal growth retardation in rats from different levels of hypoxia. Biol Neonate. 1986; 49:85–89. [PubMed: 3697431]
71. Deem S, Berg JT, Kerr ME, Swenson ER. Effects of the RBC membrane and increased perfusate viscosity on hypoxic pulmonary vasoconstriction. J Appl Physiol. 2000; 88:1520–1528. [PubMed: 10797107]
72. Deem S, Hedges RG, McKinney S, Polissar NL, Alberts MK, Swenson ER. Mechanisms of improvement in pulmonary gas exchange during isovolemic hemodilution. J Appl Physiol. 1999; 87:132–141. [PubMed: 10409567]
73. DeGraff AC Jr, Grover RF, Johnson RL Jr, Hammond JW Jr, Miller JM. Diffusing capacity of the lung in Caucasians native to 3,100 m. J Appl Physiol. 1970; 29:71–76. [PubMed: 5425040]

74. Dempsey JA. Exercise-induced arterial hypoxemia in healthy human subjects at sea level. J Physiol (London). 1984; 355:161–175. [PubMed: 6436475]
75. Ding DJ, Martin JG, Macklem PT. Effects of lung volume on maximal methacholine-induced bronchoconstriction in normal humans. J Appl Physiol (1985). 1987; 62:1324–1330. [PubMed: 3553143]
76. Djonov V, Schmid M, Tschanz SA, Burri PH. Intussusceptive angiogenesis: Its role in embryonic vascular network formation. Circ Res. 2000; 86:286–292. [PubMed: 10679480]
77. Doctor A, Platt R, Sheram ML, Eischeid A, McMahon T, Maxey T, Doherty J, Axelrod M, Kline J, Gurka M, Gow A, Gaston B. Hemoglobin conformation couples erythrocyte S-nitrosothiol content to O_2 gradients. Proc Natl Acad Sci U S A. 2005; 102:5709–5714. [PubMed: 15824313]
78. Doctor A, Stamler JS. Nitric oxide transport in blood: A third gas in the respiratory cycle. Compr Physiol. 2011; 1:541–568. [PubMed: 23737185]
79. Doerschuk CM, Sekhon HS. Pulmonary blood volume and edema in postpneumonectomy lung growth in rats. J Appl Physiol (1985). 1990; 69:1178–1182. [PubMed: 2246167]
80. Droma TS, McCullough RG, McCullough RE, Zhuang JG, Cymerman A, Sun SF, Sutton JR, Moore LG. Increased vital and total lung capacities in Tibetan compared to Han residents of Lhasa (3658 m). Am J Phys Anthropol. 1991; 86:341–351. [PubMed: 1746642]
81. Duncker HR. Structure of avian lungs. RespirPhysiol. 1972; 14:44–63.
82. Dunnill MS. Postnatal growth of the lung. Thorax. 1962; 17:329–333.
83. Dutrieue B, Vanholsbeeck F, Verbanck S, Paiva M. A human acinar structure for simulation of realistic alveolar plateau slopes. J Appl Physiol. 2000; 89:1859–1867. [PubMed: 11053337]
84. Eldridge MW, Podolsky A, Richardson RS, Johnson DH, Knight DR, Johnson EC, Hopkins SR, Michimata H, Grassi B, Feiner J, Kurdak SS, Bickler PE, Wagner PD, Severinghaus JW. Pulmonary hemodynamic response to exercise in subjects with prior high-altitude pulmonary edema. J Appl Physiol. 1996; 81:911–921. [PubMed: 8872663]
85. Enomoto A, Harada T, Maita K, Shirasu Y. Epiphyseal lesions of the femur and tibia in rats following oral chronic administration of zinc dimethyldithiocarbamate (ziram). Toxicology. 1989; 54:45–58. [PubMed: 2916241]
86. Feder ME, Burggren WW. Skin breathing in vertebrates. Scientific American. 1985; 253:126–142.
87. Federspiel WJ. Pulmonary diffusing capacity: Implications of two-phase blood flow in capillaries. Respir Physiol. 1989; 77:119–134. [PubMed: 2799105]
88. Fehrenbach H, Voswinckel R, Michl V, Mehling T, Fehrenbach A, Seeger W, Nyengaard JR. Neoalveolarisation contributes to compensatory lung growth following pneumonectomy in mice. Eur Respir J. 2008; 31:515–522. [PubMed: 18032439]
89. Felici M, Filoche M, Sapoval B. Diffusional screening in the human pulmonary acinus. J Appl Physiol. 2003; 94:2010–2016. [PubMed: 12679351]
90. Felici M, Filoche M, Sapoval B. Renormalized random walk study of oxygen absorption in the human lung. Phys Rev Lett. 2004; 92:068101. [PubMed: 14995277]
91. Felici M, Filoche M, Straus C, Similowski T, Sapoval B. Diffusional screening in real 3D human acini–a theoretical study. Respir Physiol Neurobiol. 2005; 145:279–293. [PubMed: 15705542]
92. Filoche M, Tai CF, Grotberg JB. Three-dimensional model of surfactant replacement therapy. Proc Natl Acad Sci U S A. 2015; 112:9287–9292. [PubMed: 26170310]
93. Florens M, Sapoval B, Filoche M. An anatomical and functional model of the human tracheobronchial tree. J Appl Physiol (1985). 2011; 110:756–763. [PubMed: 21183626]
94. Forrest JB, Weibel ER. Morphometric estimation of pulmonary diffusion capacity. VII. The normal Guinea pig lung. Respir Physiol. 1975; 24:191–202. [PubMed: 1179048]
95. Forster RE. Diffusion and chemical reaction as limiting factors in CO_2 equilibration in lungs. Fed Proc. 1982; 41:2125–2127. [PubMed: 6804271]
96. Foster DJ, Moe OW, Hsia CC. Upregulation of erythropoietin receptor during postnatal and postpneumonectomy lung growth. Am J Physiol Lung Cell Mol Physiol. 2004; 287:L1107–L1115. [PubMed: 15286000]

97. Foster DJ, Yan X, Bellotto DJ, Moe OW, Hagler HK, Estrera AS, Hsia CCW. Expression of epidermal growth factor and surfactant proteins during postnatal and compensatory lung growth. Am J Physiol Lung Cell Mol Physiol. 2002; 283:L981–990. [PubMed: 12376351]

98. Foucquier A, Filoche M, Moreira AA, Andrade JS Jr, Arbia G, Sapoval B. A first principles calculation of the oxygen uptake in the human pulmonary acinus at maximal exercise. Respir Physiol Neurobiol. 2013; 185:625–638. [PubMed: 23201099]

99. Frank AO, Chuong CJ, Johnson RL. A finite-element model of oxygen diffusion in the pulmonary capillaries. J Appl Physiol. 1997; 82:2036–2044. (editorial comment appears in 2082(2036):1717–1718). [PubMed: 9173974]

100. Fredberg, JJ. Airway dynamics: Recursiveness, randomness, and reciprocity in linear system simulation and parameter estimation. In: Chang, HK.; Paiva, M., editors. Respiratory Physiology: An Analytical Approach. New York, Basel: Marcel Dekker; 1989. p. 167-194.

101. Fredberg JJ, Moore JA. The distributed response of complex branching duct networks. J Acoust Soc Am. 1978; 63:954–961. [PubMed: 670560]

102. Frisancho AR. Human growth and pulmonary function of a high altitude Peruvian Quechua population. Human Biology. 1969; 41:364–379.

103. Frisancho AR. Developmental adaptation to high altitude hypoxia. Int J Biometeor. 1977; 21:135–146.

104. Frisancho AR, Newman MT, Baker P. Differences in stature and cortical thickness among highland Quechua Indian boys. American Journal of Clinical Nutrition. 1970; 23:382–385. [PubMed: 5441173]

105. Fu Z, Heldt GP, West JB. Increased fragility of pulmonary capillaries in newborn rabbit. Am J Physiol Lung Cell Mol Physiol. 2003; 284:L703–L709. [PubMed: 12676761]

106. Fuller B. Tensegrity. Portfolio Artnews Annual. 1961; 4:112–127.

107. Fung YC, Sobin SS. Theory of sheet flow in lung alveoli. J Appl Physiol. 1969; 26:472–488. [PubMed: 5775333]

108. Geelhaar A, Weibel ER. Morphometric estimation of pulmonary diffusion capacity. 3. The effect of increased oxygen consumption in Japanese Waltzing mice. Respir Physiol. 1971; 11:354–366. [PubMed: 5573326]

109. Gehr P, Bachofen M, Weibel ER. The normal human lung: Ultrastructure and morphometric estimation of diffusion capacity. Respir Physiol. 1978; 32:121–140. [PubMed: 644146]

110. Gehr P, Hugonnaud C, Burri PH, Bachofen H, Weibel ER. Adaptation of the growing lung to increased VO_2: III. The effect of exposure to cold environment in rats. Respir Physiol. 1978; 32:345–353. [PubMed: 663447]

111. Gehr P, Mwangi DK, Ammann A, Maloiy GM, Taylor CR, Weibel ER. Design of the mammalian respiratory system. V. Scaling morphometric pulmonary diffusing capacity to body mass: Wild and domestic mammals. Respir Physiol. 1981; 44:61–86. [PubMed: 7232887]

112. Gehr P, Sehovic S, Burri PH, Claassen H, Weibel ER. The lung of shrews: Morphometric estimation of diffusion capacity. Respiration physiology. 1980; 40:33–47. [PubMed: 7394364]

113. Gérard M, Moinard J, Téchoueyres P, Varéne N, Guénard H. Pulmonary diffusion limitation after prolonged strenuous exercise. Respir Physiol. 1991; 83:143–154. [PubMed: 2068412]

114. Gil J, Bachofen H, Gehr P, Weibel ER. Alveolar volume-surface area relation in air- and saline-filled lungs fixed by vascular perfusion. J Appl Physiol Respir Environ Exerc Physiol. 1979; 47:990–1001. [PubMed: 511725]

115. Giuntini C. Ventilation/perfusion scan and dead space in pulmonary embolism: Are they useful for the diagnosis? Q J Nucl Med. 2001; 45:281–286. [PubMed: 11893964]

116. Gledhill N, Froese AB, Buick FJ, Bryan AC. VA/Q inhomogeneity and $AaDO_2$ in man during exercise: Effect of SF6 breathing. J Appl Physiol. 1978; 45:512–515. [PubMed: 711565]

117. Glenny RW, Robertson HT. Spatial distribution of ventilation and perfusion: Mechanisms and regulation. Compr Physiol. 2011; 1:375–395. [PubMed: 23737178]

118. Gonzalez NC, Clancy RL, Wagner PD. Determinants of maximal oxygen uptake in rats acclimated to simulated altitude. J Appl Physiol. 1993; 75:1608–1614. [PubMed: 8282610]

119. Gow AJ, Stamler JS. Reactions between nitric oxide and haemoglobin under physiological conditions. Nature. 1998; 391:169–173. [PubMed: 9428761]
120. Grebenkov DS, Filoche M, Sapoval B, Felici M. Diffusion-reaction in branched structures: Theory and application to the lung acinus. Phys Rev Lett. 2005; 94:050602. [PubMed: 15783623]
121. Green M, Mead J, Turner JM. Variability of maximum expiratory flow-volume curves. J Appl Physiol. 1974; 37:67–74. [PubMed: 4836570]
122. Greville HW, Arnup ME, Mink SN, Oppenheimer L, Anthonisen NR. Mechanism of reduced maximum expiratory flow in dogs with compensatory lung growth. J Appl Physiol. 1986; 60:441–448. [PubMed: 3949649]
123. Grover RF, Johnson RL Jr, McCullough RG, McCullough RE, Hofmeister SE, Campbell WB, Reynolds RC. Pulmonary hypertension and pulmonary vascular reactivity in beagles at high altitude. J Appl Physiol. 1988; 65:2632–2640. [PubMed: 2975278]
124. Guenard H, Varene N, Vaida P. Determination of lung capillary blood volume and membrane diffusing capacity in man by the measurements of NO and CO transfer. Respir Physiol. 1987; 70:113–120. [PubMed: 3659606]
125. Hachenberg T, Wendt M, Schreckenberg U, Meyer J, Hermeyer G, Muller KM, Lawin P. Single breath N2 washout in papain-induced pulmonary emphysema. Intensive Care Med. 1989; 15:308–313. [PubMed: 2768646]
126. Haefeli-Bleuer B, Weibel ER. Morphometry of the human pulmonary acinus. Anat Rec. 1988; 220:401–414. [PubMed: 3382030]
127. Hajari AJ, Yablonskiy DA, Sukstanskii AL, Quirk JD, Conradi MS, Woods JC. Morphometric changes in the human pulmonary acinus during inflation. J Appl Physiol (1985). 2012; 112:937–943. [PubMed: 22096115]
128. Haldane J, Smith JL. The absorption of oxygen by the lungs. J Physiol (London). 1897; 22:231–258.
129. Hammond MD, Hempleman SC. Oxygen diffusing capacity estimates derived from measured VA/Q distributions in man. Respiration physiology. 1987; 69:129–147. [PubMed: 3114851]
130. Harding R, Hooper SB, Han VK. Abolition of fetal breathing movements by spinal cord transection leads to reductions in fetal lung liquid volume, lung growth, and IGF-II gene expression. Pediatr Res. 1993; 34:148–153. [PubMed: 8233716]
131. Harrison GA, Kuchemann EF, Moore MAS, Boyce AJ, Baju T, Mourant AE, Godber MJ, Glasgow BG, Kopec AC, Tills D, Clegg EJ. The effects of altitude variation in Ethiopean Populations. Philos Trans R Soc Lond B Biol Sci. 1969; 256:147–182.
132. Heidelberger E, Reeves RB. Factors affecting whole blood O_2 transfer kinetics: Implications for theta(O_2). J Appl Physiol. 1990; 68:1865–1874. [PubMed: 2361889]
133. Heller H, Schuster KD. Stratification does not limit O_2 uptake in rabbit lungs. Acta Physiol Scand. 1998; 162:21–26. [PubMed: 9492898]
134. Herring MJ, Avdalovic MV, Quesenberry CL, Putney LF, Tyler NK, Ventimiglia FF, St George JA, Hyde DM. Accelerated structural decrements in the aging female rhesus macaque lung compared with males. Am J Physiol Lung Cell Mol Physiol. 2013; 304:L125–L134. [PubMed: 23144321]
135. Herring MJ, Putney LF, Wyatt G, Finkbeiner WE, Hyde DM. Growth of alveoli during postnatal development in humans based on stereological estimation. Am J Physiol Lung Cell Mol Physiol. 2014; 307:L338–L344. [PubMed: 24907055]
136. Hess WR. Das Prinzip des kleinsten Kraftverbrauches im Dienste hämodynamischer Forschung. Archiv für Anatomie und Physiologie. Archiv für Anatomie und Physiologie. 1914:1–62.
137. Hibbert M, Lannigan A, Raven J, Landau L, Phelan P. Gender differences in lung growth. Pediatr Pulmonol. 1995; 19:129–134. [PubMed: 7659468]
138. Hislop A, Howard S, Fairweather DV. Morphometric studies on the structural development of the lung in Macaca fascicularis during fetal and postnatal life. J Anat. 1984; 138(Pt 1):95–112. [PubMed: 6706842]
139. Hlastala MP, Scheid P, Piiper J. Interpretation of inert gas retention and excretion in the presence of stratified inhomogeneity. Respir Physiol. 1981; 46:247–259. [PubMed: 7323489]

140. Hoffman AM, Shifren A, Mazan MR, Gruntman AM, Lascola KM, Nolen-Walston RD, Kim CF, Tsai L, Pierce RA, Mecham RP, Ingenito EP. Matrix modulation of compensatory lung regrowth and progenitor cell proliferation in mice. Am J Physiol Lung Cell Mol Physiol. 2010; 298:L158–L168. [PubMed: 19915155]
141. Holland RA, Shibata H, Scheid P, Piiper J. Kinetics of O_2 uptake and release by red cells in stopped-flow apparatus: Effects of unstirred layer. Respir Physiol. 1985; 59:71–91. [PubMed: 3975504]
142. Holland RA, van Hezewikj W, Zubzanda J. Velocity of oxygen uptake by partly saturated adult and fetal human red cells. Respir Physiol. 1977; 29:303–314. [PubMed: 882729]
143. Hopkins SR, Bayly WM, Slocombe RF, Wagner H, Wagner PD. Effect of prolonged heavy exercise on pulmonary gas exchange in horses. J Appl Physiol. 1998; 84:1723–1730. [PubMed: 9572823]
144. Hopkins SR, Gavin TP, Siafakas NM, Haseler LJ, Olfert IM, Wagner H, Wagner PD. Effect of prolonged, heavy exercise on pulmonary gas exchange in athletes. J Appl Physiol. 1998; 85:1523–1532. [PubMed: 9760350]
145. Hopkins SR, McKenzie DC, Schoene RB, Glenny RW, Robertson HT. Pulmonary gas exchange during exercise in athletes. I. Ventilation-perfusion mismatch and diffusion limitation. J Appl Physiol. 1994; 77:912–917. [PubMed: 8002547]
146. Hoppeler H, Altpeter E, Wagner M, Turner DL, Hokanson J, König M, Stalder-Navarro VP, Weibel ER. Cold acclimation and endurance training in guinea pigs: Changes in lung, muscle and brown fat tissue. Respir Physiol. 1995; 101:189–198. [PubMed: 8570921]
147. Hoppeler H, Lindstedt SL. Malleability of skeletal muscle in overcoming limitations: Structural elements. J Exp Biol. 1985; 115:355–364. [PubMed: 4031775]
148. Hopper JL, Hibbert ME, Macaskill GT, Phelan PD, Landau LI. Longitudinal analysis of lung function growth in healthy children and adolescents. J Appl Physiol. 1991; 70:770–777. [PubMed: 2022569]
149. Horsfield K. Pulmonary airways and blood vessels considered as confluent trees. The Lung: Scientific Foundations. 1997; 1:1073–1079.
150. Horsfield K, Dart G, Olson DE, Filley GF, Cumming G. Models of the human bronchial tree. J Appl Physiol. 1971; 31:207–217. [PubMed: 5558242]
151. Hsia CC. Coordinated adaptation of oxygen transport in cardiopulmonary disease. Circulation. 2001; 104:963–969. [PubMed: 11514387]
152. Hsia CC. Recruitment of lung diffusing capacity: Update of concept and application. Chest. 2002; 122:1774–1783. [PubMed: 12426283]
153. Hsia CC. Lessons from a canine model of compensatory lung growth. Curr Top Dev Biol. 2004; 64:17–32. [PubMed: 15563942]
154. Hsia CC. Signals and mechanisms of compensatory lung growth. J Appl Physiol. 2004; 97:1992–1998. [PubMed: 15475557]
155. Hsia CC, Dane DM, Estrera AS, Wagner HE, Wagner PD, Johnson RL Jr. Shifting sources of functional limitation following extensive (70%) lung resection. J Appl Physiol. 2008; 104:1069–1079. [PubMed: 18258800]
156. Hsia CC, Fryder-Doffey F, Stalder-Nayarro V, Johnson RL Jr, Reynolds RC, Weibel ER. Structural changes underlying compensatory increase of diffusing capacity after left pneumonectomy in adult dogs. J Clin Invest. 1993; 92:758–764. [PubMed: 8349815]
157. Hsia CC, Herazo LF, Ramanathan M, Johnson RL Jr. Cardiac output during exercise measured by acetylene rebreathing, thermodilution, and Fick techniques. J Appl Physiol. 1995; 78:1612–1616. [PubMed: 7615476]
158. Hsia CC, Herazo LF, Ramanathan M, Johnson RL Jr, Wagner PD. Cardiopulmonary adaptations to pneumonectomy in dogs. II. VA/Q relationships and microvascular recruitment. J Appl Physiol. 1993; 74:1299–1309. [PubMed: 8482671]
159. Hsia CC, Hyde DM, Ochs M, Weibel ER. An official research policy statement of the American Thoracic Society/European Respiratory Society: Standards for quantitative assessment of lung structure. Am J Respir Crit Care Med. 2010; 181:394–418. [PubMed: 20130146]

160. Hsia CC, Johnson RL Jr. Further examination of alveolar septal adaptation to left pneumonectomy in the adult lung. Respir Physiol Neurobiol. 2006; 151:167–177. [PubMed: 16563882]

161. Hsia CC, Johnson RL Jr, Dane DM, Wu EY, Estrera AS, Wagner HE, Wagner PD. The canine spleen in oxygen transport: Gas exchange and hemodynamic responses to splenectomy. J Appl Physiol. 2007; 103:1496–1505. [PubMed: 17673565]

162. Hsia CC, Johnson RL Jr, McDonough P, Dane DM, Hurst MD, Fehmel JL, Wagner HE, Wagner PD. Residence at 3,800 m altitude for five months in growing dogs enhances lung diffusing capacity for oxygen that persists at least 2.5 years. J Appl Physiol. 2007; 102:1448–1455. [PubMed: 17218427]

163. Hsia CC, Johnson RL Jr, Shah D. Red cell distribution and the recruitment of pulmonary diffusing capacity. J Appl Physiol. 1999; 86:1460–1467. [PubMed: 10233105]

164. Hsia CC, Johnson RL Jr, Wu EY, Estrera AS, Wagner H, Wagner PD. Reducing lung strain after pneumonectomy impairs oxygen diffusing capacity but not ventilation-perfusion matching. J Appl Physiol. 2003; 95:1370–1378. [PubMed: 12794035]

165. Hsia CC, Schmitz A, Lambertz M, Perry SF, Maina JN. Evolution of air breathing: Oxygen homeostasis and the transitions from water to land and sky. Compr Physiol. 2013; 3:849–915. [PubMed: 23720333]

166. Hsia CC, Wu EY, Wagner E, Weibel ER. Preventing mediastinal shift after pneumonectomy impairs regenerative alveolar tissue growth. Am J Physiol Lung Cell Mol Physiol. 2001; 281:L1279–L1287. [PubMed: 11597921]

167. Hsia CC, Yan X, Dane DM, Johnson RL Jr. Density-dependent reduction of nitric oxide diffusing capacity after pneumonectomy. J Appl Physiol. 2003; 94:1926–1932. [PubMed: 12562671]

168. Hsia CCW. Respiratory function of hemoglobin. N Engl J Med. 1998; 338:239–247. [PubMed: 9435331]

169. Hsia CCW. Quantitative morphology of compensatory lung growth. Eur Resp Rev. 2006; 15:148–156.

170. Hsia, CCW. Pulmonary diffusion, ventilation-perfusion ratio and arterial oxygen homeostasis. In: Connes, P.; Hue, O.; Perry, S., editors. Exercise Physiology: From Cellular to an Integrative Approach. Amsterdam, Netherlands: IOS Press; 2010. p. 95-116.

171. Hsia CCW, Berberich MA, Driscoll B, Laubach VE, Lillehei CW, Massaro DJ, Perkett EA, Pierce RA, Rannels DE, Ryan RM, Tepper RS, Townsley MI, Veness-Meehan KA, Wang N, Warburton D. Mechanisms and limits of induced postnatal lung growth. Am J Respir Crit Care Med. 2004; 170:319–343. [PubMed: 15280177]

172. Hsia CCW, Carlin JI, Ramanathan M, Cassidy SS, Johnson RL Jr. Estimation of diffusion limitation after pneumonectomy from carbon monoxide diffusing capacity. Respir Physiol. 1991; 83:11–21. [PubMed: 2028103]

173. Hsia CCW, Chuong CJC, Johnson RL Jr. Critique of the conceptual basis of diffusing capacity estimates: A finite element analysis. J Appl Physiol. 1995; 79:1039–1047. [PubMed: 8567500]

174. Hsia CCW, Chuong CJC, Johnson RL Jr. Red cell distortion and conceptual basis of diffusing capacity estimates: A finite element analysis. J Appl Physiol. 1997; 83:1397–1404. [PubMed: 9338451]

175. Hsia CCW, Fryder-Doffey F, Stalder-Navarro V, Johnson RL Jr, Weibel ER. Structural changes underlying compensatory increase of diffusing capacity after left pneumonectomy in adult dogs [Published erratum in J. Clin. Invest., 93(2):913, 1994.]. J Clin Invest. 1993; 92:758–764. [PubMed: 8349815]

176. Hsia CCW, Herazo LF, Fryder-Doffey F, Weibel ER. Compensatory lung growth occurs in adult dogs after right pneumonectomy. J Clin Invest. 1994; 94:405–412. [PubMed: 8040282]

177. Hsia CCW, Herazo LF, Ramanathan M, Johnson RL Jr. Cardiopulmonary adaptations to pneumonectomy in dogs. IV. Membrane diffusing capacity and capillary blood volume. J Appl Physiol. 1994; 77:998–1005. [PubMed: 8002557]

178. Hsia CCW, Johnson RL Jr, Shah D. Red cell distribution and the recruitment of pulmonary diffusing capacity. J Appl Physiol (1985). 1999; 86:1460–1467. [PubMed: 10233105]

179. Hsia, CCW.; Johnson, RL., Jr; Weibel, ER. Compensatory lung growth: Relationship to postnatal lung growth and adaptation in destructive lung disease. In: Harding, R.; Pinkerton, KE.; Plopper,

CG., editors. The Lung: Development, Aging and the Environment. London: Academic Press; 2004. p. 187-199.

180. Hsia CCW, Polo Carbayo JJ, Yan X, Bellotto DJ. Enhanced alveolar growth and remodeling in guinea pigs raised at high altitude. Respir Physiol Neurobiol. 2005; 147:105–115. [PubMed: 15848128]
181. Hsia CCW, Ramanathan M, Estrera AS. Recruitment of diffusing capacity with exercise in patients after pneumonectomy. Am Rev Respir Dis. 1992; 145:811–816. [PubMed: 1554207]
182. Hsia CCW, Zhou XS, Bellotto DJ, Hagler HK. Regenerative growth of respiratory bronchioles in dogs. Am J Physiol Lung Cell Mol Physiol. 2000; 279:L136–L142. [PubMed: 10893212]
183. Huang W, Yen RT, McLaurine M, Bledsoe G. Morphometry of the human pulmonary vasculature. J Appl Physiol. 1996; 81:2123–2133. [PubMed: 8941537]
184. Hughes JM, Bates DV. Historical review: The carbon monoxide diffusing capacity (DLCO) and its membrane (DM) and red cell (Theta.Vc) components. Respir Physiol Neurobiol. 2003; 138:115–142. [PubMed: 14609505]
185. Hunter C, Barer GR, Shaw JW, Clegg EJ. Growth of the heart and lungs in hypoxic rodents: A model of human hypoxic disease. Clin Sci Mol Med. 1973; 46:375–391.
186. Hurford WE, Hochachka PW, Schneider RC, Guyton GP, Stanek KS, Zapol DG, Liggins GC, Zapol WM. Splenic contraction, catecholamine release, and blood volume redistribution during diving in the Weddell seal. J Appl Physiol. 1996; 80:298–306. [PubMed: 8847318]
187. Hyde DM, Blozis SA, Avdalovic MV, Putney LF, Dettorre R, Quesenberry NJ, Singh P, Tyler NK. Alveoli increase in number but not size from birth to adulthood in rhesus monkeys. Am J Physiol Lung Cell Mol Physiol. 2007; 293:L570–L579. [PubMed: 17586691]
188. Ijsselstijn H, Tibboel D, Hop WJ, Molenaar JC, de Jongste JC. Long-term pulmonary sequelae in children with congenital diaphragmatic hernia. Am J Respir Crit Care Med. 1997; 155:174–180. [PubMed: 9001308]
189. Ingber DE. Tensegrity I. Cell structure and hierarchical systems biology. J Cell Sci. 2003; 116:1157–1173. [PubMed: 12615960]
190. Irvin CG, Bates JH. Measuring the lung function in the mouse: The challenge of size. Respir Res. 2003; 4:4. [PubMed: 12783622]
191. Jelkmann W. Erythropoietin after a century of research: Younger than ever. Eur J Haematol. 2007; 78:183–205. [PubMed: 17253966]
192. Jensen FB. The dual roles of red blood cells in tissue oxygen delivery: Oxygen carriers and regulators of local blood flow. J Exp Biol. 2009; 212:3387–3393. [PubMed: 19837879]
193. Jia L, Bonaventura C, Bonaventura J, Stamler JS. S-nitrosohaemoglobin: A dynamic activity of blood involved in vascular control. Nature. 1996; 380:221–226. [PubMed: 8637569]
194. Johnson RL Jr, Cassidy SS, Grover RF, Schutte JE, Epstein RH. Functional capacities of lungs and thorax in beagles after prolonged residence at 3,100 m. J Appl Physiol. 1985; 59:1773–1782. [PubMed: 4077786]
195. Johnson RL Jr, Heigenhauser GJF, Hsia CCW, Jones NL, Wagner PD. Determinants of Gas Exchange and AcidBase Balance During Exercise. Compr Physiol. 2011; First published in print 1996. doi: 10.1002/cphy.cp120112Supplement 29: Handbook of Physiology, Exercise: Regulation and Integration of Multiple Systems: 515–584
196. Johnson RL Jr, Hsia CCW. Functional recruitment of pulmonary capillaries (Commentary). J Appl Physiol. 1994; 76:1405–1407. [PubMed: 8045811]
197. Juhos LT, Green DP, Furiosi NJ, Freeman G. A quantitative study of stenosis in the respiratory bronchiole of the rat in NO_2-induced emphysema. Am Rev Respir Dis. 1980; 121:541–549. [PubMed: 7416584]
198. Kang MY, Katz I, Sapoval B. A new approach to the dynamics of oxygen capture by the human lung. Respir Physiol Neurobiol. 2015; 205:109–119. [PubMed: 25447682]
199. Karas RH, Taylor CR, Jones JH, Lindstedt SL, Reeves RB, Weibel ER. Adaptive variation in the mammalian respiratory system in relation to energetic demand. VII. Flow of oxygen across the pulmonary gas exchanger. Respiration physiology. 1987; 69:101–115.
200. Kaushik SS, Freeman MS, Cleveland ZI, Davies J, Stiles J, Virgin-car RS, Robertson SH, He M, Kelly KT, Foster WM, McAdams HP, Driehuys B. Probing the regional distribution of pulmonary

gas exchange through single-breath gas- and dissolved-phase 129Xe MR imaging. J Appl Physiol (1985). 2013; 115:850–860. [PubMed: 23845983]

201. Kaushik SS, Freeman MS, Yoon SW, Liljeroth MG, Stiles JV, Roos JE, Foster WM, Rackley CR, McAdams HP, Driehuys B. Measuring diffusion-limitation with a perfusion-limited gas-hyperpolarized 129Xe gas-transfer spectroscopy in patients with idiopathic pulmonary fibrosis. J Appl Physiol (1985). 2014; 117:577–585. [PubMed: 25038105]
202. Kaza AK, Kron IL, Kern JA, Long SM, Fiser SM, Nguyen RP, Tribble CG, Laubach VE. Retinoic acid enhances lung growth after pneumonectomy. Ann Thorac Surg. 2001; 71:1645–1650. [PubMed: 11383815]
203. Kaza AK, Kron IL, Leuwerke SM, Tribble CG, Laubach VE. Keratinocyte growth factor enhances post-pneumonectomy lung growth by alveolar proliferation. Circulation. 2002; 106:I120–124. [PubMed: 12354720]
204. Kaza AK, Kron IL, Long SM, Fiser SM, Stevens PM, Kern JA, Tribble CG, Laubach VE. Epidermal growth factor receptor up-regulation is associated with lung growth after lobectomy. Ann Thorac Surg. 2001; 72:380–385. [PubMed: 11515870]
205. Kaza AK, Laubach VE, Kern JA, Long SM, Fiser SM, Tepper JA, Nguyen RP, Shockey KS, Tribble CG, Kron IL. Epidermal growth factor augments postpneumonectomy lung growth. J Thorac Cardiovasc Surg. 2000; 120:916–921. [PubMed: 11044318]
206. Kennedy JD. Lung function outcome in children of premature birth. J Paediatr Child Health. 1999; 35:516–521. [PubMed: 10634975]
207. Khan MA, Ellis R, Inman MD, Bates JH, Sanderson MJ, Janssen LJ. Influence of airway wall stiffness and parenchymal tethering on the dynamics of bronchoconstriction. Am J Physiol Lung Cell Mol Physiol. 2010; 299:L98–L108. [PubMed: 20435686]
208. Kleiber, M. The Fire of Life: An Introduction to Animal Energetics. New York: Wiley; 1961. p. 1-454.
209. Kleinbongard P, Schulz R, Rassaf T, Lauer T, Dejam A, Jax T, Kumara I, Gharini P, Kabanova S, Ozuyaman B, Schnurch HG, Godecke A, Weber AA, Robenek M, Robenek H, Bloch W, Rosen P, Kelm M. Red blood cells express a functional endothelial nitric oxide synthase. Blood. 2006; 107:2943–2951. [PubMed: 16368881]
210. Knudsen L, Weibel ER, Gundersen HJ, Weinstein FV, Ochs M. Assessment of air space size characteristics by intercept (chord) measurement: An accurate and efficient stereological approach. J Appl Physiol (1985). 2010; 108:412–421. [PubMed: 19959763]
211. Koh DW, Roby JD, Starcher B, Senior RM, Pierce RA. Postpneumonectomy lung growth: A model of reinitiation of tropoelastin and type I collagen production in a normal pattern in adult rat lung. Am J Respir Cell Mol Biol. 1996; 15:611–623. [PubMed: 8918368]
212. König MF, Lucocq JM, Weibel ER. Demonstration of pulmonary vascular perfusion by electron and light microscopy. J Appl Physiol. 1993; 75:1877–1883. [PubMed: 8282645]
213. Kovar J, Sly PD, Willet KE. Postnatal alveolar development of the rabbit. J Appl Physiol. 2002; 93:629–635. [PubMed: 12133873]
214. Koyama T, Mochizuki M. A study on the relationship between the oxygenation velocity of the red blood cell and the flow velocity in a rapid flow method. Jpn J Physiol. 1969; 19:534–546. [PubMed: 5307439]
215. Krogh, A. The Comparative Physiology of Respiratory Mechanisms. Philadelphia: University of Pennsylvania Press; 1941. p. 1-172.
216. Krogh A, Krogh M. On the rate of diffusion of carbonic oxide into the lungs of man. Skandinavisches Archiv Für Physiologie. 1910; 23:236–247.
217. Kurz H, Burri PH, Djonov VG. Angiogenesis and vascular remodeling by intussusception: From form to function. News Physiol Sci. 2003; 18:65–70. [PubMed: 12644622]
218. Kutchai H. Role of the red cell membrane in oxygen uptake. Respir Physiol. 1975; 23:121–132. [PubMed: 1129546]
219. Lahiri S, DeLaney RG, Brody JS, Simpser M, Velasquez T, Motoyama EK, Polgar C. Relative role of environmental and genetic factors in respiratory adaptation to high altitude. Nature London. 1976; 261:133–135. [PubMed: 1272381]

220. Landesberg LJ, Ramalingam R, Lee K, Rosengart TK, Crystal RG. Upregulation of transcription factors in lung in the early phase of postpneumonectomy lung growth. Am J Physiol Lung Cell Mol Physiol. 2001; 281:L1138–L1149. [PubMed: 11597905]

221. Lechner AJ, Banchero N. Lung morphometry in guinea pigs acclimated to hypoxia during growth. Respir Physiol. 1980; 42:155–169. [PubMed: 7221218]

222. Lechner AJ, Banchero N. Advanced pulmonary development in newborn guinea pigs (Cavia porcellus). Am J Anat. 1982; 163:235–246. [PubMed: 7091012]

223. Lechner AJ, Blake CI, Banchero N. Pulmonary development in growing guinea pigs exposed to chronic hypercapnia. Respiration. 1987; 52:108–114. [PubMed: 3118439]

224. Lee E, Little AG, Hsu WH, Skinner DB. Effect of pneumonectomy on extravascular lung water in dogs. J Surg Res. 1985; 38:568–573. [PubMed: 4010266]

225. Lenfant C, Torrance J, English E, Finch CA, Reynafarje C, Ramos J, Faura J. Effect of altitude on oxygen binding by hemoglobin and on organic phosphate levels. J Clin Invest. 1968; 47:2652–2656. [PubMed: 5725278]

226. Leuwerke SM, Kaza AK, Tribble CG, Kron IL, Laubach VE. Inhibition of compensatory lung growth in endothelial nitric oxide synthase-deficient mice. Am J Physiol Lung Cell Mol Physiol. 2002; 282:L1272–L1278. [PubMed: 12003783]

227. Li D, Fernandez LG, Dodd-o J, Langer J, Wang D, Laubach VE. Upregulation of hypoxia-induced mitogenic factor in compensatory lung growth after pneumonectomy. Am J Respir Cell Mol Biol. 2005; 32:185–191. [PubMed: 15626779]

228. Liu M, Liu J, Buch S, Tanswell AK, Post M. Antisense oligonucleotides for PDGF-B and its receptor inhibit mechanical strain-induced fetal lung cell growth. Am J Physiol. 1995; 269:L178–184. [PubMed: 7653578]

229. Liu M, Qin Y, Liu J, Tanswell AK, Post M. Mechanical strain induces pp60src activation and translocation to cytoskeleton in fetal rat lung cells. J Biol Chem. 1996; 271:7066–7071. [PubMed: 8636139]

230. Liu M, Skinner SJ, Xu J, Han RN, Tanswell AK, Post M. Stimulation of fetal rat lung cell proliferation in vitro by mechanical stretch. Am J Physiol. 1992; 263:L376–383. [PubMed: 1415562]

231. Liu M, Xu J, Tanswell AK, Post M. Inhibition of mechanical strain-induced fetal rat lung cell proliferation by gadolinium, a stretch-activated channel blocker. J Cell Physiol. 1994; 161:501–507. [PubMed: 7962131]

232. Low FN. The pulmonary alveolar epithelium of laboratory mammals and man. Anat Rec. 1953; 117:241–263. [PubMed: 13104990]

233. Lund DP, Mitchell J, Kharasch V, Quigley S, Kuehn M, Wilson JM. Congenital diaphragmatic hernia: The hidden morbidity. J Pediatr Surg. 1994; 29:258–262. discussion 262–254. [PubMed: 8176602]

234. Maina JN, Thomas SP, Hyde DM. A morphometric study of the lungs of different sized bats: Correlations between structure and function of the chiropteran lung. Philos Trans R Soc Lond [Biol]. 1991; 333:31–50.

235. Mandelbrot, BB. The Fractal Geometry of Nature. New York: WH Freeman and Co; 1983. p. 495

236. Manier G, Guenard H, Castaing Y, Varene N, Vargas E. Pulmonary gas exchange in Andean natives with excessive polycythemia–effect of hemodilution. J Appl Physiol. 1988; 65:2107–2117. [PubMed: 3209554]

237. Mansell AL, Collins MH, Johnson E Jr, Gil J. Postnatal growth of lung parenchyma in the piglet: Morphometry correlated with mechanics. Anat Rec. 1995; 241:99–104. [PubMed: 7879927]

238. Marrades RM, Diaz O, Roca J, Campistol JM, Torregrosa JV, Barbera JA, Cobos A, Felez MA, Rodriguez-Roisin R. Adjustment of DLCO for hemoglobin concentration. Am J Respir Crit Care Med. 1997; 155:236–241. [PubMed: 9001318]

239. Marshall BE. Importance of hypoxic pulmonary vasoconstriction with atelectasis. Adv Shock Res. 1982; 8:1–12. [PubMed: 7136935]

240. Martin EA, Ritman EL, Turner RT. Time course of epiphyseal growth plate fusion in rat tibiae. Bone. 2003; 32:261–267. [PubMed: 12667553]

241. Marven SS, Smith CM, Claxton D, Chapman J, Davies HA, Primhak RA, Powell CV. Pulmonary function, exercise performance, and growth in survivors of congenital diaphragmatic hernia. Arch Dis Child. 1998; 78:137–142. [PubMed: 9579155]
242. Massaro D, Teich N, Massaro GD. Postnatal development of pulmonary alveoli: Modulation in rats by thyroid hormones. Am J Physiol. 1986; 250:R51–R55. [PubMed: 3942254]
243. Massaro GD, Massaro D. Postnatal lung growth: Evidence that the gas-exchange region grows fastest at the periphery. Am J Physiol. 1993; 265:L319–322. [PubMed: 8238365]
244. Massaro GD, Massaro D. Retinoic acid treatment abrogates elastase-induced pulmonary emphysema in rats [published erratum appears in Nat Med 1997 Jul;3(7):805]. Nat Med. 1997; 3:675–677. [PubMed: 9176496]
245. Massaro GD, Olivier J, Massaro D. Short-term perinatal 10% O_2 alters postnatal development of lung alveoli. Am J Physiol. 1989; 257:L221–L225. [PubMed: 2801949]
246. Mathieu-Costello O, Willford DC, Fu Z, Garden RM, West JB. Pulmonary capillaries are more resistant to stress failure in dogs than in rabbits. J Appl Physiol. 1995; 79:908–917. [PubMed: 8567535]
247. Mauderly JL. Effect of age on pulmonary structure and function of immature and adult animals and man. Fed Proc. 1979; 38:173–177. [PubMed: 761650]
248. Mauroy B, Filoche M, Weibel ER, Sapoval B. An optimal bronchial tree may be dangerous. Nature. 2004; 427:633–636. [PubMed: 14961120]
249. McAnulty RJ, Guerreiro D, Cambrey AD, Laurent GJ. Growth factor activity in the lung during compensatory growth after pneumonectomy: Evidence of a role for IGF–1. Eur Respir J. 1992; 5:739–747. [PubMed: 1628732]
250. McBride JT. Postpneumonectomy airway growth in the ferret. J Appl Physiol. 1985; 58:1010–1014. [PubMed: 3980371]
251. McDonough P, Dane DM, Hsia CC, Yilmaz C, Johnson RL Jr. Long-term enhancement of pulmonary gas exchange after high-altitude residence during maturation. J Appl Physiol. 2006; 100:474–481. [PubMed: 16210430]
252. McMahon TJ, Ahearn GS, Moya MP, Gow AJ, Huang YC, Luchsinger BP, Nudelman R, Yan Y, Krichman AD, Bashore TM, Califf RM, Singel DJ, Piantadosi CA, Tapson VF, Stamler JS. A nitric oxide processing defect of red blood cells created by hypoxia: Deficiency of S-nitrosohemoglobin in pulmonary hypertension. Proc Natl Acad Sci U S A. 2005; 102:14801–14806. [PubMed: 16203976]
253. McMurtrie HL, Cleary HJ, Alvarez BV, Loiselle FB, Sterling D, Morgan PE, Johnson DE, Casey JR. The bicarbonate transport metabolon. J Enzyme Inhib Med Chem. 2004; 19:231–236. [PubMed: 15499994]
254. Metzger RJ, Klein OD, Martin GR, Krasnow MA. The branching programme of mouse lung development. Nature. 2008; 453:745–750. [PubMed: 18463632]
255. Miller JM, Johnson RL Jr. Effect of lung inflation on pulmonary diffusing capacity at rest and exercise. J Clin Invest. 1966; 45:493–500. [PubMed: 5937024]
256. Mochizuki M. A theoretical study on the velocity factor of oxygenation of the red cell. Jpn J Physiol. 1966; 16:658–666. [PubMed: 5298362]
257. Morrell NW, Nijran KS, Biggs T, Seed WA. Regional matching of ventilation and perfusion during lobar bronchial occlusion in man. Clin Sci (Lond). 1995; 88:179–184. [PubMed: 7720342]
258. Moya MP, Gow AJ, Califf RM, Goldberg RN, Stamler JS. Inhaled ethyl nitrite gas for persistent pulmonary hypertension of the newborn. Lancet. 2002; 360:141–143. [PubMed: 12126827]
259. Murray CD. The physiological principle of minimum work: I. The vascular system and the cost of blood volume. Proc Natl Acad Sci U S A. 1926; 12:207–214. [PubMed: 16576980]
260. Nagaya M, Akatsuka H, Kato J, Niimi N, Ishiguro Y. Development in lung function of the affected side after repair of congenital diaphragmatic hernia. J Pediatr Surg. 1996; 31:349–356. [PubMed: 8708902]
261. Niermeyer S, Yang P, Shanmina, Drolkar, Zhuang J, Moore LG. Arterial oxygen saturation in Tibetan and Han infants born in Lhasa, Tibet. N Engl J Med. 1995; 333:1248–1252. [PubMed: 7566001]

262. Nobuhara KK, Fauza DO, DiFiore JW, Hines MH, Fackler JC, Slavin R, Hirschl R, Wilson JM. Continuous intrapulmonary distension with per-fluorocarbon accelerates neonatal (but not adult) lung growth. J Pediatr Surg. 1998; 33:292–298. [PubMed: 9498405]
263. Nolen-Walston RD, Kim CF, Mazan MR, Ingenito EP, Gruntman AM, Tsai L, Boston R, Woolfenden AE, Jacks T, Hoffman AM. Cellular kinetics and modeling of bronchioalveolar stem cell response during lung regeneration. Am J Physiol Lung Cell Mol Physiol. 2008; 294:L1158–L1165. [PubMed: 18375744]
264. Ochs M. A brief update on lung stereology. J Microsc. 2006; 222:188–200. [PubMed: 16872418]
265. Ochs M, Nyengaard JR, Jung A, Knudsen L, Voigt M, Wahlers T, Richter J, Gundersen HJ. The number of alveoli in the human lung. Am J Respir Crit Care Med. 2004; 169:120–124. [PubMed: 14512270]
266. Ochs, M.; Weibel, ER. Functional design of the human lung for gas exchange. In: Fishman, AP.; Elias, JA.; Fishman, JA.; Grippi, MA.; Senior, RM.; Pack, AI., editors. Fishman's Pulmonary Diseases and Disorders. New York: McGraw Hill; 2008. p. 23-69.
267. Okada O, Presson RG Jr, Kirk KR, Godgey PS, Capen RL, Wagner WW. Capillary perfusion patterns in single alveolar walls. J Appl Physiol. 1992; 72:1838–1844. [PubMed: 1601793]
268. Oldmixon EH, Carlsson K, Kuhn C III, Butler JP, Hoppin FG Jr. alpha-Actin: Disposition, quantities, and estimated effects on lung recoil and compliance. J Appl Physiol (1985). 2001; 91:459–473. [PubMed: 11408464]
269. Olgiati R, Levine D, Smith JP, Briscoe WA, King TK. Diffusing capacity in idiopathic scoliosis and its interpretation regarding alveolar development. Am Rev Respir Dis. 1982; 126:229–234. [PubMed: 7103249]
270. Paiva M, Engel LA. Model analysis of gas distribution within human lung acinus. J Appl Physiol. 1984; 56:418–425. [PubMed: 6706753]
271. Paiva M, Engel LA. Model analysis of intra-acinar gas exchange. Respir Physiol. 1985; 62:257–272. [PubMed: 3936144]
272. Paiva M, Engel LA. Theoretical studies of gas mixing and ventilation distribution in the lung. Physiol Rev. 1987; 67:750–796. [PubMed: 3299409]
273. Papadakis K, Luks FI, De Paepe ME, Piasecki GJ, Wesselhoeft CW Jr. Fetal lung growth after tracheal ligation is not solely a pressure phenomenon. J Pediatr Surg. 1997; 32:347–351. [PubMed: 9044151]
274. Paxson JA, Gruntman A, Parkin CD, Mazan MR, Davis A, Ingenito EP, Hoffman AM. Age-dependent decline in mouse lung regeneration with loss of lung fibroblast clonogenicity and increased myofibroblastic differentiation. PLoS One. 2011; 6:e23232. [PubMed: 21912590]
275. Paxson JA, Parkin CD, Iyer LK, Mazan MR, Ingenito EP, Hoffman AM. Global gene expression patterns in the post-pneumonectomy lung of adult mice. Respir Res. 2009; 10:92. [PubMed: 19804646]
276. Pearson OP, Pearson A. A stereological analysis of the ultrastructure of the lungs of wild mice living at low and high altitude. J Morphol. 1976; 150:359–368. [PubMed: 978747]
277. Pedersen SF, Cala PM. Comparative biology of the ubiquitous Na+/H +exchanger, NHE1: Lessons from erythrocytes. J Exp Zoolog A Comp Exp Biol. 2004; 301:569–578.
278. Pedley TJ, Schroter RC, Sudlow MF. The prediction of pressure drop and variation of resistance within the human bronchial airways. Respir Physiol. 1970; 9:387–405. [PubMed: 5425201]
279. Perry SF, Christian A, Breuer T, Pajor N, Codd JR. Implications of an avian-style respiratory system for gigantism in sauropod dinosaurs. J Exp Zool Part A Ecol Genet Physiol. 2009; 311:600–610.
280. Petersson J, Glenny RW. Imaging regional PAO_2 and gas exchange. J Appl Physiol (1985). 2012; 113:340–352. [PubMed: 22604886]
281. Phalen RF, Yeh HC, Schum GM, Raabe OG. Application of an idealized model to morphometry of the mammalian tracheobronchial tree. Anat Rec. 1978; 190:167–176. [PubMed: 629400]
282. Phansalkar AR, Hanson CM, Shakir AR, Johnson RL Jr, Hsia CC. Nitric oxide diffusing capacity and alveolar microvascular recruitment in sarcoidosis. Am J Respir Crit Care Med. 2004; 169:1034–1040. [PubMed: 14977623]

283. Phillips CG, Kaye SR. Diameter-based analysis of the branching geometry of four mammalian bronchial trees. Respir Physiol. 1995; 102:303–316. [PubMed: 8904021]
284. Piiper J, Scheid P. Model for capillary-alveolar equilibration with special reference to O_2 uptake in hypoxia. Respir Physiol. 1981; 46:193–208. [PubMed: 6798659]
285. Piiper J, Scheid P. Models for a comparative functional analysis of gas exchange organs in vertebrates. J Appl Physiol Respir Environ Exerc Physiol. 1982; 53:1321–1329. [PubMed: 6818205]
286. Pirlo AF, Benumof JL, Trousdale FR. Atelectatic lobe blood flow: Open vs. closed chest, positive pressure vs. spontaneous ventilation. J Appl Physiol Respir Environ Exerc Physiol. 1981; 50:1022–1026. [PubMed: 7014540]
287. Prisk GK. Gas exchange under altered gravitational stress. Compr Physiol. 2011; 1:339–355. [PubMed: 23737176]
288. Prisk GK, Guy HJ, Elliott AR, Deutschman RA III, West JB. Pulmonary diffusing capacity, capillary blood volume, and cardiac output during sustained microgravity. J Appl Physiol. 1993; 75:15–26. [PubMed: 8376261]
289. Probyn ME, Wallace MJ, Hooper SB. Effect of increased lung expansion on lung growth and development near midgestation in fetal sheep. Pediatr Res. 2000; 47:806–812. [PubMed: 10832742]
290. Prommer N, Ehrmann U, Schmidt W, Steinacker JM, Radermacher P, Muth CM. Total haemoglobin mass and spleen contraction: A study on competitive apnea divers, non-diving athletes and untrained control subjects. Eur J Appl Physiol. 2007; 101:753–759. [PubMed: 17874121]
291. Rabinovitch M, Gamble WJ, Miettinen OS, Reid L. Age and sex influence on pulmonary hypertension of chronic hypoxia and on recovery. Am J Physiol. 1981; 240:H62–72. [PubMed: 6450541]
292. Rannels DE, Rannels SR. Compensatory growth of the lung following partial pneumonectomy. Exp Lung Res. 1988; 14:157–182. [PubMed: 3286238]
293. Ravikumar P, Bellotto DJ, Hsia CC. Persistent structural adaptation in the lungs of guinea pigs raised at high altitude. Respir Physiol Neurobiol. 2015; 208:37–44. [PubMed: 25534146]
294. Ravikumar P, Bellotto DJ, Johnson RL Jr, Hsia CCW. Non-uniform compensatory alveolar grwoth folowing extensive (70%) lung resection (Abstract). Am J Respir Crit Care Med. 2008; 177:A545.
295. Ravikumar P, Bellotto DJ, Johnson RL Jr, Hsia CC. Permanent alveolar remodeling in canine lung induced by high-altitude residence during maturation. J Appl Physiol. 2009; 107:1911–1917. [PubMed: 19833809]
296. Ravikumar P, Yilmaz C, Bellotto DJ, Dane DM, Estrera AS, Hsia CC. Separating in vivo mechanical stimuli for postpneumonectomy compensation: Imaging and ultrastructural assessment. J Appl Physiol. 2013; 114:961–970. [PubMed: 23329819]
297. Ravikumar P, Yilmaz C, Dane DM, Bellotto DJ, Estrera AS, Hsia CC. Defining a stimuli-response relationship in compensatory lung growth following major resection. J Appl Physiol (1985). 2014; 116:816–824. [PubMed: 24481960]
298. Remmers JE, Mithoefer JC. The carbon monoxide diffusing capacity in permanent residents at high altitudes. Respir Physiol. 1969; 6:233–244. [PubMed: 5773391]
299. Reynolds JD, Bennett KM, Cina AJ, Diesen DL, Henderson MB, Matto F, Plante A, Williamson RA, Zandinejad K, Demchenko IT, Hess DT, Piantadosi CA, Stamler JS. S-nitrosylation therapy to improve oxygen delivery of banked blood. Proc Natl Acad Sci U S A. 2013; 110:11529–11534. [PubMed: 23798386]
300. Robertson HT, Altemeier WA, Glenny RW. Physiological implications of the fractal distribution of ventilation and perfusion in the lung. Ann Biomed Eng. 2000; 28:1028–1031. [PubMed: 11144664]
301. Rodriguez M, Bur S, Favre A, Weibel ER. Pulmonary acinus: Geometry and morphometry of the peripheral airway system in rat and rabbit. Am J Anat. 1987; 180:143–155. [PubMed: 3673919]
302. Rodriguez-Roisin R, Wagner PD. Clinical relevance of ventilation-perfusion inequality determined by inert gas elimination. Eur Respir J. 1990; 3:469–482. [PubMed: 2163880]

303. Rose GL, Cassidy SS, Johnson RL Jr. Diffusing capacity at different lung volumes during breath holding and rebreathing. J Appl Physiol. 1979; 47:32–36. [PubMed: 468670]

304. Ross KA, Thurlbeck WM. Lung growth in newborn guinea pigs: Effects of endurance exercise. Respir Physiol. 1992; 89:353–364. [PubMed: 1410848]

305. Roughton FJ, Forster RE. Relative importance of diffusion and chemical reaction rates in determining the rate of exchange of gases in the human lung, with special reference to true diffusing capacity of pulmonary membrane and volume of blood in the lung capillaries. J Appl Physiol. 1957; 11:290–302. [PubMed: 13475180]

306. Saltin B, Blomqvist G, Mitchell JH, Johnson RL Jr, Wildenthal K, Chapman CB. Response to exercise after bed rest and after training. Circulation. 1968:37–38. 1–78.

307. Sanchez-Esteban J, Tsai SW, Sang J, Qin J, Torday JS, Rubin LP. Effects of mechanical forces on lung-specific gene expression. Am J Med Sci. 1998; 316:200–204. [PubMed: 9749563]

308. Sanchez-Esteban J, Wang Y, Cicchiello LA, Rubin LP. Cyclic mechanical stretch inhibits cell proliferation and induces apoptosis in fetal rat lung fibroblasts. Am J Physiol Lung Cell Mol Physiol. 2002; 282:L448–L456. [PubMed: 11839538]

309. Sapoval B. General formulation of Laplacian transfer across irregular surfaces. Phys Rev Lett. 1994; 73:3314–3316. [PubMed: 10057345]

310. Sapoval B, Filoche M, Weibel ER. Smaller is better–but not too small: A physical scale for the design of the mammalian pulmonary acinus. Proc Natl Acad Sci U S A. 2002; 99:10411–10416. [PubMed: 12136124]

311. Schaffartzik W, Arcos J, Tsukimoto K, Mathieu-Costello O, Wagner PD. Pulmonary interstitial edema in the pig after heavy exercise. J Appl Physiol. 1993; 75:2535–2540. [PubMed: 8125872]

312. Schaffartzik W, Poole DC, Derion T, Tsukimoto K, Hogan MC, Arcos JP, Bebout DE, Wagner PD. VA/Q distribution during heavy exercise and recovery in humans: Implications for pulmonary edema. J Appl Physiol (1985). 1992; 72:1657–1667. [PubMed: 1601769]

313. Scheid P, Hlastala MP, Piiper J. Inert gas elimination from lungs with stratified inhomogeneity: Theory. Respir Physiol. 1981; 44:299–309. [PubMed: 6267676]

314. Scheid P, Piiper J. Intrapulmonary gas mixing and stratification. Pulm Gas Exch. 1980:87–130.

315. Schreider JP, Raabe OG. Structure of the human respiratory acinus. Am J Anat. 1981; 162:221–232. [PubMed: 7315750]

316. Schuster KD, Heller H. Assessment of stratified inhomogeneity within distal alveolar space with respect to oxygen uptake. Adv Exp Med Biol. 1990; 277:637–645. [PubMed: 2096664]

317. Schutte JE, Lilljeqvist RE, Johnson RL Jr. Growth of lowland native children of European ancestry during sojourn at high altitude (3,200 m). Am J Phys Anthropol. 1983; 61:221–226. [PubMed: 6881324]

318. Sekhon HS, Smith C, Thurlbeck WM. Effect of hypoxia and hyperoxia on postpneumonectomy compensatory lung growth. Exp Lung Res. 1993; 19:519–532. [PubMed: 8253056]

319. Sekhon HS, Thurlbeck WM. Lung cytokinetics after exposure to hypobaria and/or hypoxia and undernutrition in growing rats. J Appl Physiol. 1995; 79:1299–1309. [PubMed: 8567576]

320. Sekhon HS, Thurlbeck WM. Lung morphometric changes after exposure to hypobaria and/or hypoxia and undernutrition. Respir Physiol. 1996; 106:99–107. [PubMed: 8946582]

321. Sekhon HS, Thurlbeck WM. Time course of lung growth following exposure to hypobaria and/or hypoxia in rats. Respir Physiol. 1996; 105:241–252. [PubMed: 8931184]

322. Sekhon HS, Wright JL, Thurlbeck WM. Pulmonary function alterations after 3 wk of exposure to hypobaria and/or hypoxia in growing rats. J Appl Physiol. 1995; 78:1787–1792. [PubMed: 7649913]

323. Sengupta P. The laboratory rat: Relating its age with human's. Int J Prev Med. 2013; 4:624–630. [PubMed: 23930179]

324. Shah DM, Prichard MN, Newell JC, Karmody AM, Scovill WA, Powers SR Jr. Increased cardiac output and oxygen transport after intraoperative isovolemic hemodilution. A study in patients with peripheral vascular disease. Arch Surg. 1980; 115:597–600. [PubMed: 7377961]

325. Shin HW, Condorelli P, George SC. Examining axial diffusion of nitric oxide in the lungs using heliox and breath hold. J Appl Physiol. 2006; 100:623–630. [PubMed: 16210445]

326. Shin HW, George SC. Impact of axial diffusion on nitric oxide exchange in the lungs. J Appl Physiol. 2002; 93:2070–2080. [PubMed: 12391103]

327. Smith PG, Moreno R, Ikebe M. Strain increases airway smooth muscle contractile and cytoskeletal proteins in vitro. Am J Physiol. 1997; 272:L20–L27. [PubMed: 9038898]

328. Spooner BS, Wessells NK. Mammalian lung development: Interactions in primordium formation and bronchial morphogenesis. J Exp Zool. 1970; 175:445–454. [PubMed: 5501462]

329. Stamler JS, Jia L, Eu JP, McMahon TJ, Demchenko IT, Bonaventura J, Gernert K, Piantadosi CA. Blood flow regulation by S-nitrosohemoglobin in the physiological oxygen gradient. Science. 1997; 276:2034–2037. [PubMed: 9197264]

330. Staub NC, Bishop JM, Forster RE. Importance of diffusion and chemical reaction rates in O_2 uptake in the lung. J Appl Physiol. 1962; 17:21–27. [PubMed: 13916422]

331. Steinacker JM, Tobias P, Menold E, Reissnecker S, Hohenhaus E, Liu Y, Lehmann M, Bartsch P, Swenson ER. Lung diffusing capacity and exercise in subjects with previous high altitude pulmonary oedema. Eur Respir J. 1998; 11:643–650. [PubMed: 9596116]

332. Stewart IB, McKenzie DC. The human spleen during physiological stress. Sports Med. 2002; 32:361–369. [PubMed: 11980500]

333. Stickland MK, Lindinger MI, Olfert IM, Heigenhauser GJ, Hopkins SR. Pulmonary gas exchange and acid-base balance during exercise. Compr Physiol. 2013; 3:693–739. [PubMed: 23720327]

334. Storey WF, Staub NC. Ventilation of terminal air units. J Appl Physiol. 1962; 17:391–397. [PubMed: 13917520]

335. Sugahara K, Matsumoto M, Baba T, Nakamura T, Kawamoto T. Elevation of serum human hepatocyte growth factor (HGF) level in patients with pneumonectomy during a perioperative period. Intensive Care Med. 1998; 24:434–437. [PubMed: 9660257]

336. Swan AJ, Tawhai MH. Evidence for minimal oxygen heterogeneity in the healthy human pulmonary acinus. J Appl Physiol. 2011; 110:528–537. [PubMed: 21071589]

337. Swindler, DR.; Wood, CD. An Atlas of Primate Gross Anatomy. Seattle WA: University of Washington Press; 1973. Part 5. Thorax; p. 184-201.

338. Takeda S, Hsia CC, Wagner E, Ramanathan M, Estrera AS, Weibel ER. Compensatory alveolar growth normalizes gas-exchange function in immature dogs after pneumonectomy. J Appl Physiol (1985). 1999; 86:1301–1310. [PubMed: 10194216]

339. Takeda S, Ramanathan M, Estrera AS, Hsia CCW. Postpneumonectomy alveolar growth does not normalize hemodynamic and mechanical function. J Appl Physiol. 1999; 87:491–497. [PubMed: 10444603]

340. Tamhane RM, Johnson RL Jr, Hsia CC. Pulmonary membrane diffusing capacity and capillary blood volume measured during exercise from nitric oxide uptake. Chest. 2001; 120:1850–1856. [PubMed: 11742912]

341. Tawhai MH, Hoffman EA, Lin CL. The lung physiome: Merging imaging-based measures with predictive computational models. Wiley Interdiscip Rev Syst Biol Med. 2009; 1:61–72. [PubMed: 20835982]

342. Tawhai MH, Hunter P, Tschirren J, Reinhardt J, McLennan G, Hoff-man EA. CT-based geometry analysis and finite element models of the human and ovine bronchial tree. J Appl Physiol. 2004; 97:2310–2321. [PubMed: 15322064]

343. Tawhai MH, Hunter PJ. Characterising respiratory airway gas mixing using a lumped parameter model of the pulmonary acinus. Respir Physiol. 2001; 127:241–248. [PubMed: 11504593]

344. Taylor CR, Weibel ER. Design of the mammalian respiratory system. I. Problem and strategy. Respir Physiol. 1981; 44:1–10. [PubMed: 7232879]

345. Tepper J, Pfeiffer J, Aldrich M, Tumas D, Kern J, Hoffman E, McLennan G, Hyde D. Can retinoic acid ameliorate the physiologic and morphologic effects of elastase instillation in the rat? Chest. 2000; 117:242S–244S. [PubMed: 10843928]

346. Thurlbeck WM. Lung growth and alveolar multiplication. Pathobiol Annu. 1975; 5:1–34. [PubMed: 1105318]

347. Thurlbeck WM. Postnatal growth and development of the lung. Am Rev Respir Dis. 1975; 111:803–844. [PubMed: 1094872]

348. Townsley MI, Parker JC, Korthuis RJ, Taylor AE. Alterations in hemodynamics and Kf,c during lung mass resection. J Appl Physiol. 1987; 63:2460–2466. [PubMed: 3436877]

349. Tschanz SA, Salm LA, Roth-Kleiner M, Barre SF, Burri PH, Schittny JC. Rat lungs show a biphasic formation of new alveoli during postnatal development. J Appl Physiol (1985). 2014; 117:89–95. [PubMed: 24764134]

350. Tucker A, McMurtry IF, Reeves JT, Alexander AF, Will DH, Grover RF. Lung vascular smooth muscle as a determinant of pulmonary hypertension at high altitude. Am J Physiol. 1975; 228:762–767. [PubMed: 234690]

351. Ulker P, Sati L, Celik-Ozenci C, Meiselman HJ, Baskurt OK. Mechanical stimulation of nitric oxide synthesizing mechanisms in erythrocytes. Biorheology. 2009; 46:121–132. [PubMed: 19458415]

352. Vadapalli A, Goldman D, Popel AS. Calculations of oxygen transport by red blood cells and hemoglobin solutions in capillaries. Artif Cells Blood Substit Immobil Biotechnol. 2002; 30:157–188. [PubMed: 12066873]

353. Vasilescu DM, Gao Z, Saha PK, Yin L, Wang G, Haefeli-Bleuer B, Ochs M, Weibel ER, Hoffman EA. Assessment of morphometry of pulmonary acini in mouse lungs by nondestructive imaging using multiscale microcomputed tomography. Proc Natl Acad Sci U S A. 2012; 109:17105–17110. [PubMed: 23027935]

354. Vaughn MW, Huang KT, Kuo L, Liao JC. Erythrocytes possess an intrinsic barrier to nitric oxide consumption. J Biol Chem. 2000; 275:2342–2348. [PubMed: 10644684]

355. Vaughn MW, Kuo L, Liao JC. Effective diffusion distance of nitric oxide in the microcirculation. Am J Physiol. 1998; 274:H1705–H1714. [PubMed: 9612383]

356. Verbanck S, Paiva M. Gas mixing in the airways and airspaces. Compr Physiol. 2011; 1:809–834. [PubMed: 23737204]

357. Vock R, Weibel ER. Massive hemorrhage causes changes in morphometric parameters of lung capillaries and concentration of leukocytes in microvasculature. Exp Lung Res. 1993; 19:559–577. [PubMed: 8253059]

358. Voswinckel R, Motejl V, Fehrenbach A, Wegmann M, Mehling T, Fehrenbach H, Seeger W. Characterisation of post-pneumonectomy lung growth in adult mice. Eur Respir J. 2004; 24:524–532. [PubMed: 15459128]

359. Voswinckel R, Ziegelhoeffer T, Heil M, Kostin S, Breier G, Mehling T, Haberberger R, Clauss M, Gaumann A, Schaper W, Seeger W. Circulating vascular progenitor cells do not contribute to compensatory lung growth. Circ Res. 2003; 93:372–379. [PubMed: 12881479]

360. Wagner PD. Ventilation-perfusion relationships. Annu Rev Physiol. 1980; 42:235–247. [PubMed: 6773469]

361. Wagner PD, Erickson BK, Kubo K, Hiraga A, Kai M, Yamaya Y, Richardson R, Seaman J. Maximum oxygen transport and utilisation before and after splenectomy. Equine Vet J. 1995; 18(suppl):82–89.

362. Wagner PD, Gillespie JR, Landgren GL, Fedde MR, Jones BW, DeBowes RM, Pieschl RL, Erickson HH. Mechanism of exercise-induced hypoxemia in horses. J Appl Physiol. 1989; 66:1227–1233. [PubMed: 2496088]

363. Wagner WW Jr, Todoran TM, Tanabe N, Wagner TM, Tanner JA, Glenny RW, Presson RG Jr. Pulmonary capillary perfusion: Intra-alveolar fractal patterns and interalveolar independence. J Appl Physiol. 1999; 86:825–831. [PubMed: 10066692]

364. Waller DA, Keavey P, Woodfine L, Dark JH. Pulmonary endothelial permeability changes after major lung resection. Ann Thorac Surg. 1996; 61:1435–1440. [PubMed: 8633955]

365. Wang CH, Popel AS. Effect of red blood cell shape on oxygen transport in capillaries. Math Biosci. 1993; 116:89–110. [PubMed: 8343620]

366. Wang PM, Kraman SS. Fractal branching pattern of the monopodial canine airway. J Appl Physiol. 2004; 96:2194–2199. [PubMed: 15133015]

367. Waters CM, Chang JY, Glucksberg MR, DePaola N, Grotberg JB. Mechanical forces alter growth factor release by pleural mesothelial cells. Am J Physiol. 1997; 272:L552–557. [PubMed: 9124613]

368. Wedel MJ. Evidence for bird-like air sacs in saurischian dinosaurs. J Exp Zool A Ecol Genet Physiol. 2009; 311:611–628. [PubMed: 19204909]

369. Weibel, ER. Morphometry of the Human Lung. New York: Springer Verlag and Academic Press; 1963.

370. Weibel ER. Principles and methods for the morphometric study of the lung and other organs. Lab Invest. 1963; 12:131–155. [PubMed: 13999512]

371. Weibel ER. Morphometric estimation of pulmonary diffusion capacity. I. Model and method. Respir Physiol. 1970; 11:54–75. [PubMed: 4992513]

372. Weibel ER. The mystery of “non-nucleated plates” in the alveolar epithelium of the lung explained. Acta Anat(Basel). 1971; 78:425–443. [PubMed: 4995841]

373. Weibel ER. Morphological basis of alveolar-capillary gas exchange. Physiol Rev. 1973; 53:419–495. [PubMed: 4581654]

374. Weibel ER. On pericytes, particularly their existence on lung capillaries. Microvasc Res. 1974; 8:218–235. [PubMed: 4140459]

375. Weibel, ER. Stereological Methods Vol I: Practical Methods for Biological Morphometry. Academic Press; 1979.

376. Weibel, ER. The Pathway for Oxygen Structure and Function in the Mammalian Respiratory System. Cambridge, MA: Harvard University Press; 1984.

377. Weibel ER. Scaling of structural and functional variables in the respiratory system. Annu Rev Physiol. 1987; 49:147–159. [PubMed: 3551794]

378. Weibel ER. Fractal geometry: A design principle for living organisms. Am J Physiol. 1991; 261:L361–369. [PubMed: 1767856]

379. Weibel, ER. Design of airways and blood vessels considered as branching trees. In: Crystal, RG.; West, JB.; Weibel, ER.; Barnes, PJ., editors. The Lung: Scientific Foundations. Philadelphia, PA: Lippincott-Raven; 1997. p. 1061-1071.

380. Weibel, ER. Symmorphosis. Cambridge, MA: Harvard University Press; 2000.

381. Weibel ER. What makes a good lung? Swiss Med Wkly. 2009; 139:375–386. [PubMed: 19629765]

382. Weibel ER. Lung Cell Biology. Compr Physiol. 2011; First published in print 1985. doi: 10.1002/cphy.cp030102Supplement 10: Handbook of Physiology, The Respiratory System, Circulation and Nonrespiratory Functions: 47–91

383. Weibel ER. Functional Morphology of Lung Parenchyma. Compr Physiol. 2011; First published in print 1986. doi: 10.1002/cphy.cp030308Supplement 12: Handbook of Physiology, The Respiratory System, Mechanics of Breathing: 89–111

384. Weibel ER. It takes more than cells to make a good lung. Am J Resp Crit Care Med. 2013; 187:342–346. [PubMed: 23418327]

385. Weibel ER. On the tricks alveolar epithelial cells play to make a good lung. Am J Respir Crit Care Med. 2015; 191:504–513. [PubMed: 25723823]

386. Weibel ER, Bachofen H. How to stabilize the pulmonary alveoli: Surfactant or fibers? News Physiol Sci. 1987; 2:72–75.

387. Weibel ER, Bacigalupe LD, Schmitt B, Hoppeler H. Allometric scaling of maximal metabolic rate in mammals: Muscle aerobic capacity as determinant factor. Respir Physiol Neurobiol. 2004; 140:115–132. [PubMed: 15134660]

388. Weibel ER, Federspiel WJ, Fryder-Doffey F, Hsia CC, Konig M, Stalder-Navarro V, Vock R. Morphometric model for pulmonary diffusing capacity. I. Membrane diffusing capacity. Respir Physiol. 1993; 93:125–149. [PubMed: 8210754]

389. Weibel ER, Gomez DM. Architecture of the human lung. Use of quantitative methods establishes fundamental relations between size and number of lung structures. Science. 1962; 137:577–585. [PubMed: 14005590]

390. Weibel ER, Hoppeler H. Exercise-induced maximal metabolic rate scales with muscle aerobic capacity. J Exp Biol. 2005; 208:1635–1644. [PubMed: 15855395]

391. Weibel ER, Hsia CC, Ochs M. How much is there really? Why stereology is essential in lung morphometry. J Appl Physiol. 2007; 102:459–467. [PubMed: 16973815]

392. Weibel ER, Knight BW. A morphometric study on the thickness of the pulmonary air-blood barrier. J Cell Biol. 1964; 21:367–396. [PubMed: 14189911]
393. Weibel ER, Marques LB, Constantinopol M, Doffey F, Gehr P, Taylor CR. Adaptive variation in the mammalian respiratory system in relation to energetic demand: VI. The pulmonary gas exchanger. Respir Physiol. 1987; 69:81–100.
394. Weibel ER, Sapoval B, Filoche M. Design of peripheral airways for efficient gas exchange. Respir Physiol Neurobiol. 2005; 148:3–21. [PubMed: 15921964]
395. Weibel ER, Taylor CR, Gehr P, Hoppeler H, Mathieu O, Maloiy GM. Design of the mammalian respiratory system. IX. Functional and structural limits for oxygen flow. Respir Physiol. 1981; 44:151–164. [PubMed: 7232884]
396. Weibel ER, Taylor CR, Hoppeler H. The concept of symmorphosis: A testable hypothesis of structure-function relationship. Proc Natl Acad Sci U S A. 1991; 88:10357–10361. [PubMed: 1946456]
397. Weibel ER, Taylor CR, O'Neil JJ, Leith DE, Gehr P, Hoppeler H, Langman V, Baudinette RV. Maximal oxygen consumption and pulmonary diffusing capacity: A direct comparison of physiologic and morphometric measurements in canids. Respir Physiol. 1983; 54:173–188. [PubMed: 6665333]
398. Weibel ER, Untersee P, Gil J, Zulauf M. Morphometric estimation of pulmonary diffusion capacity. VI. Effect of varying positive pressure inflation of air spaces. Respir Physiol. 1973; 18:285–308. [PubMed: 4746958]
399. West JB. How well designed is the human lung? Am J Respir Crit Care Med. 2006; 173:583–584. [PubMed: 16387797]
400. West JB, Dollery CT, Heard BE. Increased vascular resistance in the lower zone of the lung caused by perivascular oedema. Lancet. 1964; 2:181–183. [PubMed: 14163134]
401. Wilson TA. Design of the bronchial tree. Nature. 1967; 213:668–669. [PubMed: 6031769]
402. Wilson TA, Bachofen H. A model for mechanical structure of the alveolar duct. J Appl Physiol Respir Environ Exerc Physiol. 1982; 52:1064–1070. [PubMed: 7085408]
403. Winkler GC, Cheville NF. The neonatal porcine lung: Ultrastructural morphology and postnatal development of the terminal airways and alveolar region. Anat Rec. 1984; 210:303–313. [PubMed: 6507895]
404. Winkler GC, Cheville NF. Morphometry of postnatal development in the porcine lung. Anat Rec. 1985; 211:427–433. [PubMed: 3993992]
405. Wirtz HR, Dobbs LG. The effects of mechanical forces on lung functions. Respir Physiol. 2000; 119:1–17. [PubMed: 10701703]
406. Wu EY, Hsia CC, Estrera AS, Epstein RH, Ramanathan M, Johnson RL Jr. Preventing mediastinal shift after pneumonectomy does not abolish physiologic compensation. J Appl Physiol. 2000; 89:182–191. [PubMed: 10904051]
407. Wu EY, Ramanathan M, Hsia CCW. Role of hematocrit in the recruitment of pulmonary diffusing capacity: Comparison of human and dogs [Published corrigenda in J. Appl. Physiol. 80(6): After Table of Contents, 1996.]. J Appl Physiol. 1996; 80:1014–1020. [PubMed: 8964719]
408. Wulfsohn D, Knust J, Ochs M, Nyengaard JR, Gundersen HJ. Stereological estimation of the total number of ventilatory units in mice lungs. J Microsc. 2010; 238:75–89. [PubMed: 20384839]
409. Xu J, Liu M, Liu J, Caniggia I, Post M. Mechanical strain induces constitutive and regulated secretion of glycosaminoglycans and proteoglycans in fetal lung cells. J Cell Sci. 1996; 109:1605–1613. [PubMed: 8799847]
410. Yamaguchi K, Nguyen-Phu D, Scheid P, Piiper J. Kinetics of O_2 uptake and release by human erythrocytes studied by a stopped-flow technique. J Appl Physiol. 1985; 58:1215–1224. [PubMed: 3988677]
411. Yan X, Bellotto DJ, Dane DM, Elmore RG, Johnson RL Jr, Estrera AS, Hsia CC. Lack of response to all-trans retinoic acid supplementation in adult dogs following left pneumonectomy. J Appl Physiol. 2005; 99:1681–1688. [PubMed: 15961609]
412. Yan X, Bellotto DJ, Foster DJ, Johnson RL Jr, Hagler HH, Estrera AS, Hsia CC. Retinoic acid induces nonuniform alveolar septal growth after right pneumonectomy. J Appl Physiol. 2004; 96:1080–1089. [PubMed: 14617528]

413. Yeh HC, Schum GM. Models of human lung airways and their application to inhaled particle deposition. Bull Math Biol. 1980; 42:461–480. [PubMed: 7378614]

414. Yilmaz C, Dane DM, Hsia CC. Alveolar diffusion-perfusion interactions during high-altitude residence in guinea pigs. J Appl Physiol. 2007; 102:2179–2185. [PubMed: 17363625]

415. Yilmaz C, Johnson RL Jr, Hsia CC. A rebreathing method for measuring lung volume, diffusing capacity and cardiac output in conscious small animals. Respir Physiol Neurobiol. 2005; 146:215–223. [PubMed: 15766909]

416. Yilmaz C, Ravikumar P, Dane DM, Bellotto DJ, Johnson RL Jr, Hsia CC. Noninvasive quantification of heterogeneous lung growth following extensive lung resection by high-resolution computed tomography. J Appl Physiol. 2009; 107:1569–1578. [PubMed: 19729592]

417. Yilmaz C, Tustison NJ, Dane DM, Ravikumar P, Takahashi M, Gee JC, Hsia CC. Progressive adaptation in regional parenchyma mechanics following extensive lung resection assessed by functional computed tomography. J Appl Physiol. 2011; 111:1150–1158. [PubMed: 21799134]

418. Young IH, Bye PT. Gas exchange in disease: Asthma, chronic obstructive pulmonary disease, cystic fibrosis, and interstitial lung disease. Compr Physiol. 2011; 1:663–697. [PubMed: 23737199]

419. Yuan S, Hannam V, Belcastro R, Cartel N, Cabacungan J, Wang J, Diambomba Y, Johnstone L, Post M, Tanswell AK. A role for platelet-derived growth factor-BB in rat postpneumonectomy compensatory lung growth. Pediatr Res. 2002; 52:25–33. [PubMed: 12084843]

420. Zeltner TB, Burri PH. The postnatal development and growth of the human lung. II. Morphology. Respir Physiol. 1987; 67:269–282. [PubMed: 3575906]

421. Zeltner TB, Caduff JH, Gehr P, Pfenninger J, Burri PH. The postnatal development and growth of the human lung. I. Morphometry. Respir Physiol. 1987; 67:247–267. [PubMed: 3575905]

422. Zhang Q, Bellotto DJ, Ravikumar P, Moe OW, Hogg RT, Hogg DC, Estrera AS, Johnson RL Jr, Hsia CC. Postpneumonectomy lung expansion elicits hypoxia-inducible factor–1alpha signaling. Am J Physiol Lung Cell Mol Physiol. 2007; 293:L497–504. [PubMed: 17513452]

423. Zhang Q, Moe OW, Garcia JA, Hsia CC. Regulated expression of hypoxia-inducible factors during postnatal and postpneumonectomy lung growth. Am J Physiol Lung Cell Mol Physiol. 2006; 290:L880–889. [PubMed: 16373673]

424. Zhang Q, Zhang J, Moe OW, Hsia CC. Synergistic upregulation of erythropoietin receptor (EPO-R) expression by sense and antisense EPO-R transcripts in the canine lung. Proc Natl Acad Sci USA. 2008; 105:7612–7617. [PubMed: 18495932]

425. Zhang S, Garbutt V, McBride JT. Strain-induced growth of the immature lung. J Appl Physiol. 1996; 81:1471–1476. [PubMed: 8904555]

426. Zuck TT. Age order of epiphyseal union in the guinea pig. Anat Rec. 1938; 70:389–399.

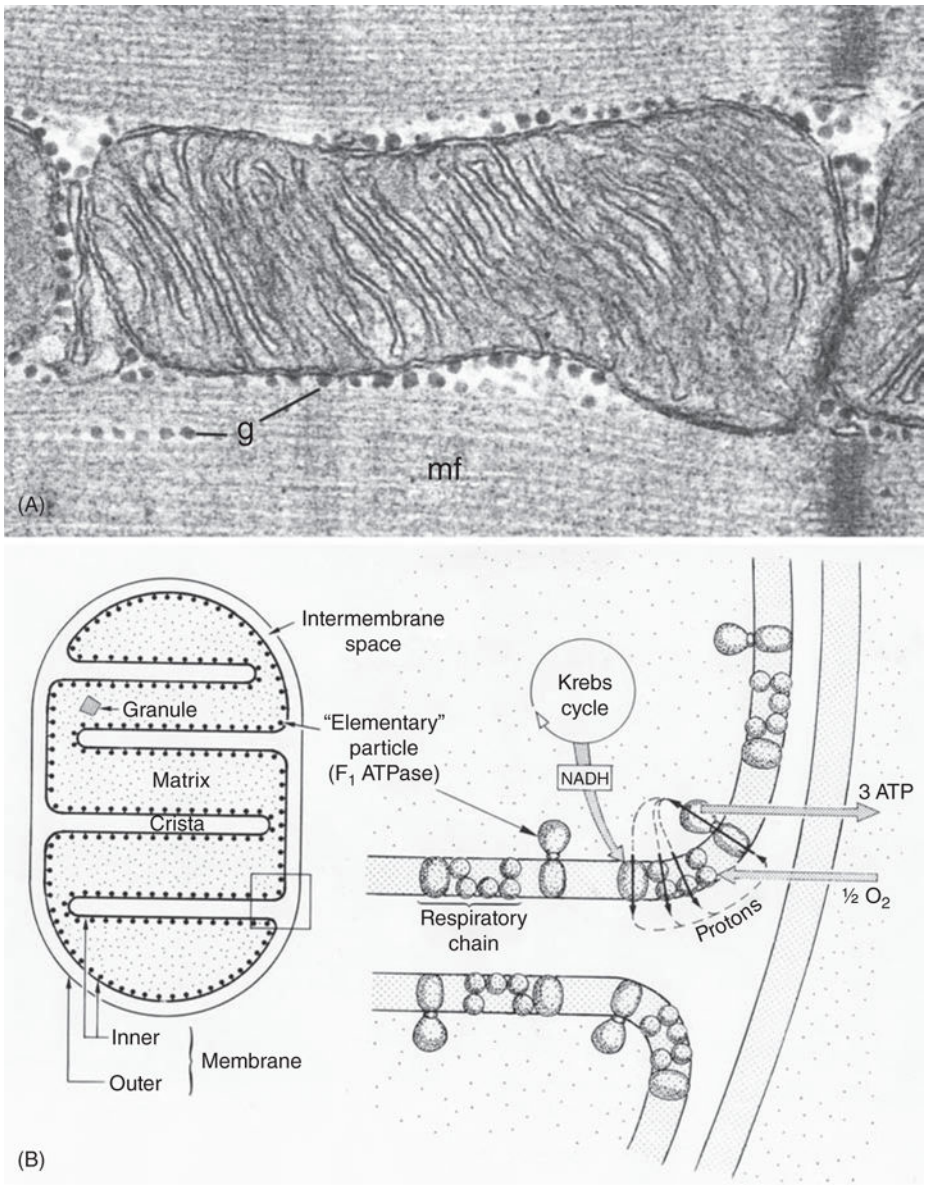

Figure 1.

(A) Electron micrograph of muscle mitochondrion shows the packing of inner membrane cristae where oxidative phosphorylation takes place, separated by matrix where the Krebs cycle is located. Note glycogen granules as fuel reserves on the surface. (B) Scheme of functional organization of mitochondria. A from (390) with permission; B from (376) with permission.

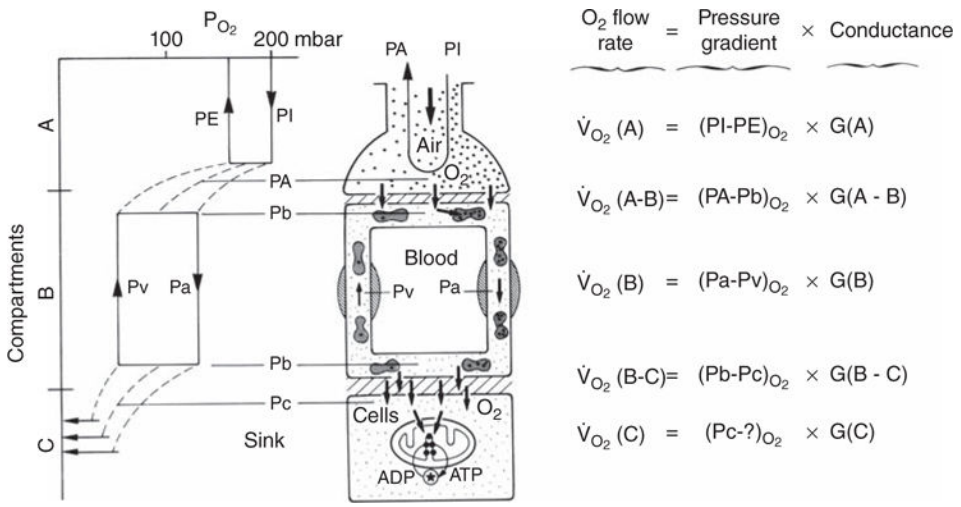

Figure 2.

Model of the mammalian pathway for oxygen in form of a cascade from the lung through the circulation of blood to the mitochondria. The oxygen flow rate through each step is the product of a conductance with a pressure difference, which decreases stepwise from inspired PO_2 (PI) to near 0 at the level of mitochondria that serve as oxygen sink. Subscripts for partial pressures P: I inspired and E expired air, A alveolar air, b capillary blood, a arterial and v mixed venous blood, c cytoplasm. Taken, with permission, from (376).

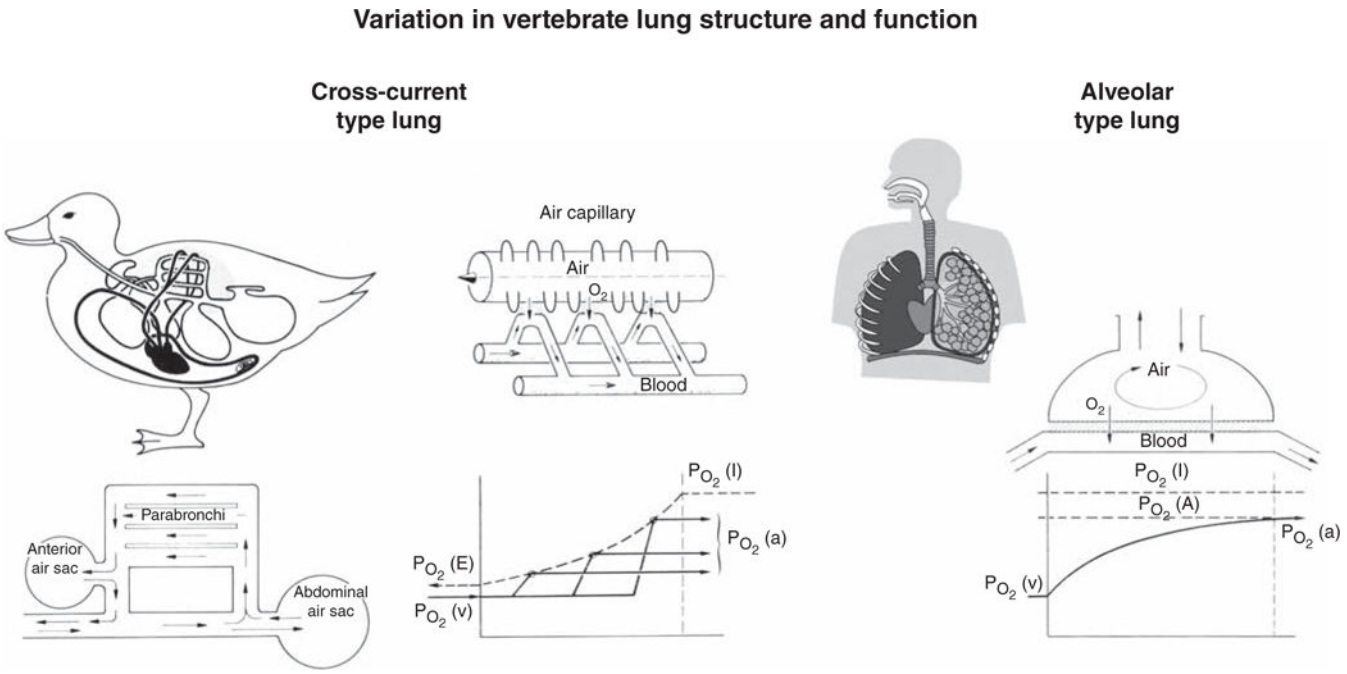

Figure 3.

Variation in vertebrate lung structure and function. In alveolar lungs as occur in mammals, gas exchange occurs by air flowing in through the airways and mixing with air contained in the alveolar pool and blood flowing by in the pulmonary capillaries. In bird lungs, air flows through parabronchi in a caudal to cranial direction using the air sacs as bellows. Gas exchange occurs in a cross-current fashion between air capillaries of the parabronchi and the blood capillaries. With this type of arrangement, arterial PO_2 may be higher than expired air PO_2. Modified, with permission, from Weibel, 1984 (376).

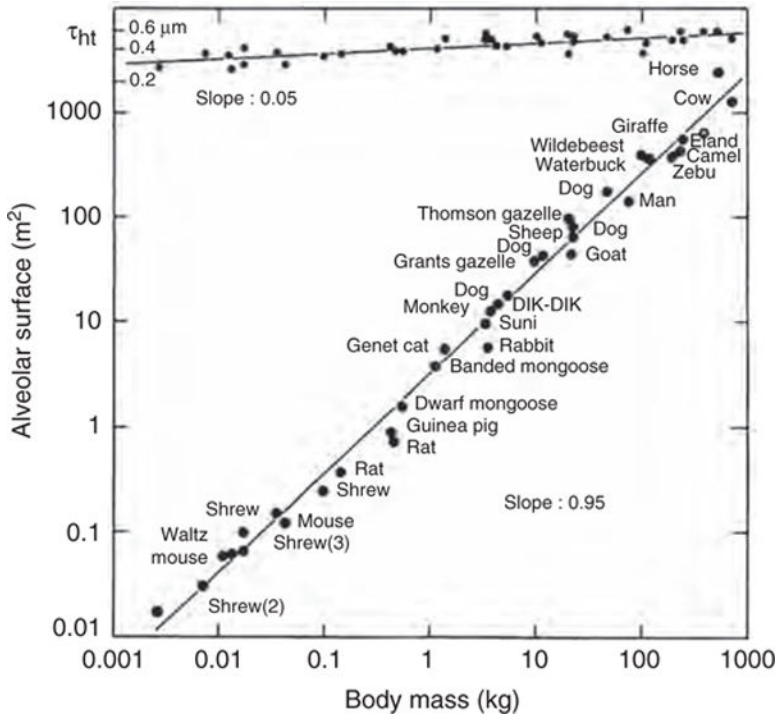

Figure 4.

Allometric plot of the alveolar surface area and the harmonic mean thickness of the air-blood barrier in mammals from the smallest species (Suncus Etruscus) to horse and cow. Taken from (111) by permission.

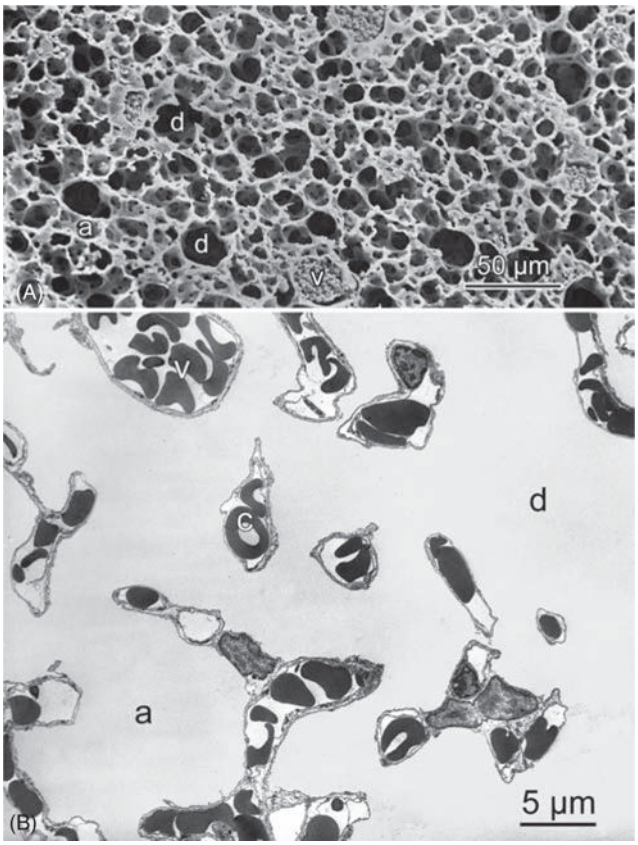

Figure 5.

Structure of the gas exchanger in the smallest mammal, an Etruscan shrew (2 g), (A) in a scanning electron micrograph that reveals the small size of alveoli (a) and alveolar ducts (d) as well as erythrocytes in a small vessel (v), resulting in a six times higher density of alveolar surface compared with a human lung (compare Fig. 13). (B) On thin sections, the alveolar capillaries are seen to form an exceptionally dense network that occupies about 20% of the parenchymal volume.

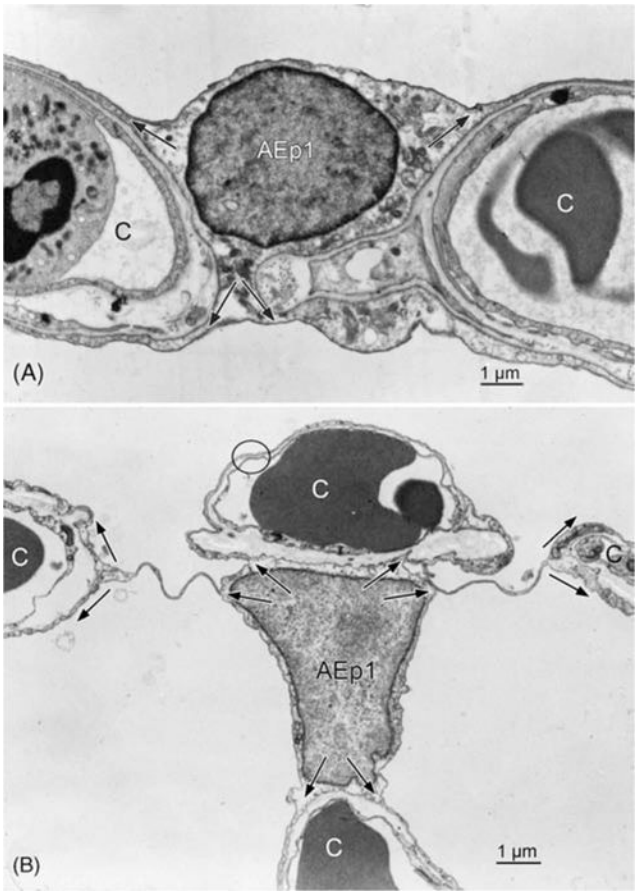

Figure 6.

Comparing fine structure of the alveolar-capillary tissue barrier in the lung of a monkey (A) and of an Etruscan shrew (B) reveals extreme attenuation of the air-blood barrier in the shrew (circle). In the monkey lung, the type-1 epithelial cell (AEp1) forms cytoplasmic leaflets on both sides of the septum (arrows). In the shrew lung, the thinning of the barrier is achieved by minimization of the epithelial cytoplasmic leaflets by highly complex branching of the type-1 epithelial cell extensions (multiple arrows), combined with similar thinning of the endothelial cell extensions of capillaries (C).

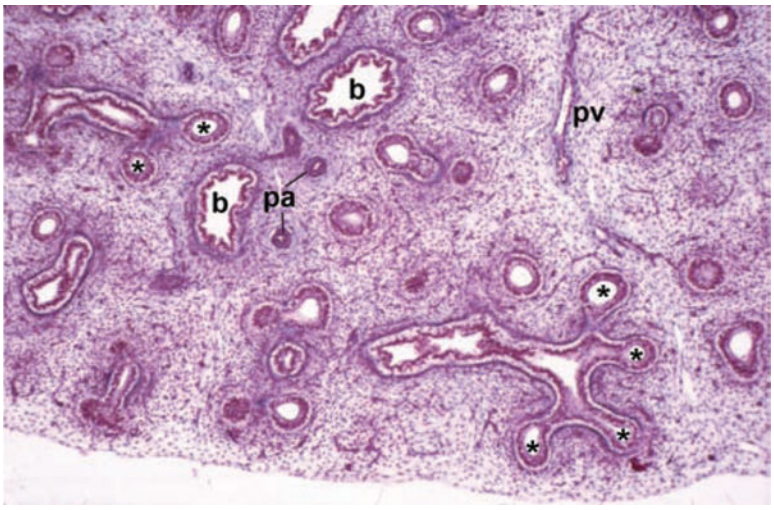

Figure 7.

Histological section of the subpleural region of human fetal lung (about 12th week of gestation, pseudoglandular stage) shows the branching pattern by dichotomy in the terminal branches ending in spherical buds (*) from where branching will continue. These terminal buds are enwrapped by loose, cell-rich mesenchyme. More central branches (b) that do not further divide have a thicker epithelium and are enwrapped by dense mesenchyme and develop smooth muscle sleeves characteristic of bronchi. Pulmonary artery branches (pa), provided by a sheath of smooth muscle, are close to the bronchi and follow their course peripherally whereas pulmonary veins (pv) are located in the wider mesenchymal septa.

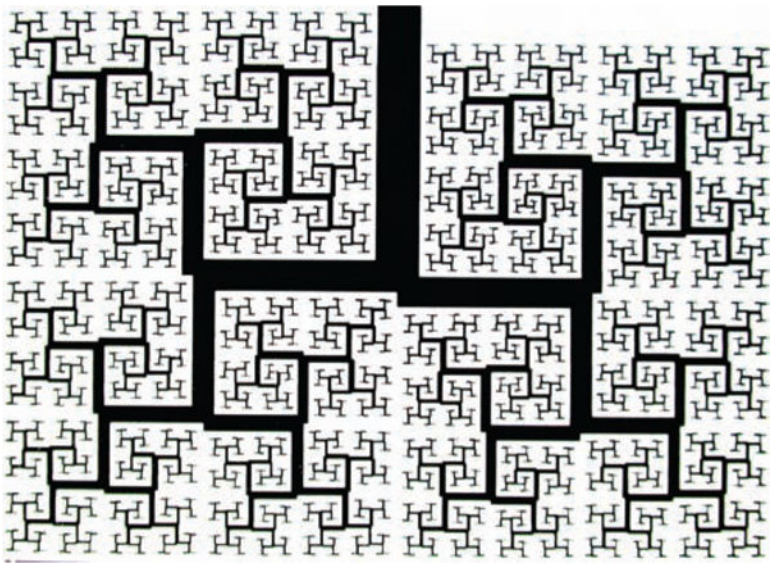

Figure 8.
Fractal tree model of Benoit Mandelbrot simulates a space-filling airway tree. Taken from (235) by permission.

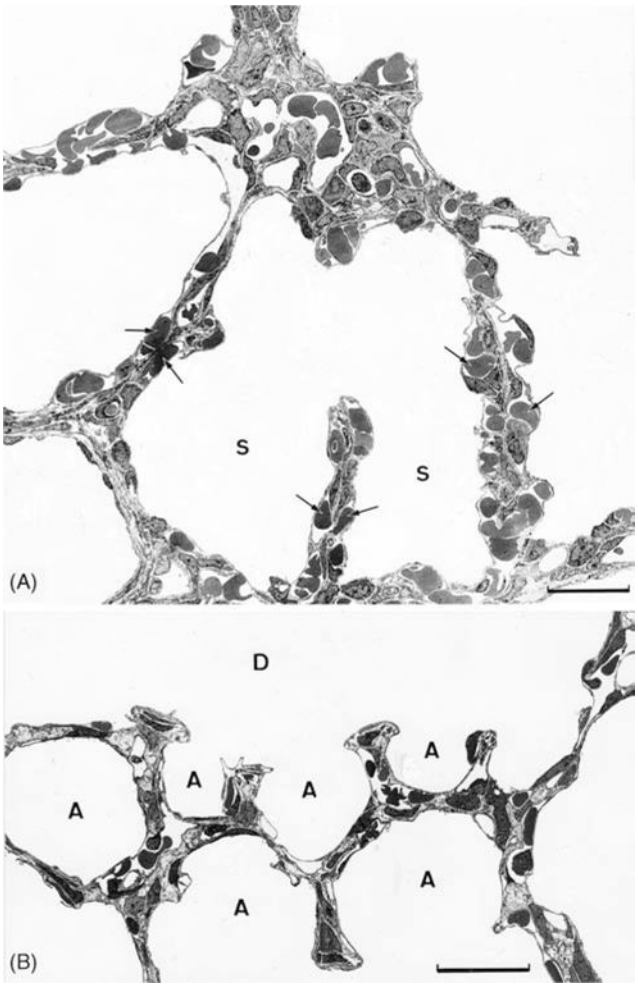

Figure 9.

(A) Rat lung at birth is made of wide saccules (S) separated by septa containing two capillary networks (paired arrows). (B) Thin section of rat lung on day 13 of postnatal development. Alveoli have formed by pulling up septa into the alveolar duct (D) corresponding to the saccule in (A); the septa contain a single capillary network. Panel A, with permission, from (39); panel B, with permission, from (376).

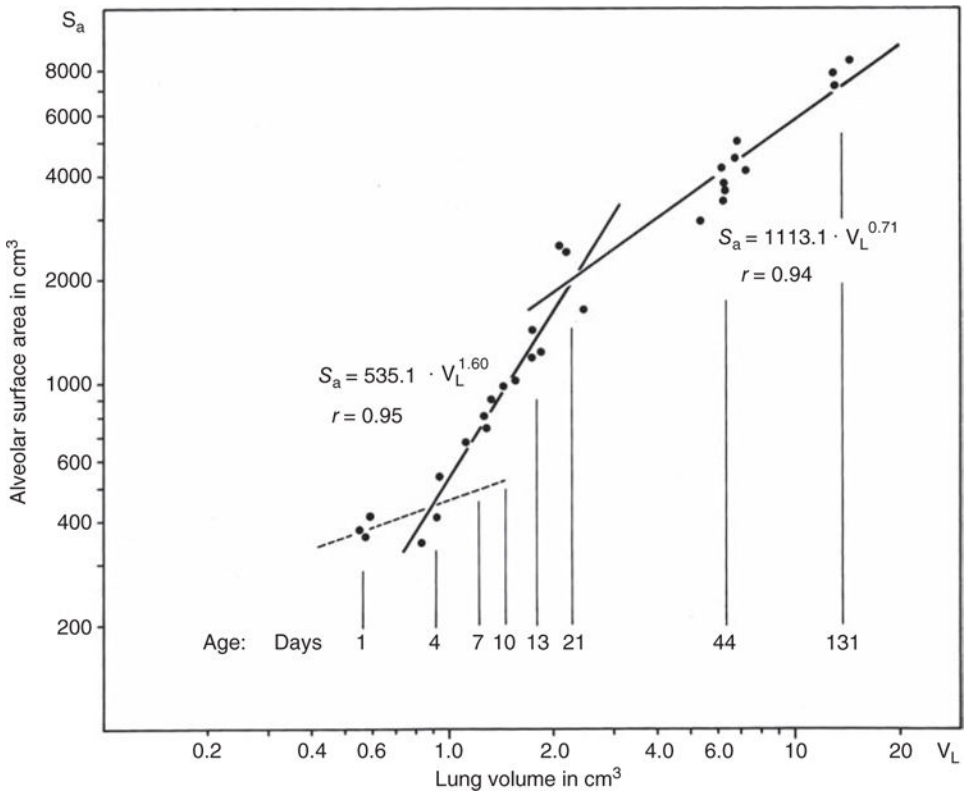

Figure 10.

As lung volume increases in the rat lung during early postnatal growth the alveolar surface is enlarged in three stages, with a prominent increase by a factor of 3 between days 4 and 21 due to the formation of alveoli. Taken, with permission, from (376).

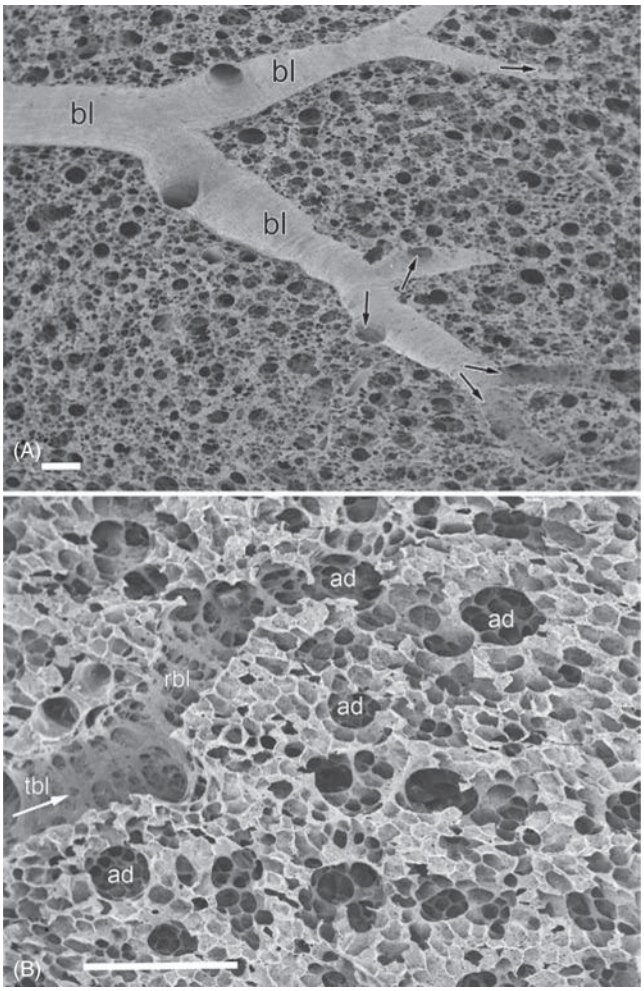

Figure 11.

Scanning electron micrographs of dog lung. (A) Longitudinal cut of a branching distal bronchiolus (bl) giving rise to transitional bronchioles (*arrows*) as origin of acini; the tip of the arrows points to the first alveoli occurring in the airway wall. (B) Origin of acinar airways (*arrow*) at transitional bronchiole (tbl) leading to a respiratory bronchiole (rbl) and several alveolar ducts (ad); the latter change very little in diameter with each generation so that total airway cross-section nearly doubles with each generation. Scale bars = 500 μm.

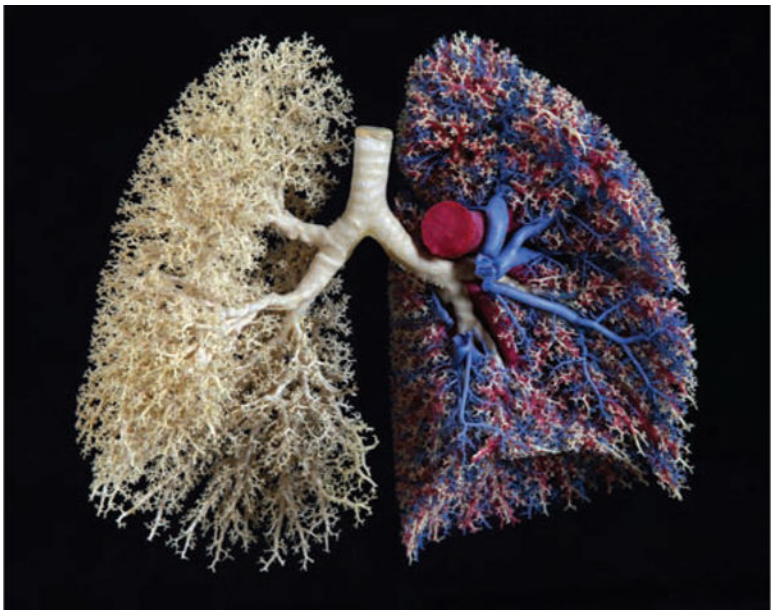

Figure 12.
Cast of human bronchial tree with airways (yellow), pulmonary arteries (red), and pulmonary veins (blue).

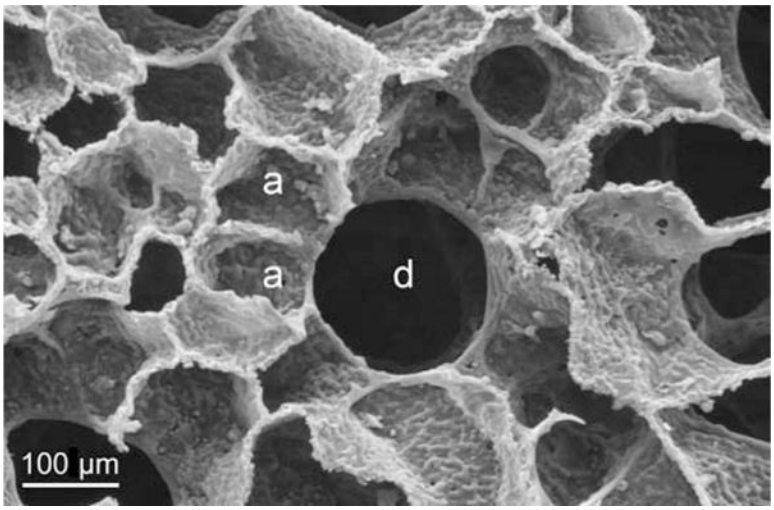

Figure 13.
Scanning electron micrograph of human lung parenchyma. Alveolar ducts (d) are surrounded by alveoli (a), which are separated by thin septa.

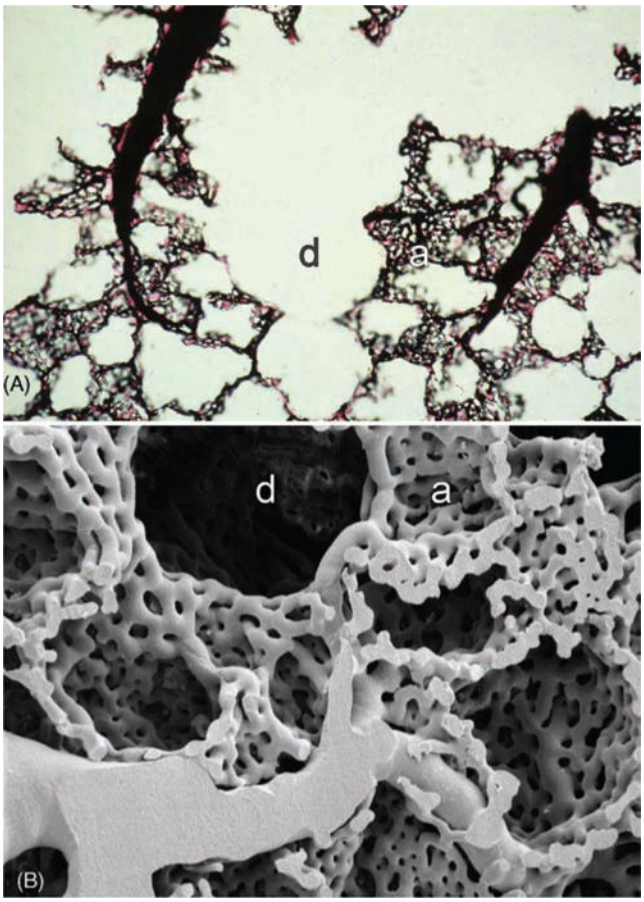

Figure 14.

Microvascular network of the lung shown in (A) by colloidal gold labeling of the plasma in a rabbit lung (212), and in (B) in a Mercox cast of a rat lung. Note relations to alveolar ducts (d) and alveoli (a). B courtesy of P.H. Burri.

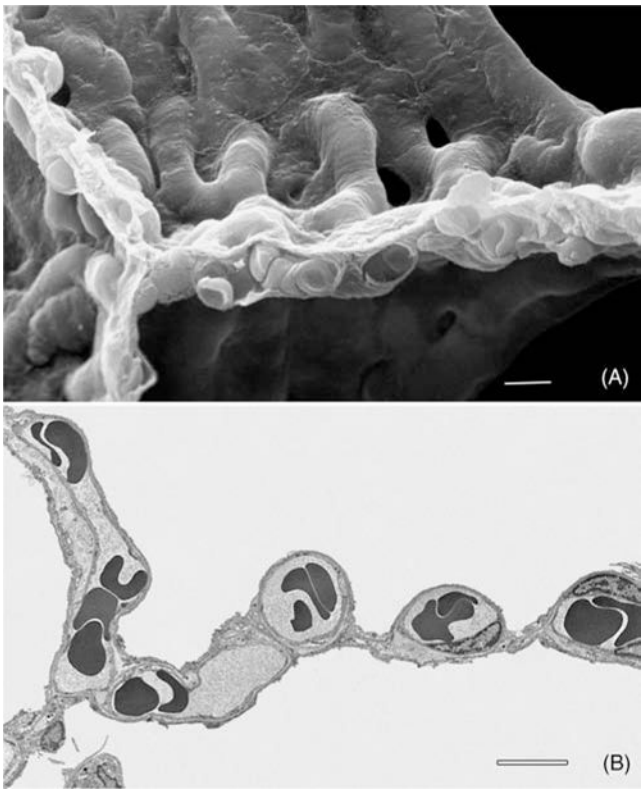

Figure 15.

Architecture of interalveolar septa in the human lung reveals that each wall contains a single capillary network with a thin tissue barrier separating the blood from the alveolar air. (A) This panel is a scanning electron micrograph from a human lung that shows the capillary network in 3D and (B) this panel is an electron micrograph of a thin section showing the capillary blood and the thin tissue barrier. Scale markers 10 μm.

Figure 16.

The alveolar capillary is lined by endothelial cells (End) that form thin cytoplasmic leaflets in the thin barrier portions. The alveoli are lined by epithelial cells, here a type-1 cell (Ep1) is shown to also form thin cytoplasmic leaflets, which are separated from the endothelial cell by a single fused basement membrane in the upper part (circle), whereas in the lower part the two basement membranes are separated to allow the formation of a slim interstitial space with processes of a fibroblast (f) and some connective tissue fibers for mechanical support (arrow).

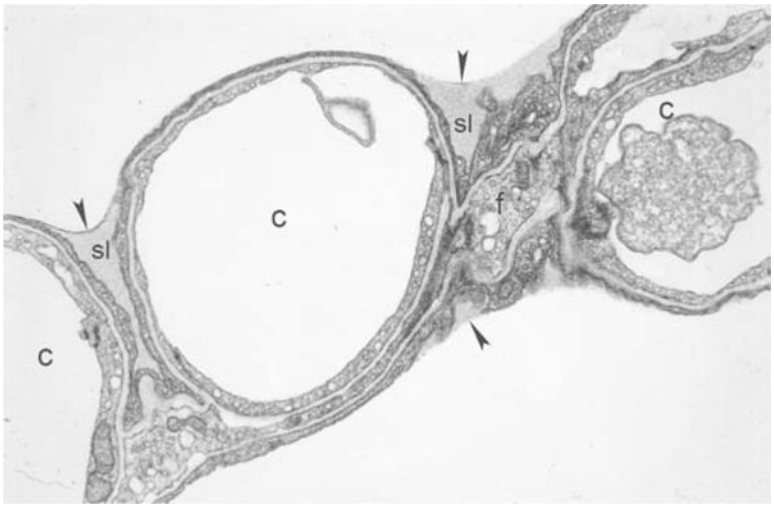

Figure 17.

Capillaries (c) in alveolar septum of perfusion-fixed rabbit lung shows preserved alveolar surface lining layer (sl) with surfactant film (arrowheads) smoothing the epithelial surface. Fibroblast (f) occurs in the thicker part of the barrier.

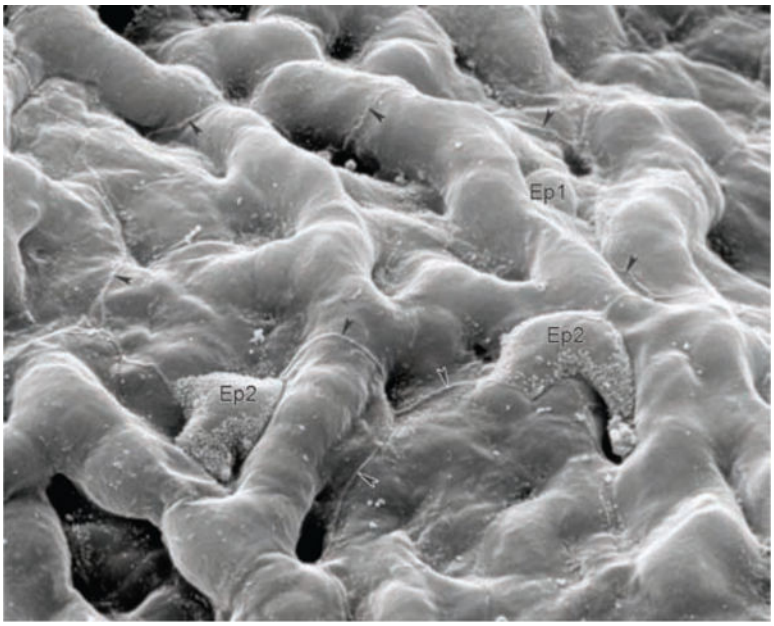

Figure 18.

Surface of the alveolar wall in the human lung seen by scanning electron microscopy reveals a mosaic of alveolar epithelium made of type-1 (Ep1) and type-2 (EP2) cells. Arrows indicate boundary of the cytoplasmic leaflet of the type-1 cell which extends over many capillaries.

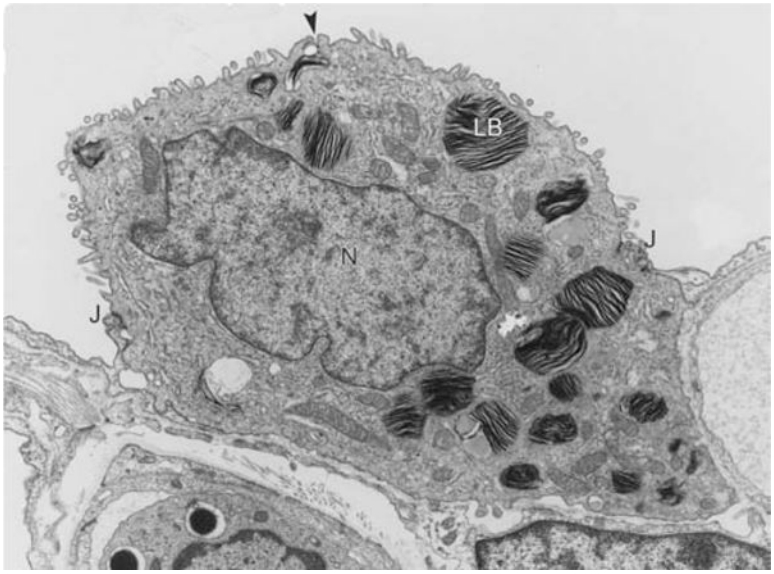

Figure 19.

A type-2 epithelial cell from a dog lung forms junctions (J) with type-1 epithelial cells (EP1). Its cytoplasm contains osmiophilic lamellar bodies (LB) as storage granules for surfactant phospholipids, and a rich complement of organelles, such as mitochondria and endoplasmic reticulum surrounding the nucleus (N). Arrowhead marks point at which a lamellar body is in the process of secretion onto the alveolar surface.

Figure 20.

Model of alveolar septum shows capillary network (red) interlaced with the network of connective tissue fibers (green) that extends from the free edge of the septum (alveolar entrance ring) at the right to the triple line on the left where three septa are joined (compare Fig. 13).

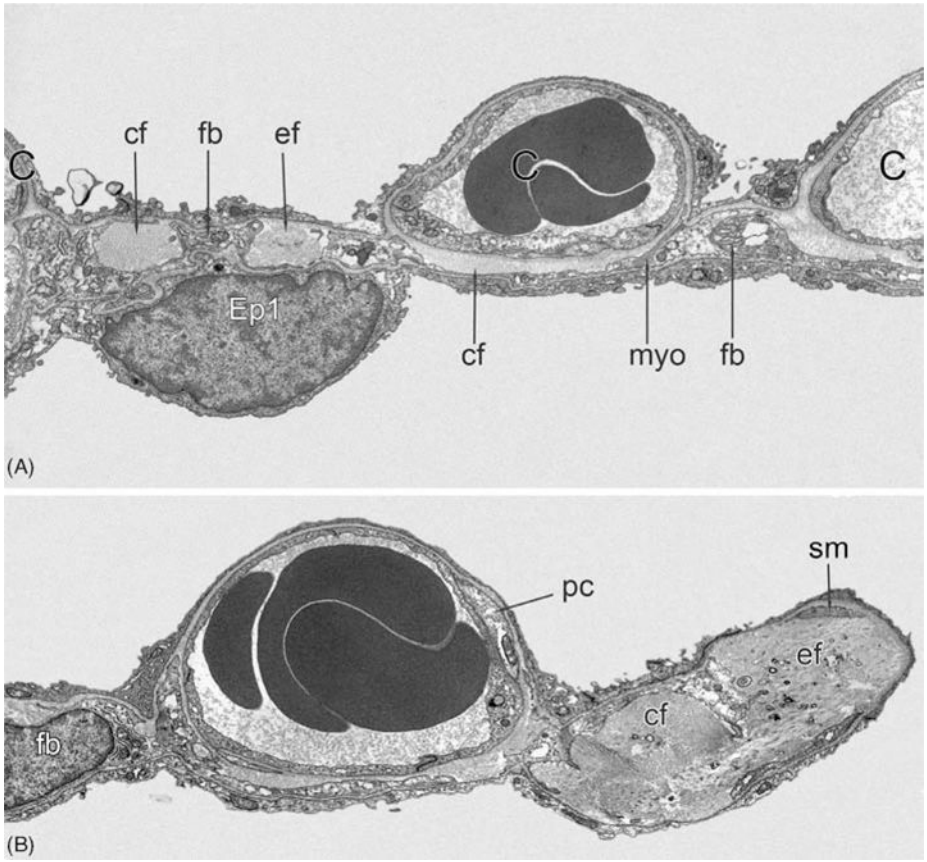

Figure 21.

Electron micrographs of alveolar septa in human lung show the relative arrangement of capillaries (C), type-1 alveolar epithelium (Ep1) and elements of the interstitium such as collagen (cf) and elastic (ef) fibers and fibroblast (fb) that focally can form myofibrils (myo) and serve as myofibroblasts bracing the interstitial space. The top panel (A) is from the mid-part of a septum, the bottom panel (B) shows the strong fibers at the free edge of the septum forming the alveolar entrance ring that may contain some smooth muscle cells (sm). A pericyte (pc) is associated with the capillary.

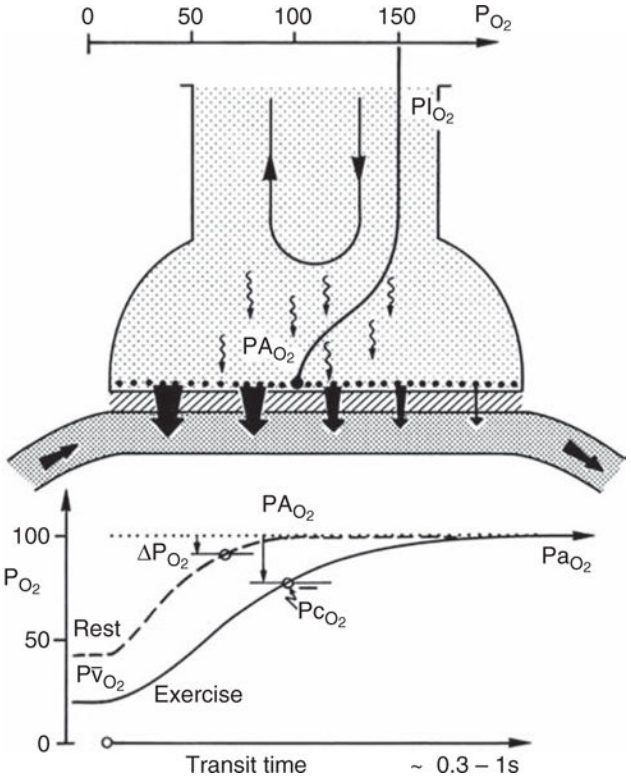

Figure 22.

Model of gas exchange showing gradual rise of capillary P_{O_2} (Pc_{O_2}) as blood flows through capillary until it approaches alveolar P_{O_2} (PA_{O_2}). Taken from Weibel (376) with permission.

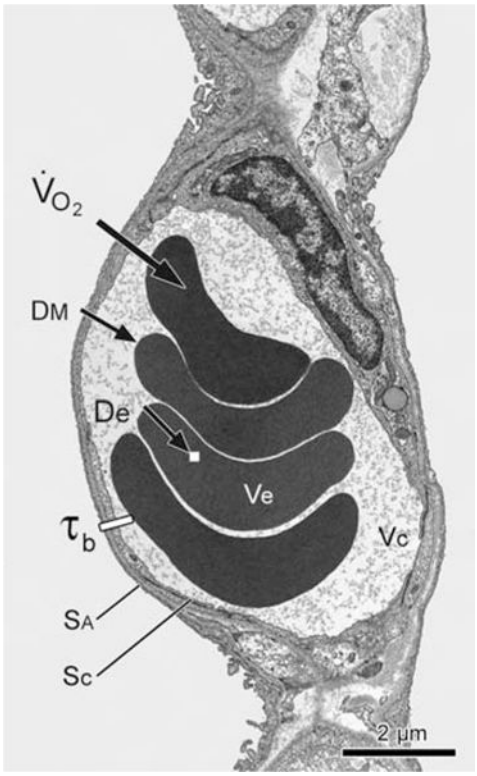

Figure 23.

Morphometric model for calculating diffusion capacity, DL. Its two components are (A) the membrane conductance DM, which extends from the alveolar surface (SA) to the nearest erythrocyte membrane traversing the tissue barrier, the capillary surface Sc, and the plasma layer over the distance τ_b; and (B) the conductance of the erythrocyte interior, De, that depends on the capillary and the erythrocyte volume, Vc and Ve, respectively. (See text.) Taken, with permission, from Ochs and Weibel (266).

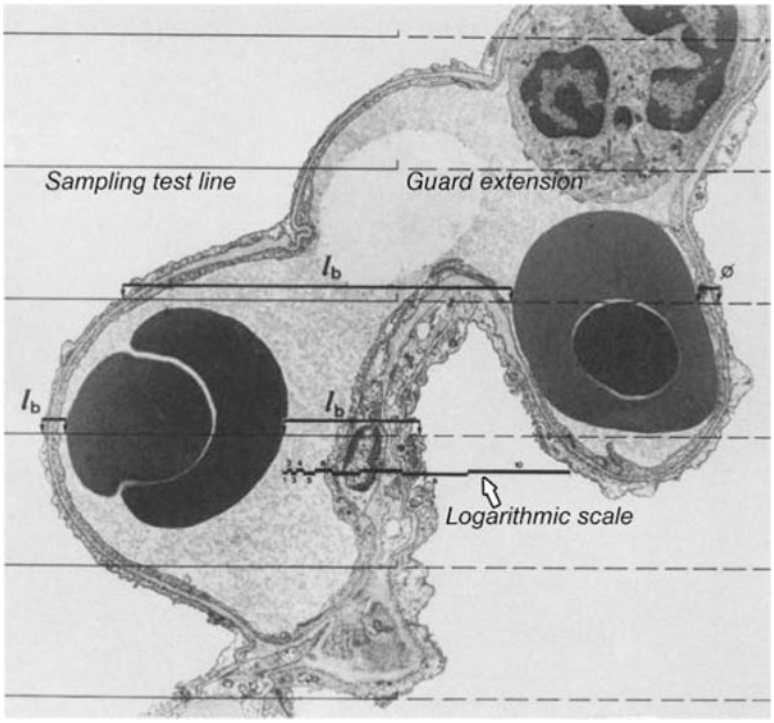

Figure 24.

Electron micrograph of human lung showing the method for measuring total barrier thickness from the intercept length l_b with random line probes. A set of test lines made of a sampling test line (solid line) followed by a guard extension (broken line) is randomly placed, when the sampling line hits the alveolar surface the distance to the nearest erythrocyte membrane is measured as the barrier intercept length l_b, preferably using a logarithmic scale. Taken, with permission, from (388).

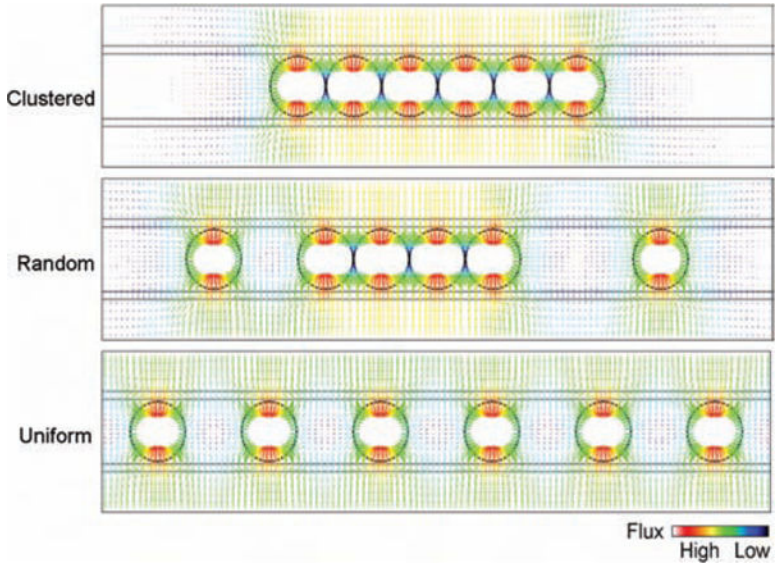

Figure 25.

The CO flux across tissue-erythrocyte barrier to binding with hemoglobin is simulated by placing different distributions of the same number of erythrocytes inside a hypothetical capillary segment. Compared to uniform erythrocyte distribution, the nonuniform clustered and random distributions show more heterogeneity in CO flux with respect to the tissue-erythrocyte membrane. Total CO flux progressively increases from clustered to random and to uniform erythrocyte distributions. Taken, with permission, from (178).

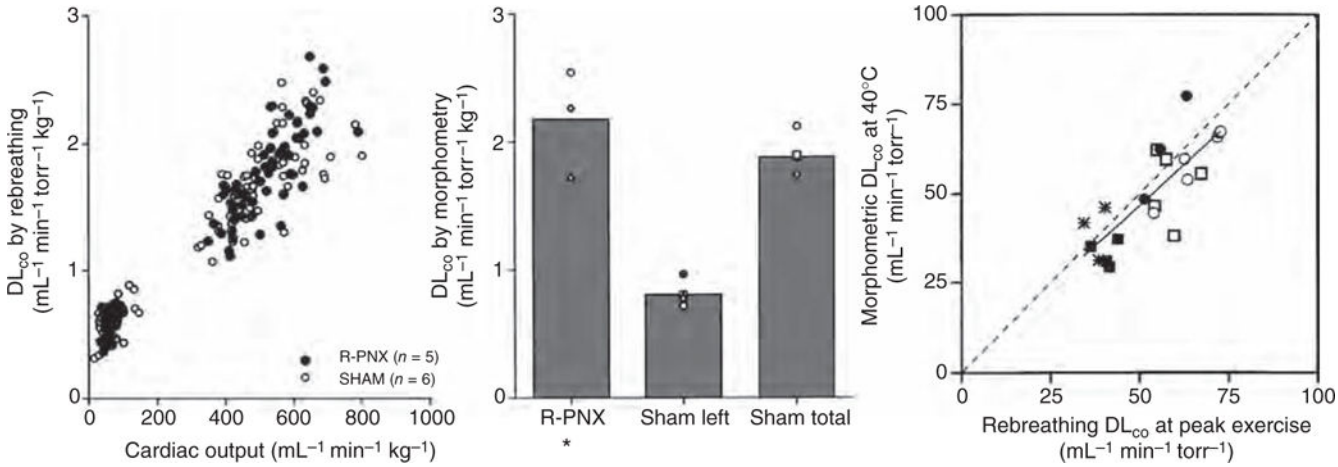

Figure 26.

Lung diffusing capacity (DL_{CO}) measured by physiological and morphometric methods. *Left*: DL_{CO} and pulmonary blood flow were measured by a rebreathing technique at rest and during exercise in dogs following right pneumonectomy (R-PNX) or in control (Sham) animals. *Middle*: DL_{CO} estimated by a morphometric model in the remaining left lung of animals after R-PNX compared with that in left lung and both lungs of control (Sham) animals. Symbols represent individual animals; bars represent group means. $*P < 0.0001$ vs. Sham left lung. *Right*: Correlation between DL_{CO} measured by a rebreathing method at peak exercise and by morphometry in different groups subjected to PNX or Sham PNX either as puppies (Sham, open circles; right PNX, closed circles) or as adults (Sham, open squares; right PNX, closed squares; left PNX, asterisks). Solid line, regression line through all data points. $DL_{CO(morphometry)} = 0.90\ DL_{CO(rebreathing)} + 1.62$, $r = 0.803$. Dashed line = identity. Taken, with permission, from (338).

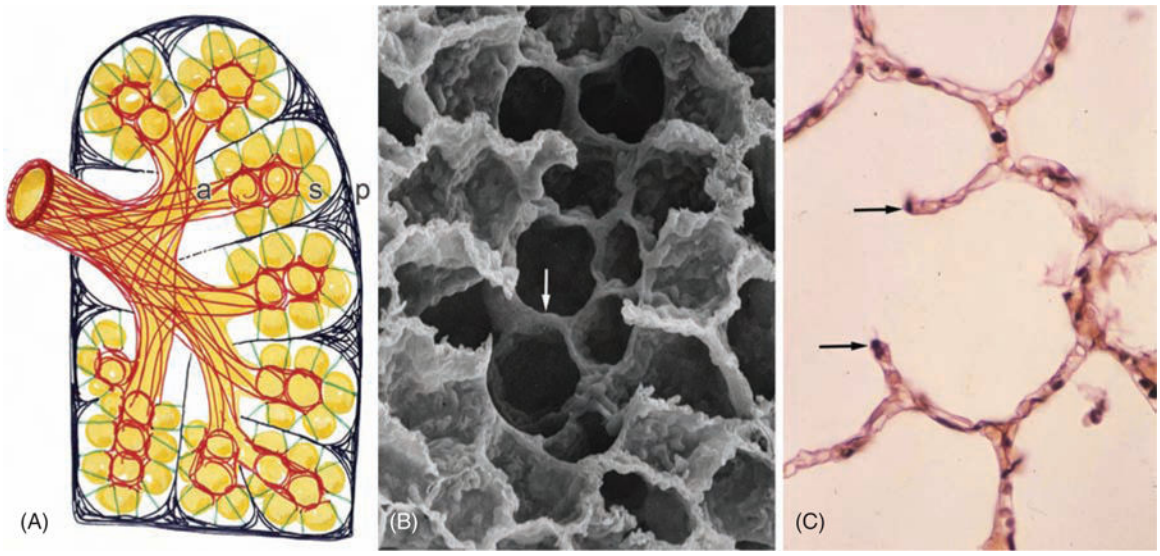

Figure 27.

Integral connectivity throughout the lung is established by (A) a fiber continuum made of axial (a, red), septal (s, green), and peripheral (p, black) fibers. (B) Scanning electron micrograph of an alveolar duct outlined by a network of axial fibers (arrow) that are seen in section (C) to be reinforced by strong fiber bundles (arrows) (compare Fig. 21). Modified, with permission, from (384).

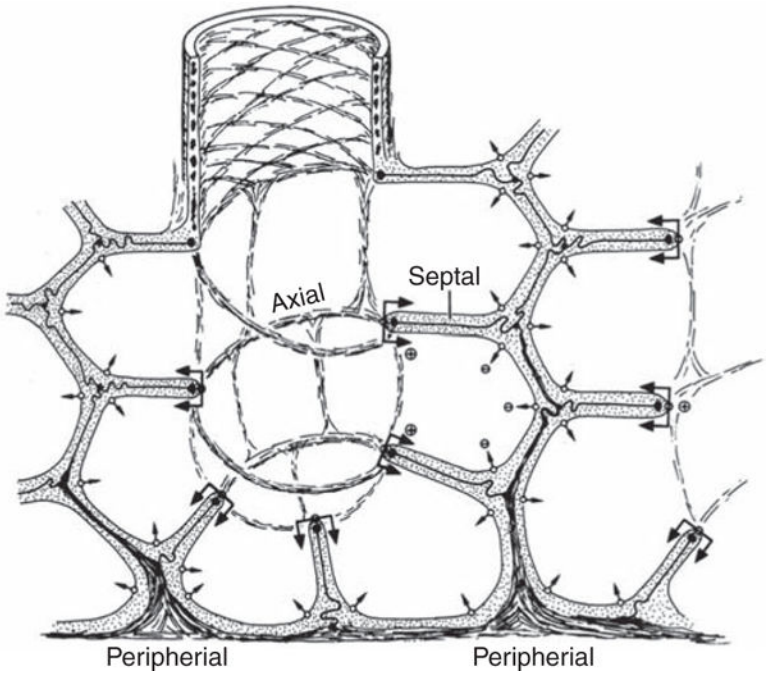

Figure 28.

Model of the disposition of axial, septal, and peripheral fibers in the acinar airway, with the effect of surface forces indicated by arrows: negative in alveoli and strongly positive on the free edge of the alveolar septum. Reprinted by permission from (376).

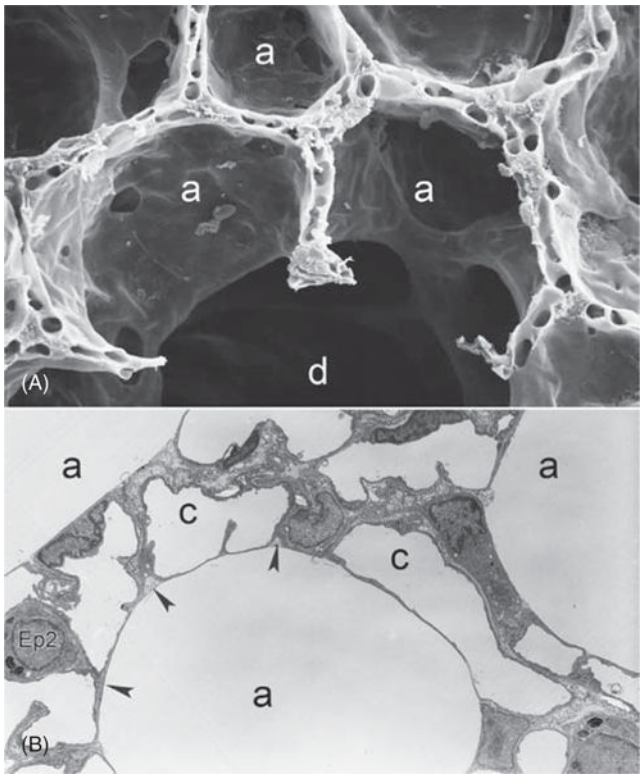

Figure 29.

(A) Scanning electron micrograph of alveoli (a) related to alveolar duct (d) in rabbit lung perfusion-fixed at an inflation level of 60% TLC. Note smooth alveolar surface. (B) Thin section of similarly prepared rat lung with empty capillaries (c) shows the pleating of the tissue barrier beneath the surface lining layer with surfactant (arrows) with the result that thick barrier portions, such as type-2 cells (Ep2) are shifted away from the surface so that thin barrier portions predominate at the free surface, resulting in a thinner diffusion barrier (398).

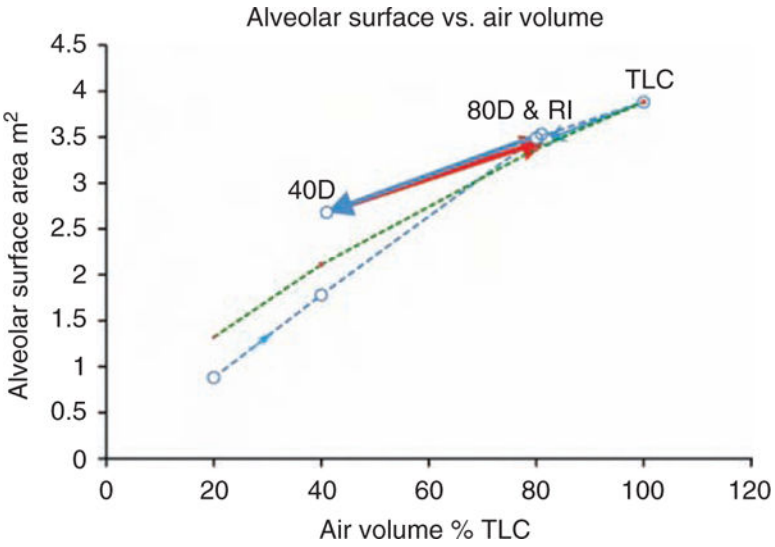

Figure 30.

Variation of alveolar surface area in perfusion-fixed rabbit lungs. Steep increase when starting from deflated lung up to TLC (broken green lines) but reduced reduction when the lung is deflated to 80% and 40% TLC (80D and 40D); reinflation (RI) from 40% to 80% TLC occurs on the deflation slope. Data taken, with permission, from (7).

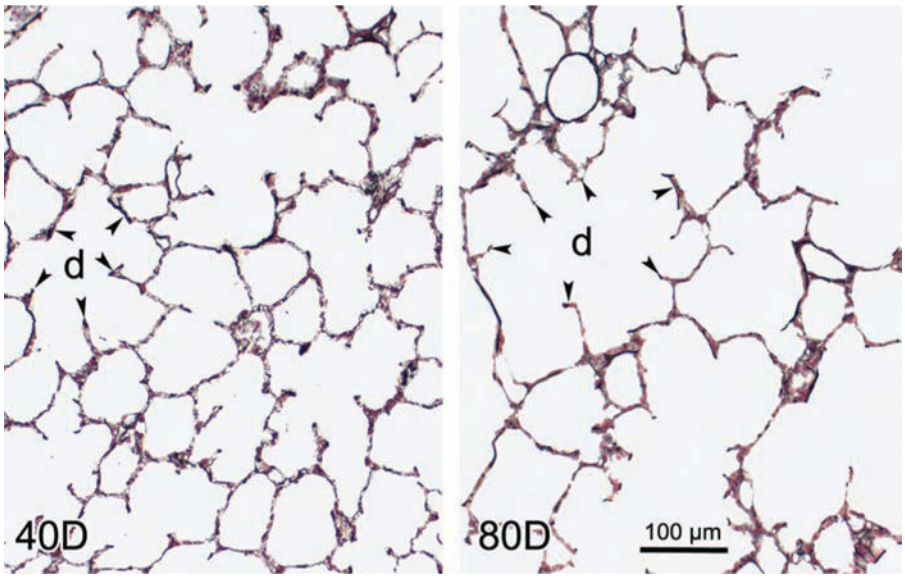

Figure 31.

Representative micrographs from the rabbit lungs deflated to 40% TLC (D40) or to 80% TLC (D80). At 80% TLC, a more or less homogeneous enlargement of air spaces was found, but predominantly involving the alveolar ducts (d) (arrows). Modified, with permission, from (210).

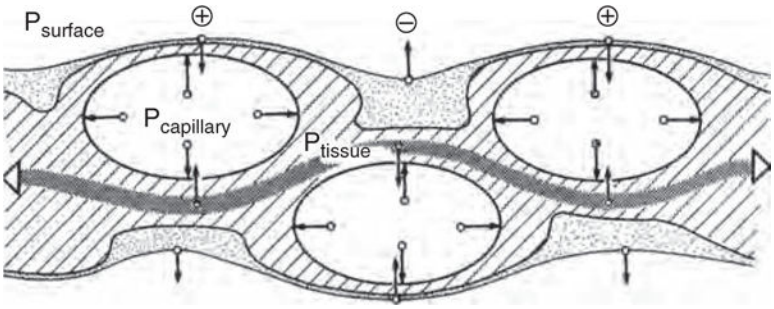

Figure 32.

Model showing the micromechanical forces of surface tension, tissue tension, and capillary distending pressure that shape the alveolar septum. Taken, with permission, from (376).

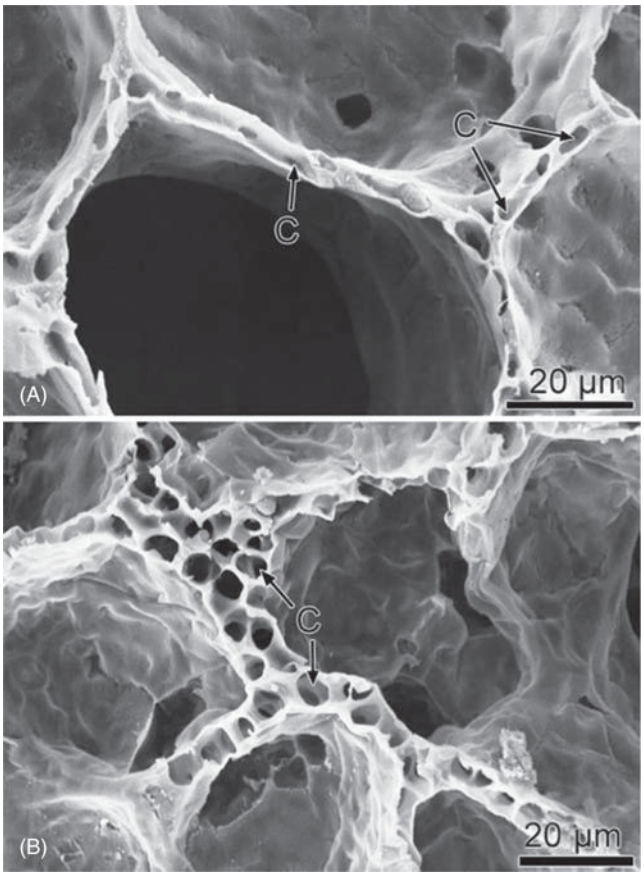

Figure 33.

Scanning electron micrographs of alveolar walls of rabbit lungs fixed under (A) zone 2 and (B) zone 3 conditions of perfusion. Note that capillaries are wide in zone 3 and slit-like in zone 2, except for “corner capillaries” at the junction of three septa, which are wide in either case. Taken, with permission, from (9).

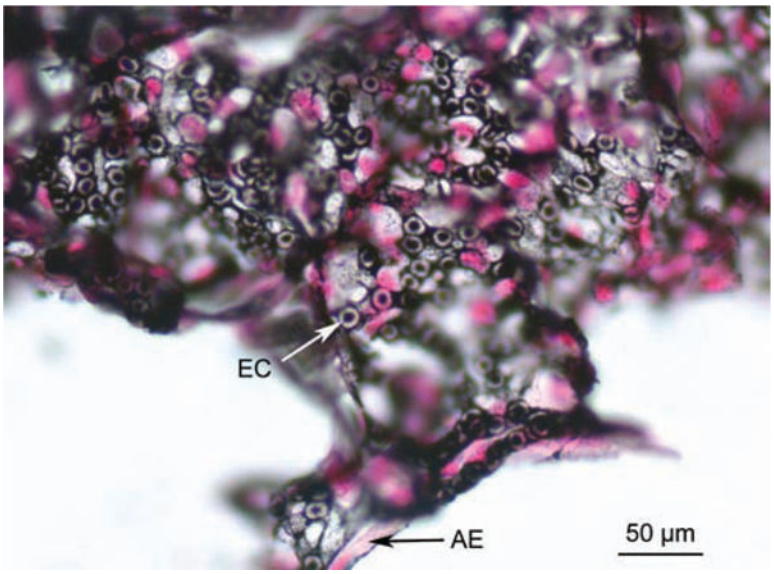

Figure 34.

Flat view of alveolar septum of rabbit lung showing the perfused capillary network with plasma marked by colloidal gold (black) and erythrocytes (EC) appearing as unstained “rings” or “bars” depending on orientation. Note that all segments have been perfused in the 2 min prior to stop of blood flow and fixation. At the bottom a strong alveolar entrance ring (AE) marks the free edge of the septum.

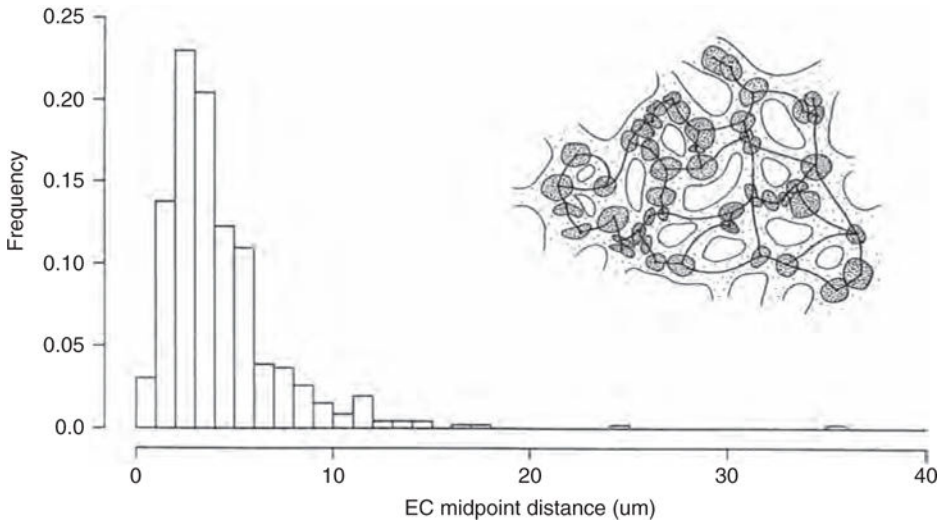

Figure 35.

Distribution of center-to-center distance between erythrocytes along the capillary path (inset) in flat views of alveolar septa in rabbit lungs fixed under controlled blood flow conditions (compare Fig. 34). Taken, with permission, from (388).

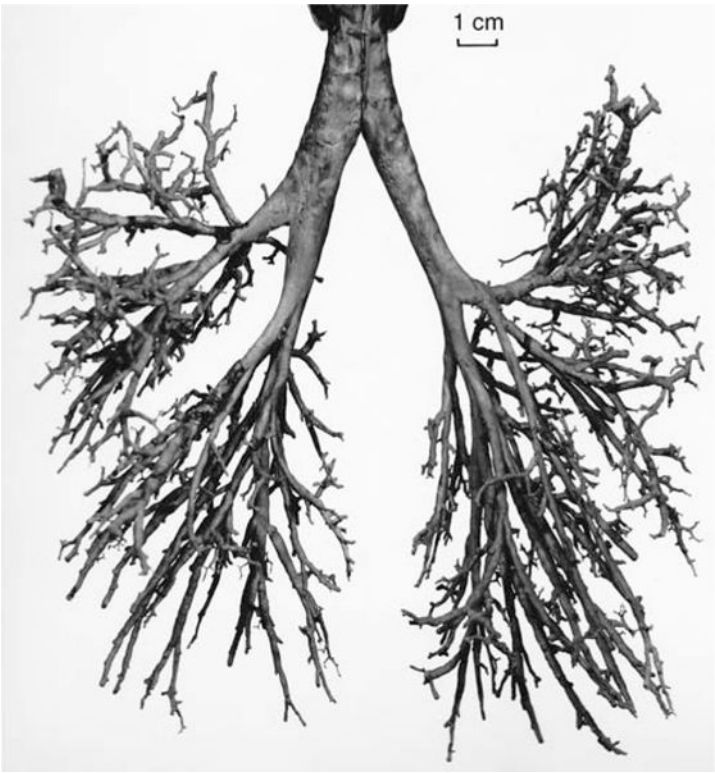

Figure 36.
Anterior view of the original plastic cast of an adult human bronchial tree used for measurements of airway dimensions in the first 10 to 15 generations. Taken, with permission, from (369,389).

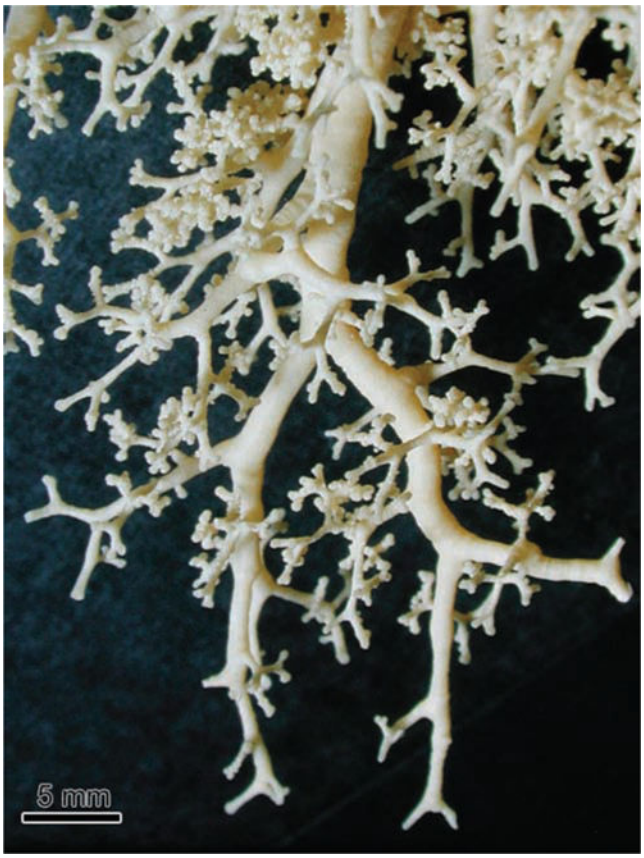

Figure 37.
Peripheral branches of airways in a contemporary human cast show a similar branching pattern as that of the more central branches shown in Figures 36 or 12.

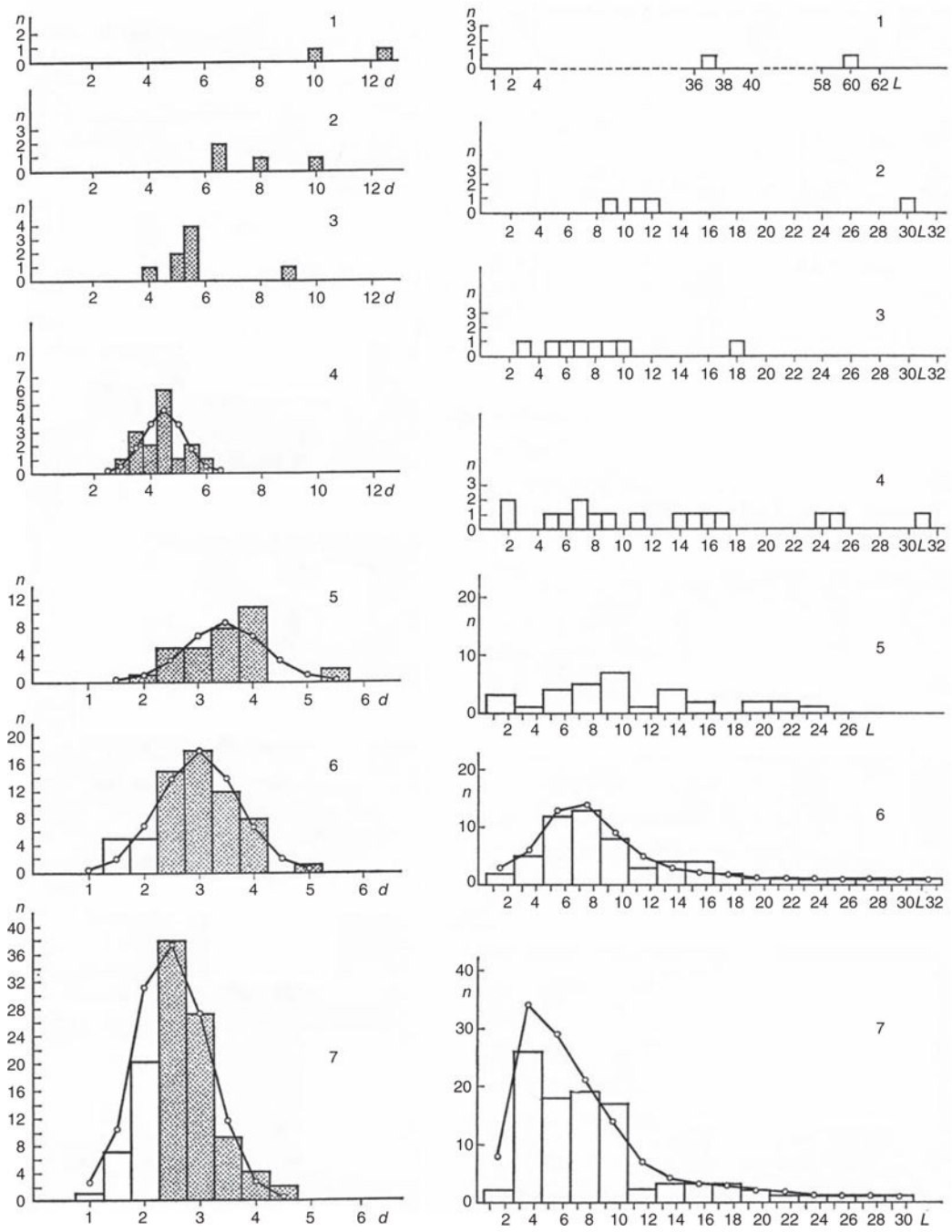

Figure 38.

Frequency distribution of the diameters (left column) and lengths (right column) of airways of the first seven generations of branching in the human lung shown in Figure 36. Taken, with permission, from (369).

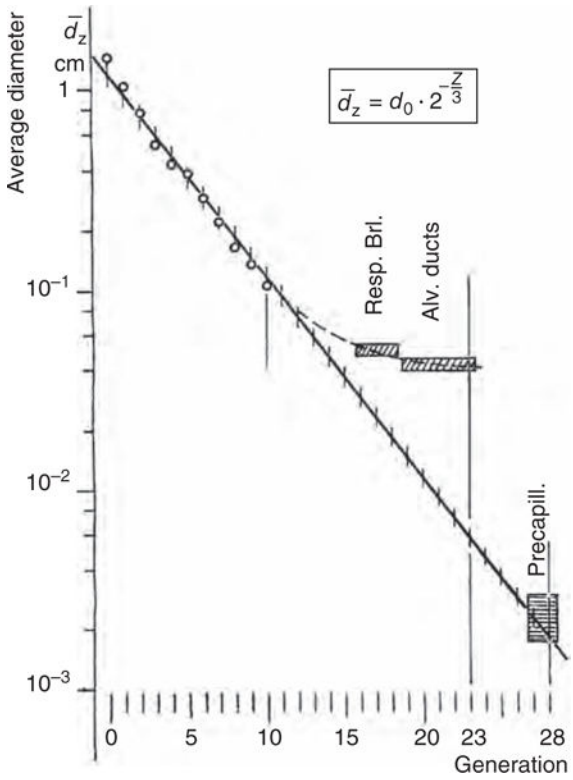

Figure 39.

Average diameter of conducting airways, respiratory bronchioles and precapillary blood vessels in the adult human lung plotted semilogarithmically as a function of the order of generation of dichotomous branching. Taken, with permission, from (389).

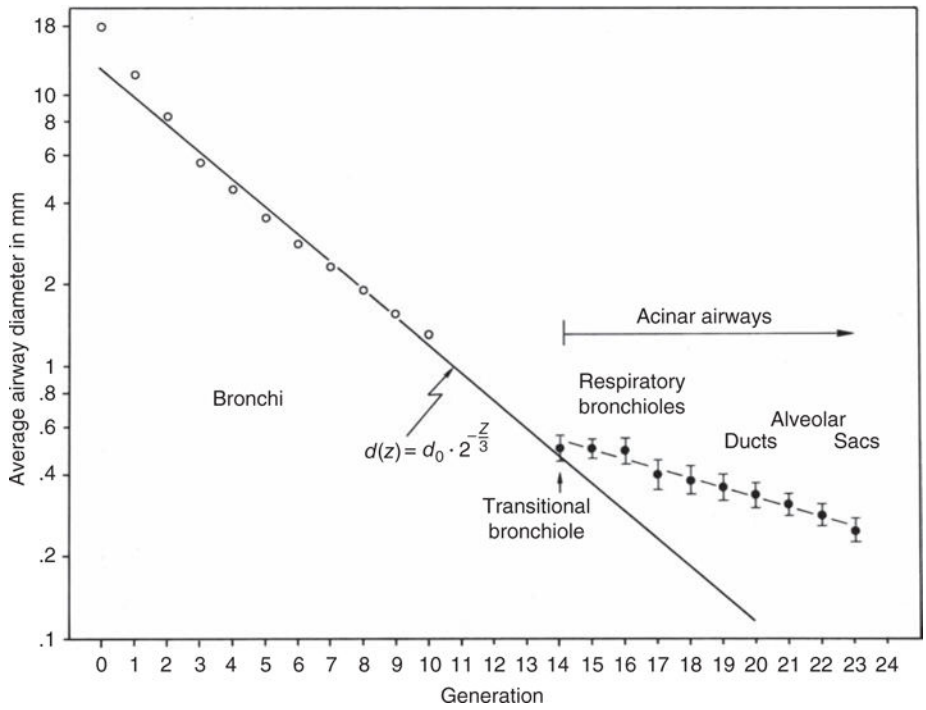

Figure 40.

Semilogarithmic plot of airway dimensions in human lung with improved dimensions of the peripheral acinar airways with transitional bronchiole in generation 14. This shows that the diameter of conducting airways is reduced by the cube root of ½ with each generation, whereas the intra-acinar airways are reduced to a lesser degree. Taken, with permission, from (126).

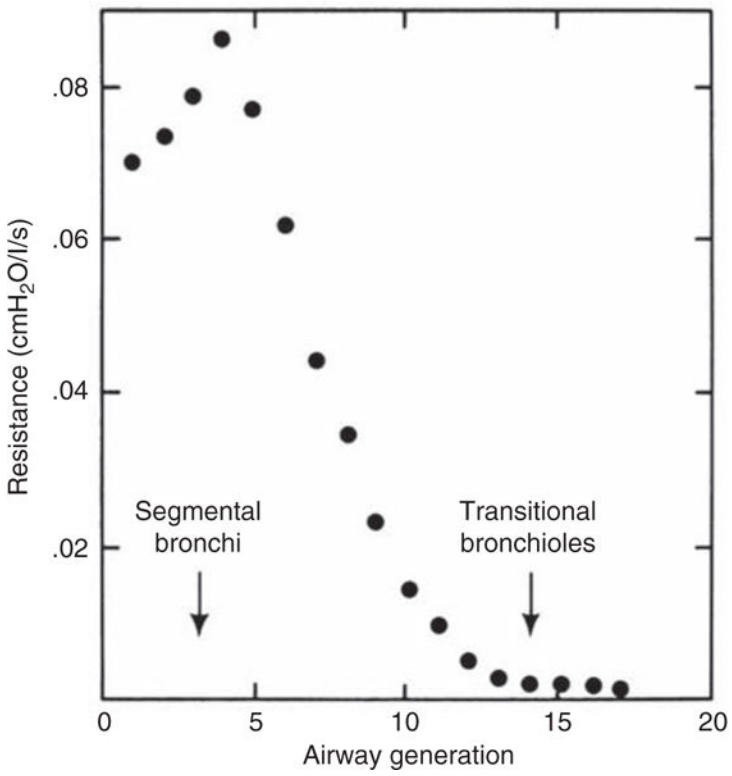

Figure 41.

Airway resistance to mass air flow is located mostly in the conducting airways and falls rapidly toward the periphery. Redrawn, with permission, after (278).

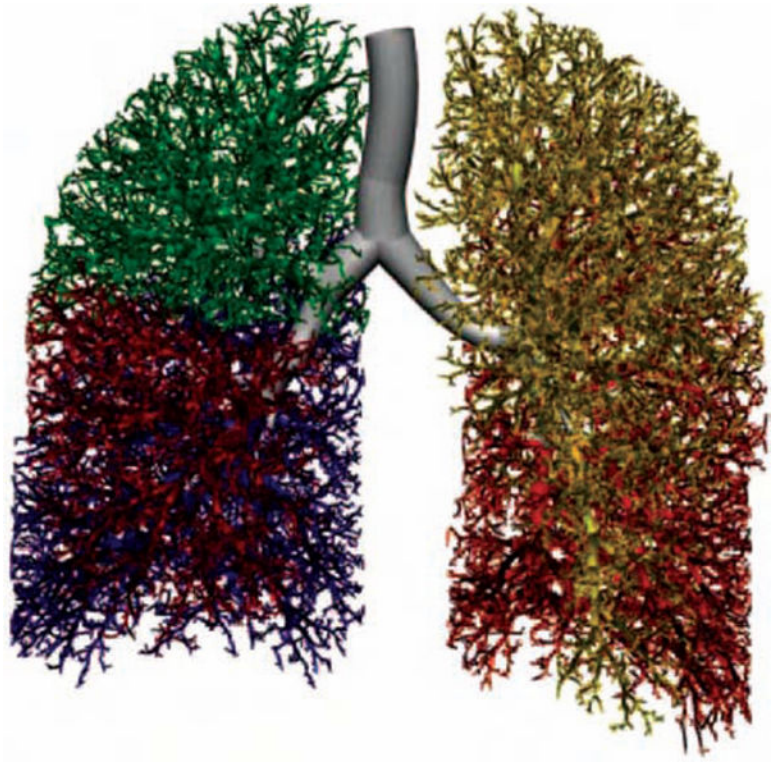

Figure 42.

Model of human airway tree derived from finite element analysis of computer-tomographic reconstructions of airways compares well with anatomical lung casts such as in Figures 12 and 37. Taken, with permission, from (342).

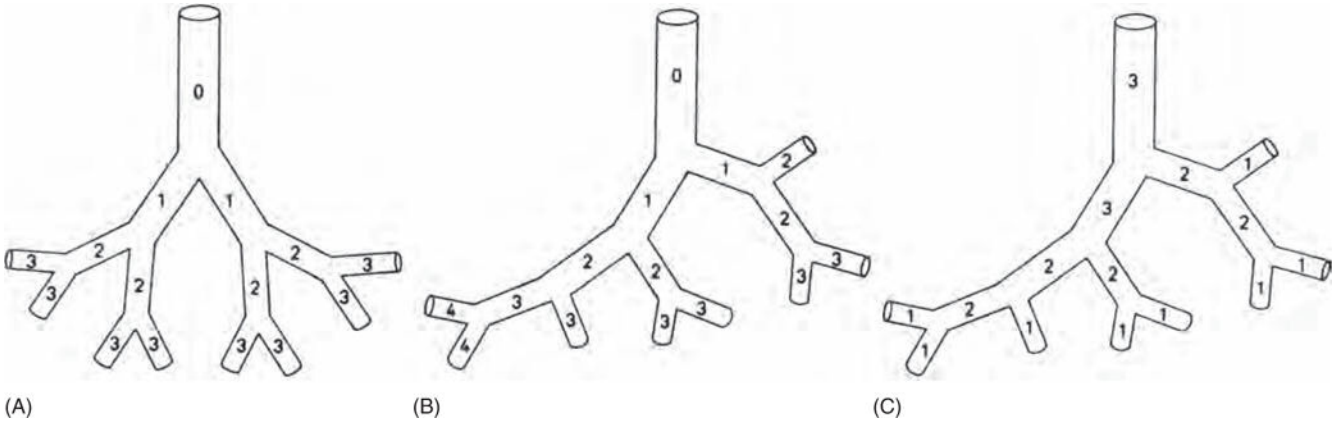

Figure 43.

Patterns of airway branching by (A) regular (symmetric) dichotomy, (B) irregular dichotomy numbered by “generations down,” (C) irregular dichotomy numbered by “orders up.”

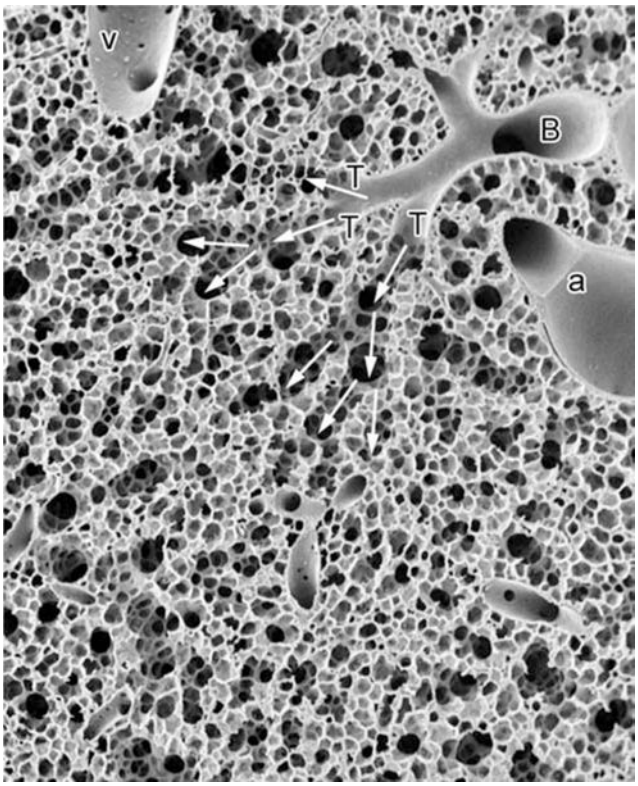

Figure 44.

Scanning electron micrograph of vascular perfusion-fixed rabbit lung shows branching of small peripheral bronchiole (B) into transitional bronchioles (T), from where the airways continue into respiratory bronchioles and alveolar ducts (arrows). Note the location of the pulmonary artery (a) and vein (v). Modified, with permission, after (376).

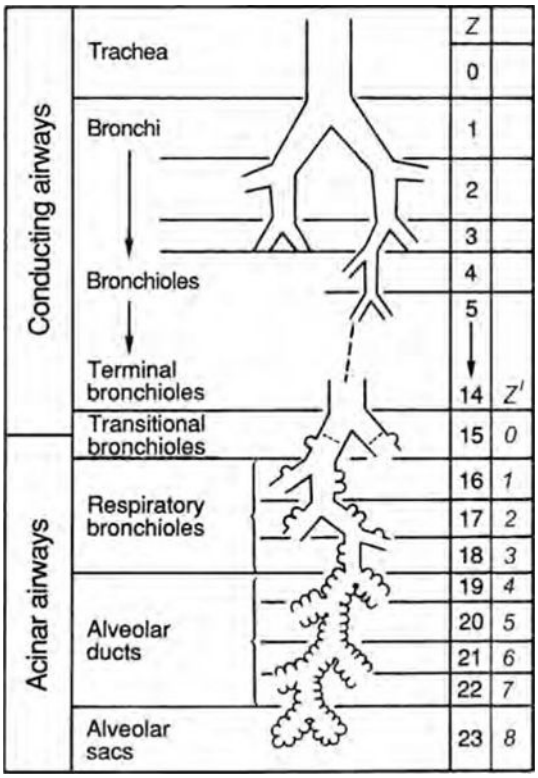

Figure 45.

Hierarchical model of the human airway tree from conducting to acinar airways. The transition from conducting to acinar airways occurs at generation $Z = 15$, on average, with the occurrence of the first alveoli. Z' is the generation of acinar airways.

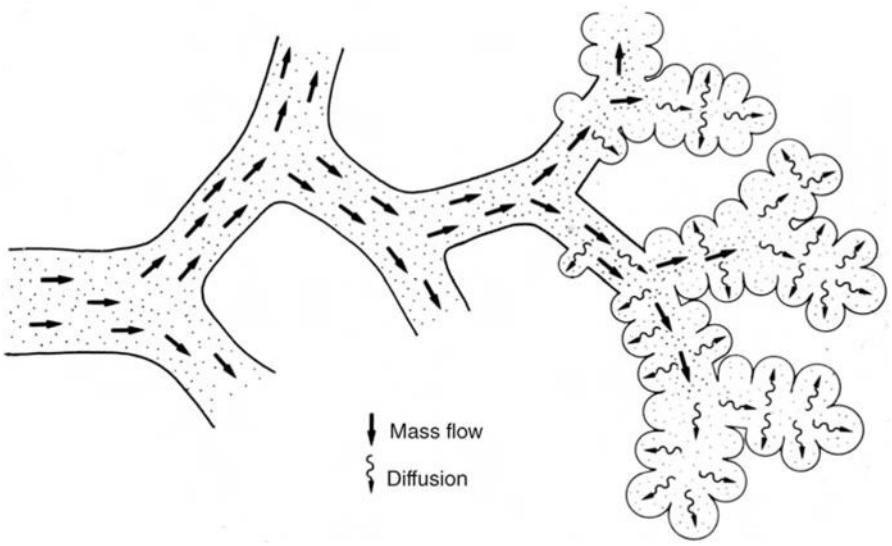

Figure 46.
Gradual transition of mass air flow to oxygen diffusion in the peripheral airways.

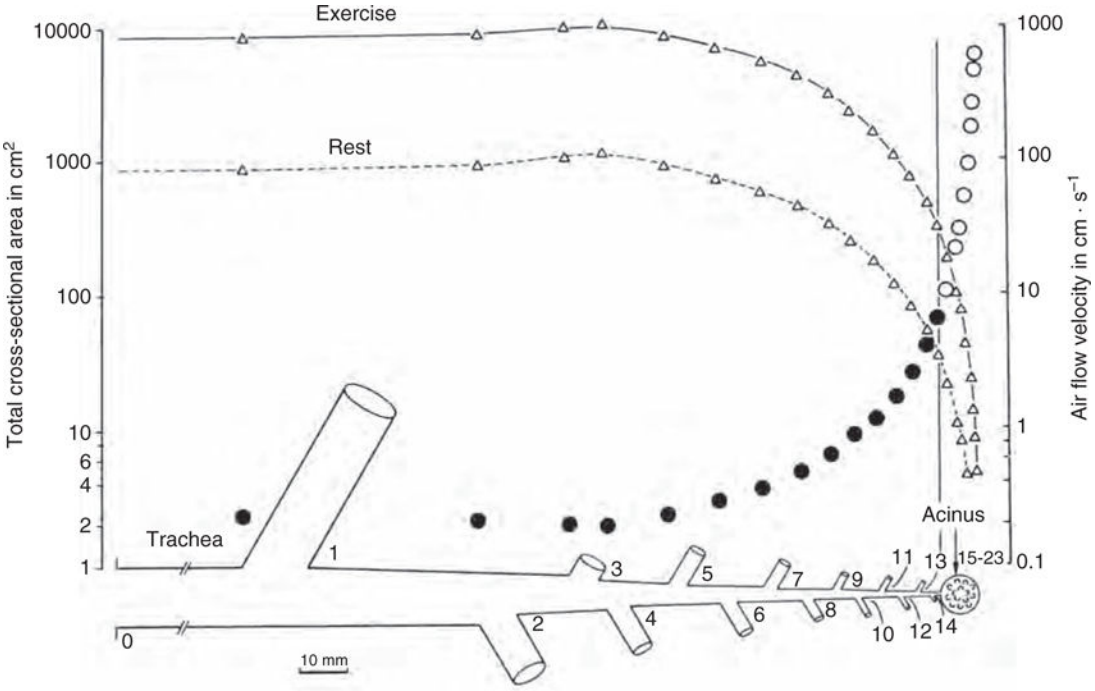

Figure 47.

Total cross-sectional area of all airways in each generation of the human lung is plotted against path length from trachea to acinar airways, showing the progressive increase of total airway cross-sectional area per generation and the resulting airflow velocity at rest and in exercise.

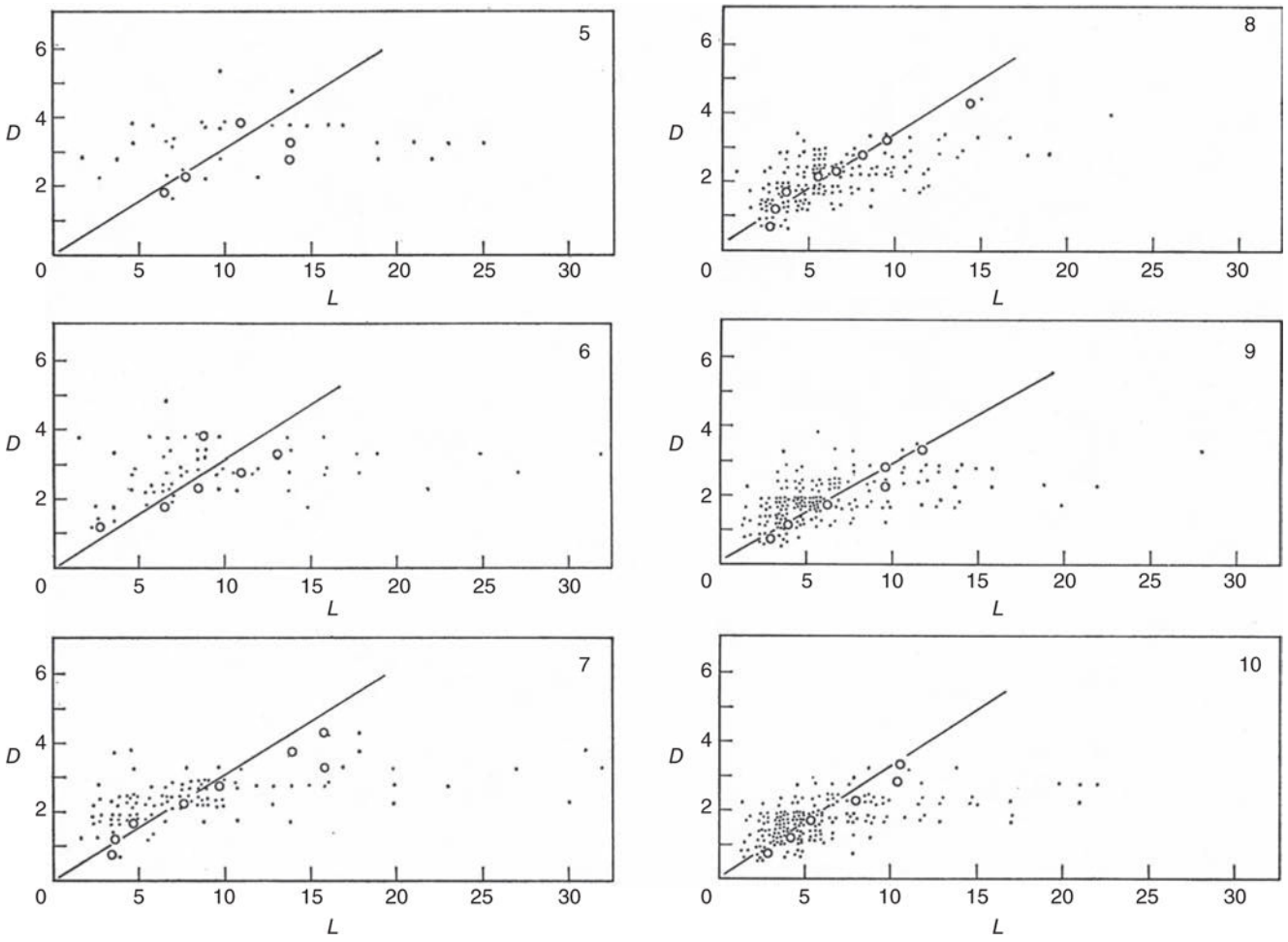

Figure 48.

Dispersion diagram of diameter and length of airway segments in the generations 5 to 10 in the human lung. Slope of diagonal corresponds to average diameter-to-length ratio in each generation which is similar in all generations. Taken, with permission, from (369).

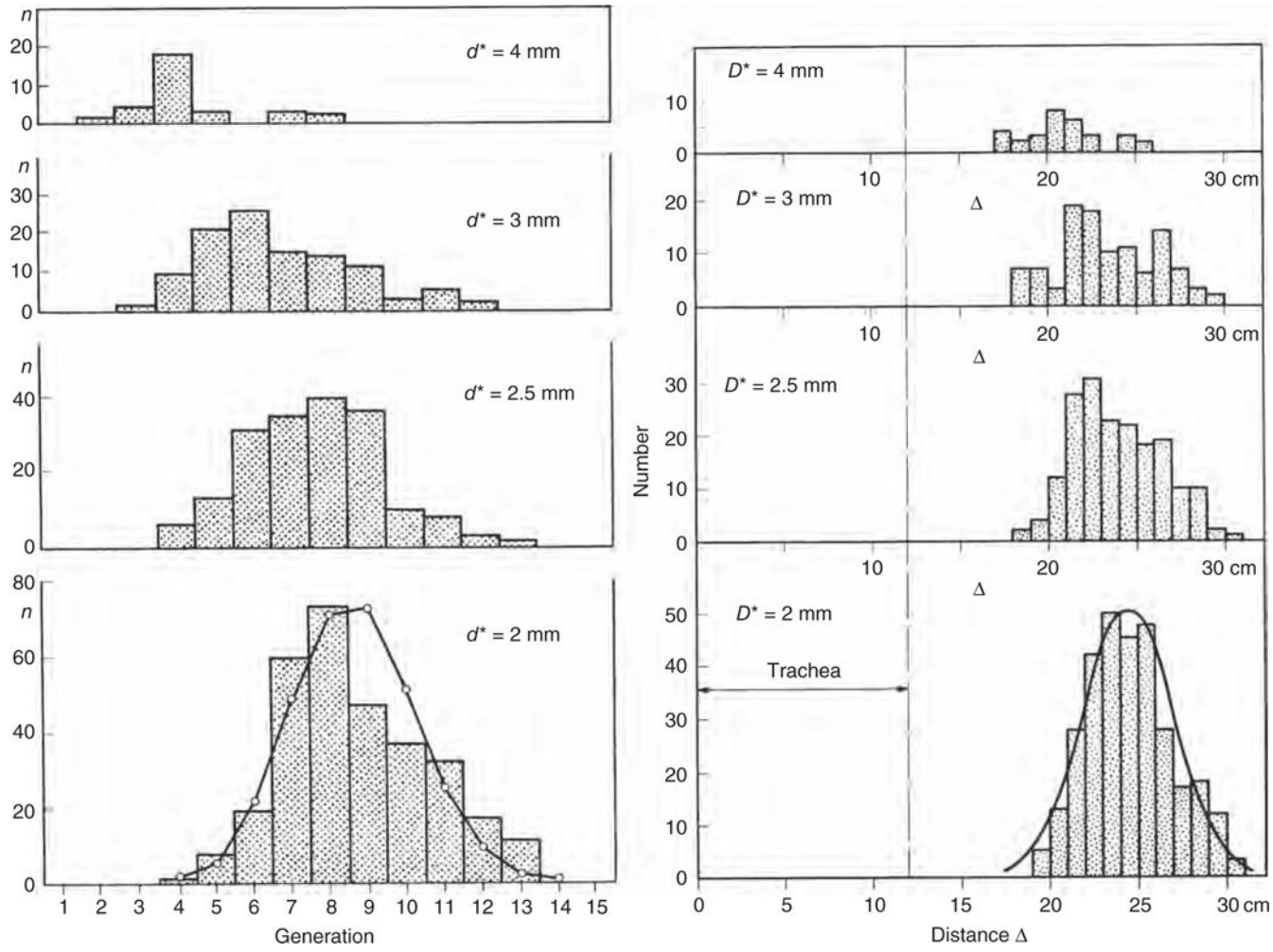

Figure 49.

Distribution of airways of diameter *d** per generations (left column) and at distance Δ from the origin of the trachea (right column). Curves for 2 mm airways are a binomial distribution with respect to generations and a normal distribution with respect to distance. Taken, with permission, from (369).

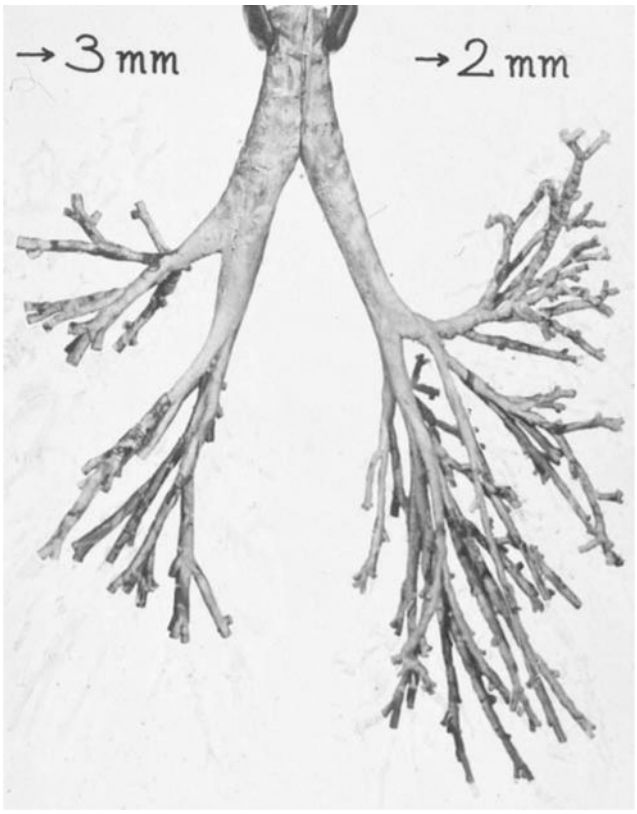

Figure 50.
View of the cast in Figure 36 showing termination at branches with diameters 3 and 2 mm, respectively. Taken, with permission, from (369).

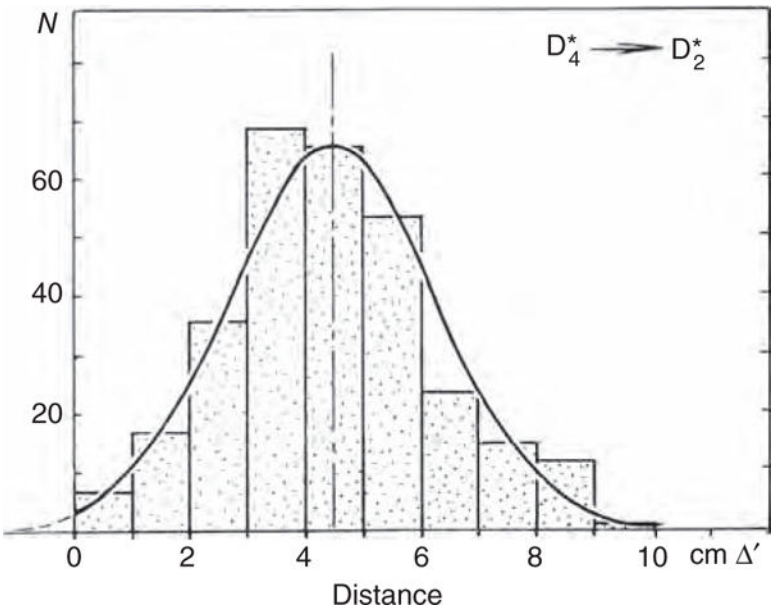

Figure 51.

Distribution of distances D' of branches of diameter $d^* = 2$ mm from their parent branches of diameter $d^* = 4$ mm. Taken, with permission, from (369).

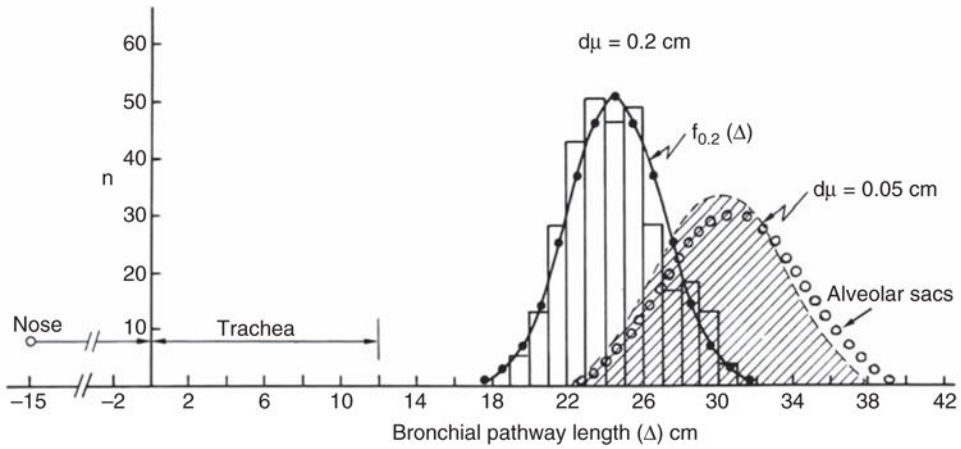

Figure 52.

Frequency distribution of airways of diameters (*d*μ) 0.2 and 0.05 cm with respect to bronchial path length from the tracheal origin. Open circles mark the position of the terminal airways, the alveolar sacs of the acinar airways. Modified, with permission, after (376).

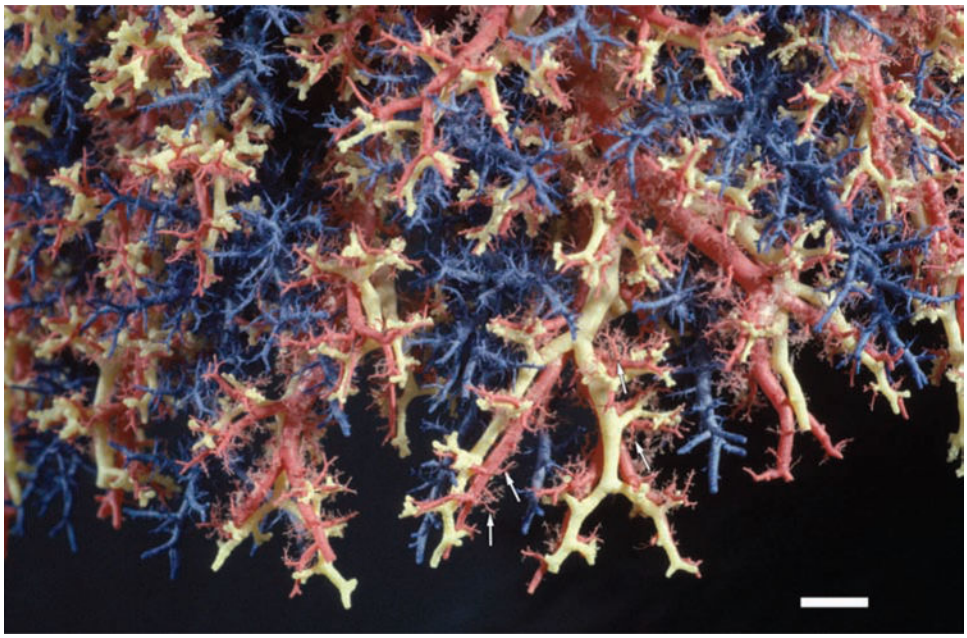

Figure 53.

Detail view of the spatial relations of airways (yellow), pulmonary arteries (red), and pulmonary veins (blue) in a cast of a human lung similar to that in Figure 12. The main tract of the arteries follow closely the airway both in terms of branching pattern and diameter; they thus determine the lung architecture in terms of bronchoarterial units. In contrast, the pulmonary veins take an intermediary position between the bronchoarterial units thus collecting blood from several adjacent units. Toward the periphery pulmonary arteries branch more frequently than the airways and thus form “supernumerary” branches (arrows) that lead blood into gas-exchange units. Scale bar 5 mm.

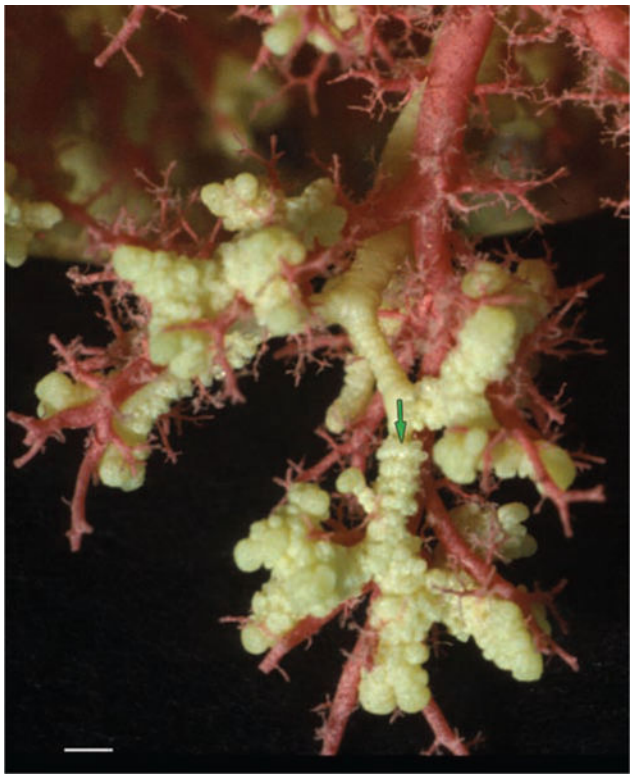

Figure 54.

Periphery of plastic cast of human airways and arteries where the airway cast extends into the first few generations of the acinus also filling alveoli. The green arrow marks the transitional bronchiole. Note that the pulmonary artery branches (red) branch along with the airways even into the acinus with many “supernumerary” to feed alveolar capillary networks (compare Fig. 14). Scale bar 1 mm.

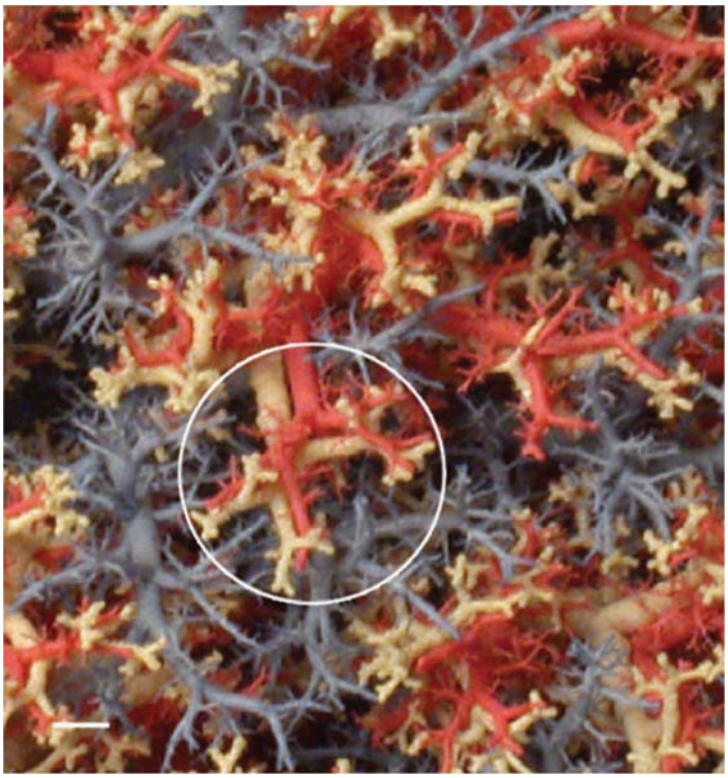

Figure 55.
Plastic cast of human lung airways and vasculature seen from the pleura with bronchoarterial units (circle) surrounded by tufts of pulmonary veins showing the mosaic architecture of peripheral respiratory units. Scale bar 5 mm.

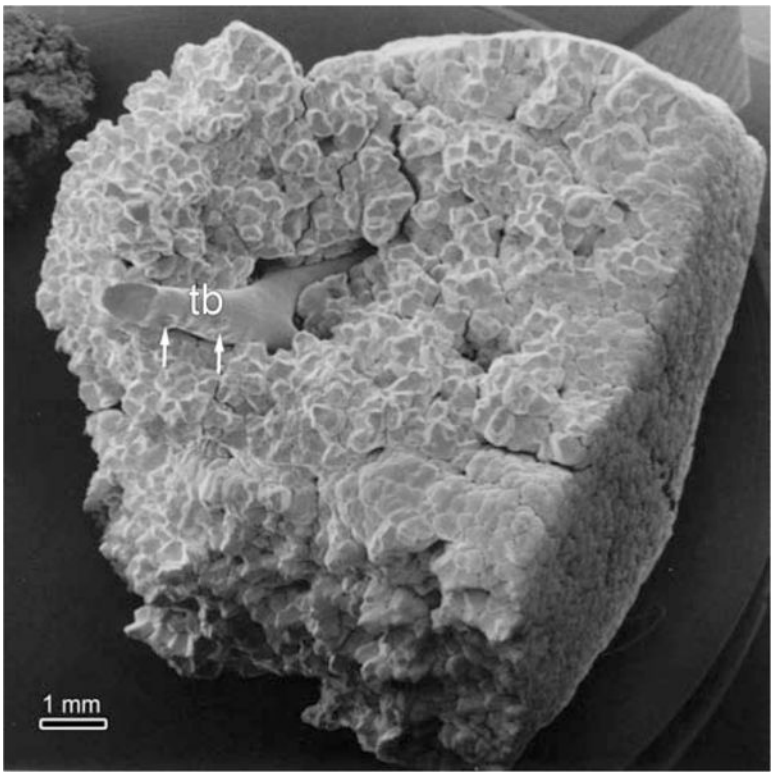

Figure 56.
Silicon rubber cast of human acinus beginning with the transitional bronchiole (tb) where the first alveoli appear (arrows). Taken, with permission, from (126).

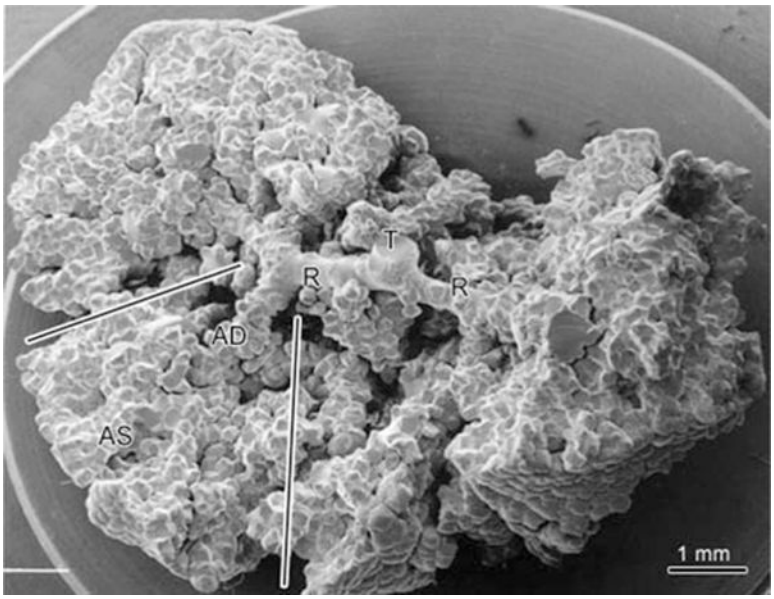

Figure 57.

Scanning electron micrograph of an acinus of a human lung where some of the alveolar ducts and sacs were trimmed off to show the internal organization with respiratory bronchioles (R) following on the transitional bronchiole (T) leading to alveolar ducts (AD) and sacs (AS). The two straight lines delimit a 1/8 subacinus. Modified taken, with permission, from (126).

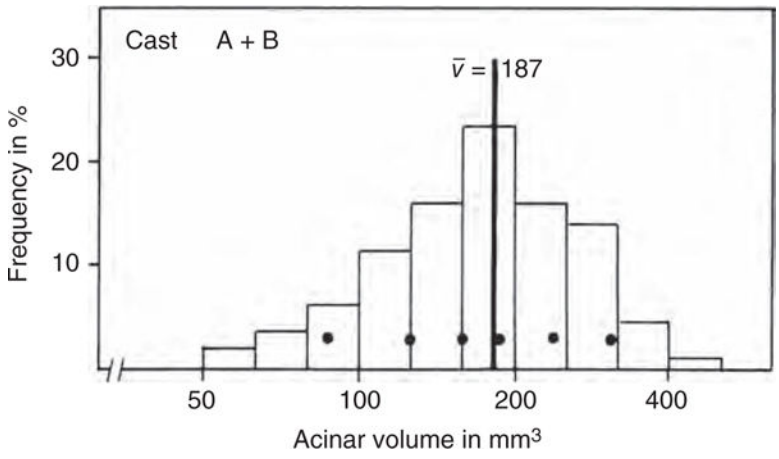

Figure 58.

Frequency distribution of acinar volume in human lungs. Taken, with permission, from (126).

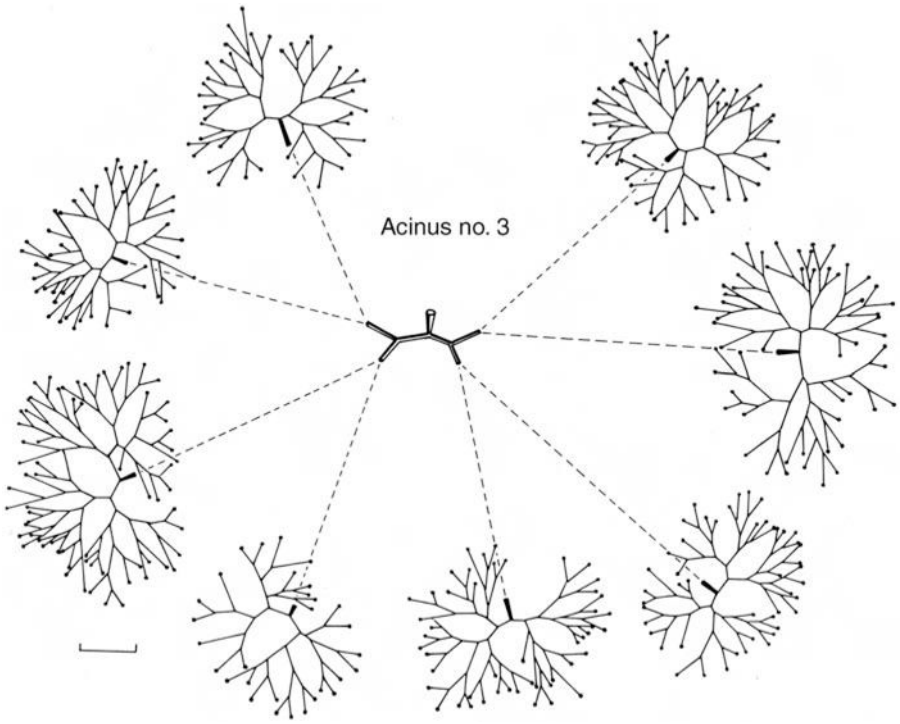

Figure 59.

Branching pattern of acinar airways in average size human acinus. The first three generations are respiratory bronchioles with incomplete alveolar sleeve. The 1/8 subacini that follow on these respiratory bronchioles represent parts of the acinus where the entire airway surface is occupied by alveoli. Taken, with permission, from (126).

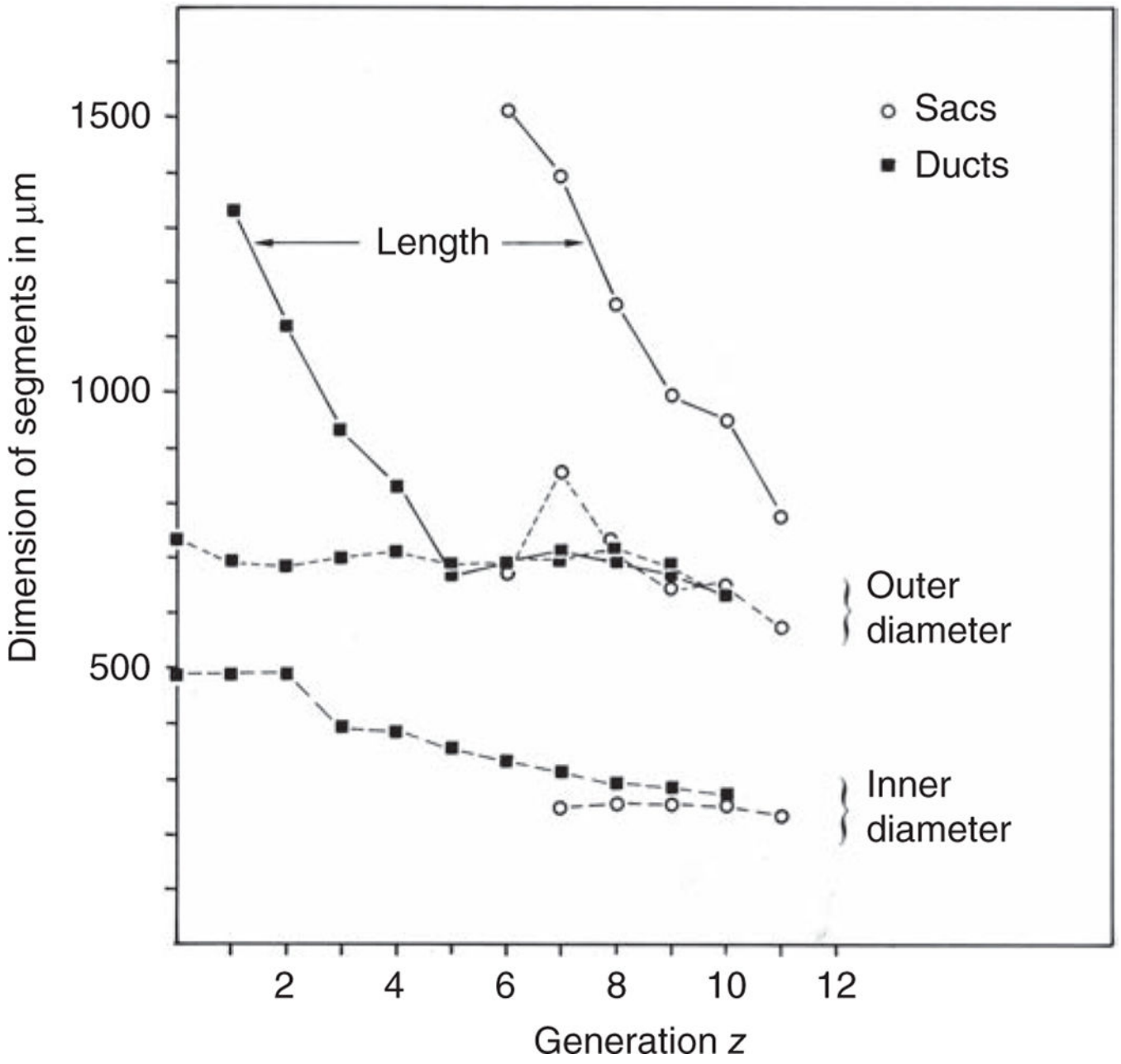

Figure 60.
Change of length and diameters of airway segments with progressive generations of branching. Taken, with permission, from (126).

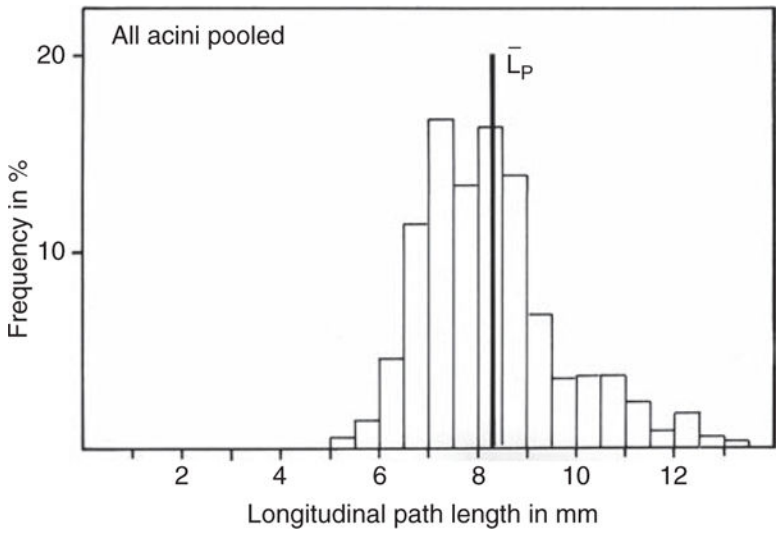

Figure 61.

Distribution of longitudinal path length from transitional bronchiole to terminal sacs. Taken, with permission, from (126).

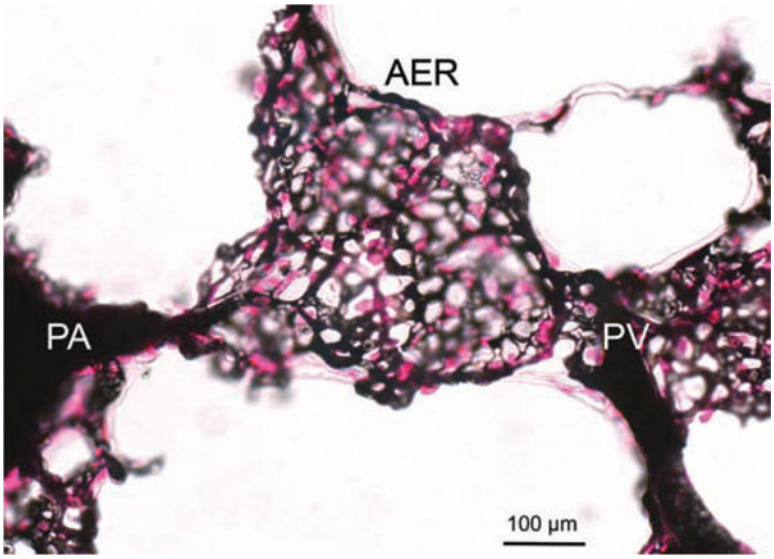

Figure 62.

Alveolar capillary network unit corresponding to an alveolar wall segment with connecting arteriole (PA) and venule (PV) extending to alveolar entrance ring (AER).

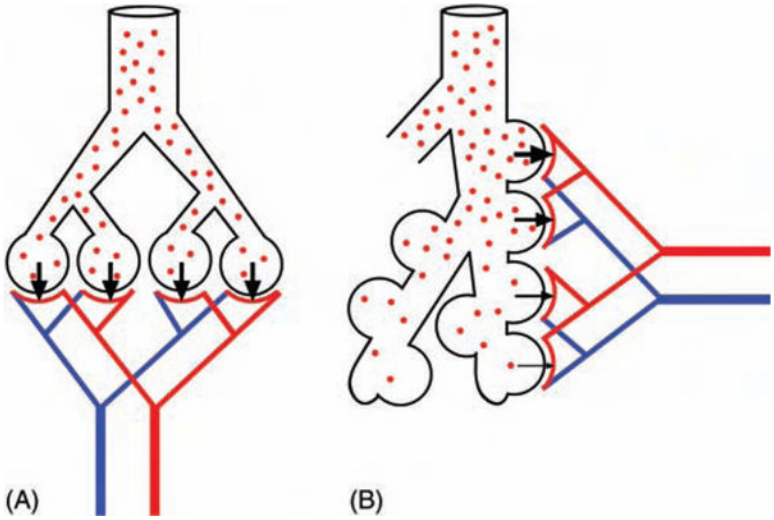

Figure 63.

Models of ventilation-perfusion relationship in the mammalian pulmonary gas exchanger. (A) Parallel ventilation-parallel perfusion. (B) Serial ventilation-parallel perfusion. Taken, with permission, from (310).

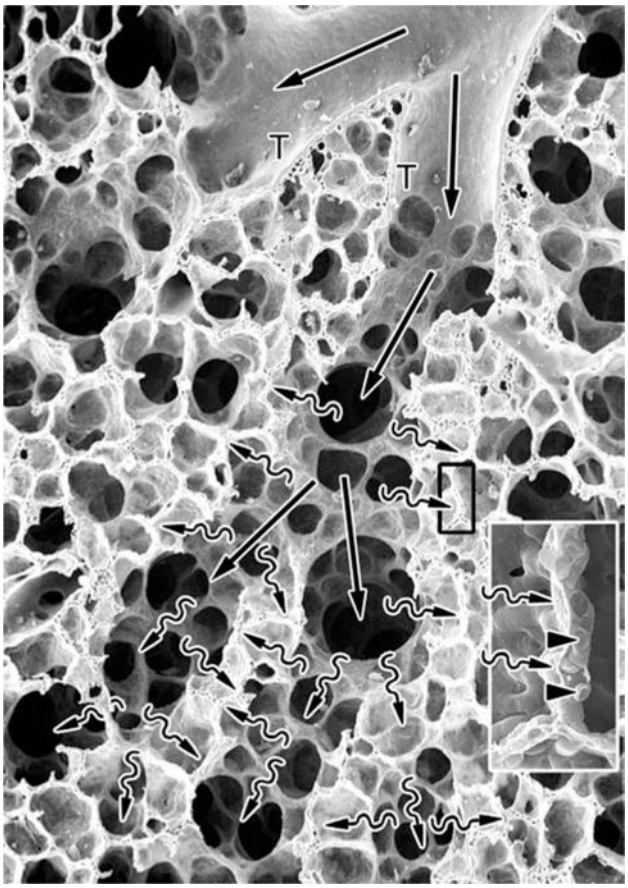

Figure 64.

Central part of the acinar airways beginning with transitional bronchiole (T) and leading into the branched alveolar ducts. On inspiration air flows in by convection (straight arrows), but as flow velocity falls diffusion of O_2 (wiggly arrows) becomes the dominant mechanism for bringing O_2 to the gas-exchange surface. All along acinar airways O_2 is absorbed by the capillary blood in the septa (inset, arrowheads). Taken, with permission, from (266).

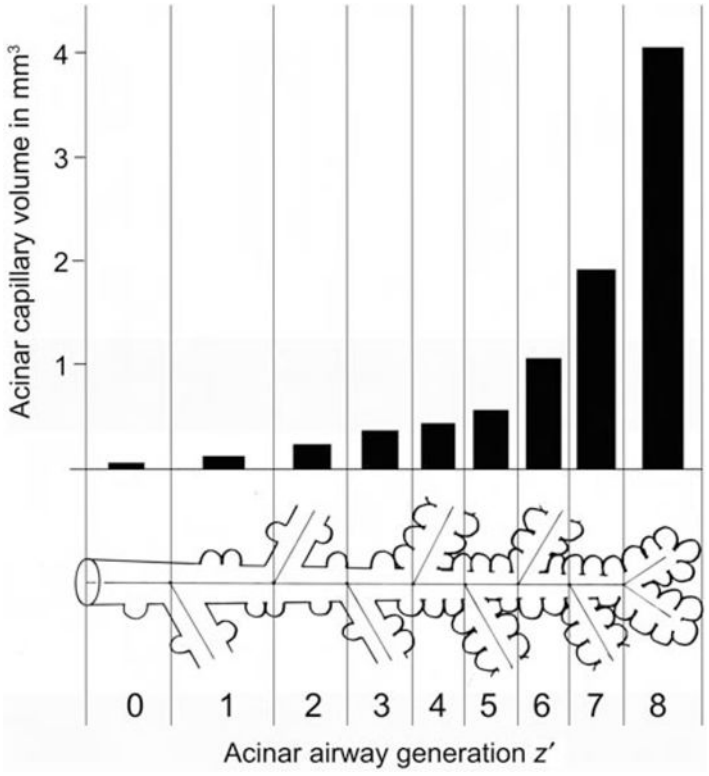

Figure 65.

Typical path model of human pulmonary acinus showing the distribution of capillary volume per acinar airway generations of a symmetric branching pattern. Gas-exchange surface shows the same distribution pattern due to doubling the number of segments with each generation.

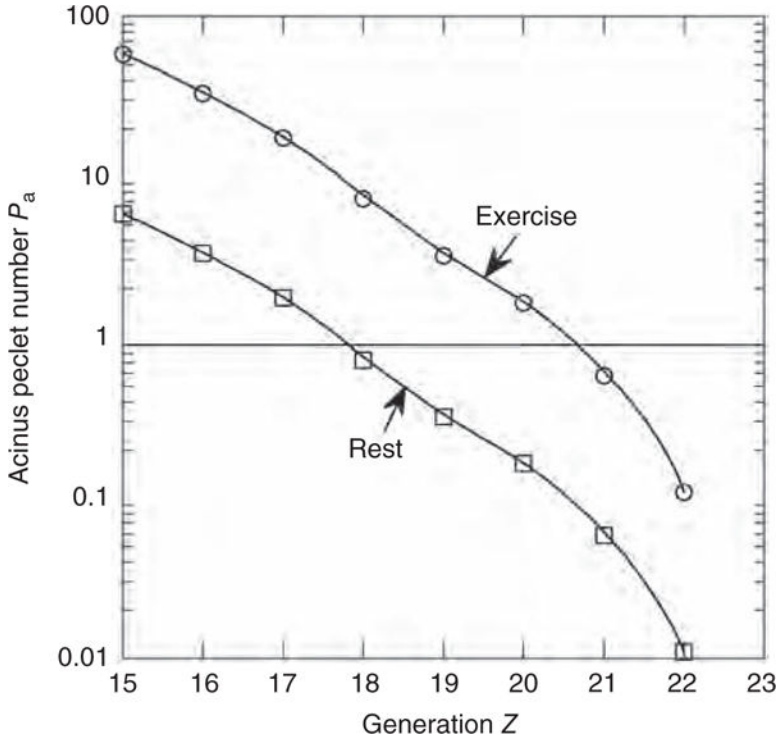

Figure 66.

Variation of the human acinus Peclet number at exercise and at rest as a function of the depth in the acinar pathway. One observes a large shift between rest and exercise. The transition from convection to diffusion is moved from generation 18 to 21. Taken, with permission, from (310).

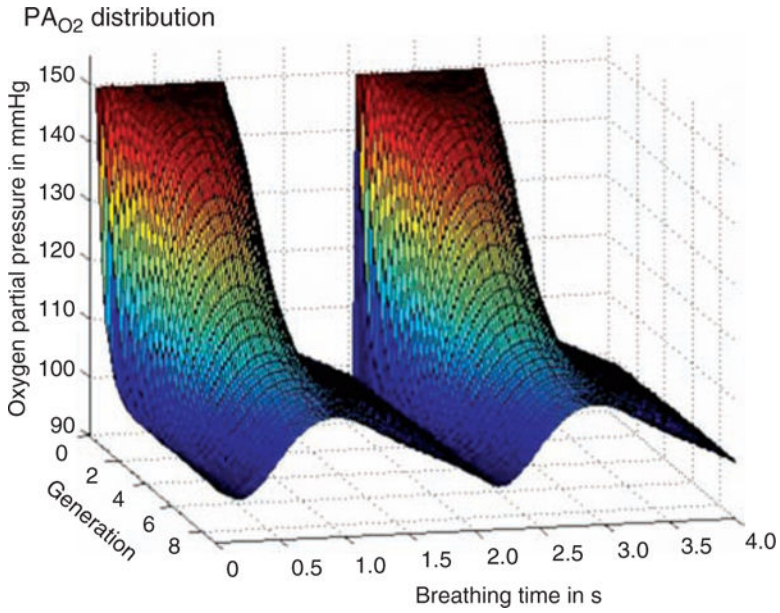

Figure 67.

Spatiotemporal distribution of the local partial pressure of oxygen $P(x,t)$, as a function of the generation (the integrative permeability is taken equal to 3.5 m/s). The time $t = 0$ corresponds to the beginning of inspiration. Note that the pressure increases to reach the value PIO_2 only after a delay corresponding to the time of flight of air from the mouth to the acinus entrance (located at the rear of the figure). Taken, with permission, from (98).

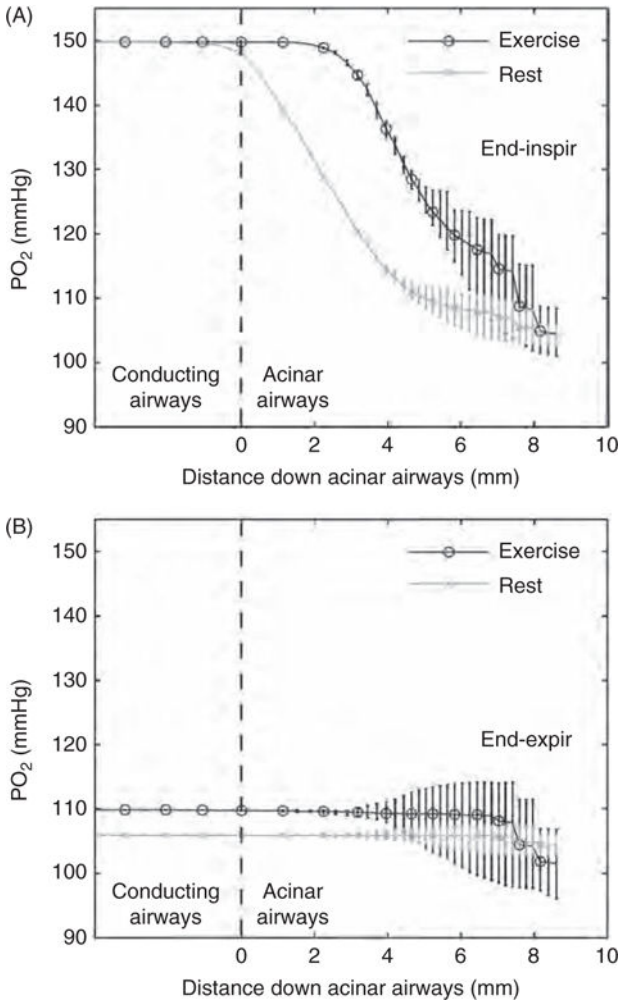

Figure 68.

Spatial variation in alveolar PO_2 down the acinar airway tree at end inspiration (A) and end expiration (B) for rest and moderate exercise conditions. Error bars show maximum and minimum values at different acinar path lengths. Taken, with permission, from (336).

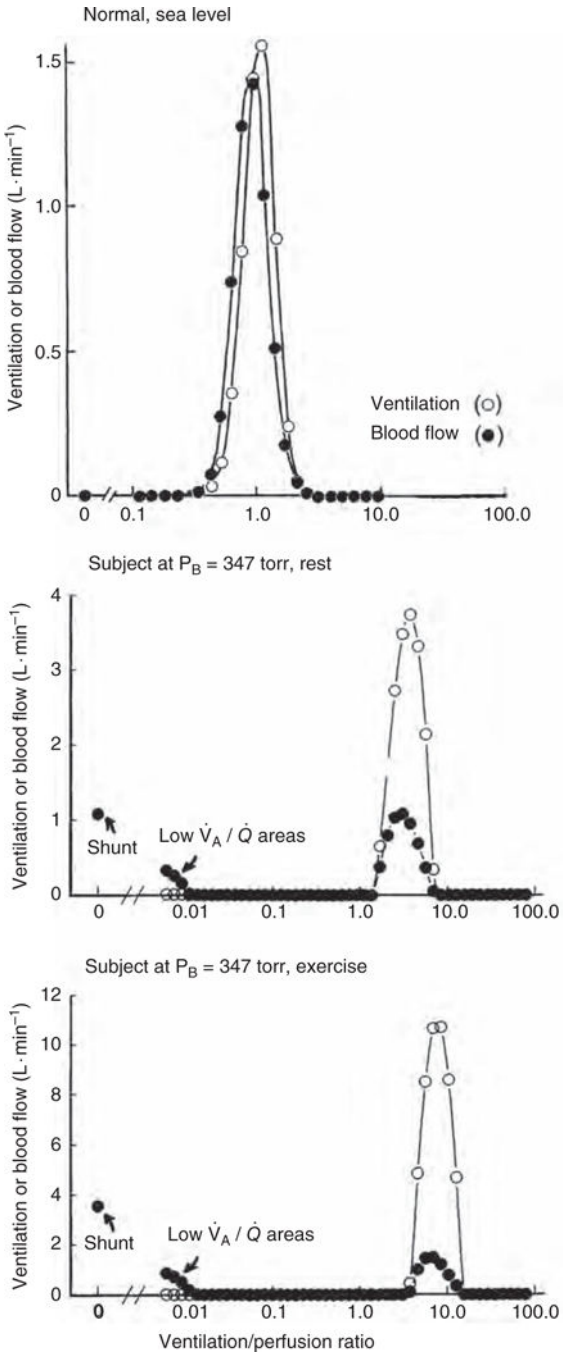

Figure 69.

Normal ventilation/perfusion $\left(\dot{V}_A/\dot{Q}\right)$ ratio distribution in a healthy subject at sea level (*upper*), and abnormal distribution in a subject who developed pulmonary edema at simulated high altitude (*middle and lower*). In the latter subject at rest, there is a 15% shunt and an additional 10% of cardiac output perfusing areas of low $\dot{V}_A/\dot{Q}$ (*middle*). Upon exercise, shunt increased to 29%, with 17% of the cardiac output perfusing low $\dot{V}_A/\dot{Q}$ areas (*lower*). Taken, with permission, from (170,195).

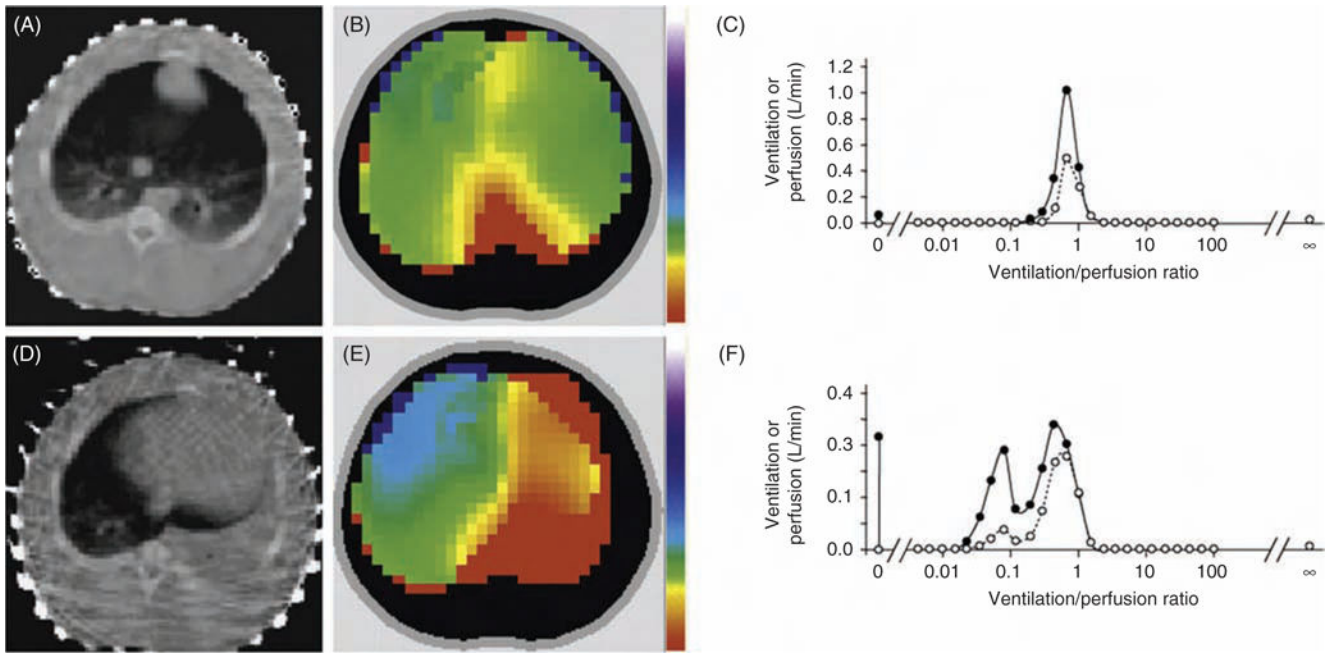

Figure 70.

Ventilation/perfusion $\left(\dot{V}_A/\dot{Q}\right)$ maps and distribution of ventilation and perfusion to different $\dot{V}_A/\dot{Q}$ compartments as derived from electrical impedance tomography. On the color scale red indicates shunt, green indicates $\dot{V}_A/\dot{Q}=1.0$, and white indicate dead space ventilation. (A–C) From a mechanically ventilated pig with normal lungs; (D–F) from the same animal after induction of atelectasis of the left lung. Taken, with permission, from Peterssen and Glenny (280) based on data of Costa et al. (56).

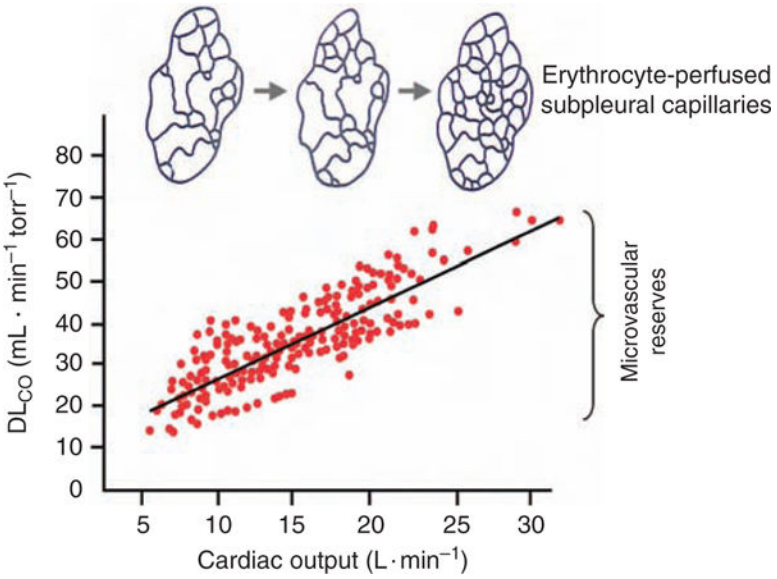

Figure 71.

Anatomical and functional microvascular recruitment of subpleural alveolar capillaries. *Upper*: Anatomical recruitment in canine lung is observed by *in vivo* videomicroscopy. The number of subpleural alveolar capillaries perfused by erythrocytes increases progressively with increasing pulmonary perfusion or vascular pressure (267). *Lower*: Functional recruitment of DL_{CO} with respect to cardiac output in healthy human subjects from rest to peak exercise indicates the utilization of microvascular reserves for gas exchange. Adapted, with permission, from (170).

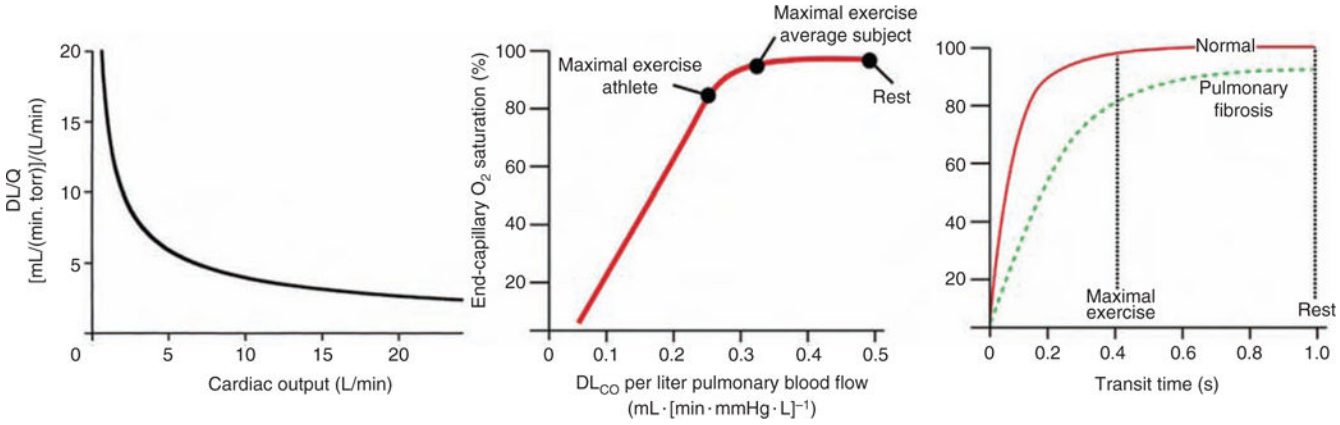

Figure 72.

Diffusion-perfusion $(\mathrm{DL}/\dot{Q})$ ratio. *Left*: The $\mathrm{DL}/\dot{Q}$ ratio normally declines as cardiac output increases from rest to exercise. *Middle:* Relationship between end-capillary blood O_2 saturation ($Sc'O_2$) and $\mathrm{DL}/\dot{Q}$. The exercise-related decline in $\mathrm{DL}/\dot{Q}$ does not alter $Sc'O_2$ in average subjects but may fall below a critical threshold in athletes who reach a higher maximal cardiac output, causing end $Sc'O_2$ to fall. *Right:* The magnitude and distribution of $\mathrm{DL}/\dot{Q}$ determine the average alveolar-capillary transit time and $Sc'O_2$, shown for a normal subject and a subject with pulmonary fibrosis. Intersections of the vertical dashed lines with the curves indicate the predicted $Sc'O_2$ at rest and maximal exercise. In pulmonary fibrosis, alveolar capillary obliteration causes $Sc'O_2$ to be lower at any given exercise intensity. In addition, $Sc'O_2$ is lower at a given mean transit time due to uneven distribution of $\mathrm{DL}/\dot{Q}$ ratio among the remaining capillaries. Adapted, with permission, from (152) and (170).

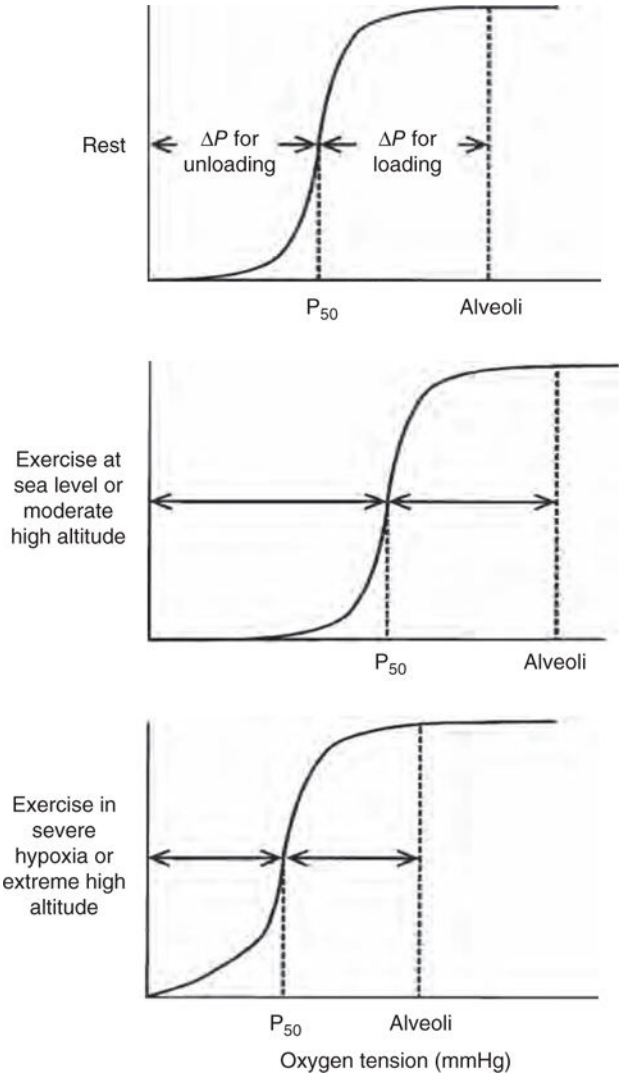

Figure 73.

Schematic diagram illustrates active regulation of O_2 loading and unloading in the lung and the periphery via the P_{50} of the ODC. Adapted, with permission, from (168).

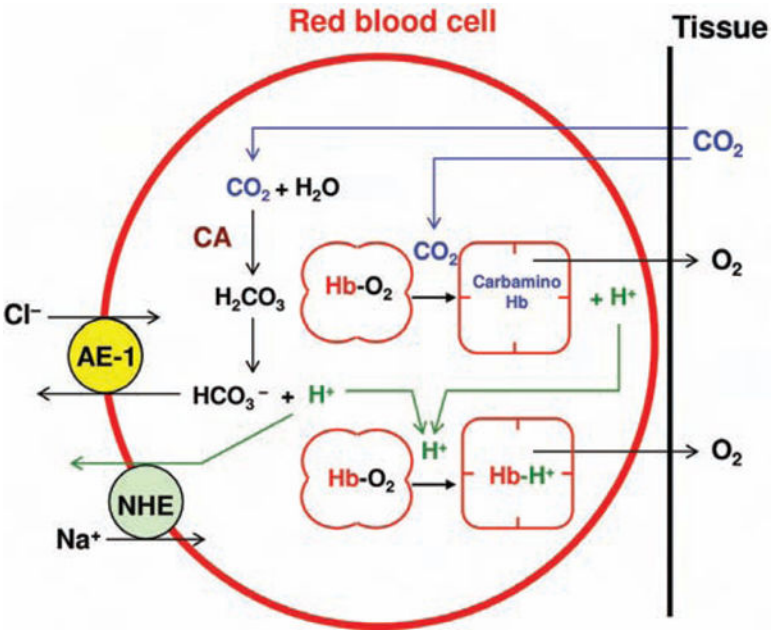

Figure 74.

Coupled O_2 and CO_2 exchange by erythrocytes. In peripheral capillaries, CO_2 diffuses from tissue into erythrocytes and is converted by carbonic anhydrase (CA) to bicarbonate (HCO_3^-) and proton (H^+). Proton binds to a histidine residue on globin to stabilize the deoxyhemoglobin conformation, thereby facilitating O_2 release to tissue. CO_2 also binds directly to oxyhemoglobin to form carbaminohemoglobin, which facilitates O_2 release. Bicarbonate is shuttled out of the cell via the membrane transporter anion exchanger (AE)-1. Any excess H+ ions are shuttled out of the cell via the NHE. In pulmonary capillaries, these reactions run in reverse.

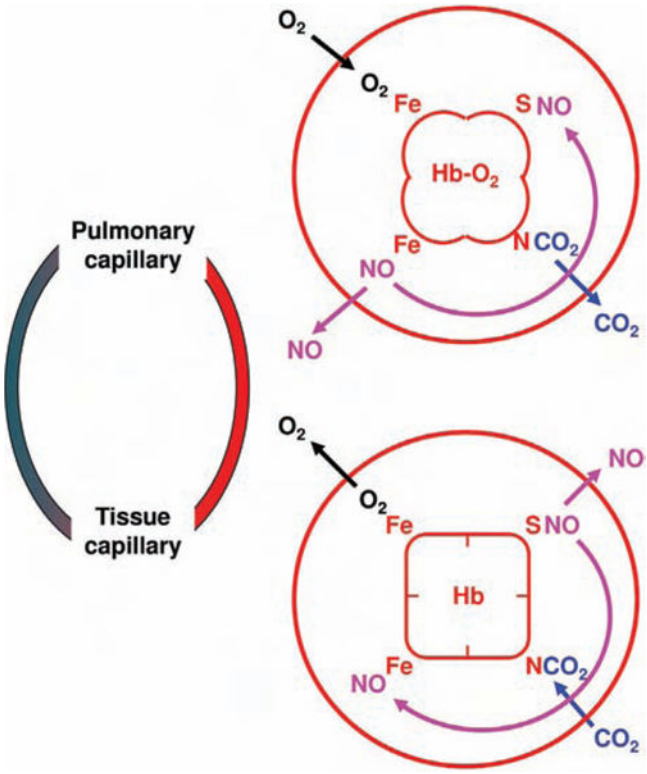

Figure 75.

Allosteric O_2-CO_2-NO interactions with hemoglobin (Hb) inside erythrocytes. CO_2 binds to terminal amine groups of the globin chain to form carbamino (NCO_2) hemoglobin. NO can bind to sulfhydryl groups at a cysteine residue (Cysβ93) to form S-nitrosohemoglobin (SNO-Hb) or be scavenged by the ferrous (Fe) binding site. In the pulmonary capillary, inspired O_2 reacts with Fe to form oxyhemoglobin (HbO_2), causing conformational changes that facilitate unloading of CO_2 from NCO_2 and NO from Fe-binding sites while facilitating the formation of SNO-Hb. The exact opposite process occurs in peripheral capillaries where O_2 is unloaded from HbO_2. Conformational changes associated with the formation of deoxyhemoglobin (Hb) facilitates CO_2 loading to form NCO_2 as well as NO dissociation from SNO-Hb. The released free NO may be scavenged by the Fe binding sites or bind other thiol carriers and exit the erythrocyte to modulate local vasodilation. These coupled interactions optimize gas exchange in the lung and the periphery.

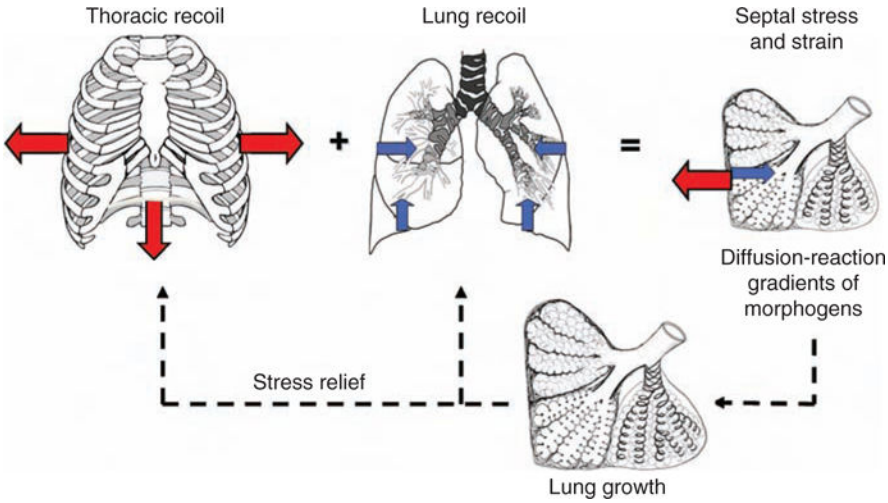

Figure 76.
Mechanical interactions between the lung and the thorax during lung growth. Adapted, with permission, from (154).

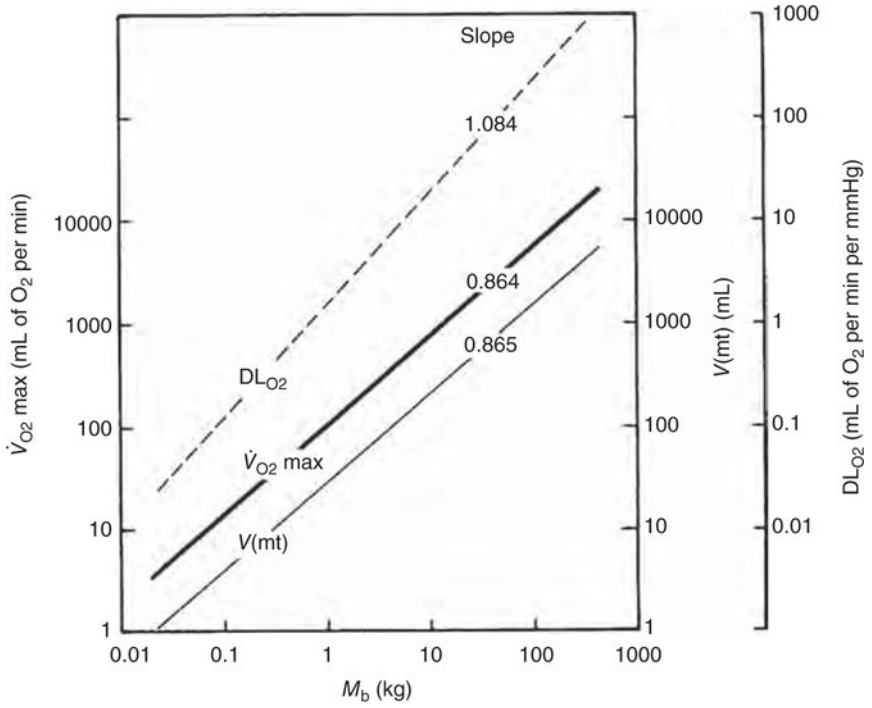

Figure 77.

Allometric scaling of maximal O_2 consumption $\left(\dot{V}_{O_2}max\right)$, muscle mitochondrial volume [V(mt)], and morphometric pulmonary diffusing capacity (DL_{O2}) in mammals weighing from 20 g to 500 kg. Taken, with permission, from (396).

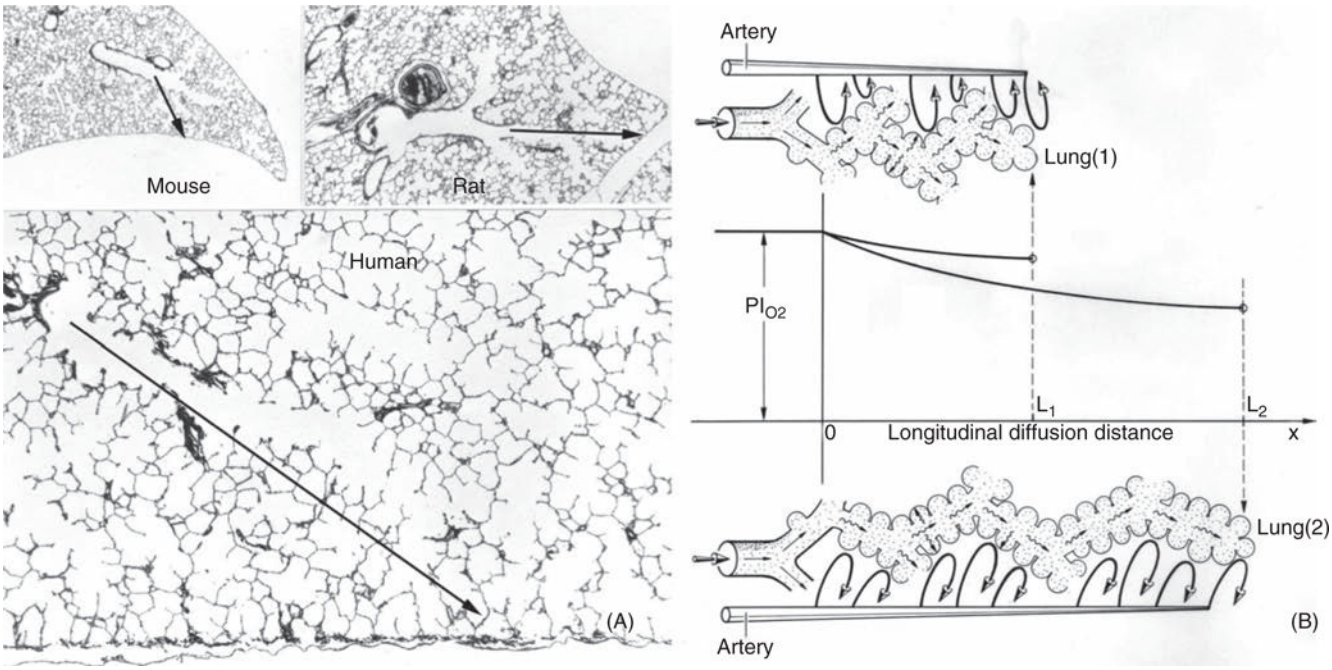

Figure 78.

Effect of the size of acinar pathway on the PO_2 profile at the alveolar surface. (A) Micrographs of mouse, rat, and human acini at same magnification; arrows indicate path length. (B) Model acini of different length showing parallel perfusion and serial ventilation with hypothetical PO_2 profiles. Taken, with permission, from (376).

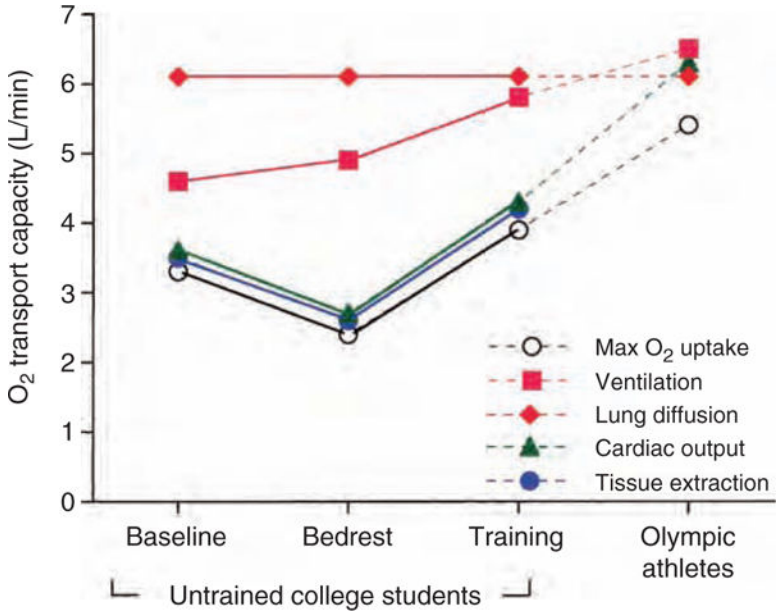

Figure 79.

Matching the capacities of O_2 transport components. Maximal O_2 uptake and the capacities of the transport steps are shown in untrained college students at baseline, and after bed rest and physical training, compared to elite Olympic athletes. The capacities of cardiac output and peripheral tissue O_2 extraction are much more malleable to physical training than that of ventilation or lung diffusion. In Olympic athletes, all capacities are well matched. Data are from Saltin et al. (306). Adapted, with permission, from (151).

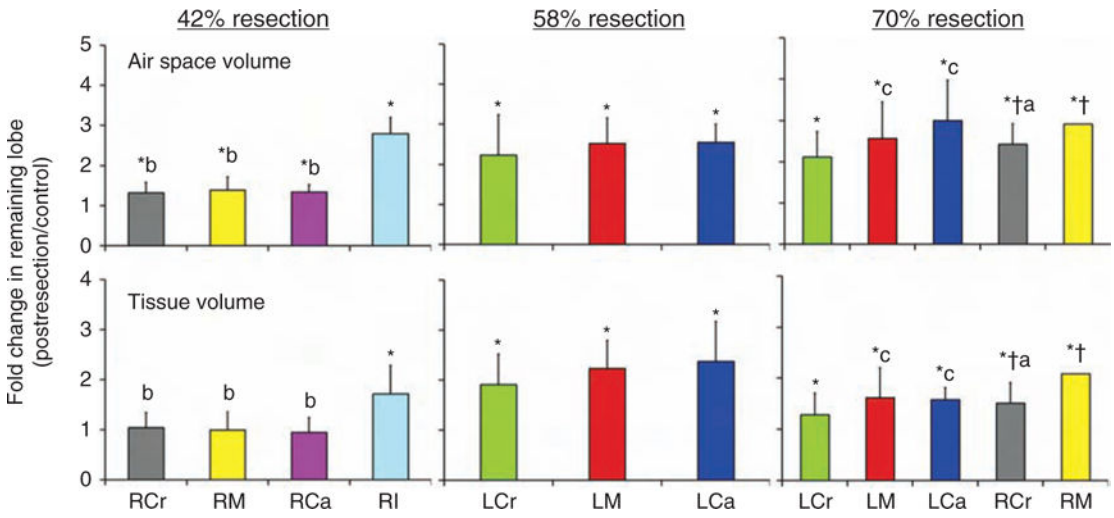

Figure 80.

Stimulus-response relationships in canine compensatory lung growth. Average fold changes in air space volume (*top*) and extravascular alveolar tissue volume (*bottom*) are shown in individual adult canine lobes that remain following different degrees of lung resection. Data are expressed as ratios with respect to the same lobe in control animals following sham lung resection. *Left:* 42% resection by left pneumonectomy; *middle:* 58% resection by right pneumonectomy; *right:* 70% resection by bilateral removal of four or five of the seven lobes. Mean ± SD. $P < 0.05$, * versus control (1.0); † versus 42%; a, versus right middle (RM) lobe; b, versus right infracardiac (RI) lobe; c, versus left cranial (LCr) lobe. Other lobes are RCr: right cranial, RCa: right caudal, LM: left middle (also known as inferior segment of LCr lobe), LCa: left caudal. Taken, with permission, from (297).

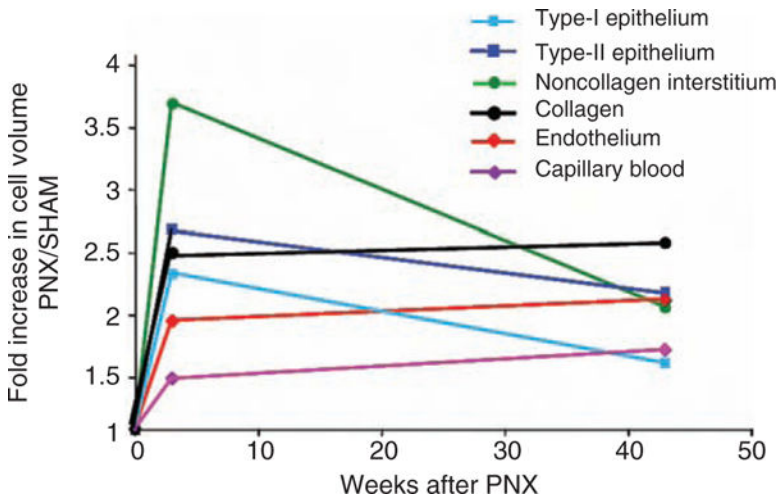

Figure 81.

Relative increases in the volume of septal tissue and blood components in the remaining lung of young canines (~3 months old) 3 weeks (Hsia, original data) or ~43 weeks (338) after undergoing right pneumonectomy. Data are expressed as ratios to that in the corresponding lung of control animals following sham pneumonectomy.

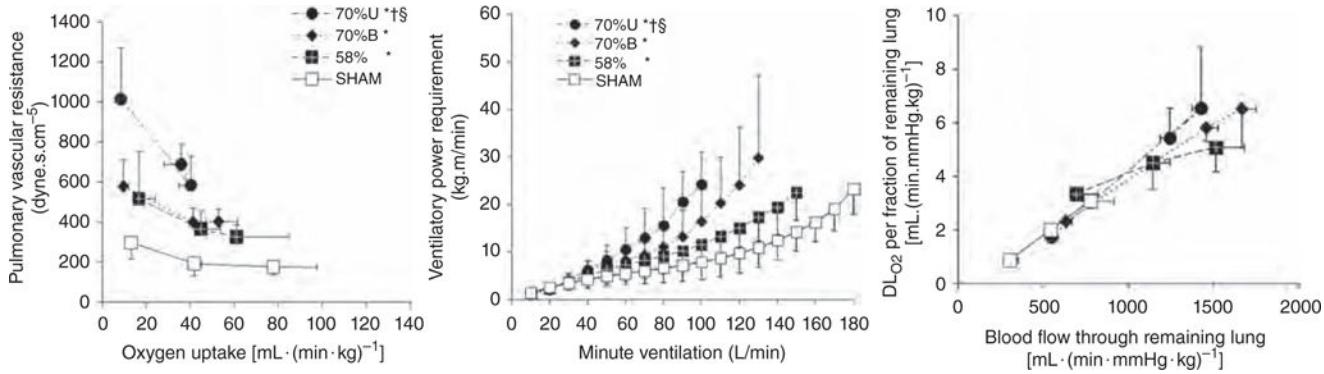

Figure 82.

Functional consequences of dysanaptic lung growth. Pulmonary vascular resistance at a given O_2 uptake (*left*) and ventilatory power requirement at a given minute ventilation (*middle*) increase with increasing lung resection (removing 58% or ~70% of total lung units) and with mediastinal distortion (U: unbalanced resection, removing ~55% and ~15% of total lung units from right and left sides respectively. B: Balanced resection, removing ~35% of total units from each side) while DL_{O2} per unit of remaining lung continues to increase along a similar relationship with respect to pulmonary blood flow (*right*), indicating more vigorous compensation in alveolar function compared to that in bronchovascular function. Values are mean ± SD. *$P < 0.05$ versus Sham. † $P < 0.05$ versus 58%. § $P < 0.05$ versus 70% balanced. Adapted, with permission, from (155).

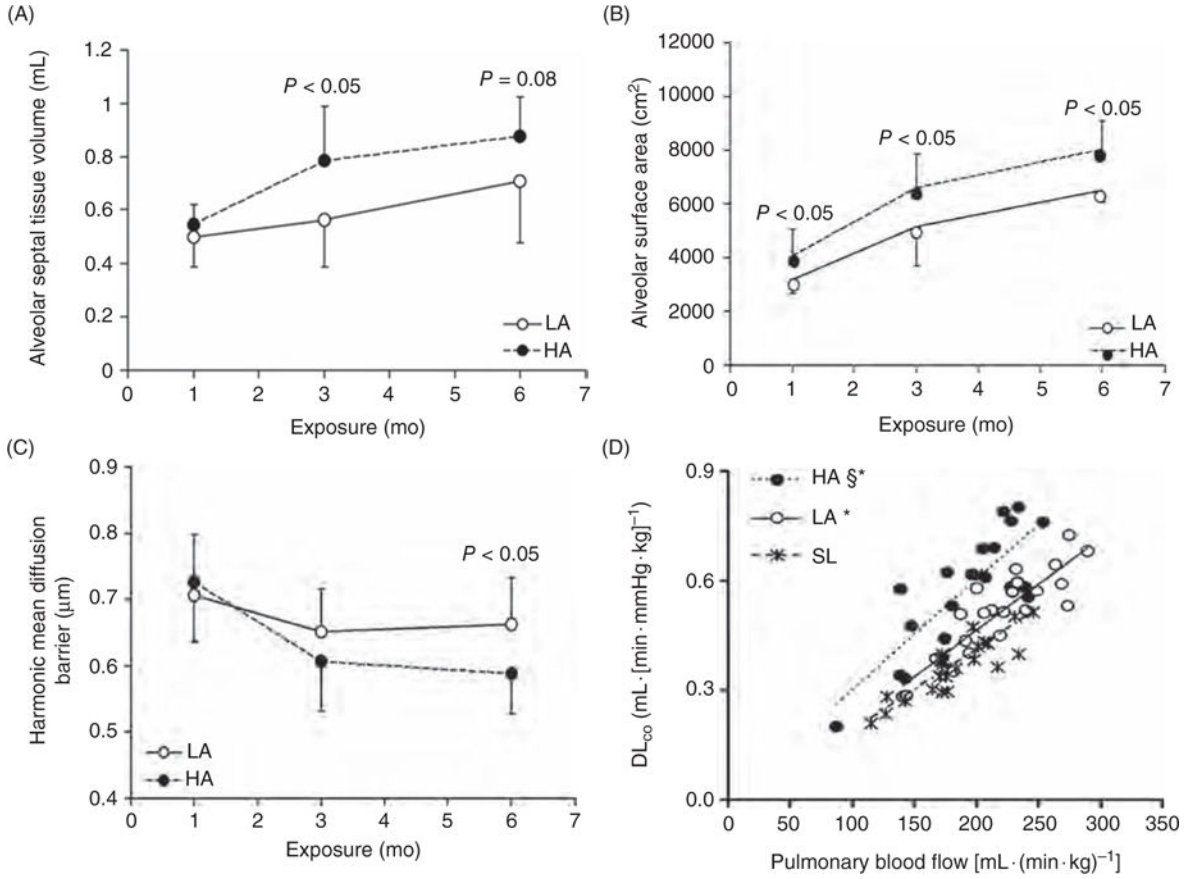

Figure 83.

Structural and functional compensation in guinea pig lungs during high altitude (HA, 3800 m) residence compared to control animals raised at a lower altitude (LA, 1200 m) or sea level (SL). (A) Alveolar septal tissue volume. (B) Alveolar surface area. (C) Harmonic mean thickness of the diffusion barrier. Adapted from (180). (D) Lung diffusing capacity for carbon monoxide (DL_{CO}) with respect to pulmonary blood flow measured after 4 months of exposure. *$P < 0.05$ versus SL, § $P < 0.05$ versus LA by comparison of regression lines. Adapted, with permission, from (414).

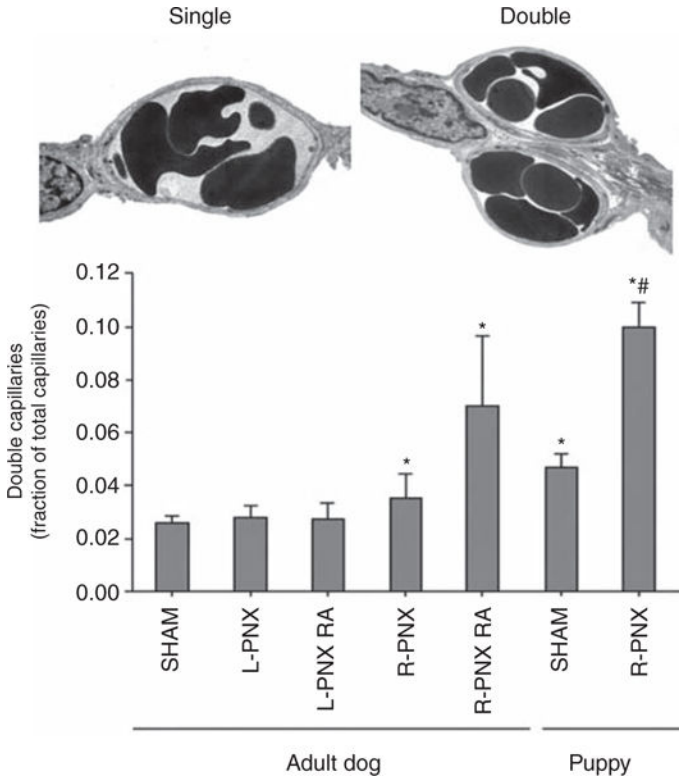

Figure 84.

An increased prevalence of "double capillary" profiles reflects an attempt at new alveolar capillary formation but also distorts alveolar septal architecture. Electron micrographs illustrate typical double and single alveolar capillary profiles. Bar graph shows the prevalence of double capillary profiles in the lung of adult dogs and puppies under different experimental conditions. Mean ± SD. Sham: normal; L-PNX: left pneumonectomy; R-PNX: right pneumonectomy; RA: pneumonectomy followed by all-trans-retinoic acid supplementation. $^{*}P < 0.05$ versus adult Sham; $^{\#}P < 0.05$ versus puppy Sham. Adapted, with permission, from (169).

Table 1

Morphometric Estimate of D_{LO_2} for Young, Healthy Adults (70-kg Body Weight, 175 cm Height)[a]

Morphometric data (mean ± 1 SE)			
Total lung volume (60% TLC)	4340	±285	mL
Alveolar surface area	130	±12	m^2
Capillary surface area	115	±12	m^2
Capillary volume	194	±30	mL
Air-blood tissue barrier thickness			
Arithmetic mean	2.2	±0.2	μm
Harmonic mean	0.62	±0.04	μm
Total barrier thickness			
Harmonic mean	1.11	±0.1	μm

		θ_{O2} (mL O_2·min^{-1}·$torr^{-1}$·mL(blood)$^{-1}$)		
***Conductances* (mL/min/mmHg)**		***1.5*[b]**	***3.0*[c]**	***1.8*[d]**
Membrane	D_{MO_2}	332	332	332
Erythrocytes	D_{EO_2}	319	639	383
Total	D_{LO_2}	163	219	178

[a] From Gehr et al. (109) and Weibel et al. (388).

[b] Holland et al. (142).

[c] Introducing "slowing factor" of Holland et al. (141, 142).

[d] "Effective" mean θO_2 considering fall along capillaries.

Table 2

Variation of Parameters Determining DL with Respiratory Dynamics–Human Lung

Parameter		Units	Air inflated–perfusion fixed[a,b,c] 40%TLC	60%TLC	80%TLC	Instillation fixed[d,e]
S(af)	Surface-alveoli free	m^2	67.6	74.1	88.4	130
S(c)[h]	Surface-capillaries	m^2	93.2	93.2	93.2	115
(Saf + Sc)/2	Surface-effective	m^2	80.4	83.7	90.8	122.5
V(c)[h]	Volume-capillaries	mL	180	180	180	194
Vc/[(Saf + Sc)/2]	Capillary volume/(surface-effective)	μm	2.24	2.15	1.98	1.58
τ_{ht}[f]	Tissue thickness-harmonic mean	μm		0.48[f]		0.62
τ_{hb}[f,g,h]	Total barrier thickness-harmonic mean	μm	0.97	0.97	0.97	1.11
DM_{O2}	Membrane-diffusing[i] capacity	mL/s·torr	4.56	4.75	5.14	6.06
De_{O2}	Erythrocyte-diffusing[i] capacity	mL/s·torr	4.5	4.5	4.5	4.85
DL_{O2}	Total diffusing[i] capacity	mL/s·torr	2.26	2.31	2.40	2.69

[a] Bachofen et al. (1987) (7).

[b] Bachofen et al. 1982 (8).

[c] Bachofen et al. (1983) (9).

[d] Gehr et al. (1978) (109).

[e] Weibel et al. (1993) (388); new model for DM.

[f] Weibel et al. (1973) (398); DL in perfusion-fixed rat lungs: τ_{ht}(perf) is reduced to about 0.7–0.8 τ_{ht} (instill).

[g] Total barrier thickness in perfused rabbit lungs estimated reducing instillation-fixed value by the difference in tissue barrier thickness only.

[h] It is assumed that variation in air inflation does not alter the values for capillary surface or volume, nor of total barrier thickness.

[i] $DM_{O2} = K_b \phi S(A)/\tau_{hb}$, where $K_b = 5.5 \cdot \times 10^{-10}$ cm^2 s^{-1} $torr^{-1}$, $\phi S(A)$ is the free alveolar surface S(af) and τ_{hb} the harmonic mean total barrier thickness (4). $De_{O2} = \theta \cdot V(c)$ where $\theta = 0.025$ mL O_2·mL $blood^{-1}$·s^{-1}·$torr^{-1}$.

Table 3

Typical Path Model of Human Airway Tree

Generation *z*	Number *N(z)*	Airway segment diameter *d(z)*	Airway segment length *l(z)*	Distance from carina to end of generation *z* Dist (0-*z*)	Total airway cross-section in generation *z* *A(z)*
		cm	cm	cm	cm^2
0	1	1.800	12	0	2.54
1	2	1.220	4.76	4.76	2.33
2	4	0.830	1.90	6.66	2.13
3	8	0.560	0.76	7.42	2.00
4	16	0.450	1.27	8.69	2.48
5	32	0.350	1.07	9.76	3.11
6	64	0.280	0.90	10.66	3.96
7	128	0.230	0.76	11.42	5.10
8	256	0.186	0.64	12.06	6.95
9	512	0.154	0.54	12.60	9.56
10	1,024	0.130	0.46	13.06	13.4
11	2,048	0.109	0.39	13.45	19.6
12	4,096	0.095	0.33	13.78	28.8
13	8,192	0.082	0.27	14.05	44.5
14	16,384	0.074	0.23	14.28	69.4
15	32,768	0.050	0.14	14.42	117.0
16	65,536	0.050	0.133	14.55	225.0
17	131,072	0.049	0.112	14.66	300.0
18	262,144	0.040	0.093	14.76	543.0
19	524,288	0.038	0.083	14.84	978.0
20	1,048,576	0.036	0.070	14.91	1743.0
21	2,097,152	0.034	0.070	14.98	2733.0
22	4,194,304	0.031	0.070	15.05	5070.0
23	8,388,608	0.029	0.070	15.12	7530.0

Source: Weibel 1997 (379).

Table 4

Typical Path Model of Human Acinus

Generation		Segments			Dimensions per generation				Path length
Airways z	Acinus z′	$N(z')$	l mm	d_{in} mm	$A_d(z')$ mm^2	$V_d(z')$ mm^3	$S_{alv}(z')$ mm^2	$V_c(z')$ mm^3	$L_p(z')$ mm
15	0	1	1.4	0.50	0.20	0.32	7	0.0104	1.4
16	1	2	1.33	0.50	0.39	0.52	23	0.0345	2.73
17	2	4	1.12	0.49	0.75	0.84	67	0.1005	3.85
18	3	8	0.93	0.40	1.00	0.93	129	0.1935	4.78
19	4	16	0.83	0.38	1.81	1.50	219	0.3285	5.61
20	5	32	0.70	0.36	3.26	2.28	349	0.5235	6.31
21	6	64	0.70	0.34	5.81	4.07	661	0.9915	7.01
22	7	128	0.70	0.31	9.11	6.38	1204	1.8060	7.71
23	8	256	0.70	0.29	16.9	13.47	2720	4.0800	8.41

Source: Weibel et al. 2005 (394).